Search for rare Higgs boson decays at a center of mass energy of $\sqrt{s} = 13$ TeV with the CMS Experiment at the LHC

Dissertation

zur Erlangung des Doktorgrades

an der Fakultät für
Mathematik, Informatik und Naturwissenschaften

Fachbereich Physik
der Universität Hamburg

vorgelegt von

Torben Lange

im Jahr

2022

in

Hamburg

Gutachter/innen der Dissertation:		
	Prof. Dr. Peter Schleper	Universität Hamburg
	Jun.-Prof. Dr. Gregor Kasieczka	Universität Hamburg
Zusamensetzung der Prüfungskommission:		
	Prof. Dr. Caren Hagner	Universität Hamburg
	Prof. Dr. Peter Schleper	Universität Hamburg
	Jun.-Prof. Dr. Gregor Kasieczka	Universität Hamburg
	Prof. Dr. Christophe Grojean	DESY / Humboldt-Universität zu Berlin
	Prof. Dr. Elisabetta Gallo	DESY / Universität Hamburg
Vorsitzende/r der Prüfungskommission:	Prof. Dr. Caren Hagner	Universität Hamburg
Vorsitzender Fach-Promotionsschuss PHYSIK:	Prof. Dr. Wolfgang J. Parak	Universität Hamburg
Leiter des Fachbereichs PHYSIK:	Prof. Dr. Günter H. W. Sigl	Universität Hamburg
Dekan der Fakultät MIN:	Prof. Dr. Heinrich Graener	Universität Hamburg
Datum der Disputation:		28th. of April 2022

Abstract

After the discovery of the Higgs boson in 2012, several of its key properties remain unmeasured, including the Higgs boson couplings to second generation fermions and the trilinear Higgs boson self-coupling. In this thesis a contribution to the first evidence of Higgs boson decays into muons ($\mathrm{H} \to \mu\mu$) and a contribution to a search for Di-Higgs boson production in final states with multiple leptons ($\mathrm{HH} \to$ Multilepton) is presented, providing crucial tests of the Standard Model of particle physics.

The main focus of this thesis lies within the $\mathrm{HH} \to$ Multilepton analysis and its $3\ell + 1\tau_\mathrm{h}$ event category. The $3\ell + 1\tau_\mathrm{h}$ category provides the strongest individual results of the analysis, especially in physics scenarios with high (positive) κ_λ or small Di-Higgs invariant masses.

For the $\mathrm{HH} \to$ Multilepton analysis, seven different event categories are devised covering different final states aimed at HH decays both into vector bosons and tau leptons. For each category, a set of parameterized boosted decision trees is trained, separating the HH signal from a set of different background processes such as single, double, and triple vector boson production, single Higgs boson production and top-quark related backgrounds. The signal extraction is then performed on adequately binned BDT distributions. Here, the background estimation for processes involving misidentified leptons or leptons with misidentified charge feature data-driven methods such as the Fake-Factor method.

Results include an observed (expected) limit at 95% CL on the signal strength modifier for Standard Model like HH production, $r = \sigma_\mathrm{HH}/\sigma^{SM}_\mathrm{HH}$, of 21.8 (19.6) and an observed (expected) limit on the coupling modifier for the trilinear Higgs boson self-coupling $\kappa_\lambda = \lambda_\mathrm{HHH}/\lambda^{SM}_\mathrm{HHH}$ of $-6.98 < \kappa_\lambda < 11.17$ ($-6.98 < \kappa_\lambda < 11.73$). Further limits on resonant Di-Higgs boson production via a new, hypothetical heavy spin-0 or spin-2 resonance in the mass range between 250 GeV and 1 TeV, as well as on non-resonant EFT HH production are investigated.

Kurzfassung

Nach der Entdeckung des Higgs-Bosons in 2012 sind mehrere seiner wichtigsten Eigentschaften bisher noch unerforscht. Das schließt die Higgs-Boson-Kopplung an Fermionen der zweiten Generation, sowie die trilineare Higgs-Boson-Selbstwechselwirkung ein. Diese Arbeit präsentiert Beiträge zur ersten Evidenz von Higgs-Boson-Zerfällen in Myonenpaare ($\mathrm{H} \to \mu\mu$) sowie zur Suche nach Doppel-Higgs-Boson-Produktion in Endzuständen mit mehereren Leptonen ($\mathrm{HH} \to$ Multilepton) und leistet so Beiträge zu wichtigen Tests des Standardmodells der Teilchenphysik.

Der Hauptfokus der Arbeit liegt auf der $\mathrm{HH} \to$ Multilepton Studie und seiner $3\ell + 1\tau_\mathrm{h}$ Ereigniskategorie. Die $3\ell + 1\tau_\mathrm{h}$ Kategorie liefert hierbei die stärksten Einzelergebnisse der Analyse, insbesondere für Physikszenarien mit besonders hohem (positivem) κ_λ oder niedriger invarianten Doppel-Higgs-Boson-Masse.

Für die $\mathrm{HH} \to$ Multilepton Studie werden sieben Ereigniskategorien definiert, welche auf Higgs-Boson-Zerfälle sowohl in Vektor-Bosonen als auch Tau-Leptonen gerichtet sind. Für jede Kategorie wird eine Reihe an parametrisierten Boosted-Decision-Trees zur Trennung des HH Signals von Untergrundprozessen wie Einzel-, Doppel- und Dreifach-Vektor-Boson-Produktion, Einzel-Higgs-Boson-Produktion und Untergrundprozessen mit Top-Quarks trainiert. Die Signalextraktion erfolgt dann auf den histogrammierten Ausgabeverteilungen. Die Untergrundbestimmung für Prozesse mit fehlidentifizierte Leptonen oder Leptonen mit Ladungsfehlmessung erfolgt durch datengetriebene Methoden wie der Fake-Faktor Methode.

Ergebnisse enthalten sowohl eine beobachtete (erwartete) obere Grenze mit 95% Konfidenzintervall auf die Signalstärke für standardmodellartiege Doppel-Higgs-Boson-Produktion $r = \sigma_{\mathrm{HH}}/\sigma_{\mathrm{HH}}^{SM}$ von 21.8 (19.6) sowie eine beobachtete (erwartete) Einschänkung auf den Kopplungsmodifikator der trilinearen Higg-Boson-Sselbstwechselwirkung $\kappa_\lambda = \lambda_{\mathrm{HHH}}/\lambda_{\mathrm{HHH}}^{\mathrm{SM}}$ von $-6.98 < \kappa_\lambda < 11.17$ ($-6.98 < \kappa_\lambda < 11.73$). Desweiteren werden sowohl resonante Doppel-Higgs-Boson-Produktion im Massenbereich von 250 GeV bis 1 TeV sowie nichtresonante EFT-Doppel-Higgs-Boson-Produktion untersucht.

List of publications

For the work presented in this thesis, (essential) contributions to the following publications have been made:

- CMS Collaboration, " Search for Higgs boson pairs decaying to WWWW, WW$\tau\tau$, and $\tau\tau\tau\tau$ in proton-proton collisions at $\sqrt{s} = 13$ TeV ", CMS-PAS-HIG-21-002, 2022, http://cds.cern.ch/record/2799151
- CMS Collaboration, "Evidence for Higgs boson decay to a pair of muons", JHEP 01 (2021), doi: 10.1007/JHEP01(2021)148, arXiv: 2009.04363

In addition, these experiment-internal documents have been prepared:

- T. Lange on behalf of the CMS pixel online team, "Measurement and optimization of the soft-error-recovery rates in the phase 1 pixel detector", CMS Detector Note CMS DN-2018/030 [CMS Internal], 2020
- D. Acosta, M. Alhusseini, P. Azzurri, P. Bortignon, D. Bourilkov, A. Brinkerhoff, S. Cooperstein, I. Dutta, R. Gerosa, L. Giannini, M. Klute, D. Kondratyev, T. Kramer, T. Lange, N. Lu, G. Mandorli, A. Marini, J. Nachtman, N. Neumeister, Y. Onel, J. Pata, O. Rieger, A. Rizzi, V. Sharma, P. Schleper, M. Spiropulu, A. Vartak, J. Vlimant, S. Xie , and X. Zuo, "Hmm analysis with the full Run2 dataset", CMS Analysis Note CMS AN-2019/124 [CMS Internal], 2020
- S. Bhowmik, A. Carvalho, R. K. Dewanjee, K. Ehataht, M. Kadastik, L. Tani, S. Sawant, C. Veelken, A. Brinkerhoff, P. Schleper, T. Kramer and T. Lange, "Search for Higgs boson pair production in multi-lepton final states using the full Run 2 dataset", CMS Analysis Note CMS AN-2020-032 [CMS Internal], 2021

Everything we know about them was wrong

- Hiccup, How to train your dragon (2010)

Amends

I would like to thank Peter Schleper, who was not only the main supervisor of my thesis but guided me through most of my scientific career. I would like to thank him for all the interesting talks we had, for his inspiration and for his enthusiasm that more than once ignited my own, thus making this incredible journey possible in the first place!
Thanks also go to Gregor Kasieczka for sharing his machine learning experience with me, providing valuable insight for both my master as well as my PhD thesis. Naturally I also would like to thank Caren Hagner, Christophe Grojean and Elisabetta Gallo, both for joining my committee as well as their extremely fast response time!
As I spend almost 6 years in the CMS group of the University of Hamburg, it almost feels like home and I am glad that I joined this welcoming and always helpful family of particle physicists. Thank you for having me all these years! Here I especially want to point out Tobias Kramer, Alexandra Tews, Malte Mrovietz, Johannes Lange, Moritz Wolf, Caroline Niemeyer, Steffen Albrecht and Karla Pena which whom I spent much time over the years on board game evenings, Doppelkopf evenings and otherwise. Thanks go also to my former colleagues Benedikt Vormwald and Jory Sonneveld for the great time at CERN I had with them and to Oliver Rieger with whom I and Tobias Kramer worked hard on the $\mathrm{H} \to \mu\mu$ analysis. Special thanks go to Marcel Rieger and Tobias Kramer who worked closely with me on the topic of Di-Higgs physics, provided valuable feedback for my thesis, and who had to endure my stressed self in the last couple of weeks of finishing my thesis. Also thank you Marcel Rieger for fixing my bike :). Thanks go also to Karla Pena, who together with Marcel Rieger joined me as a coffee companion, providing the necessary caffeine and fun needed to finish the last pages of my thesis. I am also thanking my office mate Stella Schaefer, who brightened my last days at the institute, laughing even about my stupidest jokes and sharing my hobby of worrying about everything. To all of you, and those I missed in this list, thank you all and I will miss you!
I would also thank my new group around Christian Veelken and everyone who was involved in the $\mathrm{HH} \to$ Multilepton analysis. When looking for the right HH analysis I was lucky to find you guys and I would like to thank you for this great collaboration. I would like to thank especially Karl Ehatäht and Laurits Tani for many fruitful Skype discussions. I am looking forward to work with you in the future.
All of this would have not been possible without my family and my friends, especially Pascal Stinemeier, Felix Giese and Alicia Wongel. Felix and Pascal you have endured me through my whole university studies and gifted me the best photo book in the world. I am looking forward to many more years of shared history and wonderful vacations. To Alicia, while you joined me and Pascal only latter, you always provided me with honest council and true friendship, and even shelter for the final days of my PhD! It is a privilege to have you all in my life.

Contents

1 Introduction

The Standard Model of particle physics developed over the last century is the so far most successful theory in describing the fundamental particles of nature and the forces between them. With the discovery of the famous Higgs boson in 2012 by the CMS and ATLAS collaborations [1, 2] all fundamental particles predicted within the context of this gauge theory have been found. While the Standard Model of particle physics describes most phenomena in agreement with experimental high energy physics data, it is not the only model and it can not explain all astrophysical observations, only to be explained by new physics beyond the Standard Model of particle physics.

In the search for new physics, this thesis focuses on the remaining unmeasured properties of the Higgs boson, to verify if it is indeed the Standard Model Higgs boson or if it carries hints of new physics beyond the Standard Model. With this thesis, contributions in two major projects are reported: the search for the decay of Higgs bosons into a pair of muons where evidence could be claimed in the CMS $\mathrm{H} \to \mu\mu$ analysis [3] and the study of processes involving the production of two Higgs bosons, resulting in the CMS $\mathrm{HH} \to$ Multilepton analysis [4].

The latter is the main focus of this thesis and involves the search for Di-Higgs boson production in final states with multiple leptons. In this, both non-resonant Di-Higgs boson production featuring so far undiscovered couplings predicted by the Standard Model of particle physics, non-resonant Di-Higgs boson production via Beyond Standard Model EFT couplings and resonant Di-Higgs boson production featuring a new massive spin-0 or spin-2 boson decaying into Higgs-Boson pairs are studied. This thesis features major contributions in the $3\ell + 1\tau_{\mathrm{h}}$ event category, the study of control regions relevant also for other final states and the combined analysis of all $\mathrm{HH} \to$ Multilepton final state categories. For the latter, a physics model is developed enabling the scanning in an EFT coupling space and is also to be used in other upcoming CMS Di-Higgs boson searches.

The thesis is structured in the following manner: Sec. 2 discusses the Standard Model of particle physics and the role of the Higgs boson within it, as well as the phenomenology and theoretical motivation of Di-Higgs boson production. Sec. 3 describes the Large Hadron Collider and the data taking with the CMS experiment. Sec. 3.3 features a contribution made to the operation of the CMS detector made during the work on this thesis. Sec. 4 explains the machine learning tools used in this thesis. The CMS $\mathrm{H} \to \mu\mu$ analysis is briefly discussed in Sec. 5 while Sec. 6 contains the $\mathrm{HH} \to$ Multilepton analysis. The results of the $\mathrm{HH} \to$ Multilepton analysis as well as the current CMS and ATLAS HH efforts and a comparison of these results to previous HH measurements is then presented in Sec. 7. Finally Sec. 8 summarizes the achievements of the presented analysis and concludes this thesis.

2

The Higgs Boson within and beyond the Standard Model

The Standard Model of particle physics (SM) is the most successful theory in describing the fundamental laws of nature, that is the laws of particles and their interactions via gauge bosons and Higgs (Yukawa) interactions. It is able to describe all fundamental particles known to mankind as well as the electromagnetic, weak and strong forces between them. Only the theory of gravity as entailed in the general theory of relativity and the so far not understood phenomena of dark matter and dark energy are currently not covered by this theory. Otherwise it is consistent with almost all experimental observations and all particles predicted by the SM are discovered by now. The last of the jigsaw pieces in the puzzle that is the SM, was the Higgs boson discovered in 2012 by the CMS and ATLAS collaborations [1, 2]. The following chapter aims at describing the SM of particle physics and the role of the Higgs boson within it. Sec. 2.1 looks at the general structure and the particle content of the SM and discusses a few of its shortcomings. In Sec. 2.2 the Higgs boson is introduced and its importance for the self consistency of the SM explained. The next sections deal with more specific properties of the Higgs boson connected to the physics studied within this thesis, with Sec. 2.3 and Sec. 2.4 dealing with the Higgs boson self-interaction and other processes connected to Di-Higgs boson production.

2.1 The Standard Model of Particle Physics

The SM developed over the course of the last century describes nature as a quantum field theory. It explains the interaction of spin-$\frac{1}{2}$ matter particles (fermions) by the exchange of spin-1 gauge bosons. Whether a fermion participates in one of the three interactions, electromagnetic, weak, or strong, depends on the charges it carries, which are related to the coupling constants to the different gauge bosons. For example, the well-known electric charge determines if a particle such as the electron participates in the electromagnetic interaction by photon exchange. In the same way the weak isospin of a particle determines its participation in weak interactions and color charged particles interact via the strong force. Fig. 2.1 shows the particle content of the SM and the different properties of its constituents. In the figure, the particles are grouped by their roles in the standard model. The quarks are the color-charged fermions forming baryonic matter such as mesons and hadrons. The leptons on the other hand are not color charged with the extremely light and electrically neutral neutrinos only interacting via the weak interaction. The most prominent (electrically) charged lepton, the electron, forms together with up and down

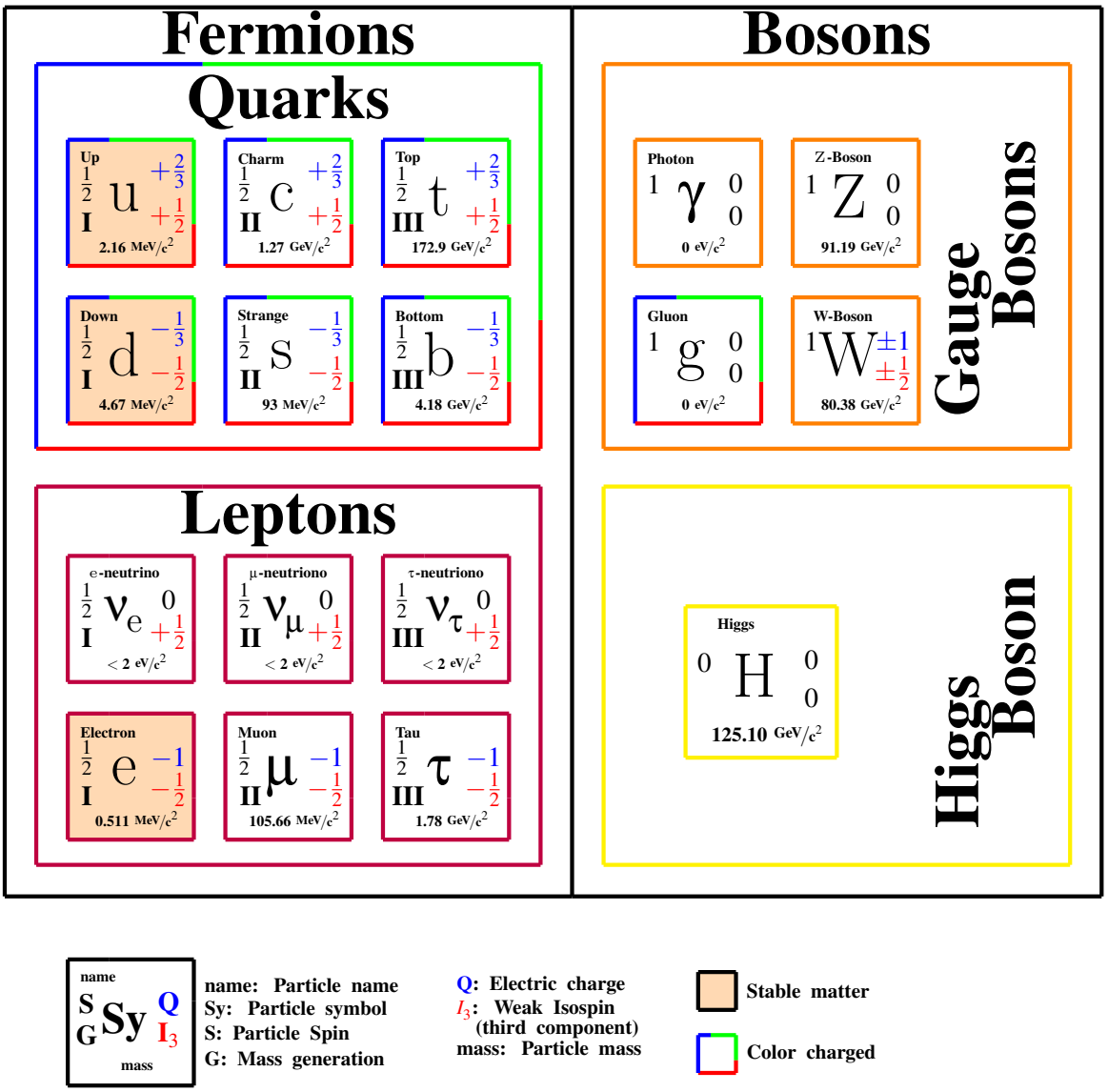

Figure 2.1: The fundamental particles in the standard model of particle physics with their respective quantum numbers grouped by their roles in the SM. The participation in one of the three forces is either indicated by a colored quantum number for the electromagnetic (blue) and weak force (red) or by a multi-colored frame for the strong force. The three particles forming atoms and thus the stable matter around us, the up quark, down quark and the electron are highlighted as well. The given masses are taken from [5].

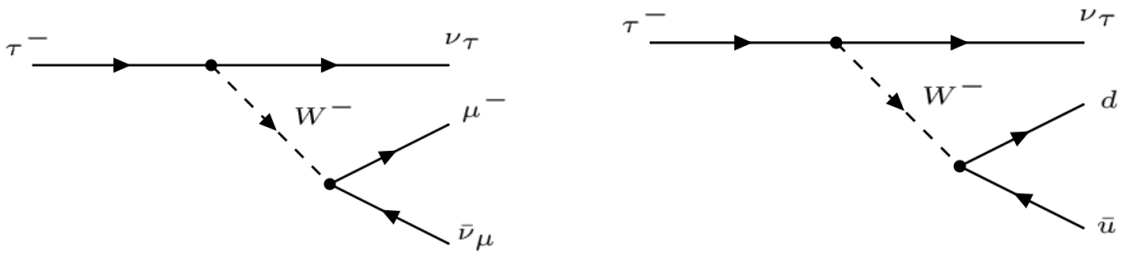

Figure 2.2: Feynman diagrams for the leptonic (**left**) and hadronic (**right**) decay of a tau lepton.

quarks the stable matter around us. The gauge bosons mediate the forces between the fermions based on their quantum charge numbers. Gauge bosons like the color charged gluon carry charge themselves, allowing also for bosonic self interactions. Finally the Higgs boson, the only spin-0 (scalar) particle of the SM, interacts with all SM particles based on their mass. The quarks and leptons come in six flavors and three generations each. The 2nd. (II) and 3rd. (III) generation fermions are heavier copies of the 1st. (I) generation particles with the same quantum numbers and interactions. As for the six flavours, for each generation the SM provides a doublet of an up and a down type particle. The up and down type particles differ in electric charge and weak isospin allowing for transitions between them via the W bosons of the weak interaction. This can be seen in Fig. 2.2 showing two possible decays of a tau lepton. The graphs in Fig. 2.2 are examples of Feynman diagrams which are not only a useful tool in understanding certain interactions but actually graphic representations of the complex integrals needed to calculate the cross section of the various particle physics processes. Looking at Fig. 2.2, a few more phenomenological aspects of the theory can be observed. First, as the W boson is over 40 times heavier as the initial τ lepton, the shown decay would violate energy conservation. However, as an intermediate process the quantum mechanical uncertainty principle allows to produce a particle like the W boson away from its "mass shell" as a virtual particle. Virtual particles can only exist for a short amount of time, depending on the width of the corresponding mass resonance and the virtualness describing how far away a particle is away from its resonance mass. Therefore the produced W boson has to decay almost immediately. This can either be leptonically into a muon or an electron or hadronically into a pair of quarks. In both cases a particle and an antiparticle, indicated by the bar, are produced. Anti-matter particles that exist for every fermion are charged flipped twins of their matter counterparts with the same mass and spin properties. Within the SM quantum numbers like the lepton number conserve the balance between matter and anti-matter particles meaning that they can only be produced in matter/anti-matter pairs. Lastly, the hadronic W boson decay on the right side of Fig. 2.2 shows the production of color charged particles. Contrary to the weak and electromagnetic charge, color charged states cannot exist in nature, as the strong color field between two color charged particles makes it energetically more favourable to create new particles when they are separated from each other. This is known as hadronization and in case of the hadronic decaying tau in Fig. 2.2 leads to the production of a number of mesons[1] like the pion. More on tau decays and their reconstruction in experimental particle physics can be found in Sec. 3.2.11. The final aspect of Fig. 2.2 is the production of neutrinos. Neutrinos are fas-

[1] Bound states of a quark and an anti quark.

cinating for their lack of interaction with other standard model particles as they only interact via the weak force. They are also an example of the difference of flavour and mass eigenstates in the SM. The SM contains flavour mixing as given by the Pontecorvo–Maki–Nakagawa–Sakata matrix (PMNS) and the Cabibbo–Kobayashi–Maskawa matrix (CKM). In the case of the neutrinos, Fig. 2.2 shows the weak eigenstates e.g. a decay involving an electron or positron will always involve an electron (anti) neutrino. However, when measuring a particle we usually speak of a mass eigenstate with a distinct mass that is due to flavour mixing realized as a mixture of flavour eigenstates. In case of neutrinos this leads to a phenomenon known as neutrino oscillation where e.g an electron neutrino can oscillate in a muon neutrino eigenstate. While in the case of neutrinos, Fig. 2.2 cites the flavour eigenstates, for quarks, usually mass eigenstates are used. This means that the W boson cannot only connect up and down particles but also particles of different generations. In the case of the top quark however, the mixture between the 3rd. generation quark and the 1st. and 2nd. generation is quite small and top quarks decay in 99% into a bottom quark and W boson.
While the SM describes most particle observations made at high energy collider experiments nearly perfect, there are shortcomings and open questions that motivate theoretical extensions beyond standard model (BSM). The following will provide just a few examples of these with a connection to the rare Higgs boson processes discussed in this thesis.

Matter-Anti-Matter Asymmetry:

As previously discussed, matter and antimatter within the SM is produced (and annihilated) in pairs, suggesting a complete symmetry between matter and antimatter in the universe. However, a completely matter dominated universe is observed [6] around us. While the SM does not provide a mechanism to provide an explanation for an asymmetry this large, many BSM models do. These include models with extended or modified Higgs sectors as for example in [7].

Dark Matter:

Cosmological observations like the rotation curves of galaxies [8] as shown in Fig. 2.3 or the study of the cosmic microwave background [9] suggest the existence of an additional only weakly interacting matter component. With the SM not providing adequate candidates for this dark matter, SM extensions such as those including a dark sector with a Higgs boson portal are motivated. These can feature for example new heavy resonances decaying into a pair of Higgs bosons [10].

Additional symmetries:

While the SM is a complete theory with few free parameters, extensions can be made offering perspectives for a wide array of BSM phenomena. One theoretically motivated extension is the inclusion of supersymmetry. Supersymmetric models are ideal to solve multiple open questions of the SM as they can provide the CP violation needed to explain the matter anti-matter asymmetry, they provide dark matter candidates, and they also deliver an elegant theory addressing issues like naturalness and the unification of the three forces at high energies. Even minimal extensions like the MSSM [11] require an extended Higgs sector with additional Higgs like bosons.

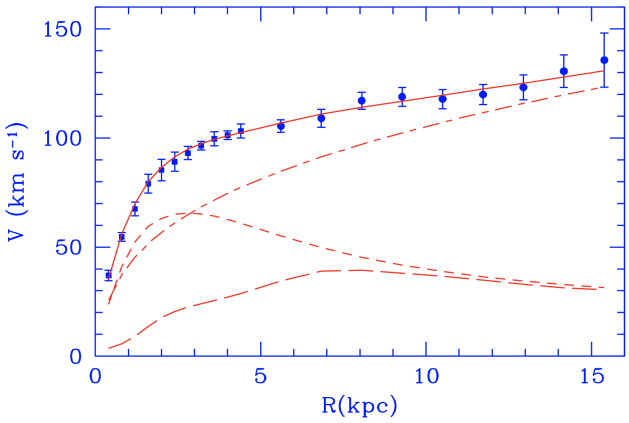

Figure 2.3: Rotation curve of the M33 galaxy as measured in astrophysical observations (points). The dashed lines show contributions from the stellar disk as gas contents of the galaxy (visible matter), the dotted-dashed lines show possible contribution of a dark matter halo and the solid line, the best fit result of a combined model [8].

Hierarchy problem:

As will be discussed in Sec. 2.2 the SM enables the unification of the electromagnetic and the weak force into one electro-weak force. From the standpoint of simplicity it would be favorable to extend this to a unification of all four fundamental forces, the electromagnetic, weak, strong force and gravity. Gravity is defined at much higher energy scales than the other forces, the Planck scale at $O(10^{19}\,\text{GeV})$. This makes the formulation of a consistent theory of everything very difficult, as the mass of particles such as the Higgs boson would receive strong corrections from higher order effects, making it difficult to keep these masses at the electroweak scale of $O(m_Z)$ [12].
An example of a theoretical model solving the hierarchy problem would be the Randall-Sundrum model. In this context, as discussed in Sec. 2.4, new heavy resonances decaying into pairs of Higgs bosons can arise.

2.2 Electroweak Unification and the Higgs Mechanism

The Higgs boson in the SM is strongly intertwined in the self-consistency of its theoretical foundation. The following will attempt a small detour into the theoretical motivations of the SM Lagrangian, the unification of the electromagnetic and weak force and subsequently the theoretical basis and properties of Higgs-Boson interactions in the SM context. As this is a well described topic in literature, more and detailed information about this topic can be found in most common particle physics textbooks such as [12] on which the following text is based heavily.

SM physics is described within the framework of quantum field theory in which fermions are described by Dirac spinors, (gauge) bosons are described by (gauge) field and their interactions arise from the requirement of invariance of the corresponding Lagrangian under local transformations of a given symmetry.
This allows the description of electromagnetic interactions in Quantum-Electro-Dynamics (QED)

via a U(1) symmetry with a local phase transformation given by:

$$\psi(x) \rightarrow \psi'(x) = e^{iq\chi(x)}\psi(x) \tag{2.1}$$

with q, the electric charge of the Dirac field ψ, and a phase shift $\chi(x)$. Applied on the Dirac equation $i\gamma^\mu\partial_\mu\psi = m\psi$, describing the relativistic properties of a Dirac field of mass m one arrives at:

$$i\gamma^\mu\partial_\mu\psi' = i\gamma^\mu(\partial_\mu + iq\partial_\mu\chi)\psi \neq i\gamma^\mu\partial_\mu\psi = m\psi \tag{2.2}$$

To fulfill the fundamental requirement of invariance under the U(1) phase transformation, an additional gauge field A_μ with the transformation property:

$$A_\mu \rightarrow A'_\mu = A_\mu + \partial_\mu\chi \tag{2.3}$$

can be introduced, restoring the U(1) invariance by introducing a new interaction term between the fermionic field ψ and the gauge field A_μ to the Dirac equation then invariant under the given transformation:

$$i\gamma^\mu D_\mu = i\gamma^\mu(\partial_\mu + iqA_\mu)\psi = m\psi \tag{2.4}$$

Similarly the weak interaction can be described by requiring the invariance under transformations in SU(2):

$$\phi(x) \rightarrow \phi'(x) = \exp[ig_W\alpha(x)\cdot\mathbf{T}]\phi(x) \tag{2.5}$$

With $\mathbf{T}$, the generators of the SU(2) group, given for example in the basis of Pauli matrices with $\mathbf{T}=\frac{1}{2}\sigma$, the local phase is given by the three functions $\alpha(x)$ and g_W the weak coupling constant. To allow for the flavor changing properties of the weak interaction, the left handed[2] fermions and right handed anti-fermions are placed in an iso-spin doublet:

$$\phi_L(x) = \begin{pmatrix} \nu_e(x) \\ e^-(x) \end{pmatrix}_L \tag{2.6}$$

with the upper and lower components corresponding to the up and down type fermions with an weak isospin of $I_W = \frac{1}{2}$. Their counterparts, the right handed fermions and left handed anti-fermions are instead placed in a singlet with $I_W = 0$ not participating in the weak interaction, describing the parity violating V-A structure of the weak interaction. As in the QED case, interaction terms of fermions with the three new bosonic fields $\mathbf{W}$ arise when demanding invariance under the given SU(2) transformation. This modifies the Dirac equation for the left handed fermions to:

$$i\gamma^\mu D_\mu\phi_L = i\gamma^\mu(\partial_\mu + ig_W T_k W^k_\mu)\phi_L = m\phi_L \tag{2.7}$$

[2]The chirality is a fundamental property of particles, the Dirac spinor can be decomposed in two chiral eigenstates, the right-handed and left-handed chiral components, by the projection operators $P_R = \frac{1}{2}(1+\gamma^5)$ and $P_L = \frac{1}{2}(1+\gamma^5)$. The concept of chirality is related to the more vivid property of helicity, the projection of the particles spin on its direction of flight. In the speed of light limit of the particle, helicity and chirality eigenstates become the same, with the spin of right handed particles pointing parallel to their direction of flight.

By rewriting the given equation, the W bosons of the weak interaction can be identified with $W_\mu^\pm = \frac{1}{\sqrt{2}}(W_\mu^{(1)} \mp i W_\mu^{(2)})$ yielding the desired charged currents $\frac{g_W}{\sqrt{2}}\bar{\nu}\gamma^\mu \frac{1}{2}(1-\gamma^5)\mathrm{e}$ and $\frac{g_W}{\sqrt{2}}\bar{\mathrm{e}}\gamma^\mu \frac{1}{2}(1-\gamma^5)\nu$ facilitating flavor changing interactions. The $\mathrm{W}^\pm$ obtained this way are coupling to the third component of the weak iso-spin $I_W^{(3)}$, equal to +$\frac{1}{2}$ for ν_L and -$\frac{1}{2}$ for e_L.
As established, the weak charged interactions only couples to left handed fermions and right handed anti-fermions. In nature however, also couplings of Z bosons to right handed fermions and left handed anti-fermions are observed. As such the remaining $W_\mu^{(3)}$ can not simply be identified with the physical Z boson.
To explain this behaviour, both symmetries U(1) of QED and SU(2) of the weak interaction, need to be unified to an U(1)×SU(2) symmetry describing the combined electro-weak interaction sector. Here the terms found for the U(1) symmetry in Eq. 2.4 are reintroduced for a bosonic field B_μ coupling to the hypercharge Y and combined with the terms of the weak interaction in Eq. 2.7 yielding:

$$D_\mu = \partial_\mu + i g_W \mathbf{T}\cdot\mathbf{W}_\mu + i g' \frac{Y}{2} B_\mu \tag{2.8}$$

The physical representations of the Z boson and the photon can then be obtained by mixing the two fields B_μ and $W_\mu^{(3)}$:

$$A_\mu = \frac{g' W_\mu^{(3)} + g_W B_\mu}{\sqrt{g_W^2 + g'^2}},\ Z_\mu = \frac{g_W W_\mu^{(3)} - g' B_\mu}{\sqrt{g_W^2 + g'^2}} \tag{2.9}$$

with the photon coupling to the electric charge q and the Z boson coupling to the weak hypercharge $Y = 2(q - I_W^{(3)})$ as observed in nature.
Establishing electroweak interactions between the derived $\mathrm{W}_\mu^\pm, \mathrm{Z}_\mu$ bosons and the photon A_μ leaves however one problem, the observed mass of the $\mathrm{W}_\mu^\pm$and Z_μ bosons. Introducing mass terms for a bosonic field such as A_μ is not possible in the theoretical framework described thus far, as these would violate gauge invariance under for example the U(1) transformation in Eq. 2.3:

$$\frac{1}{2} m_\gamma^2 A_\mu A^\mu \rightarrow \frac{1}{2} m_\gamma (A_\mu - \partial_\mu \chi)(A^\mu - \partial^\mu \chi) \neq \frac{1}{2} m_\gamma^2 A_\mu A^\mu \tag{2.10}$$

To resolve this, an iso-spin doublet of two complex scalar "Higgs" fields are introduced:

$$\phi = \begin{pmatrix} \phi^+ \\ \phi^0 \end{pmatrix} = \frac{1}{\sqrt{2}} \begin{pmatrix} \phi_1 + i\phi_2 \\ \phi_3 + i\phi_4 \end{pmatrix} \tag{2.11}$$

with the corresponding Lagrangian $\mathscr{L}$ and the Higgs potential $V(\phi)$:

$$\mathscr{L} = (\partial_\mu \phi)^\dagger (\partial^\mu \phi) - V(\phi^2), \qquad V(\phi) = \mu^2 \phi^\dagger \phi + \lambda (\phi^\dagger \phi)^2 \tag{2.12}$$

The Higgs potential is shown in Fig. 2.4 for an adequately chosen $\mu^2 < 0, \lambda > 0$. An infinite amount of minima defined by the vacuum expectation value v satisfying $|v|^2 = -\frac{\mu^2}{\lambda}$ is found. By

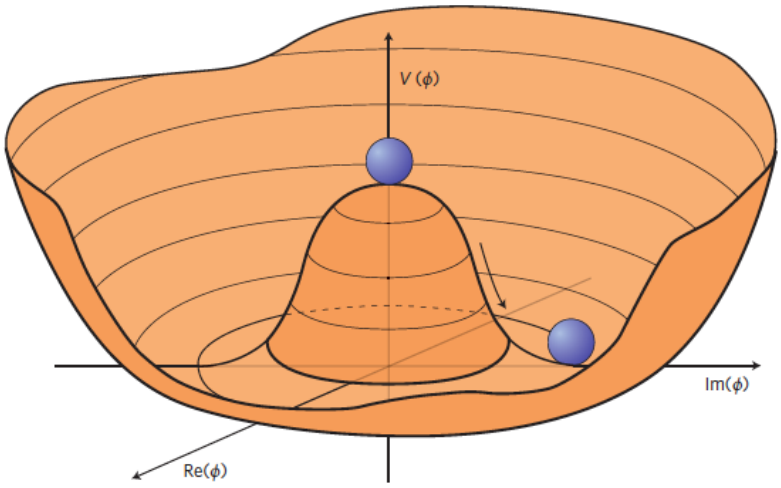

Figure 2.4: Simplified illustration of the Higgs potential $V(\phi)$ for $\mu^2 < 0$. The SM ϕ is an iso-spin doubled with two real and two imaginary components. The two components shown here can be interpreted as belonging to the electrical neutral ϕ^0 component [13].

choosing the minimum:

$$\phi(x) = \frac{1}{\sqrt{2}} \begin{pmatrix} 0 \\ v + h(x) \end{pmatrix} \tag{2.13}$$

where $h(x)$ are small excitations around the vacuum expectation value v yielding the Higgs boson. The $\mathrm{U}(1)_Y \times \mathrm{SU}(2)_L$ symmetry is spontaneously broken.
For the chosen $\phi(x)$ and the covariant derivative D_μ in Eq. 2.8, the Higgs Lagrangian in Eq. 2.12 changes to:

$$\begin{aligned} \mathscr{L} = (D_\mu \phi)^\dagger (D^\mu \phi) - V(\phi) = \frac{1}{2}(\partial_\mu h)(\partial^\mu h) + \frac{1}{8} g_W^2 (W_\mu^{(1)} + i W_\mu^{(2)})(W^{(1)\mu} - i W^{(2)\mu})(v+h)^2 \\ + \frac{1}{8}(g_W W_\mu^{(3)} - g' B_\mu)(g_W W^{(3)\mu} - g' B^\mu)(v+h)^2 - \lambda v^2 h^2 - \lambda v h^3 - \frac{1}{4}\lambda h^4 \end{aligned} \tag{2.14}$$

By collecting the terms quadratic in the gauge boson fields, mass terms can be identified:

$$\begin{aligned} &\frac{1}{8} v^2 g_w^2 (W_\mu^{(1)} W^{(1)\mu} + W_\mu^{(2)} W^{(2)\mu}) + \frac{1}{8} v^2 (g_W W_\mu^{(3)} - g' B_\mu)(g_W W^{(3)\mu} - g' B^\mu) = \\ &\frac{1}{2} m_W^2 W_\mu^{(1)} W^{(1)\mu} + \frac{1}{2} m_W^2 W_\mu^{(2)} W^{(2)\mu} + \frac{v^2}{8} \begin{pmatrix} W_\mu^{(3)} & B_\mu \end{pmatrix} \begin{pmatrix} g_W^2 & -g_W g' \\ -g_W g' & g'^2 \end{pmatrix} \begin{pmatrix} W^{(3)\mu} \\ B^\mu \end{pmatrix} \\ &= \frac{1}{2} m_W^2 W_\mu^{(+)} W^{(+)\mu} + \frac{1}{2} m_W^2 W_\mu^{(-)} W^{(-)\mu} + \frac{1}{2} m_Z^2 Z_\mu Z^\mu \end{aligned} \tag{2.15}$$

with $m_W = \frac{1}{2} g_W v$ and $m_Z = \frac{1}{2} v \sqrt{g_W^2 + g'^2}$. The Lagrangian now also contains terms quadratic, cubic and quartic in h where the quadratic term can be identified with a Higgs boson mass term with $m_H = \sqrt{2\lambda} v$. The cubic and quartic terms correspond to self interactions of the Higgs boson defining the three point Higgs boson interaction vertex discussed in Sec. 2.3 and shown in Fig. 2.7 and a quartic Higgs boson interaction, currently beyond the reach of experimental sensitivity. Similarly terms containing both the fields of the gauge bosons as well as the Higgs field facilitate

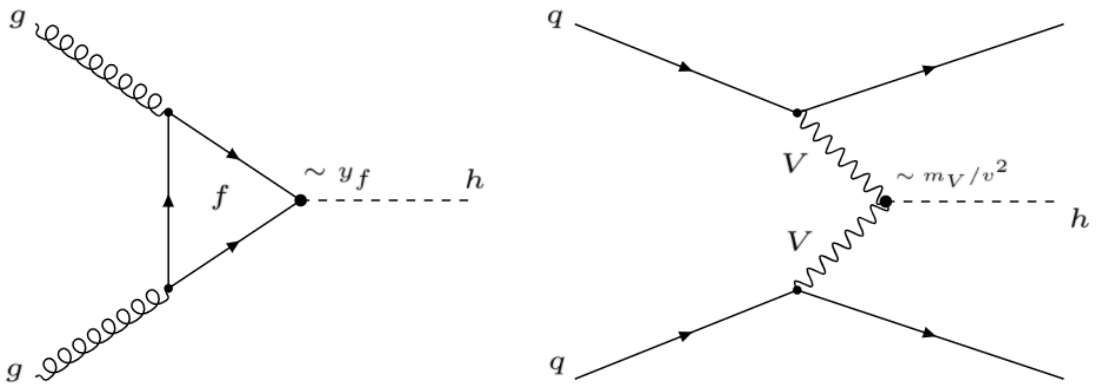

Figure 2.5: The two main single-Higgs boson production diagrams at the LHC, gluon-gluon fusion on the left and vector boson-fusion on the right. The V in the right plots can stand for both, W and Z bosons.

interaction vertices between the Higgs boson and the W and Z bosons proportional to the bosons mass $\propto m_V^2/v$. The described Higgs mechanism can be extended to explain the fermion masses as well. Here terms proportional to $\bar{L}\phi R + (\bar{L}\phi R)^\dagger$ are introduced, with L corresponding to the isospin doubled of left handed fermions and R representing the singlets of right handed fermions. Similarly to the bosonic case, terms mixing the fermion fields with the Higgs are found, yielding to a Higgs boson coupling to fermions proportional to the fermions mass $\propto \sqrt{2}m_f/v$. This is known as the Higgs Yukawa coupling. The introduced couplings of the Higgs boson yield several possible Higgs boson production mechanisms and decays. As the Higgs boson couplings depend on the particle masses, decays in heavy fermions such as b quarks and τ leptons as well as W and Z bosons are the most prevalent. While the top quark itself is too heavy to play a direct role in Higgs boson decays, the main mode of Higgs boson production at the LHC is given by the gluon-gluon fusion ($\mathrm{gg}f$ or ggH) process shown in Fig. 2.5 involving a fermion loop with the main contribution arising from top quarks. Beside the strong top Yukawa coupling, $\mathrm{gg}f$ at the LHC is also driven by the composite nature of the protons as described in Sec. 2.5 where the proton parton density function (PDF) heavily favors processes involving gluons in the initial state. The second largest Higgs boson production mechanism at the LHC, vector boson fusion (VBF or qqH), is about 10 times smaller than $\mathrm{gg}f$ and is driven by the Higgs boson couplings to bosons instead. Fig. 2.6 shows for the most prevalent Higgs boson production mechanisms at the LHC their cross section as well as an overview of the different Higgs boson branching fractions.

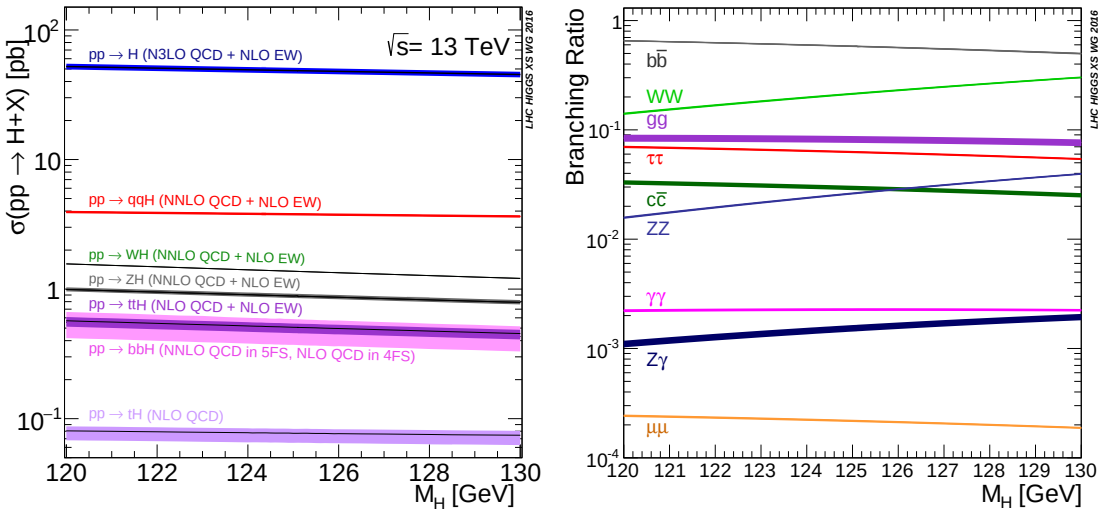

Figure 2.6: Cross sections for different production modes of single Higgs boson production at the LHC for a center of mass energy of $\sqrt{s} = 13$ TeV on the left. The shown cross sections correspond from highest to lowest cross sections to the total single Higgs boson production cross section, vector boson fusion (qqH), associated production of a Higgs boson and a vector boson (WH and ZH), associated production of a Higgs boson and a pair of top-quarks ($\mathrm{t\bar{t}H}$), associated production of a Higgs boson and a pair of bottom-quarks ($\mathrm{b\bar{b}H}$) and associated production of a Higgs boson and a top-quark (tH). The branching fractions of the most likely Higgs boson decays on the right. The dependency on the Higgs boson mass in a 5 GeV window around the observed Higgs boson mass of about 125 GeV is shown in both plots [14].

2.3 Boxes and Triangles – Non-Resonant Di-Higgs Boson Production

The study of processes involving the production of two separate Higgs bosons is connected to multiple physics phenomena like the so far unmeasured trilinear Higgs boson self-coupling. The following aims at explaining these phenomena and their connection to the phenomenology of Di-Higgs boson production. More about this topic can be found in [15] on which this section is based. First non-resonant production is discussed, that in contrast to the resonant production discussed in Sec 2.4 does not involve the decay of a possible new heavy resonance into two Higgs bosons. Within the Standard Model of particle physics, two Higgs bosons can either be produced by processes involving already observed couplings like the top Yukawa coupling y_t in a similar fashion to the various single Higgs boson production modes, or, more interestingly, through so far unobserved couplings, constraining possible SM extensions further.

Di-Higgs Boson Production in the SM

Analogously to single Higgs boson production, Di-Higgs boson production can be divided into a number of production modes as gluon-gluon fusion like (ggHH) or vector boson fusion like (qqHH) production. Fig. 2.7 shows some of the different leading order SM Feynman diagrams contributing to Di-Higgs boson production. In the case of the main HH production mode at the LHC ggHH, the two main contributions are given by the simultaneous production of two Higgs bosons via the top Yukawa coupling y_t ($\square$), and the production via the trilinear Higgs boson self-coupling λ ($\triangle$). As discussed in Sec. 2.2, the latter is a consequence of the terms cubic in h

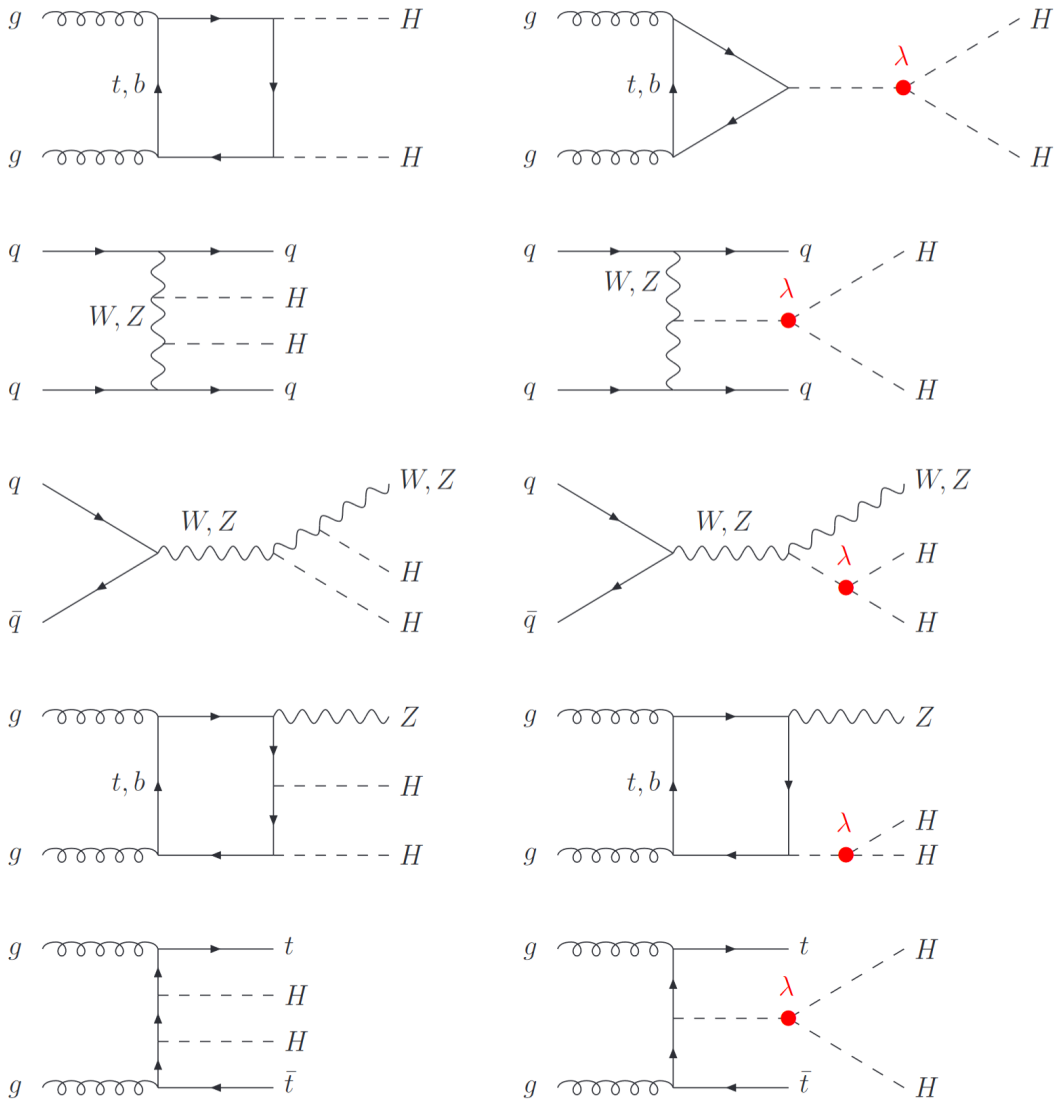

Figure 2.7: The Feynman diagrams for Di-Higgs boson production at leading order within the Standard Model of particle physics. From top to bottom the various production modes analogously to single Higgs boson production: gluon-gluon fusion (ggHH), vector-boson fusion (qqHH), Double-Higgs boson strahlung of vector bosons and fermions (WH and ZH) as well as Di-Higgs boson production associated with top quarks (ttHH). The trilinear Higgs boson self-coupling λ is highlighted [15].

within the SM Lagrangian, fixing the SM trilinear Higgs boson self-coupling at $\lambda_{\mathrm{HHH}}^{\mathrm{SM}} = \frac{m_{\mathrm{H}}^2}{2v^2}$. Fig. 2.8 shows the cross section of these different production modes for the LHC with a center of mass energy of $\sqrt{s} = 14$ TeV.

The trilinear Higgs Boson Self-Coupling and ggHH Production

Looking at Fig. 2.8, two observations can be made. Firstly, the total cross section for a standard model like Higgs self-coupling (λ_{HHH}) scenario of $\lambda_{\mathrm{HHH}}/\lambda_{\mathrm{HHH}}^{\mathrm{SM}} = \kappa_\lambda = 1$ is extremely small in the order of $30\,\mathrm{fb}^{-1}$. The standard model NNLO cross section [17–19]. of the main production mode (ggHH) for the LHC at a center of mass energy of $\sqrt{s} = 13$ TeV amounts to:

$$\sigma_{\mathrm{ggHH}}^{\mathrm{SM}}\,[\mathrm{fb}] = 31.05^{+6\%}_{-23\%}\ (\text{QCD scale} + m_{\mathrm{t}}) \pm 3\%\ (\alpha_s\text{+PDF}) \tag{2.16}$$

Secondly, the κ_λ dependence of the cross sections in the various production modes shows a parabolic shape. This leads to the unintuitive observation that a higher trilinear coupling than in the SM not necessarily leads to an increased overall cross section. Usually a quadratic dependence of the cross section on the modified coupling with an ever growing cross section is expected. The cross section at the level of NLO [20, 21] / NNLO [22] calculation can be parameterized in dependence of κ_λ as:

$$\begin{aligned}\sigma_{\mathrm{ggHH}}^{\mathrm{NLO}}(\kappa_\lambda)\,[\mathrm{fb}] &= 62.5339 - 44.3231\cdot\kappa_\lambda + 9.6340\cdot\kappa_\lambda^2 \\ \sigma_{\mathrm{ggHH}}^{\mathrm{NNLO}}(\kappa_\lambda)\,[\mathrm{fb}] &= 70.3874 - 50.4111\cdot\kappa_\lambda + 11.0595\cdot\kappa_\lambda^2\end{aligned} \tag{2.17}$$

The uncertainty on the NNLO cross section from the scale of QCD interactions and the mass of the top quark varies with κ_λ as well as described in [18]. This can be parameterized as:

$$\begin{aligned}\sigma_{\mathrm{ggHH}}(\kappa_\lambda)[\mathrm{fb}] + 1\sigma &= \max(76.6075 - 56.4818\cdot\kappa_\lambda + 12.635\cdot\kappa_\lambda^2, 75.4617 - 56.3164\cdot\kappa_\lambda + 12.7135\cdot\kappa_\lambda^2) \\ \sigma_{\mathrm{ggHH}}(\kappa_\lambda)[\mathrm{fb}] - 1\sigma &= \min(57.6809 - 42.9905\cdot\kappa_\lambda + 9.58474\cdot\kappa_\lambda^2, 58.3769 - 43.9657\cdot\kappa_\lambda + 9.87094\cdot\kappa_\lambda^2)\end{aligned} \tag{2.18}$$

Both the κ_λ dependent uncertainty in Eq. 2.18 as well as the κ_λ dependent *k*-factor $\sigma_{\mathrm{ggHH}}^{\mathrm{NNLO}}(\kappa_\lambda)/\sigma_{\mathrm{ggHH}}^{\mathrm{NLO}}(\kappa_\lambda)$ derived with Eq. 2.17 are taken into account in the extraction of HH results in this thesis (see.Sec. 7.2.1).

Both the observation of a low SM cross section as well as the described κ_λ dependence can be explained by the destructive interference of the different Feynman diagrams, for instance the $\triangle$ and the $\square$ Feynman diagrams in the ggHH case. The $\triangle$ diagram involves an off-shell Higgs boson going into two on-shell Higgs bosons. Since the SM Higgs boson has compared to its mass of 125.09 GeV [23] a very small decay width of about 4 MeV, the $\triangle$ process is suppressed. In addition the two Higgs bosons are produced nearly at rest with respect to each other. For invariant Di-Higgs mass m_{HH}, this leads to a characteristic narrow mass spectrum close to the kinematic edge of two times the Higgs boson mass. For the $\square$ process no such limitation exists, leading to a broad but steadily falling m_{HH} spectrum after the kinematic turn on around the same mass regime of 250-300 GeV. Thus the destructive interference between these two diagrams does not only influence the production cross section, but also the kinematic properties of the

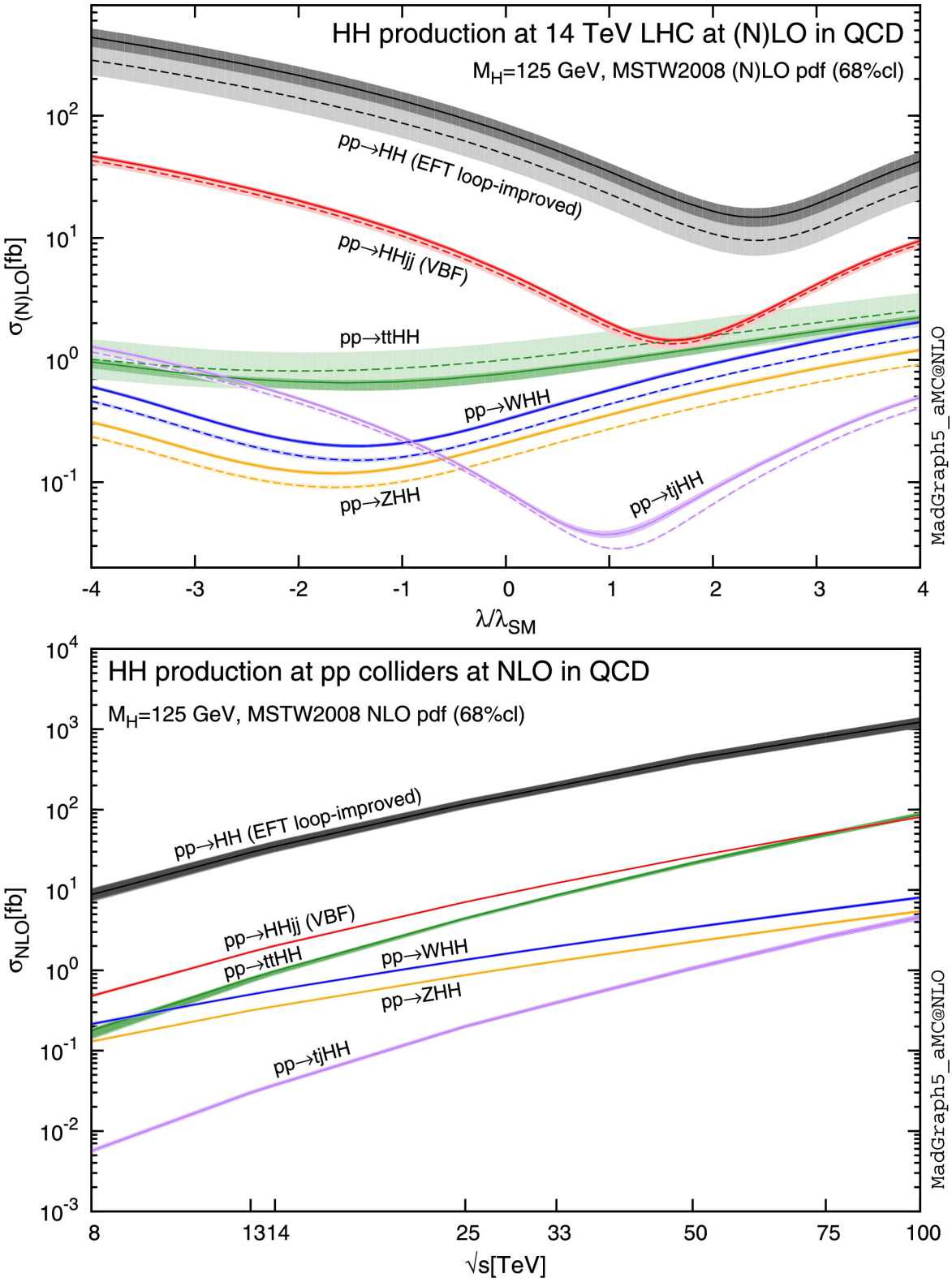

Figure 2.8: The production cross section for non-resonant Di-Higgs boson production at the LHC for different values of the trilinear Higgs boson self-coupling $\kappa_\lambda = \lambda_{\mathrm{HHH}}/\lambda^{\mathrm{SM}}_{\mathrm{HHH}}$ at a center of mass energy of $\sqrt{s} = 14$ TeV on the top and for different center of mass energies with fixed standard model like couplings on the bottom. The plots shown correspond to NLO QCD calculations taken from [16]. The uncertainty given by linear sum of scale and and PDF uncertainties is displayed as color bands in the top figure and line thickness in the bottom figure. The dashed lines with the lighter colored uncertainty bands in the upper picture correspond to calculations at LO QCD.

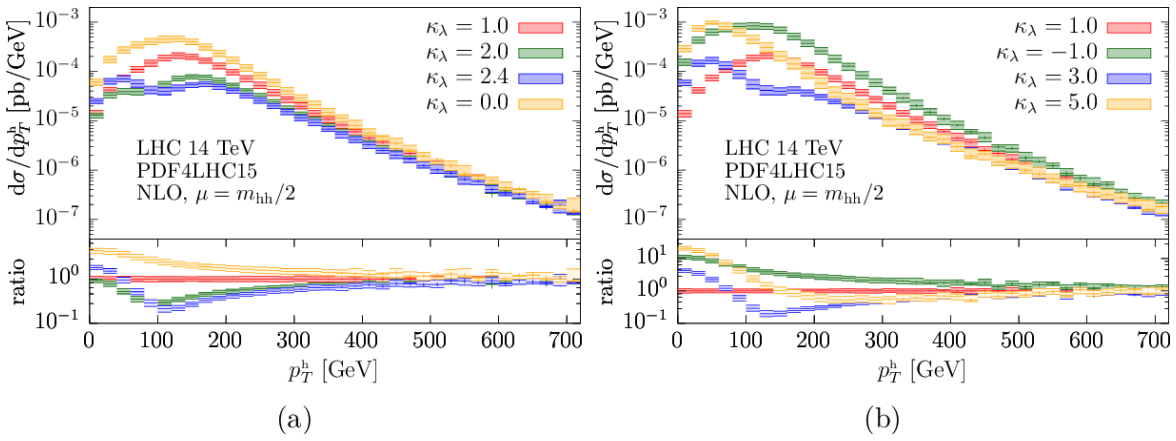

(a) (b)

Figure 2.10: The single Higgs boson p_T spectrum for Di-Higgs boson production at the LHC for a center of mass energy of $\sqrt{s} = 14$ TeV for various values of the trilinear Higgs boson self-coupling relative to the Standard Model of particle physics $\kappa_\lambda = \lambda/\lambda_{HHH}^{SM}$ [24]. The figure on the left shows a narrow κ_λ range around the region of maximum interference, while the right figure shows a broader range of κ_λ scenarios.

produced Higgs bosons. This leads to drastic variations in the m_{HH} spectrum with κ_λ and thus also for the kinematic properties of the subsequent Higgs boson decay products. The effects of this interference are shown in Fig. 2.9 and Fig. 2.10, showing the m_{HH} spectrum as well as the resulting Higgs boson p_T for various choices of λ.

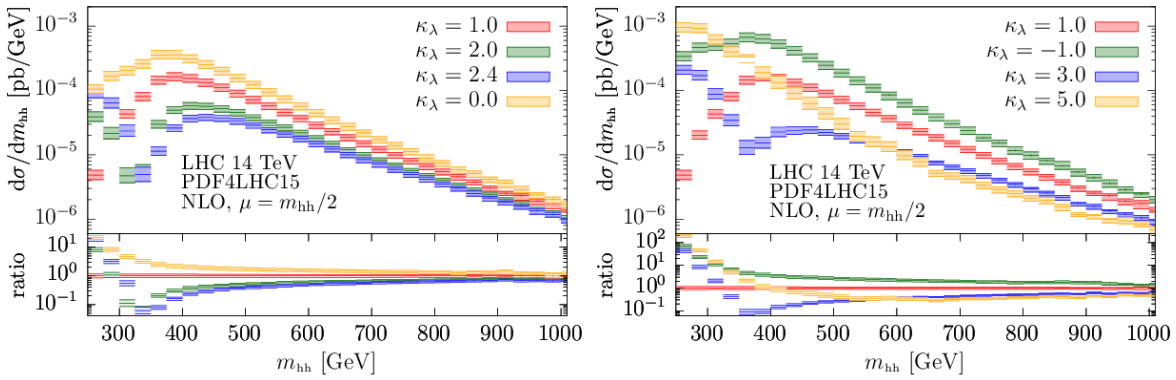

(a) (b)

Figure 2.9: The invariant mass spectrum for Di-Higgs boson production at the LHC for a center of mass energy of $\sqrt{s} = 14$ TeV for various values of the trilinear Higgs boson self-coupling relative to the Standard Model of particle physics $\kappa_\lambda = \lambda/\lambda_{HHH}^{SM}$ [24]. The figure on the left shows a narrow κ_λ range around the region of maximum interference, while the right figure shows a broader range of κ_λ scenarios.

Beside its strong influence on the Di-Higgs boson production cross section and the kinematic properties of the expected Di-Higgs boson signal, the trilinear Higgs boson self-coupling also has an effect on the single Higgs boson production and branching fractions through higher order effects. This can be seen in Fig. 2.11. Both effects play a notable effect in the search for Di-Higgs boson signals on a broader range of κ_λ and are are taken into account in the extraction of HH results in this thesis (see.Sec. 7.2.1). The parametrization of the Higgs boson branching fraction scaling and the single Higgs boson production scaling are taken from [25] and [26].

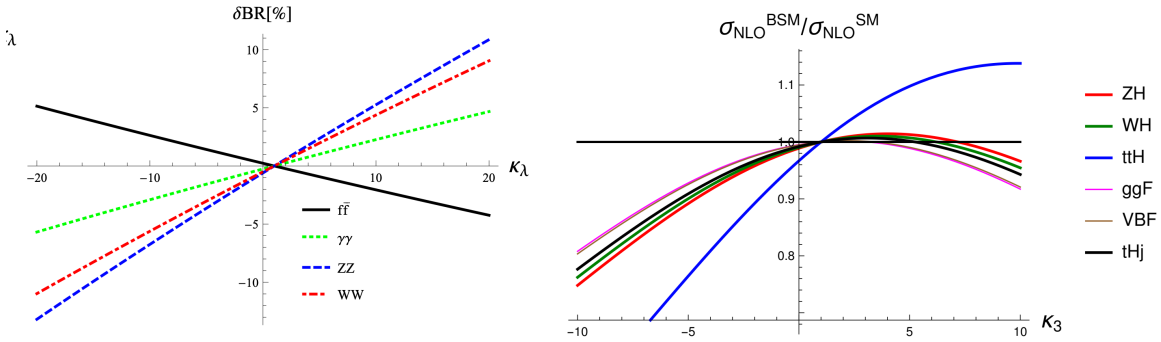

Figure 2.11: The dependence of the single Higgs boson branching fractions on the trilinear Higgs boson self-coupling $\kappa_\lambda = \kappa_3 = \lambda_{\mathrm{HH}}/\lambda_{\mathrm{SM}}$ on the left [25]. The dependence of the single Higgs boson production cross section for various production modes on the Higgs boson self-coupling on the right [26].

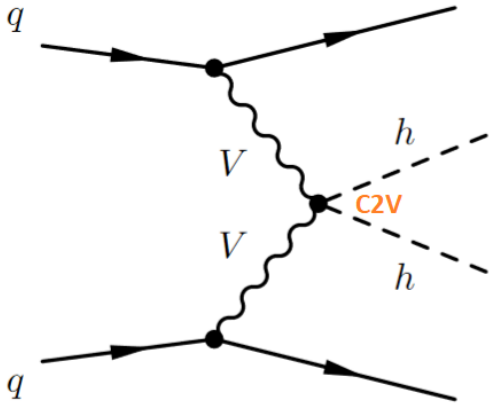

Figure 2.12: The LO Feynman diagram contributing to the Di-Higgs boson qqHH production mode involving the Standard Model coupling c_{2V} [27].

VBF like qqHH production

Di-Higgs boson measurements also allow to constrain another, so far unobserved Standard Model coupling, the coupling between two vector bosons and two Higgs bosons, c_{2V}. This coupling contributes with the diagram shown in Fig. 2.12 to the subleading qqHH production mode and interferes with the other two leading order qqHH diagrams shown in the second row of Fig. 2.7. To provide adequate sensitivity on this coupling, the study of event categories tailored to the specific VBF like signature are needed. This usually involves the study of additional forward particle jets produced in the detector by additional final state quarks in the qqHH production mode.
As the requirements on the Multilepton signatures presented in this thesis are already quite strong, the analysis presented in Sec 6 does not offer enough expected signal to allow for a focus on these qqHH specific signatures.

BSM Di-Higgs Boson Production and EFT Couplings

This thesis also looks at the effects of new beyond Standard Model phenomena on non-resonant Di-Higgs boson production. Since the amount of theoretical models containing beyond Standard Model Di-Higgs boson production can be arbitrarily large, instead of full physics models, these Standard Model extensions are probed using an effective field theory approach (EFT). Contrary

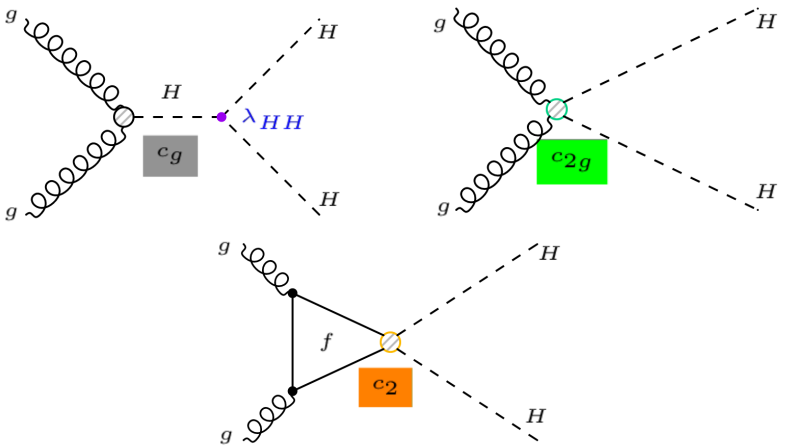

Figure 2.13: LO Feynman diagrams involving the EFT couplings cg, $c2g$ and $c2$ for the leading ggHH production mode.

to a full model, an EFT only looks at the effective coupling behaviour between particles. From an experimental standpoint of view this allows the study of any number of theoretical models at once.

Within the context of the Di-Higgs boson studies presented here, an EFT framework containing 5 BSM couplings is used. Besides potentially modified versions of λ and the top Yukawa coupling y_t this encloses the three couplings c_2, c_g and c_{2g} describing contact interactions of Higgs bosons with gluons or top-/anti-top pairs that for example could be mediated by new heavy particles. This follows the EFT Lagrangian given in Eq. 2.19, corresponding to extensions of the Standard Model with up to dimension 6 operators as in [28].

$$\begin{aligned}\mathscr{L}_H = \frac{1}{2}\partial_\mu H \partial^\mu H - \frac{1}{2}m_H^2 H^2 - \kappa_\lambda \lambda_{SM} v H^3 - \frac{m_t}{v}(v + \kappa_t H + \frac{c_2}{v}HH)(\bar{t}_L t_R + \text{h.c.}) \\ + \frac{1}{4}\frac{\alpha_s}{3\pi v}(c_g H - \frac{c_{2g}}{2v}HH)G^{\mu\nu}G_{\mu\nu}\end{aligned} \tag{2.19}$$

Feynman diagrams featuring these five couplings in the leading ggHH production mode are shown in Fig. 2.13. It should be noted that this EFT representation corresponds to the Higgs Effective Field Theory formalism (HEFT), one of two formalisms commonly present in literature. As this thesis discusses EFT physics in terms of the introduced HEFT couplings λ, y_t, c_2, c_g and c_{2g}, the second formalism, the Standard Model Effective Field Theory approach (SMEFT) is not discussed here. A good summary of both formalisms and their connection to Di-Higgs boson physics can be found in [15].

As the study of a 5-dimensional parameter space leads to a very large amount of possible signal scenarios, the presented HH analysis focuses on a set of EFT benchmark scenarios, condensing the set of possible signal kinematics arising from the 5-dimensional parameter space into a small number of investigated scenarios. These benchmarks are discussed in Sec. 6.2.4. Also studied is a reduced parameter scenario without the couplings c_g and c_{2g} to the color charged sector in Eq. 2.19 focusing only on λ, y_t and c_2. This and especially a scan in the $y_t - c_2$ plane is performed in the presented analysis and further discussed in Sec. 7.2.1.

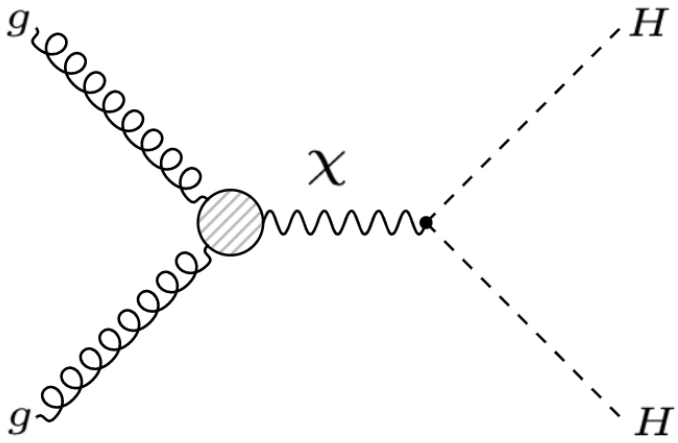

Figure 2.14: An example Feynman diagram for Di-Higgs boson production in a decay of a heavy resonance χ.

2.4 Gravitons, Radions and the Resonant Di-Higgs Boson Production

While the study of and the search for final states involving two Higgs boson decays is motivated by the non-resonant Di-Higgs boson production in the SM and BSM variations thereof, the same final states also allow for the search of new heavy particles decaying into a pair of Higgs bosons. This is refereed to as resonant Di-Higgs boson production. A Feynman diagram of the HH decay of such as new particle χ is shown in Fig. 2.14.

The search for resonant Di-Higgs boson production presented in this thesis is rather model unspecific, looking at heavy spin-0 and spin-2 particles in the mass range between 250 and 1000 GeV. The width of the new resonance is assumed to be small compared to the experimental Di-Higgs mass resolution and thus neglected assuming a sharp peak in m_{HH} around the resonance mass.

This sort of BSM resonances is motivated by many different models, with examples being:

- Models with an extended Higgs sector, where a second Higgs iso-spin doublet (see Sec. 2.2) is introduced, usually leading to 5 instead of one Higgs bosons. Here one of the neutral non SM Higgs bosons could decay into a pair of SM Higgs bosons. These two-Higgs doublet model are for example featured in [29] and [30].

- Many BSM scenarios feature a hidden sector containing additional particles not interacting with most SM particles thus explaining phenomena such as dark matter. A subset of these models contains a so called Higgs portal, where interactions between the hidden sector and the SM sector are facilitated via interactions between the "hidden" Higgs bosons and the Higgs boson in the SM. Depending on the mass ratio of the Higgs bosons in the hidden sector and in the SM sector, resonant decays into two SM Higgs bosons can be observed. This is for example described in [31] and [32].

- To solve the hierarchy problem between the weak scale of particle physics interactions and the Planck scale of gravitational physics, models with extra dimensions can be introduced in the context of string theory. An example of this would be the Randall-Sundrum

model described in [33]. As shown in [34] these can feature heavy spin-0 (radion) or spin-2 (graviton) resonances able to decay into two SM Higgs bosons.

2.5 High energy particle physics with proton-proton interactions

Proton-Proton (pp) collisions with a circular collider allow for high interaction rates at high center of mass energies and therefore provide excellent potential for the discovery of new physics at ever increasing energy scales. This makes them different from e.g. electron-positron colliders, where the Bremstrahlung losses of electrons do not allow for the use of circular colliders and thus high interaction rates at high center of mass energies. High interaction rates however come at a cost intertwined with the composite nature of the proton.
The proton is a bound state of three quarks, two up-quarks (u) and an anti-down quark ($\overline{\mathrm{d}}$) held together via the strong interaction. The visible structure of the proton depends strongly on the energy scale probed. At high enough energy scales the interactions between the three quarks are resolved, showing gluon exchanges between these valence quarks. These gluons can be virtual, constantly splitting into and recombining from quark/anti-quark pairs giving rise to a sea of virtual particles within the proton. This has three main effects on the application of pp collisions in experimental particle physics.

- At high enough energy scales, the collision of two protons does not only allow for interactions between the valence quarks of both protons, but also interactions involving the sea quarks and gluons making up the then resolved proton structure.

- pp collisions involve more particles than the two partons of the two interacting protons that form the hard processes. Events observed at experiments such as CMS (see Sec. 3.1) also contain interactions of the proton remnants that don't participate in the hard interaction, producing a multitude of particle signatures overlaying the final state particles of the hard process. This is known as underlying event and together with the occurrence of multiple simultaneous pp interactions (pile-up) puts an additional challenge on event reconstruction.

- While the momenta and energy of the colliding protons is relatively well known, the relative momenta of the colliding partons and thus the center of mass of the collision is not known. This means the momentum balance along the proton beam axis is not known and constraints on momentum conservation along the beam axis cannot be used in the event reconstruction. This also means that, the hard interaction processes do not occur at a fixed center of mass energy and, in combination with the diverse particle content in the proton, allows for a large amount of different initial states and processes at the LHC.

Due to this composite nature of the proton, the cross section and kinematics of a given process is not fully determined by the matrix element of the hard interaction process between partons. For this, the parton density functions (PDFs) describing the probability for a given particle type within the proton to carry a given fraction of the protons energy are needed. The fraction of

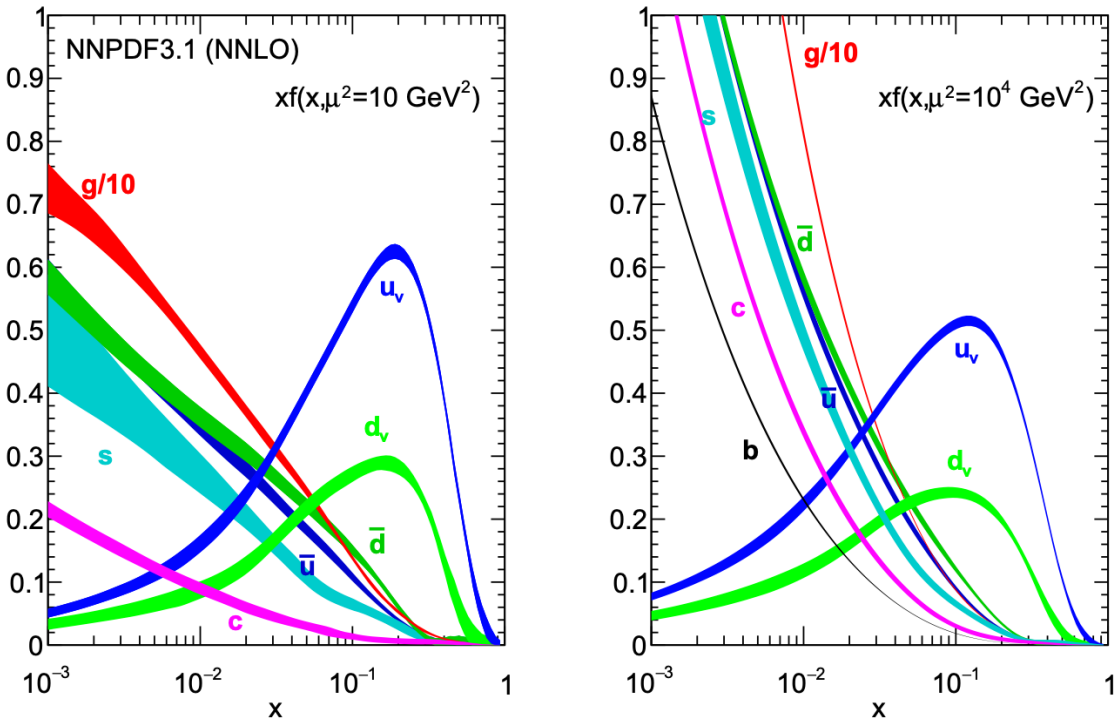

Figure 2.15: Proton parton density functions as given in the `NNPDF3.1` PDFs set [35] for an energy scale of $\mu^2 = 10\,\mathrm{GeV}^2$ and $\mu^2 = 10^4\,\mathrm{GeV}^2$.

the proton momentum carried by the different partons is usually given in terms of the Bjorken scaling variable x which describes the fraction of the proton momentum carried by each parton in the infinite momentum frame where $E_\mathrm{p} >> m_\mathrm{p}$. In this frame, the energy of the parton is then given by $E_\mathrm{part} = xE_\mathrm{p}$ [12]. The PDFs of the different proton components such as gluons, sea- and valence quarks then describe the probability to find a particle of the given type at a given x. The PDFs themselves depend on the energy scale μ^2 of the interaction, given by the negative four-momentum transfer of the hard interactions.

The PDFs can not be calculated from theory and are instead determined experimentally. The PDF sets used for the simulation of particle physics events in this thesis are given in Sec. 6.2.2. Fig. 2.15 shows PDFs for the `NNPDF3.1` PDFs set [35] used for the simulation of collision events in 2017 and 2018 collision data. As can be seen, for low x the probability for gluon scattering is greatly enhanced. As the center of mass energy between the two protons with $\sqrt{s} = 13$ TeV at the LHC is much higher than the energy scale of electro-weak physics at $O(m_\mathrm{Z})$, most collisions occur at low x making the LHC effectively a gluon collider.

3

The CMS Experiment and Reconstruction of High Energy Collision Data

The experimental data used in this thesis is gathered with the **C**ompact **M**uon **S**olenoid experiment (CMS) [36] located at the P5 collision point of the **L**arge **H**adron **C**ollider (LHC) [37] near Geneva. The following will describe the accelerator in Sec 3.1 and the CMS experiment and its various subsystems as well as basic particle reconstruction in Sec. 3.2. Sec. 3.3 gives a more in-depth look into detector operation on the example of single event-upsets.

3.1 The Large Hadron Collider and the CERN Accelerator Complex

The phenomena described in Sec. 2 can be studied in various ways. For example, particles can be observed directly by studying the interaction of cosmic radiation in earth's atmosphere as done by large telescope arrays like the Pierre Auger Observatory [38] or by neutrino experiments like the Kamiokande experiment [39] studying cosmic, solar and nuclear neutrinos. They can also be observed indirectly as done in astronomic observations hunting for annihilation signatures in cosmic radiation. As for the Higgs boson and other high energy physics phenomena the most promising experimental signatures are studied using particle colliders. The LHC is the world's largest circular collider with a center of mass energy of up to $\sqrt{s} = 14$ TeV for proton-proton collisions.

The LHC features four main detector experiments CMS, ATLAS [40], LHCb [41] and ALICE [42] located at 4 different interaction points. LHCb and ALICE are specialized experiments focusing on b-physics and heavy-ion interactions, while CMS and ATLAS are general purpose detectors. As such they aim to study a wide range of particle physics interactions with the discovery and study of the Higgs boson being one of their main goals.

The LHC itself is part of a larger accelerator complex, shown in Fig. 3.1. A pre-accelerator chain consisting of the LINAC 2 linear accelerator, the Booster, the Proton Synchrotron (PS) and the Super Proton Synchrotron (SPS) circular accelerators, that enhance proton energies to 450 GeV before their final energy of currently 6.5 TeV inside the LHC is reached. Circular colliders such as the LHC allow for a very high luminosity with currently up to 60 collisions per bunch crossing every 25 ns [45]. This allows to measure even extremely rare processes such as the HH production. The luminosity quantifies the cross section dependent number of observed events and is defined as:

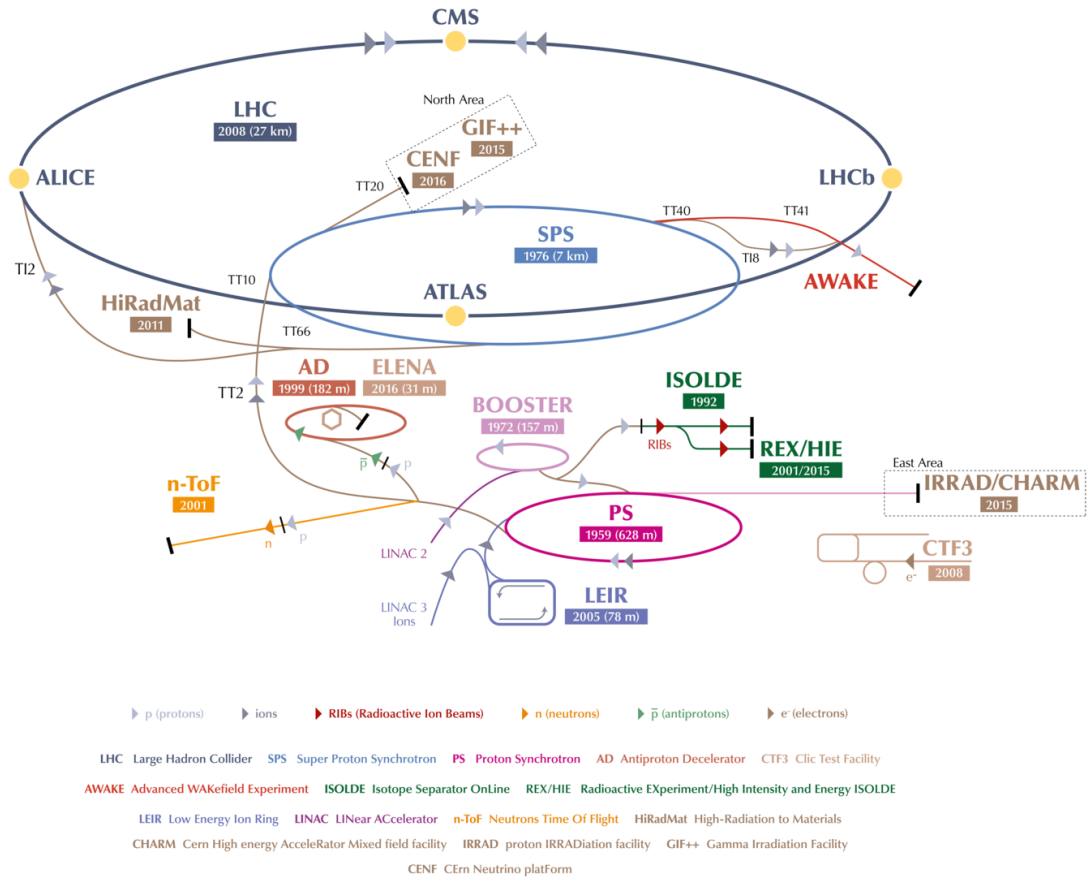

Figure 3.1: The CERN accelerator complex located near Geneva on the border between France and Switzerland. The LHC is schematically shown as a blue circle with its four main experiments CMS, ATLAS, LHCb and ALICE. The pre-accelerators LINAC, PS and SPS feeding the LHC with 450 GeV protons as well as other accelerators and experiments featured at CERN are shown as well [43, 44].

$$\mathscr{L} = f\frac{n_1 n_2}{4\pi\sigma_x\sigma_y}$$

Here f is the collision frequency, n_i the number of particles per bunch and σ_i the beam bunch size in x and y directions transverse to the particle beam. The number of observed events for a cross section σ is given by $\sigma \times \mathbf{L} = \sigma \times \int \mathscr{L} dt$. The current peak luminosity reached at the LHC is about $\mathscr{L} = 2 \times 10^{34}\text{cm}^{-2}\text{s}^{-1}$, leading to a time integrated luminosity of $\mathbf{L} = 140\,\text{fb}^{-1}$ recorded with CMS and ATLAS experiments over the 2016-2018 Run 2 data taking period[1]. To illustrate this, one can compare the integrated luminosity with the cross section of the main process studied in this thesis, $\sigma_{\text{HH}} = 31.05\,\text{fb}^{-1}$ (ggHH) corresponding to about 4260 Di-Higgs boson events over the whole data taking period [14]. The physics implications of a proton-proton (pp) collider with composite particles, compared to e.g. lepton colliders, are discussed in Sec. 2.5.

[1] $1\,\text{b} = 10^{-28}\,\text{m}^2$

Figure 3.2: The CMS experiment inside the cavern of interaction point P5 of the LHC on the French side of the accelerator ring. The experiment here is opened for maintenance during the shutdown between LHC Run 2 and Run 3 and offers a view inside the barrel part of the experiment.

3.2 The Compact Muon Solenoid

The data used in this thesis was recorded between 2016 and 2018 with the CMS experiment at the LHC P5 interaction point. A picture of the opened CMS experiment can be seen in Fig. 3.2. Like its sister experiment ATLAS, the CMS experiment is a general-purpose detector designed to access a wide range of SM and BSM physics with special emphasis on the discovery and study of the Higgs boson. The design is cylindrical around the interaction point where the proton beams collide. From the inner tracker to the outer muon system, several subsystems are designed to measure energy and momentum and to identify the produced particles during the pp interactions. CMS name-giving feature is a huge 4 T solenoid magnet surrounded by a massive iron yoke that houses a precise muon system. The solenoid has a diameter of 6 m enabling the encapsulation of the tracking systems and most of the two calorimeters. This gives CMS a compact design compared to other detectors such as ATLAS.
It has a length of 21.6 m and a diameter of 14.6 m and a weight of about 12 500 t.

3.2.1 CMS Coordinates

The CMS coordinate system is displayed in Fig. 3.3. It is centered around the beam pipe with its origin in the center of the detector. The direction of the z-axis is given by the beam direction that faces the Jura Mountains. The x-axis points to the center of the LHC ring while the y-axis points upwards. The angles ϕ between the x and the y-z plane as well as the angle θ to the z axis can be used to describe the direction of particles traversing the detector. As protons are composite particles (see Sec. 2.5), the momentum in z-direction of the colliding proton fragments forming the "hard process" is not known. Therefore, energy (E) and momentum (p) measurements are mostly projected to the transverse x-y plane (E_T/p_T). For the same reason, instead of θ, the

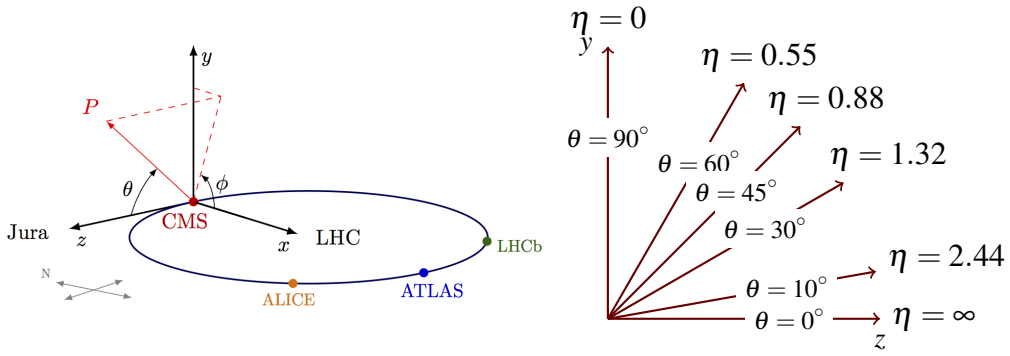

Figure 3.3: The CMS coordinate system on the left and a visualisation of the pseudorapidity η [46, 47].

pseudorapidity η and the rapidity y are commonly used. They are defined as:

$$\eta = -\ln\left[\tan(\frac{\theta}{2})\right], \; y = \frac{1}{2}\ln\left(\frac{E+p_{\mathrm{T}}}{E-p_{\mathrm{T}}}\right) \tag{3.1}$$

Differences of η or y are Lorentz invariant. Angular distances are usually given by the quantity $\Delta R = \sqrt{\Delta\phi^2 + \Delta\eta^2}$. To complete the polar coordinate system given by the angles ϕ and η and the coordinate z along the x axis, the distance r is defined as the distance to the center in the transverse plane. In discussions of CMS structure, the terms 'barrel', refers to the central low $|\eta|$ region of the detector and 'end-cap' refers the high $|\eta|$ region of the detector.

3.2.2 The Particle Flow Algorithm

The layered design of the CMS detector allows for particle identification as every particle type interacts with different types of the detector. From the interaction point outwards, the tracking system, calometric system, the magnet and the muon system are passed by the particles created in the proton-proton collision. The magnetically bend tracks charged particles leave in the tracking system allow for the measurement of the p_{T} of particles and of their electric charge. The excellent 3D spatial resolution of the inner tracking system allows for the precise reconstruction of the point of origin of charged particles. Thus the identification of primary and displaced secondary vertices is possible, allowing for the identification of particles with distinct lifetimes. Most particles are stopped in the calorimeter systems producing scintillation light that enables the measurement of particle energies. This also allows the identification of neutral particles, which are not associated to tracks. To distinguish between predominantly electromagnetically interacting particles like electrons or photons and mainly hadronically interacting particles like protons and neutrons, the calorimeter system consists of two subsystems, the electromagnetic calorimeter (ECAL) transversed by most hadrons and the hadronic calorimeter (HCAL). While some high-energetic particles are not fully stopped by the hadronic calorimeter or shortly after, only two SM particles can traverse the whole detector, namely muons, and neutrinos. The former are electrically charged but as minimally ionizing particles loose only very little energy traversing the detector. They leave additional tracks in the outer muon system, allowing for their identification and additional input for the momentum reconstruction. Neutrinos do not interact with the detector significantly and thus are only measured indirectly, namely from the momentum imbalance

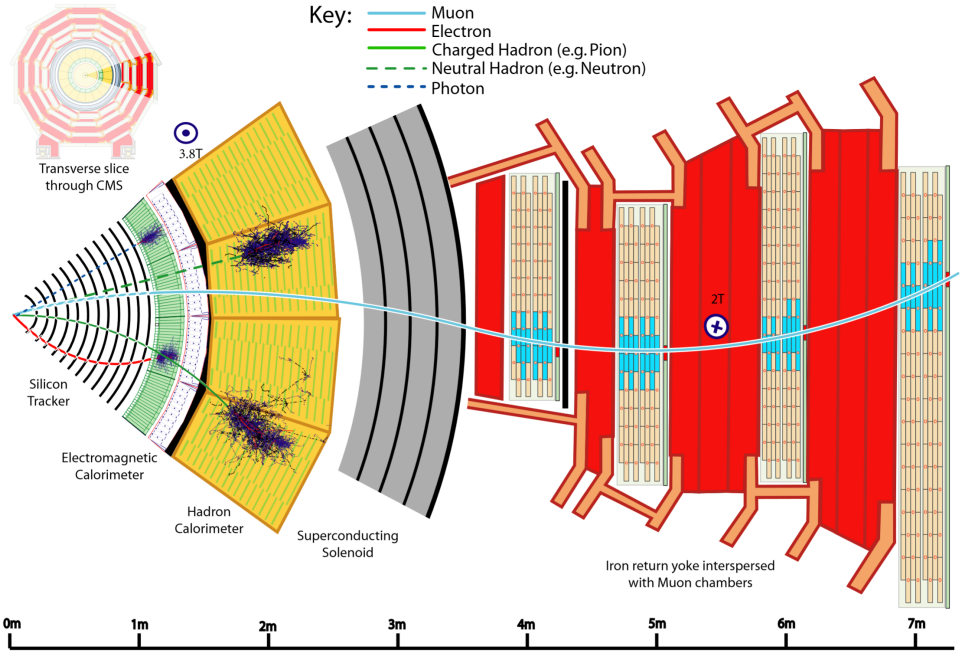

Figure 3.4: Schematic overview of the CMS detector showing a transverse slice through the different sub-detectors. The characteristic signatures of different particles such as muons, electrons, charged hadrons as the π^-, neutral hadrons such as neutrons and photons leave in the detector are shown as well [48].

of the reconstructed particles they recoil against. More complex signatures of composite particles can be reconstructed by their decay products, for instance decaying neutral pions. This can include in the case of charged decay products the observation of a displaced vertex corresponding to the characteristic decay length of the mother particle, the determination of a characteristic resonant mass from the decay products or in the case of the neutral pion the observation of the energy deposit from the decay into photons. Examples of all the described signatures can be seen in Fig. 3.4. The particle flow algorithm of CMS uses the logic and information above to find particle candidates for electrons, muons, photons, hadrons and subsequently jets. Jets are then further refined by additional quality and isolation criteria to serve as basis for analysis level objects. Particle flow objects are then further augmented by additional algorithms as described in Sec. 3.2.12 and Sec. 3.2.11 to reconstruct and identify more complex objects like hadronically decaying taus or the jets produced by b-quarks. More details on basic object reconstruction in particle flow is found in [48].

3.2.3 The Inner Tracking System

The CMS tracking system as shown in Fig. 3.5 consists of several subsystems. The innermost system is the pixel detector, surrounding the beam pipe. The pixel detector is used as a vertex detector to find the primary vertex of the hard interaction process allowing the distinction of particle signatures from multiple proton-proton collisions. It also provides the identification of secondary vertices from short lived particles and seeds the track finding algorithms of CMS that together with hits in the strip detectors produce track candidates for charged particles. It consists of two parts, first the cylindrical barrel BPIX detector covering the central region up to $|\eta| \approx 1$, and secondly the forward-facing FPIX extending the pixel detector coverage to $|\eta| = 2.5$. Until

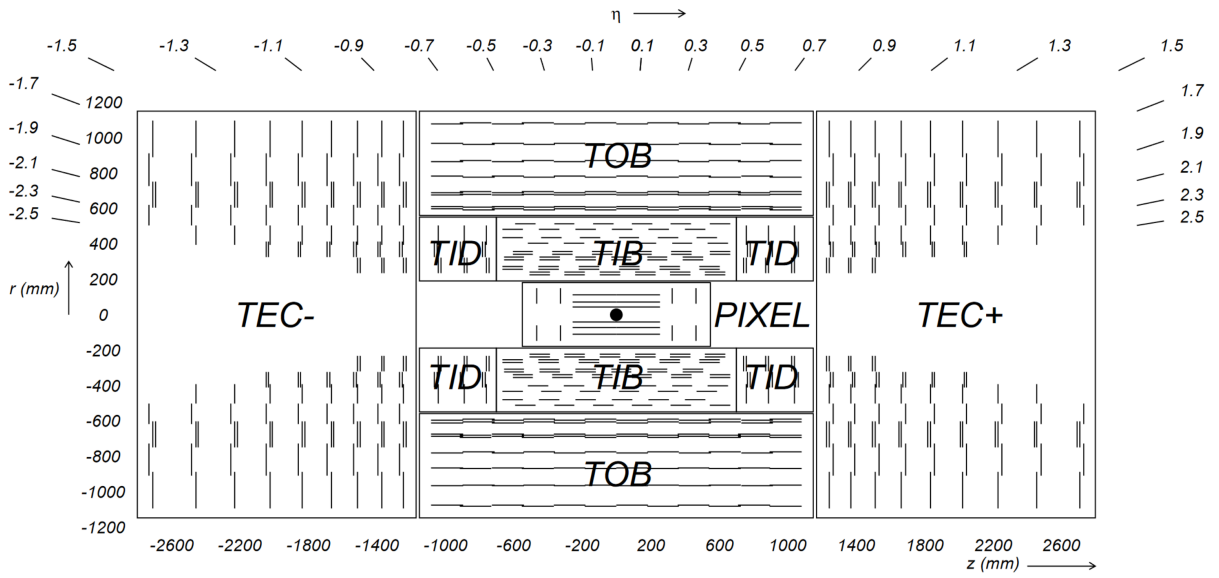

Figure 3.5: The CMS tracking system with its sub-detectors, the silicon pixel detector in the center, surrounded by the strip-tracker Tracker Inner Barrel (TIB) and Tracker Outer Barrel (TOB) detectors in the barrel region, and the Tracker Inner Disk (TID) and the Tracker End Caps (TEC) in the end cap region [36].

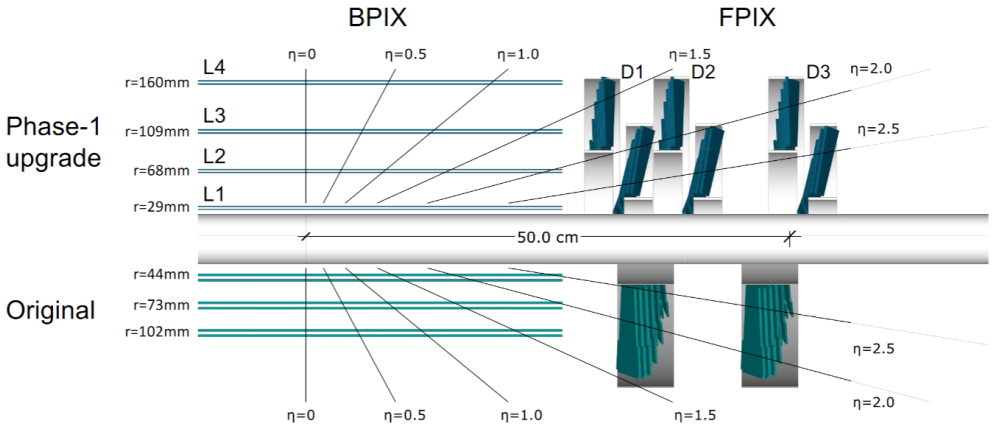

Figure 3.6: The layout of the CMS pixel detector before and after the 2016 phase 1 upgrade. The pixel detector surrounds the beam pipe and consists out of 3 (4) pixel layers in the barrel region and 2 (3) disks in the forward region [49].

the end of 2016, the pixel detector consisted of three 53 cm long layers at $r = 4.4$, 7.3 and 10.2 cm in the barrel part and of two discs at z=±34.5 cm and ±46.5 cm. As shown in Fig. 3.6, the pixel detector was upgraded between the data taking in 2016 and 2017, including now four layers in BPIX at r=2.9, 6.8, 10.9 and 16 cm and three disks with two separate rings at z=± 30.9-33.8 cm, ± 38.4-41.3 cm and ± 47.9-50.8 cm. A picture of one half of the new 4-layered pixel detector can be seen in Fig. 3.7. As the pixel detector is the innermost detector, with the first layer only a few centimeters away from the collision point, it has to withstand a high flux of high energetic particles. At the same time the detector needs to provide a high granularity for fast measurement of around 1000 particles per collision every 25 ns. Further, the material budget i.e. the stopping power of the tracker and its support electronics, cooling and structure, needs to be minimal. This is to not reduce the energy measurement resolution of the outer CMS detectors such as the ECAL and HCAL. The design choice that follows these requirements is the

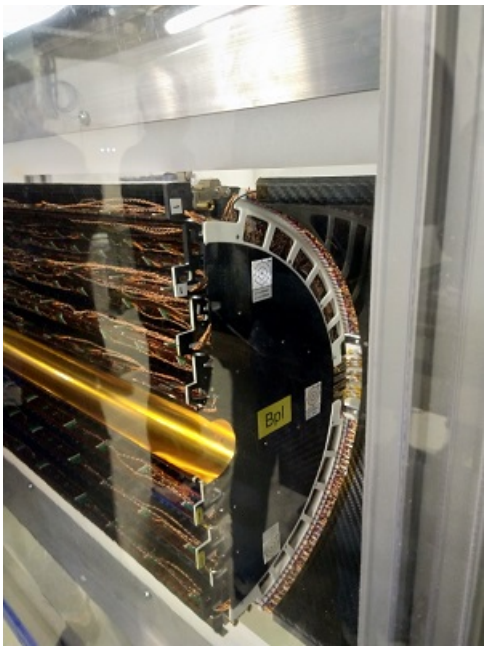

Figure 3.7: One half of the barrel BPIX detector with its four pixel layers. Photo taken during the long shutdown between the LHC data taking Run 2 and Run 3 where the pixel detector was extracted for maintenance in January of 2019.

usage of silicon semiconductor sensors in the entire tracking system. The pixel sensors provide a two-dimensional hit measurement with a pixel cell size of about $100 \times 150\,\mu\text{m}^2$. The spatial resolution of the detector was measured to be $9.5\,\mu$m in the r-ϕ direction and $22.2\,\mu$m in the z-direction for the BPIX layer three [49]. More about the operational challenges of the pixel detector in this high radiation environment can be found in Sec. 3.3. The rest of the tracking system, with its length of 5.8 m and a diameter of 2.5 m, consists of 10 layers of strip detectors in the barrel region and 12 disks in the endcap region. As seen in Fig. 3.5, these are subdivided into four sub detectors, the **T**racker **I**nner **B**arrel (TIB), **T**racker **O**uter **B**arrel (TOB), **T**racker **I**nner **D**isks (TID) and **T**racker **E**nd**C**aps (TEC). For reference, the spatial resolution of the TIB is given as $23\,\mu$m in layers 1 and 2 and $35\,\mu$m in layers 3 and 4 [36, 49].

3.2.4 Particle showers and the Calometric System

Calorimeters are used to measure particle showers from high energetic particles interacting with the detector material. Depending on the detector material and the original particle, electromagnetic or hadronic particle showers can occur.

Electromagnetic showers are caused by mainly electromagnetically interacting particles such as photons, electrons or positrons. As shown in Fig. 3.8, electrons and positrons produce bremsstrahlung photons that subsequently create electron-positron pairs, doubling the showers particle content every radiation length[2] X_0 until a critical average energy per particle is reached. The shower is stopped when the shower particles lose their remaining energy via ionization.

A hadronic particle shower behaves similar with the distinction that new particles are created via the strong interaction, producing a multitude of hadrons and mesons as well as electromagnetic sub-showers.

[2] $X_0 \propto \frac{1}{n \cdot Z^2 \cdot \ln Z}$, with n the density of nuclei and Z the charge number of nuclei in the absorber material.

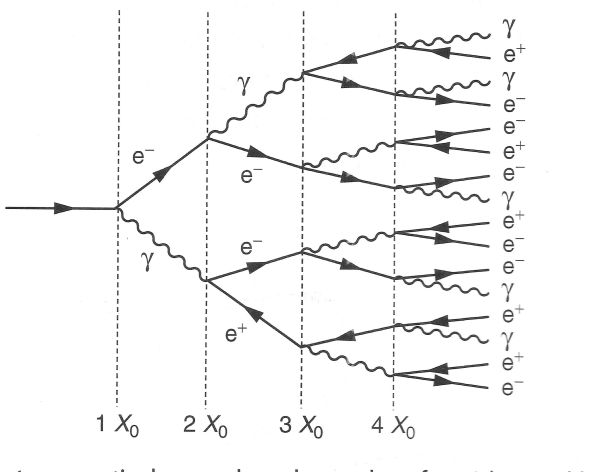

Figure 3.8: An electromagnetic shower induced by an electron doubling its particle content by bremstrahlung and pair production every radiation length X_0 [12].

To induce and measure these particle cascades, a calorimeter often consists of a passive absorber material facilitating the shower interactions and an active detector material, stopping and measuring the lower energetic shower particles. This is often done by a scintillating material in which charged particles produce light proportional to their kinetic energy, which is then measured by photo-sensors and converted into an electrical signal.
The measurement of these two shower types in CMS is performed by the electromagnetic calorimeter (ECAL) and the hadronic calorimeter (HCAL).
The ECAL implores a high Z material to trigger electromagnetic interactions, and enough electromagnetic radiation lengths to stop most electromagnetically interacting particles.
While this does not prevent hadronic interaction, the number of hadronic interaction lengths[3] λ_I in the ECAL is low enough that hadronically interacting particles lose most of their energy in the HCAL. This allows easier particle identification by using the two distinct detectors [12].

CMS ECAL

The CMS ECAL consists mostly of lead tungsten ($PbWO_4$) crystals, combining a high Z absorber material with the scintillating properties of an active detector material. As can be seen in Fig. 3.9, the high density crystals are transparent and allow scintillation light to travel to the photo detectors, which are attached at the end of each crystal. This choice of combined active detector and passive absorber material allows for a very precise energy resolution compared to typical sampling calorimeters consisting of alternating absorber and detector layers:

$$\left(\frac{\sigma}{E[\mathrm{GeV}]}\right)^2 = \left(\frac{2.8\%}{\sqrt{E[\mathrm{GeV}]}}\right)^2 + \left(\frac{0.12\%}{E[\mathrm{GeV}]}\right)^2 + (0.3\%)^2$$

Similar to the tracking detector, the ECAL consists of a cylindrical barrel part around the beam axis closed by two end caps extending the coverage to $|\eta| = 3$. The general ECAL layout can be seen in Fig. 3.10.
The barrel part (EB) extending up to $|\eta| = 1.479$ consists out of 61200 crystals with a granularity

[3] $\lambda_I \propto n$, with n the density of nuclei in the absorber material.

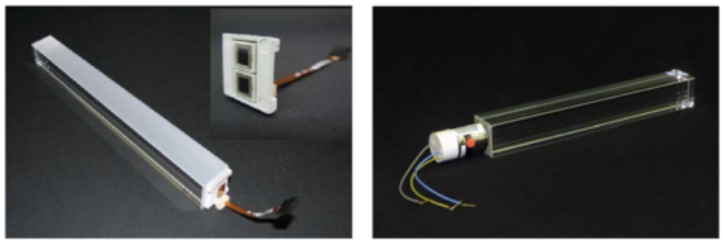

Figure 3.9: Lead-tungsten ($PbWO_4$) crystals with photo detectors, for the barrel part (left) and encap part of the CMS ECAL [36].

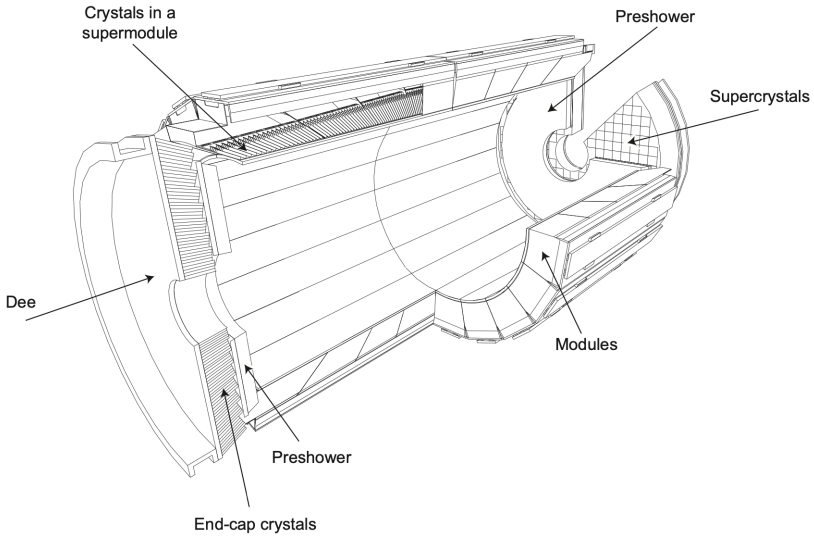

Figure 3.10: The general layout of the CMS ECAL and its sub components. The barrel part (EB) covering a region up to $|\eta| < 1.479$ consists out of modules containing 400-500 $PbWO_4$ crystals each grouped into supermodules containing four modules. The endcap region (EE) up to $|\eta| < 3$ is covered by four "D" shaped detectors consisting of supercrystals grouping 5×5 $PbWO_4$ crystals into 156 supercrystals per Dee. An additional pre-shower detector is placed in front of the EE covering $1.653 < |\eta| < 2.6$ with a high granularity sampling calorimeter, assisting pion and electron identification [36].

of 0.0174×0.0174 in η-ϕ and a length corresponding to $25.8\,X_0$, starting at r=1.29 m.
To avoid cracks in the ECAL coverage as much as possible, the shapes of the crystal are slightly altered based on η. Further they are put into modules of 400-500 crystals and combined into supermodules consisting out of four modules or 1700 crystals.
The two endcaps (EE) at $z = \pm 315.4$ cm consist of a total of 14848 crystals organized in two halves or Dees per endcap, with 156 super crystals, a 5×5 unit of $PbWO_4$ crystals each.
The crystals have a front surface of $28.62 \times 28.62\,\mathrm{mm}^2$ and a length corresponding to a radiation length of $24.7\,X_0$.
An additional pre-shower detector is placed in front of the EE, consisting out of two layers. Each is made from a lead radiator to initiate showering and is followed by a silicon strip sensor. This sampling calorimeter with a thickness of $2 + 1\,X_0$ has a high granularity offering an improved position measurement for electrons and photons. This is needed for the identification of neutral pions and the distinction of electrons and minimal ionizing particles (MIP) such as muons in the forward detector region $1.653 < |\eta| < 2.6$.

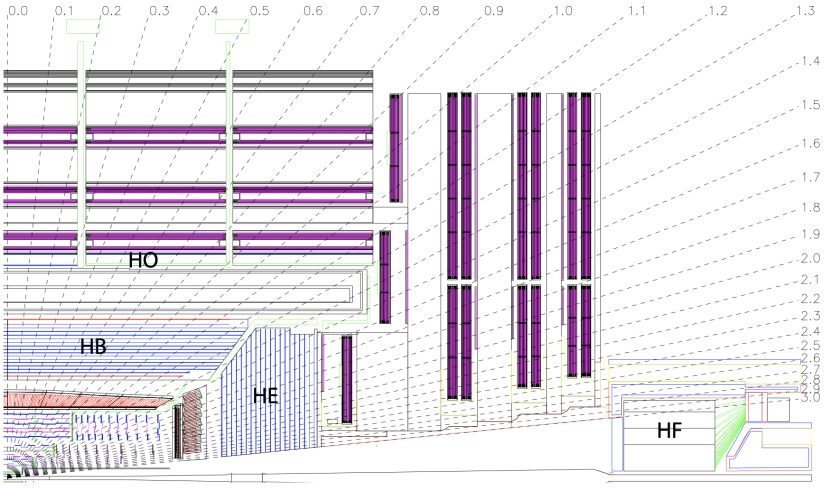

Figure 3.11: Longitudinal slice of the CMS detector, showing the position of the different HCAL sub-detectors, the barrel calorimeter HB within the CMS solenoid, the end cap calorimeter HE, the forward calorimeter HF and the outer calorimeter HO placed outside the CMS solenoid [36].

CMS HCAL

The CMS HCAL is a classical sampling calorimeter, consisting of a barrel detector (HB) between the EB at $r = 1.77\,\text{m}$ and the CMS solenoid at $r = 2.95\,\text{m}$, an endcap detector (HE), covering particles up to $|\eta| < 3$, a forward detector (HF) placed 11.2 m away from the interaction point and an outer calorimeter (HO) in the barrel region extending the HCAL beyond the solenoid. This tail catcher is necessary, because the size of the solenoid restricts the amount of HCAL material and thus its stopping power. Showers produced by high energetic particles can punch through the HB and extend beyond the magnet. The general structure of the HCAL and its position within the CMS detector can be seen in Fig. 3.11. The HB consists of alternating layers of brass and steel absorber plates and Kuraray SCSN81 plastic scintillator, divided into two times 18 wedges in ϕ with a further subdivision of the active detector material into 16 sectors or towers in η. The HB is shown in Fig. 3.12. It covers the range up to $|\eta| = 1.3$ and allows for a granularity of $\Delta\eta \times \Delta\phi = (0.087 \times 0.087)$. The total absorber thickness at $\eta = 0$ is 5.8 λ_I with an additional 1.1 λ_I from the ECAL. The absorber thickness further increases by $\frac{1}{\sin\theta}$ for more forward flying particles.

Covering the η range from $|\eta| = 1.3$ to $|\eta| = 3$, the HE sits in the difficult spot at the end of the 4T solenoid, and requires the use of non-magnetic materials while providing enough stopping power to contain the high energetic particles in the forward region of the detector. This leads to the choice of brass as absorber material, which provides a thickness of about 10 λ_I together with the ECALs EE. Within the absorber material, 18 scintillator layers with Kuraray SCSN81 in the outer 17 and Bicron BC408 scinillator are placed in the innermost layer. The active material is arranged into trays, providing a detector granularity of $\Delta\eta \times \Delta\phi = (0.087 \times 0.087)$ for $|\eta| < 1.6$ and $\Delta\eta \times \Delta\phi = (0.17 \times 0.17)$ for $1.6 < |\eta| < 3.0$.

The HO indirectly uses the solenoid as absorber material with $\frac{1.4}{\sin\theta}\,\lambda_I$. A massive iron yoke for returning the magnetic field is placed around the magnetic coil (see Sec. 3.2.5). It consists of 5 rings, containing the HO as its first sensitive layer, followed subsequently by the muon detectors (see Sec. 3.2.6). Because the detector thickness is the lowest at $\eta = 0$, the innermost ring contains

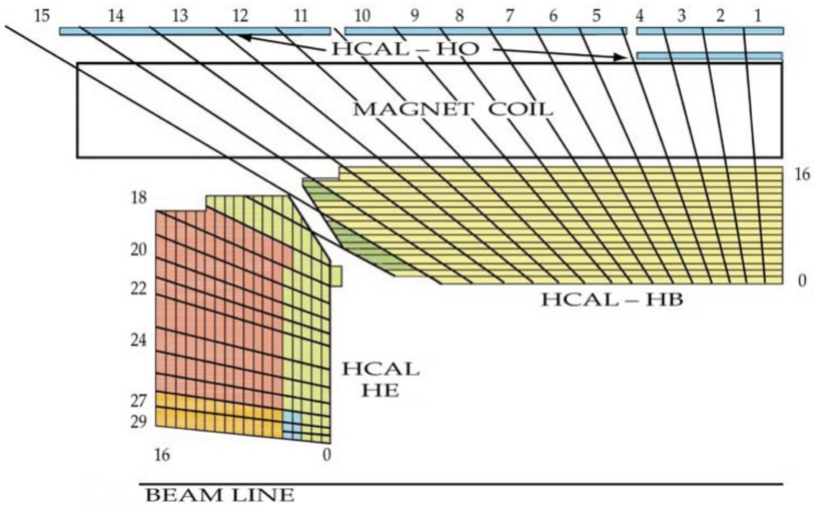

Figure 3.12: The separation of the HCAL HB, HE and HO detectors in the $r-z$ plane into readout towers in η. The section shown corresponds to a quarter of the three sub-detectors [36].

an additional 19.5 cm iron piece surrounded by two scintillator layers while the HO in the other rings contains only one layer. This extends the total HCAL thickness to a minimum of $11.8\,\lambda_I$. Similar to the other HCAL sub-detectors, the HO has a granularity of $\Delta\eta \times \Delta\phi = (0.087 \times 0.087)$. The HF extends the CMS detector to a range of $|\eta| < 5$ working in a region of extremely high particle flux with $\approx 88\%$ of the energy left in the detector being deposited in the two forward calorimeters. The HF is a Cherenkov detector, detecting the Cherenkov light that is produced by charged particles that travel faster than the speed of light in the given medium. The HF consists of quartz fibers serving as the active detector material within a steel absorber structure. As the detector captures the Cherenkov light of charged particles, the fibers forming $(\Delta\eta \times \Delta\phi) = (0.175 \times 0.175)$ towers mostly focus on the electromagnetic sub-component of hadronic showers [36].

The energy resolution of the HCAL depends greatly on the electromagnetic and neutral sub-components of the hadronic shower and thus varies greatly between different particle types as well as HCAL subsystems. To give a general idea of the HCAL performance one can look at the combined ECAL+HCAL energy resolution of charged pions as measured in test beam studies [50] and is found to be:

$$\frac{\sigma}{E[\text{GeV}]} = \frac{84.7\%}{\sqrt{E[\text{GeV}]}} + 7.4\%$$

The energy resolution of jets shown in Fig. 3.13. is about 20% for low energy jets ($p_{\text{T}} <$ 100 GeV) and 5-10% for high energetic jets ($p_{\text{T}} > 100$ GeV) [36]. More about jet reconstruction can be found in Sec. 3.2.10.

3.2.5 The CMS Solenoid

Surrounding the ECAL and the HCAL, the CMS experiment features one of the largest solenoids in the world with a diameter of 6 m and a length of 12.5 m. The superconducting coil provides a magnetic field strength of up to 4 T within the solenoid. The magnetic field is returned in a massive iron yoke that surrounds the solenoid and houses the HO HCAL sub-detector (see Sec. 3.2.4)

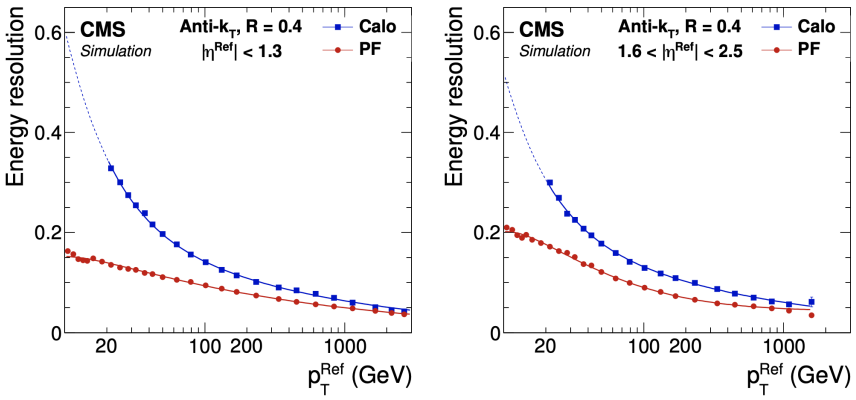

Figure 3.13: The jet energy resolution of jets clustered with the anti-k$_T$ algorithm [51] described in Sec. 3.2.10 for simulated CMS events at $\sqrt{s} = 13$ TeV. CALO jets, clustered only from ECAL and HCAL energy deposits as well as particle flow (PF) jets clustered from all reconstructed particle flow objects [48].

as well as the muon system described in Sec. 3.2.6. This allows to bend charged particles in the whole detector, allowing for charge identification and for improved momentum resolution. The size of the magnet allows to house (most of) both calorimeters. This reduces the amount of material passed and thus the energy lost before entering the instrumentation region. The iron return yoke is segmented into 5 rings along z and 6 endcaps [36].

3.2.6 The Muon System

The muon system constitutes CMS outermost layers. The basic muon reconstruction is described in Sec. 3.2.8.

The muon (tracking) system consists of three sub types of gaseous detectors, first the drift tube chambers (DT) in the barrel region covering up to $|\eta| = 1.2$, second, the cathode strip chambers (CSC) in the end-cap region covering $0.9 < |\eta| < 2.4$ and third, resistive plate chambers (RPC) in both the barrel and end-cap regions.

The muon barrel sub-detector (MB) as seen in Fig. 3.14 consists of four layers in each ring of the iron yoke (see Sec. 3.2.5) each consisting of 12 sectors in ϕ. Ten of these sectors contain one DT chamber with two DT chambers in the fourth layer of sector 4 and 10 as seen in Fig. 3.15 holding both the DT and RPC subsystems. Each DT chamber contains 2-3 super layers (SL) each combining four layers of drift chambers. Two of the SL are measuring the muon track position in the $r-\phi$ plain achieving a global resolution of 100 μm with 8 hits in the two SL. In the three inner layers, each DT chamber also contains a third SL oriented to measure the z axis instead. The drift cells themselves consist of an anode wire in an electric field. The track position is then determined by measuring the drift time of the ionization signal to the anode wire.

The layout of the muon system end cap region can be seen in Fig. 3.16. The CSC, covering each either 10° or 20° in ϕ are grouped such that they overlap and provide full ϕ coverage with the exception of the ME1/3 ring. Muons in the endcap region $1.2 < |\eta| < 2.4$ cross 3-4 chambers while muons in the overlap region $0.9 < |\eta| < 1.2$ travel through both, the barrel DT chambers as well as some CSC. The CSC are multi-wire proportional gas chambers that allow for a precise measurement in the difficult magnetic environment of the muon end caps. The CSC wires run

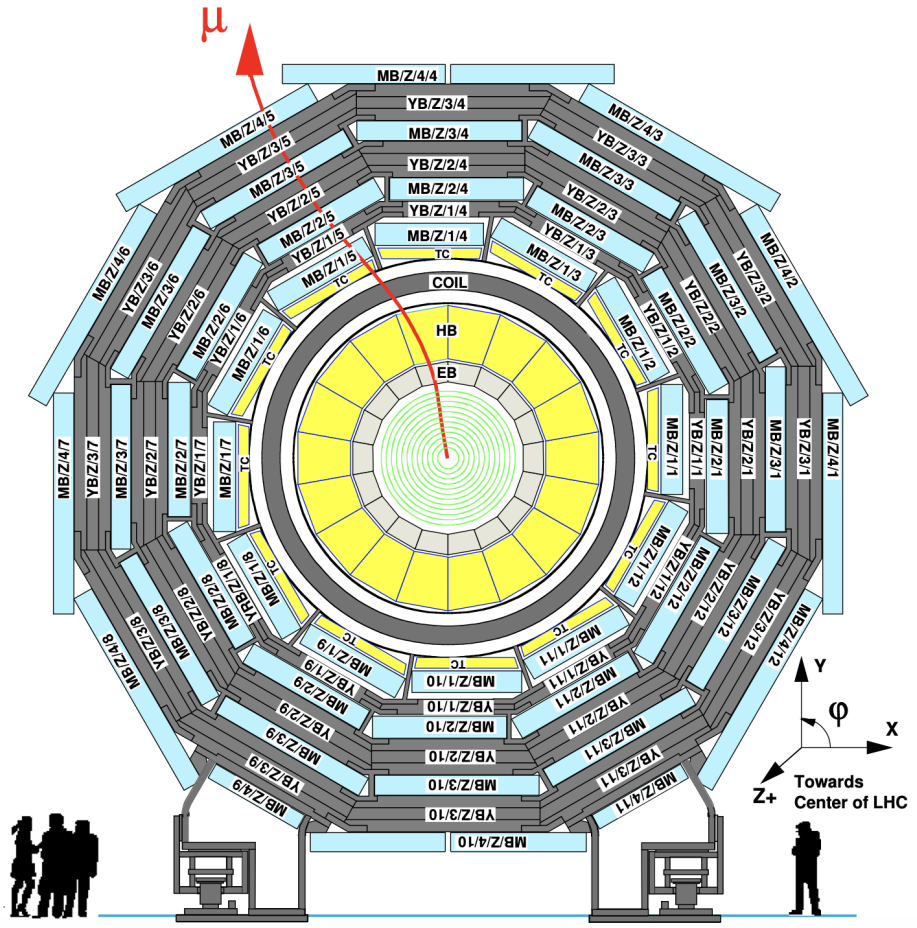

Figure 3.14: $r-\phi$ view of the CMS detector showing the layout of the DT chambers of the MB detector for one wheel of the CMS iron yoke. The MB is split into twelve sectors consisting of four layers of chambers in between the iron support structure. Sectors 4 and 10 hold 2 DT chambers in the outermost layers while all other layers and sectors only contain one [36].

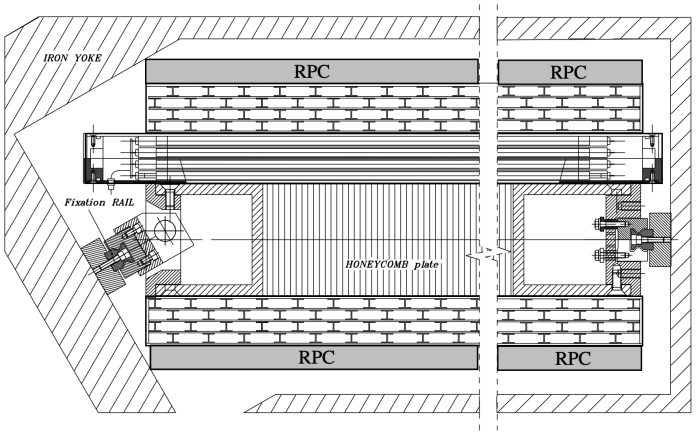

Figure 3.15: $r-\phi$ view of the drift tube chambers within the barrel muon system. Each chamber contains two super layers (SL) separated by a light weight honeycomb plate consisting of 4 layers of rectangular drift cells measuring the track position in the $r-\phi$ plane. All DT chambers except the outermost ones in layer 4 contain an additional SL in between the other two, measuring the track position along z. The DT chambers also contain RPC [36].

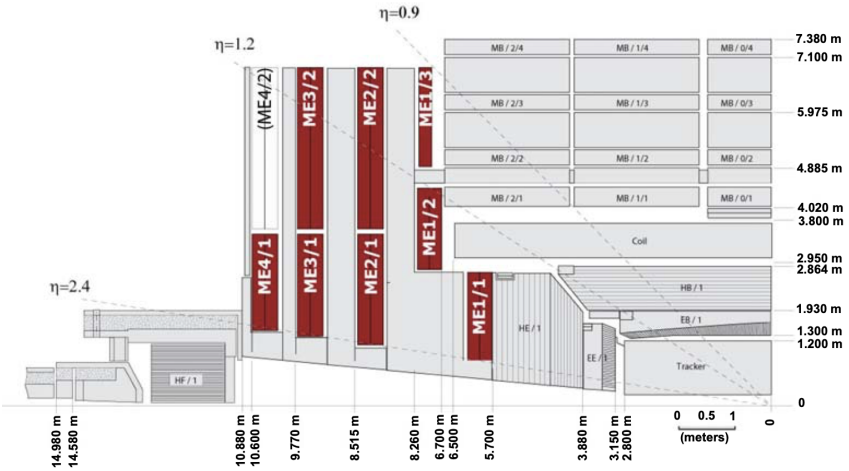

Figure 3.16: $r-\phi$ view showing a quarter of the CMS detector with the position of the cathode strip chambers in the end cap muon system [36].

along ϕ allowing for a measurement in r. To allow for a measurement along the wires in ϕ, finely segmented cathode strips running orthogonal to the wires are used.
Finally, the RPC are gaseous parallel-plate detectors with an extremely fast readout. While they also contribute to muon track measurements, their primary function is the assistance in the trigger system (see Sec. 3.2.7), with a response time much shorter than 25 ns.
In the barrel region, two RPC planes are contained in each of the two inner DT chambers. Further there is one RPC plane in each of the two outer DT chambers adding up to 6 planes in total. In the end cap region, four layers of RPC up to a coverage of $|\eta| = 1.9$ are installed [36, 52].

3.2.7 The CMS trigger system

To enable the measurement of the rarest processes, the LHC operates at an extremely high luminosity with bunch crossings happening every 25 ns leading to 40 million interaction events every second. While this is impressive, such a high number of events come with two main problems. Firstly, the data size needed to store all the relevant information of one event amounts to approximately 0.5 MB making the storage of 40 million events per second (20 TB/s) a computational impossibility for any feasible time period. Secondly, even though each event contains multiple proton-proton collisions, only a small fraction of events actually contains hard interactions targeted with the CMS physics program. This makes their study a literal search for the needle in a haystack.
Therefore, CMS makes use of a 2-stage triggering system reducing the data readout to a manageable event rate of up to 400 Hz. The first stage, the hardware-based L1 trigger, uses basic particle candidates based of energy clusters in the HCAL and ECAL as well as hits in the DT, CSC and RPC muon subsystem to decide within 4 μs whether to reject an event or to accept it for further processing. This reduces the trigger rate to a maximum of about 100 kHz. This provides the necessary time for a full event readout and the processing by the software-based high level trigger (HLT), which makes the final storage decision.
In contrast to the L1 trigger, the HLT uses the complete event information to perform a simplified

event reconstruction, providing objects such as electrons, muons, taus and jets similar to those in the final offline event analysis. Based on these a customizeable trigger menu designed for the needs of the current physics program is implemented. HLT triggers with a high rate are prescaled by skipping events and latter scaling the recorded events with the corresponding pre-scale factor. This allows for balancing the different physics needs while also recording data streams for detector calibration, detector monitoring and minimal bias events representing the entire physics content of all collision events while staying within the data processing limits with a recording rate of about 400 Hz [53].

3.2.8 Muon reconstruction

Being MIPs, muons usually travel through the whole detector, and leave a track in the inner tracking system as well as in the outer muon system while only depositing small amount of energy in the ECAL and HCAL. Depending on the hits in the tracker, we can distinguish between three muon types:

1. Standalone muons leave at least hits in the DT and CSC subsystems. These are clustered to form segments used as seeding input for a pattern recognition algorithm to fit all RPC, DT and CSC hits along the muon trajectory to a standalone muon track.

2. Tracker muons: Tracks found in the inner tracking system reconstructed by a pattern recognition algorithm with a $p_{\mathrm{T}} > 0.5$ GeV and $p > 2.5$ GeV that are compatible with at least one muon segment are classified as tracker muons. Physics wise, these correspond to lower energetic muons stopped in the iron yoke.

3. Global muon: If a track in the inner tracker and a standalone muon track can be matched, a global muon track is fitted to all hits of both tracks, improving the momentum resolution of high p_{T} muons compared to a (inner) tracker only fit.

Within CMS analyses, usually global and tracker muons are used, leading to an excellent muon reconstruction efficiency of 99 %. For the use as an analysis level object, muon candidates obtained in the above described manner are further refined as described in Sec. 6.3 [48].

3.2.9 Electron reconstruction

Most electrons emit a sizeable fraction of their energy in the form of bremsstrahlung photons before depositing their energy in the ECAL. An inclusive tracking algorithm is used to identify all kinds of radiating and non-radiating electrons as well as electrons contained in jets. ECAL deposits over 4 GeV are used as electron seeds, as well as tracks found by an iterative tracking algorithm exceeding 2 GeV.
For electrons seeded by tracks, the potential energy loss of photons is taken into account by refitting potential tracking candidates with a Gaussian-sum filter (GSF). For electrons seeded from GSF tracks, the corresponding ECAL deposit must not be compatible with three or more tracks. The high chance of photon radiation is used to distinguish electrons from charged hadrons. In case of a non-radiating electron, the energy of the ECAL deposit closest to an extrapolated track is required to be compatible with the tracks p_{T} to form an electron seed. For electrons seeded

from ECAL clusters, energy deposited in the HCAL closer than $R = 0.15$ must not exceed 15 % of the ECAL clusters energy. To form the electron candidate, all ECAL clusters associated with the GSF tracks tangents or the ECAL supercluster formed from electron and photon ECAL energy deposits along the electrons trajectory are combined, with an additional E and η dependent energy correction of the ECAL clusters. For the final electron direction, the GSF track direction is used. Before being used as analysis level objects as described in Sec. 6.3 additional quality criteria are applied [48].

3.2.10 Jet Reconstruction - the Anti-k$_T$ Algorithm

Because color-charged particles cannot exist freely within nature, quarks and gluons produced within CMS hadronize, and produce a cascade of charged and neutral particles commonly referred to as a jet.
For jet reconstruction, particle flow objects are clustered by a jet algorithm such as the anti-k$_T$ algorithm which will be described in the following. Two distances are calculated for each particle flow candidate i:

1. $d_{ij} = \min({p_{\mathrm{T}i}}^{2p}, {p_{\mathrm{T}j}}^{2p}) \frac{(y_i - y_j)^2 + (\phi_i - \phi_j)^2}{R^2}$, as distance parameter between two particles i, j
2. $d_{iB} = {p_{\mathrm{T}i}}^{2p}$, as distance parameter between particle i and the beam

with y_i the rapidity of object i and R, p adjustable parameters of the algorithm. As long as $d_{ij} < d_{iB}$ particles i and j are combined, if $d_{ij} > d_{iB}$ or no other remaining objects are found, i is classified as a jet. The parameter p steers the ordering in which objects are merged, for the anti-k$_T$ algorithm $p = -1$, hence the name anti-k$_T$ with k$_T$ being another symbol for the transverse momentum p_{T}. Choosing a negative p leads to cone shaped jets of radius R where softer particles are merged around central objects with higher p_{T}. Within CMS, usually jets of cone size $R = \sqrt{\Delta\eta^2 + \Delta\phi^2} = 0.4$ or "AK4" jets are used as standard jets, while jets with $R = 0.8$ or "AK8" jets are used for merged topologies, i.e., boosted top or W boson decays. Jets obtained by the anti-k$_T$ algorithm undergo further quality criteria as described in Sec. 6.3 before being used as analysis level objects. They also serve as input for e.g. τ_{h} reconstruction (see Sec. 3.2.11 or are used to tag certain physics objects such as b-quarks as described in Sec. 3.2.12. [51] .

3.2.11 Tau Reconstruction - The Deep Tau Algorithm

The HH analysis presented in this thesis makes heavy use of τ leptons, requiring a special reconstruction and tagging algorithm that is presented in the following. Because τ leptons only have a mean lifetime of about 290.6 fs [5] corresponding to $c \cdot \tau$ =0.087 mm in the detector, τ leptons can only be seen indirectly by their decay products. As described in Sec. 2.1 τ leptons either decay leptonically into a muon or an electron and two neutrinos or into a neutrino and a hadronically decaying W boson. Thus when talking about τ reconstruction in particle physics, only hadronically decaying τ (labeled τ_{h}) are considered because leptonically decaying τ are already reconstructed as muons or electrons. Vice versa, only electrons, muons (and leptonically decaying τ) are referred to as leptons.
The τ_{h} identification uses the hadron-plus-strips algorithm (HPS) [54, 55] developed for the

Decay mode	Resonance	$\mathscr{B}(\%)$	
Leptonic decays		35.2	
$\tau^- \to e^- \bar{\nu}_e \nu_\tau$			17.8
$\tau^- \to \mu^- \bar{\nu}_\mu \nu_\tau$			17.4
Hadronic decays		64.8	
$\tau^- \to h^- \nu_\tau$		11.5	
$\tau^- \to h^- \pi^0 \nu_\tau$	$\rho(770)$		25.9
$\tau^- \to h^- \pi^0 \pi^0 \nu_\tau$	$a_1(1260)$		9.5
$\tau^- \to h^- h^+ h^- \nu_\tau$	$a_2(1260)$		9.8
$\tau^- \to h^- h^+ h^- \pi^0 \nu_\tau$			4.8
Other			3.3

Table 3.1: Possible decay modes of τ into leptons and hadrons with their respective branching fraction $\mathscr{B}$. For hadronic decays, also the corresponding meson resonances are given [5, 56]. h denotes electrically charged low mass mesons such as pions and kaons as well as their exited states.

$\sqrt{s} = 7,8$ TeV LHC data. In this analysis a newer version optimized for the $\sqrt{s} = 13$ TeV data taken in 2015-2018 [56]. The algorithm uses the constituents of particle flow jets, orienting itself on the possible τ decay final states summarized in Tab. 3.1

τ_h candidates

The signature of τ_h is defined by an odd number of charged hadrons $h^\pm$ plus a number of neutral pions π^0.

Neutral pions decay nearly instantly into a pair of photons, that in rare cases converts into $e^- e^+$ pairs while traversing the tracker. To identify and reconstruct the neutral pions, all electrons and photons, falling into a "strip" of dynamically defined size $\Delta\eta \times \Delta\phi$, are clustered together to form a π^0 candidate. These strips are seeded by photon and electron constituents of a particle flow jet in the following manner:

1. A new strip is seeded by the highest p_T e/γ not yet included in a strip.
2. The e/γ with the next highest p_T within:
   $\Delta\eta = f(p_T^{e/\gamma}) + f(p_T^{strip})$, $f(p_T) = 0.2 p_T^{-0.66}$
   $\Delta\phi = g(p_T^{e/\gamma}) + g(p_T^{strip})$, $g(p_T) = 0.35 p_T^{-0.71}$
   is merged with the strip.
3. The strip position is recomputed by the p_T weighted average of all e/γ within the strip.
4. The strip is complete, once no e/γ candidate can be found within the dynamic $\Delta\eta \times \Delta\phi$ window. If any e/γ are left, a new strip is seeded with the highest p_T e/γ.

The charged hadrons entering the τ_h reconstruction must originate from the primary vertex of the event, be it with a relatively loose restriction on the impact parameter of $d_{xy} < 0.1$ cm to account for the τ lifetime. To ensure sufficient quality of the underlying tracks, selected hadrons are further required to have a $p_T > 0.5$ GeV.

Based on these "hadrons" and "strips", τ_h candidates with up to three $h^\pm$ and zero to two π^0 are constructed. For each jet, only the highest p_T candidate is kept.

τ_h neural network discriminator

Different from the original approach in [56], the DeepTau algorithm used in this thesis uses a multivariate convolutional deep neural network to separate τ_h candidates from jets, electrons and muons. For this, the CMS detector is divided into a grid of cells with $\Delta\eta \times \Delta\phi = 0.02 \times 0.02$ within a signal cone of $\Delta R = 0.1$ and $\Delta\eta \times \Delta\phi = 0.05 \times 0.05$ outside the signal and within an isolation cone of $\Delta R = 0.5$ around the τ_h candidates major axis. For each particle flow candidate in one of these two grids, up to 37 variables in addition to a number of global variables such as the τ_h candidates four-momentum enter the network. This high number of input variables allows for an excellent discrimination of τ_h candidates, improving the τ_h identification efficiency by about 20 %. This can be seen in Fig. 3.17 where DeepTau is compared to the previous algorithm [56]. For the application in CMS analyses, 8 working points from VVVLoose-VVTight on the discriminator outputs against jets and electrons, and four working points on the discriminator against muons from VLoose-Tight are defined. In the HH analysis presented in this thesis, the medium working point against jets, the VLoose working point against muons and the VVVLoose and VLoose working points against electrons are used. More information about the performance and training of the DeepTau DNN can be found in [57], [58], and [59]. This analysis uses the `Deep Tau v2.1` training of the DeepTau algorithm.

3.2.12 b-jet tagging and the DeepJet algorithm

Electrons and muons leave fairly distinct signatures in the detector, but color charged particles such as gluons or quarks hadronize, leaving particle jets of many charged and uncharged particles in the detector. While at first glance, these complex objects only offer little information about the mother particles of the jet, besides the overall energy deposit left in the detector and the particles general direction, the type of the mother particle subtly influences the jets substructure.
These differences in jet shape and composition are used in jet-substructure techniques to separate jets induced from comparatively heavy b-quarks from other jets induced by lighter quarks or gluons. Modern algorithms such as DeepJet even allow further distinction between b-quark induced, charm-quark induced, gluon-induced and light-quark $(\mathrm{u},\mathrm{d},\mathrm{s})$ induced jets.
DeepJet is a neural network-based algorithm making use of around 650 input features containing track quality criteria, track displacement and secondary vertex information. In addition global features are used, such as the number of reconstructed primary vertices to judge the pileup content of the event. A full list of input variables can be found in the appendix of [60].
The sophisticated DeepJet architecture, shown in Fig. 3.18, allows to make use of this high number of low level input features using convolutional as well as recurrent neural network layers. The excellent performance for DeepJet can be seen in Fig. 3.19. Based on this, the three working points DeepJet-L, DeepJet-M and DeepJet-T are defined on the b-jet vs light jet (udsg) discriminant, for a b-jet misidentification probability of 10%, 1% and 0.1% respectively.

3.2.13 Prompt lepton MVA

The lepton selection in the HH part of this thesis uses an additional BDT discriminant to further refine the object definition of muons and electrons with respect to the rejection of non-prompt leptons, i.e., from b-jets as well as misidentified leptons.

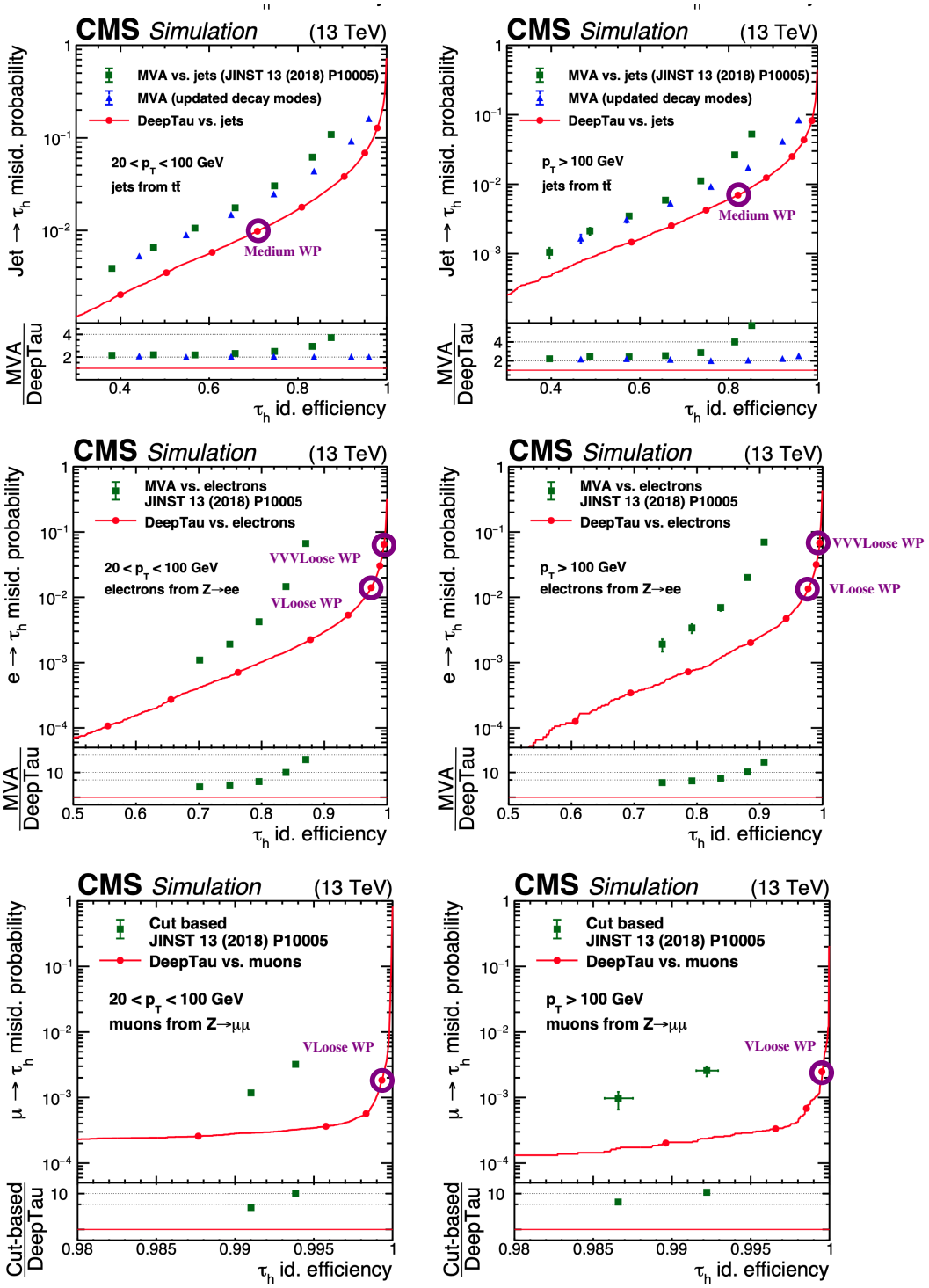

Figure 3.17: The performance of the DeepTau identification algorithm for differentiation against jets (**top**), electrons (**middle**) and muons (**bottom**). The working points used in this thesis are shown, giving the corresponding Tau ID efficiency and jet/electron/muon to tau misidentification rate [59].

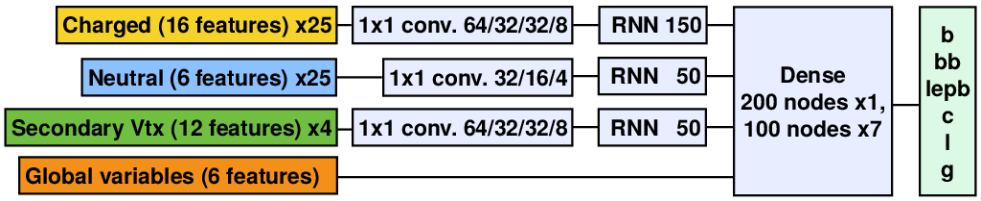

Figure 3.18: The neural network architecture of the DeepJet neural network. The input features are separated into four different branches. The low-level input variables belonging to charged and neutral jet constituents as well as secondary vertices within the jet undergo a feature transformation by a convolutional network layer before being combined in a recurrent neural network and finally being processed together with the global features in a dense layer [60].

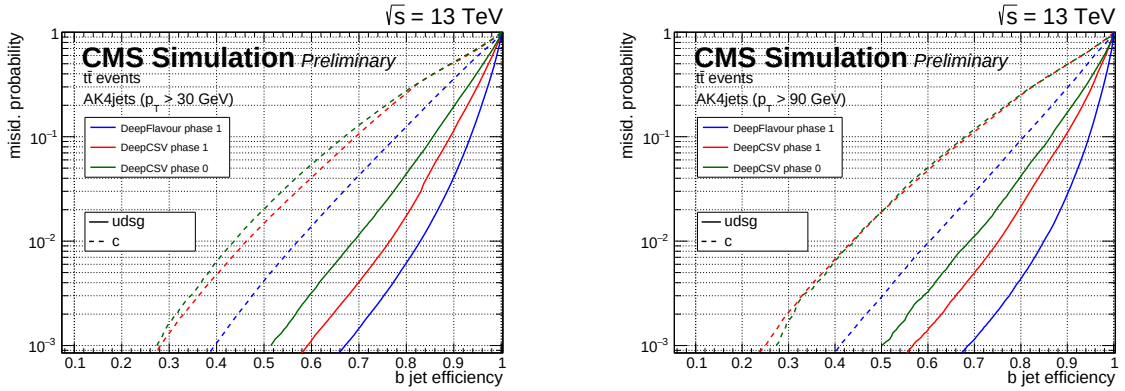

Figure 3.19: Performance of the DeepJet algorithm for the separation of b-quark induced jets vs $\mathrm{uds}\gamma$ or charm quark induced jets. The comparison to the previously used deepCSV algorithm is shown. The performance was determined on $\mathrm{t\bar{t}}$ events in $\sqrt{s} = 13$ TeV 2017 data recorded with the CMS experiment [61].

This approach was originally developed for the CMS search for $t\bar{t}\mathrm{H}$ production with Multilepton final states [62]. For the presented analysis, the BDTs working points have been optimized such as accounting for the higher-lepton multiplicities in the targeted final states. The BDT uses the leptons kinematics, lepton quality criteria such as their isolation, properties of the nearest jet, such as its b-tagging score (see Sec. 3.2.12) and impact parameters[4].
Different trainings are performed for muons and electrons with prompt leptons from W/Z decays and from leptonic τ decays in $\mathrm{t\bar{t}H}$ events as signal and non-prompt leptons from $\mathrm{t\bar{t}}-$jets events as background. The training is performed separately for the 2016 and 2017/2018 to account for the difference in "phase-0" and "phase-1" CMS detector conditions.

3.3 Detector Operation: Single Event Upsets in the Pixel Detector

The data needed for the successful analysis work presented in this thesis does not only rely on detector design but also on the continued effort of detector operation. Within this thesis it was possible to make a small contribution to these efforts. The following shows an example of the challenges faced in the day-to-day operation of the big undertaking that is CMS.

[4] Closest distance of track and primary vertex along z-axis (d_z), in the xy plane d_{xy} or in 3D d_{3D}.

These challenges include dealing with effects of the high radiation environment on the operation of the innermost CMS tracking detector, with the innermost layer of the pixel detector only being about 3 cm away from the center of the experiment. Here, the electronics of the otherwise radiation hard silicon detector face disturbances in operation caused by the influence of ionizing radiation.

To understand this, a deeper explanation of the data acquisition within the pixel detector subsystem is given in the following. Read-out chips (ROC) collecting the hit information of the pixel sensors are grouped into modules containing 16 ROCs. Depending on the layer of the pixel detector these contain a number of token bit managers (TBM) channeling the information of the ROCs into a number of read-out channels while also providing the modules with the LHC internal clock. If a readout is triggered, the TBM sends a token through its corresponding read-out chain with each ROC appending its corresponding hit information. After the TBM receives the token back from the last ROC it sends the data via pixel-opto hybrids (POHs) converting the electrical into optical signals to the back-end electronics outside the CMS cavern. These POHs and other support electronics of the pixel detector are organized in portcards and configured by CCUs[5] reviving their commands from the back end electronics outside the experimental cavern. More about the data acquisition system of the CMS tracker can be found in [63].

All of these electronic components close to the interaction point can be affected by the flip of bits in their hardware registers due to ionizing radiation causing a so called single event upset or SEU. The SEUs affecting the pixel detector can be classified in one of two categories, soft errors that can be recovered during data taking by reprogramming the affected hardware and Single Event Latch-ups (SEL) in which the TBM are caught in a stuck state that can only be resolved by turning the low voltage supply of the chip on and off. For technical reasons, SELs could only be handled in between LHC fills during the data taking in 2017 and 2018, when no pp collisions took place, allowing for the build up of a number of malfunctioning modules during data taking. For the soft errors, an online recovery system is in place. Once triggered, data taking is paused and the affected channels are recovered by reprogramming the affected hardware components. This soft-error recovery (SER) is triggered either by the failure of a portcard or the accumulation of masked TBM channels with different thresholds for the different layers of the pixel detector. TBM channels are masked when 64 consecutive "out of sync errors" corresponding each to 255 missed read-outs are recorded. As SEL affected hardware can not be recovered through this soft-error recovery, not recovered channels are blacklisted after the third SER attempt to avoid the continuous triggering of SER by SEL affected channels. As each SER pauses the data taking for about 5 seconds, the SER serves as a trade-off between data quality and the amount of data taken.

As part of this thesis, the trigger rate of SER and their channel recovery efficiency have been measured as documented in [64] serving as future input to the design of the soft-error recovery system. Over a period of 2 month in September and October 2018 628 SER attempts have been recorded. This corresponds to 2.12 ± 1.46 SER per $100\,\mathrm{pb}^{-1}$ of data taken. About 56 ROCs where recovered per SER attempt. Without counting SER attempts triggered by the failure of portcards with about 200 ROCs, about 18 ROCs where recovered per SER attempt. As the described sys-

[5] Command and Control Units

tem does not detect the failure of single ROCs that also can be affected by SEU, the true number of recovered ROCs is higher. This effect can be gauged by studying the data of the CMS data quality monitoring [65], which records the number of ROCs that have not been sending data over more than 10 lumi sections[6]. From this it can be estimated that the rate of additionally recovered ROCs per SER is about 35 ROCs per SER. These numbers stand in contrast to about 23 ROCs per SER that can not be recovered most often due to SELs.

[6] One lumi section lasts about 23 seconds and is the lowest granularity unit in which the LHC data taking is split.

4

How to train with your (two) Higgs bosons - Machine Learning Methods

The use of machine learning techniques has become an important part of modern particle physics as they provide a convenient solution to complex task such as the identification and separation of different particle physics processes. Sec. 4.1 introduces the concept of boosted decision trees (BDT) used in the analysis presented in this thesis to separate the different H (see Sec. 5) or HH (see Sec. 6.6) signals from various background processes. Similar to other multivariate analysis (MVA) tools, the internal structure of a BDT can be tweaked to suit the needs of the desired task and the amount of available training data. The hyperparameters used in the HH analysis (Sec. 6) are tweaked by the means of an evolutionary algorithm presented in Sec. 4.2.

4.1 Boosted Decision Trees

The general idea behind any MVA technique is to use a mathematical model with trainable parameters to approximate a complex function. An example of this would be the separation of two or more processes by assigning them different functional values based on a set of input variables. The model is trained by adjusting the trainable parameters such that the loss function measuring the distance of the approximated functional value from the desired target is minimized. This is done by iteratively evaluating the loss function on a set of training data with examples containing the desired output for a given set of input variables. In the desired classification task, this would be events of different processes with labels identifying the given process, for example as signal events with a label of 1 or as background events with a label of 0.
The loss function usually serves a second purpose. By adding regularization terms, the loss is designed such that the trained model keeps a balance between accuracy in fulfilling its trained task and the complexity of the model. If the model is too complex, it can even describe statistical fluctuations in the training data, which then are not present in new data, thereby lowering the performance of the model. This difficulty is known as overtraining and corresponds to the concept of overfitting.
In case of BDTs, these concepts are implemented using decision trees. Simply phrased, a decision tree sorts input events in a set of categories called leafs by a set of chained criteria. To arrive at the desired function, each leaf then can be assigned a score, assigning each event a functional value. In the simple example of one decision tree, the choice of the criterion separating events in each node of the tree and the score assigned to each leaf are learnable parameters. In the case of

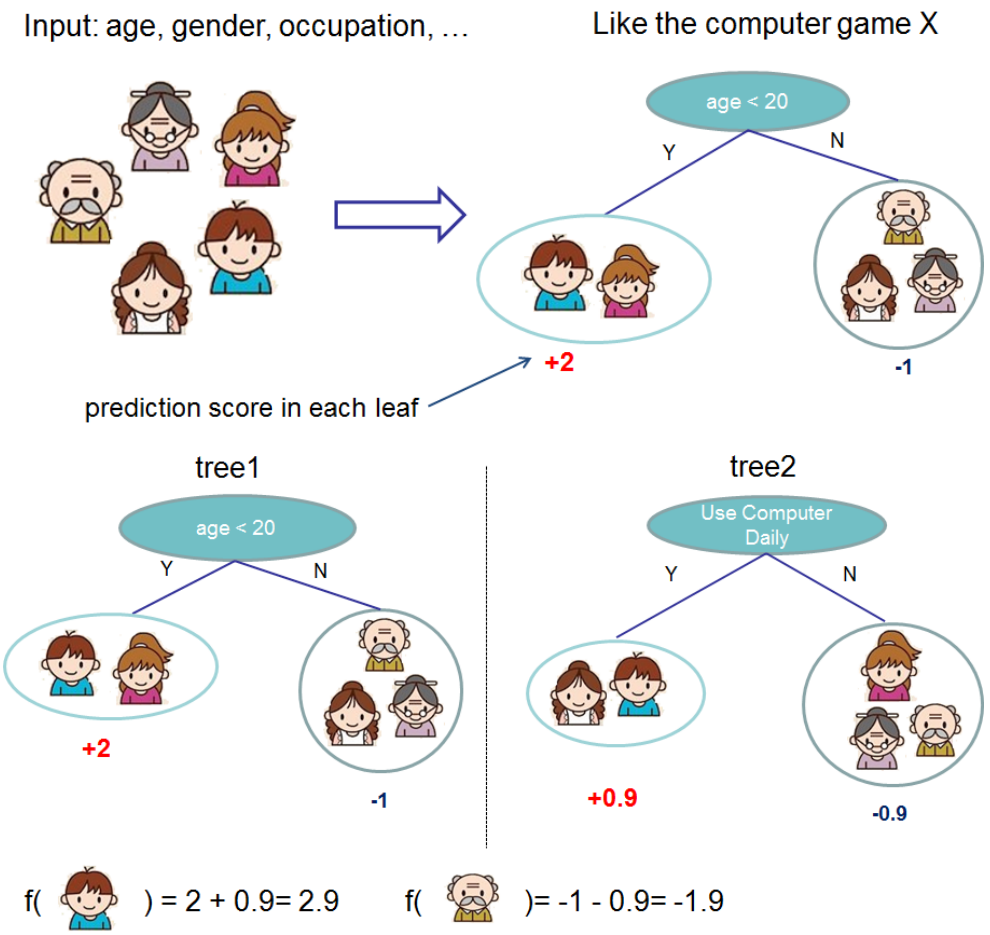

Figure 4.1: Visualisation of the concept of tree ensembles to separate two categories, members of a family who like or dislike a certain computer game. Two trees of depth 1 are shown, separating members of a family based on their age and computer use which can be assumed correlated to the question of the classification task. Each leaf gets a score assigned and the final score of each family member is obtained by summing over all leaves they are assigned to [67].

BDTs, not a single tree is used but an ensemble of trees, where the final score of each event is obtained by the sum of the leaf scores assigned to the given event. This is visualized in an example shown in Fig. 4.1 from the documentation of the `XGBoost` package [66, 67] which is used in this thesis to implement BDTs for the HH analysis in Sec. 6. BDTs are only one concept based on the use of tree ensembles, with another one being random forests. The concept of BDTs is defined by how they are trained, namely in an additive manner, where iteratively one tree at a time is added and within each tree one split or node at a time is added on the already existing structure of trees from the previous iteration. Therefore each iterative step consists out of two parts, optimizing the parameters of the newly added tree structures by minimizing the corresponding loss function terms using a gradient based algorithm and then finding the next possible splitting or tree addition further reducing (boosting) the overall loss. This concept is know as gradient boosting, hence the name Boosted Decision Trees. The training and possible structure of the BDT is governed by a set of parameters set before the training, such as the maximum number of allowed trees and their depth. These parameters are commonly referred to as hyperparameters. The `XGBoost` hyperparameters considered in this thesis are the following:

- **n_estimators:** Maximum number of considered trees.

- **subsample:** Fraction of randomly sampled events of the training data before growing a new tree. Lower values can help against overtraining. Subsampling is done once every booster iteration.

- **colsample_bytree:** Fraction of randomly sampled input variables for the optimization of each tree. Lower values can help against overtraining. This is done once for every tree.

- **gamma:** Minimum amount of loss reduction required for adding a new split in a tree. Higher values make the training more conservative.

- **learning_rate:** Rescales weights of newly added tree structures by reducing the influence of each individual tree in order to leave room for the improvement by new trees. This concept is known as shrinkage and is similar to the concept of a learning rate in other MVA techniques, where the learning rate steers the step size when searching for the minimum of a loss function.

- **max_depth:** Maximum depth of the considered trees. Higher numbers make the tree more complex but can lead to overtraining.

- **min_child_weight:** Minimum amount of weighted events in each leaf.

For the training of the BDT methods in this thesis, two things need to be optimized, the choice of the above hyperparameters and the choice of possible input variables/features in the training dataset. The former is done by an evolutionary algorithm described in Sec. 4.2. The latter is done by finding physics inspired variables and selecting the most relevant ones as described in Sec. 6.6. For this, an input variable ranking implemented in `XGBoost` evaluating the gain of each feature. The gain is measured as the improvement in accuracy/purity splits using the given feature provide for the branches these splits are on, i.e the accuracy of the branch before the split compared to the accuracy of the two created branches.

4.2 The Particle Swarm Algorithm

For the optimization of BDT hyperparameters in the $\mathrm{HH} \rightarrow$ Multilepton analysis presented in Sec. 6 of this thesis, the particle swarm algorithm [68] was used. To optimize the model performance, a fitness function, a modified *dScore* [69] was designed to balance the need for accuracy on an test dataset and the amount of observed overtraining. It is given by:

$$dScore = AUC_{\text{test}} - \kappa \cdot \frac{AUC_{\text{test}} - AUC_{\text{train}}}{1 - AUC_{\text{test}}} \tag{4.1}$$

where AUC_{X} is the area under the Receiver Operator Characteristic[1] for the training/test dataset and κ an adjustable parameter steering the importance of overtraining prevention on the optimization target. The adjusted *dScore* compared to the measure developed in [69] increases the

[1] These curves show the relation of selection efficiency on signal and background for different splittings on a variable such as an BDT or neural network output.

importance of the overtraining penalizing term depending on the overall accuracy of the model, such that with higher accuracy, the optimization against overtraining becomes more and more important. In the iterative Particle Swarm Optimization method (PSO) an ensemble or swarm of hyperparameter configurations is generated distributed over the whole space of available parameter configurations. This allows for the efficient scan of all possible hyperparameters for the configuration yielding the best *dScore*. In each iteration the particles or configurations in the swarm move closer to the optimal *dScore* by updating the positions of each particle i in the following manner:

$$x_i^{k+1} = x_i^k + w \cdot p_i^k + F_i^k \,; \qquad p_i^{k+1} = x_i^{k+1} - x_i^k \tag{4.2}$$

with x_i^k the position x of the particle i in the hyperparameter space in iteration k, p_i^k the momentum of particle i given by the distance and direction traveled in the parameter space in the previous update, a weight w steering the importance of the momentum, and an attractive force F towards the currently known best configuration of the particle itself ($\hat{x}$) and the swarm ($\hat{\hat{x}}$). Its given by:

$$F_i^k = c_1 \cdot r_1 \cdot (\hat{x}_i^k - x_i^k) + c_2 \cdot r_2 \cdot (\hat{\hat{x}}^k - x_i^k) \tag{4.3}$$

Here, c_1, c_2 are adjustable parameters steering the relative attraction of the two terms, and r_j random numbers between 0 and 1. The inclusion of the attraction to the particles best configuration allows the particle to find new best locations, preventing the whole swarm flying towards a local maximum in *dScore*. The momentum p prevents the particle from getting stuck at a local maximum.

5

The CMS $\mathrm{H} \to \mu\mu$ Analysis

As established in Sec. 2.2, the coupling of the Higgs boson to particles of the SM is predicted to be proportional to the particles mass $\sim m_f/v$ for fermions and $\sim m_V^2/v$ for the gauge bosons of the weak interaction. So far the couplings to both Z and W bosons, the heavy third generation t- and b-quarks, and third generation τ lepton have been confirmed experimentally by the CMS and ATLAS collaborations [70–83]. As can be seen in Fig. 5.1 all measurements are, within their respective uncertainties, in agreement with the SM prediction.

Overview of the CMS Run 2 $\mathrm{H} \to \mu\mu$ analysis

To establish the Higgs boson coupling to second generation fermions, the most likely discovery channel is the decay of the Higgs boson into a pair of muons. Despite the muons low mass of only 105.66 MeV [5] and a correspondingly low SM branching fraction of the Higgs boson into muons of 2.18×10^{-4} [14], the clean signature and high mass resolution of the corresponding Di-Muon pair allows for the potential discovery of a signal peak on a steeply falling spectrum of mostly $\mathrm{Z}/\gamma^* \to \mu\mu$ dominated background. To further increase the significance of the signal

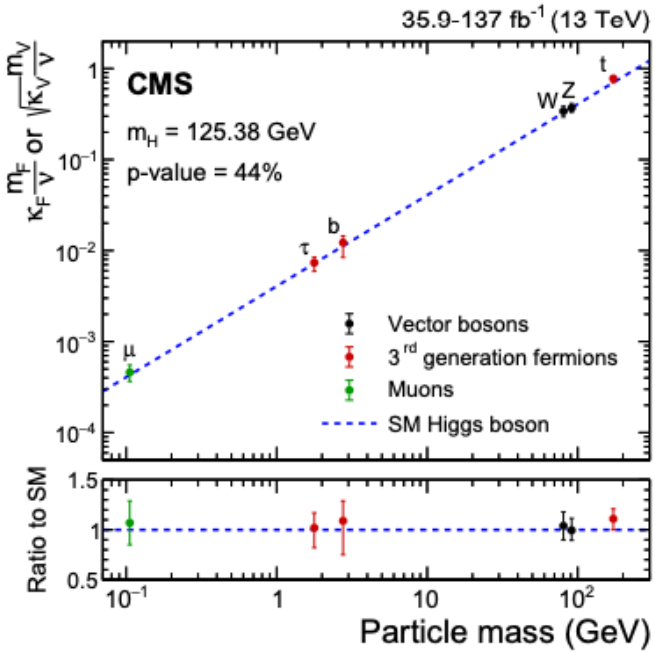

Figure 5.1: Best fit values for the reduced coupling strength modifiers of the κ-framework [84] for Higgs boson couplings to fermions and the gauge bosons of the weak interaction. The error bars correspond to the 68% CL interval of the measured coupling strength parameters. All measurements so far are, within their given uncertainties, in agreement with the SM prediction given by the dashed blue line [3].

peak, the CMS $\mathrm{H} \to \mu\mu$ analysis for the full LHC Run 2 dataset of 137 fb^{-1} [3] studies multiple Higgs boson production modes in a set of orthogonal event categories. By doing this, in addition to the clean signature of the oppositely charged Di-Muon mass pair, each category is able to capitalize on the distinct features of the corresponding production mode. The different categories are defined in the following way:

- Events containing b-tagged jets are associated with either hadronic, or in case additional leptons are present, leptonic $\mathrm{t\bar{t}H}$ decays.
- Events containing no b-tagged jets but containing one (two) additional leptons are associated with leptonic WH (ZH) decays.
- Events not falling into any of the $\mathrm{t\bar{t}H}$ or $\mathrm{WH/ZH}$ categories but containing an additional Di-Jet pair with an invariant mass above 400 GeV and a separation in $\eta > 2.5$ are associated with qqH production.
- The remaining 96% of Di-Muon events are studied in an inclusive category dominated by ggH events.

For the qqH category the signal extraction is performed by a maximum likelihood fit of the data with signal and background templates estimated from Monte Carlo simulation. This is performed on adequately chosen bins of a deep neural network classifier.
In all but the qqH category, the signal extraction consist of a binned maximum likelihood fit to the steeply falling Di-Muon mass spectrum in the mass range 110 GeV $\leq m_{\mu\mu} \leq$ 150 GeV. For this, the signal peak is modelled by a double sided Crystal-Ball function on top of the background modelled by a set of monotonically decreasing functions such as a modified version of the Breit-Wiegner function, Bernstein polynomials or a set of exponential functions. Bias studies are performed to quantify the influence of the choice in background parametrization and were found to be negligible. To enhance the sensitivity further, the ggH, $V\mathrm{H}$ and $\mathrm{t\bar{t}H}$ categories are subdivided based on a set of BDT discriminators into low and high signal significance $S/\sqrt{B}$ regions.

The final fit results are summarized in Fig. 5.2 with the left plot showing the Di-Muon mass in the range 110 GeV-150 GeV for events of the qqH category according to the signal and background rates extracted from the maximum likelihood fit. The events are weighted by the $\frac{S}{S+B}$ ratio as a function of the DNN output. The right plot shows the Di-Muon mass spectrum for the same range but for all categories weighted by $\frac{S}{S+B}$. The signal is shown for the best fit signal strength of $1.19^{+0.40}_{-0.39}\,(\mathrm{stat.})^{+0.15}_{-0.14}\,(\mathrm{syst.})$ for a Higgs boson mass of 125.38 GeV [85]. This corresponds to an observed (expected) significance of 3.0 (2.5) standard deviations and therefore the first evidence of $\mathrm{H} \to \mu\mu$ decays.

Study of a $V\mathrm{H}$ hadronic event category

For this thesis, the prospects for including a $V\mathrm{H}$ hadronic channel in the context of the CMS $\mathrm{H} \to \mu\mu$ analysis are studied. As potential $V\mathrm{H}$ hadronic events are already treated within the in-

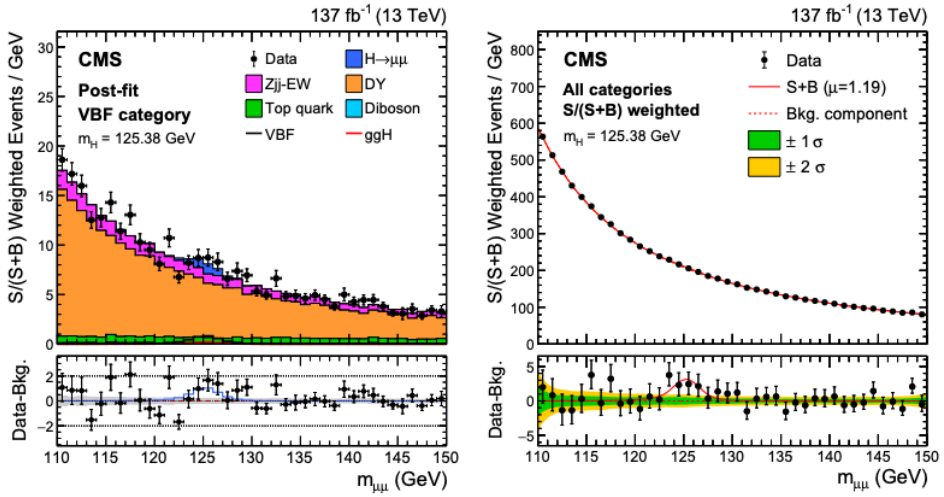

Figure 5.2: The postfit distribution of $m_{\mu\mu}$ for the qqH category with events weighted proportionally to $\frac{S}{S+B}$ as a function of the categories DNN output on the left and the distribution of $m_{\mu\mu}$ for all categories weighted by $\frac{S}{S+B}$. The shown signal corresponds to a best fit value of $\sigma/\sigma_{\mathrm{SM}} = \mu = 1.19$ [3].

clusive ggH category, the main target of a dedicated $V\mathrm{H}$ category would not only be the optimal separation of H signal events from background events, but also achieving a relatively high purity of $V\mathrm{H}$ events. Similar to other sub-channels, the signal extraction is designed as a 'bump hunt' on the falling $m_{\mu\mu}$ spectrum between 110 GeV and 150 GeV.

The base selection of the $V\mathrm{H}$ hadronic category requires a pair of jets within an invariant mass window around the $\mathrm{W/Z}$ boson mass $60\,\mathrm{GeV} \leq m_{jj} \leq 110\,\mathrm{GeV}$ in addition to the oppositely charged pair of muons. Furthermore, b-jets are vetoed to reduce the contribution of $\mathrm{t\bar{t}}$ background events and to orthogonalize the $V\mathrm{H}$ selection to that of the $\mathrm{t\bar{t}H}$ channel. Additional leptons are vetoed to remove overlap with the $V\mathrm{H}$ leptonic categories. Forward jets with $|\eta| > 2.5$ are vetoed to increase the purity of $V\mathrm{H}$ events compared to other $\mathrm{H} \to \mu\mu$ signals.

Within a signal mass window of $120\,\mathrm{GeV} \leq m_{\mu\mu} \leq 130\,\mathrm{GeV}$ this leads to an expected significance of signal (S) over background (B) $\mathrm{S}/\sqrt{\mathrm{B}} = 0.25$ with a purity of the $V\mathrm{H}$ signal compared to all $\mathrm{H} \to \mu\mu$ decays of 24.6%, yielding a significance for the $V\mathrm{H}$ signal of 0.062 with the full Run 2 LHC dataset. The partially blinded Di-Muon mass spectrum after these basic selection criteria is shown in the left part of Fig. 5.3 for the 2018 data taking period. Starting from this base selection, both a cut based and a BDT based approach are tested. For the cut based approach several kinematic quantities are tested with the goal to optimize the significance of the $V\mathrm{H}$ signal over background $\frac{V\mathrm{H}}{\sqrt{B}}$. The optimization was performed on Monte Carlo simulation for the 2018 dataset, yielding the following selection:

- The mass window on the invariant Di-Jet mass is tightened to $64\,\mathrm{GeV} \leq m_{jj} \leq 106\,\mathrm{GeV}$
- The Di-Jet system originating from the W or Z boson decay in signal is expected to point in the opposite direction of the Di-Muon system originating from the Higgs boson decay. Therefore the angle between both pairs is required to be close to π: $|\Delta R(jj,\mu\mu) - \pi| < 0.4$
- While the jets in signal originate from W or Z boson decays into a pair of quarks, the main background from $\mathrm{Z}/\gamma^* \to \mu\mu$ decays mostly features gluon induced jets from initial and/or final state radiation (ISR/FSR). Jets from (light) quarks can be separated from gluon

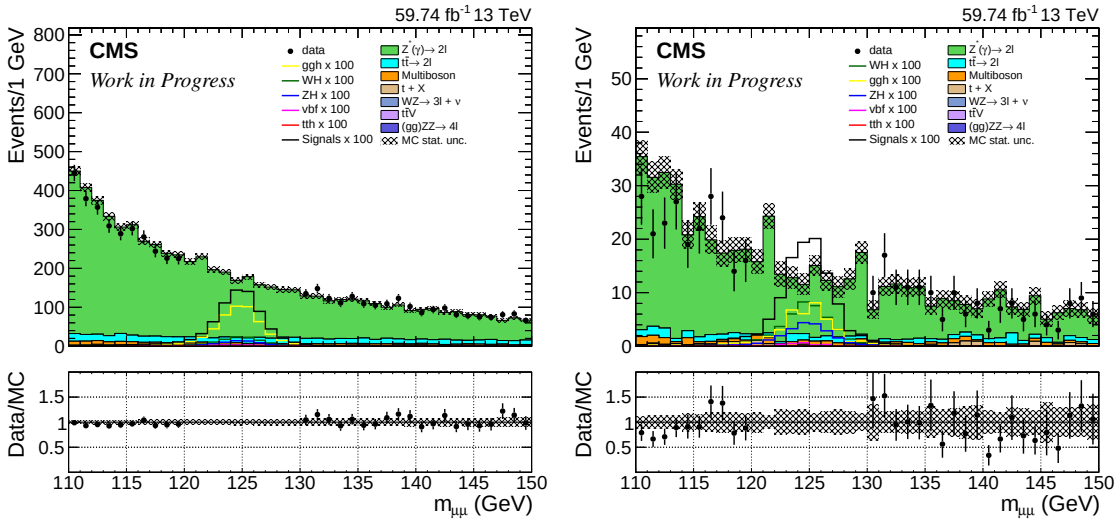

Figure 5.3: The distribution of $m_{\mu\mu}$ for events passing the VH hadronic base selection on the left and for events passing the selection criteria of the cut-based optimization approach on the right. Data and simulated events shown, correspond to the 2018 LHC dataset as recorded by CMS. The Di-Muon mass spectrum is blinded in the signal sensitive mass region between 120 GeV and 130 GeV. The shown uncertainty bands correspond to statistical uncertainties only.

induced jets using an MVA approach, the Quark-Gluon Likelihood (QGL), introduced in [86]. The larger of the two QGL from the two selected jets is required to be greater than 0.65.

- Compared to the ISR/FSR jets in the $\mathrm{Z}/\gamma^* \to \mu\mu$ background, the Di-Jet system in the VH signal is observed to be slightly boosted, a p_T of the Di-Jet system greater than 75 GeV is required.

- Finally, the smaller of the two QGL is required to be greater than 0.25. This last cut does not increase the significance $\frac{VH}{\sqrt{B}}$ but enhances the purity of the VH signal by about 10%.

The result of the described selection can be seen in the right part of Fig. 5.3 showing the Di-Muon mass spectrum for the 2018 dataset in the VH hadronic category definition of the cut based approach. A significance of $\frac{VH}{\sqrt{B}} = 0.075$ ($\frac{S}{\sqrt{B}} = 0.125$) and a purity of about 60% can be achieved in the full Run 2 dataset utilizing only about 2.3 signal events or 0.3% of signal events otherwise contained in the inclusive ggH category. To gauge the sensitivity, 95% CL upper limits on the $\mathrm{H} \to \mu\mu$ cross section σ were extracted for an early version of the $\mathrm{H} \to \mu\mu$ analysis including most of the final systematic uncertainties. An expected upper limit of $17.36 \times \sigma_\mathrm{SM}$ was found.
For the BDT based approach, a BDT implemented in `TMVA` [87] was trained on simulated $\mathrm{Z}/\gamma^* \to \mu\mu$ background and VH signal events for the 2016 dataset. As input 11 variables were selected including the maximum and minimum QGL of the two selected jets, the invariant mass, p_T and opening angles $\Delta\phi(j,j)$ and $\Delta\eta(j,j)$ of the Di-Jet system, the p_T of the two selected jets relative to m_{jj}, the opening angles $\Delta\eta(jj,\mu\mu)$ and $|\Delta\phi(jj,\mu\mu) - \pi|$ between the Di-Jet and Di-Muon systems and the $\eta_{\mu\mu}$ of the Di-Muon system. These variables add information characterizing the Di-Jet system and W/Z boson decays to the information used in the cut based approach. As the Di-Muon system in signal is produced more centrally in the detector compared

	VH hadronic BDT
Method	kBDT
input variable transformation	Gaussian
NTreees	120
BoostType	Grad
Shrinkage	0.5
UseBaggedBoost	True
nCuts	30
MaxDepth	3
MinNodeSize	10%
NegWeightTreatment	Pray

Table 5.1: TMVA [87] configuration used for the training of the VH hadronic BDT.

Variable	Importance	Separation
$\Delta\eta(\mu\mu, jj)$	1.733e-01	1.711e-01
$Max(QGL)$	1.032e-01	6.034e-02
m_{jj}	9.895e-02	6.133e-02
$Min(QGL)$	9.521e-02	4.153e-02
$p_{\mathrm{T}}(j_2)/m_{jj}$	8.558e-02	1.297e-01
$p_{\mathrm{T}}(j_1)/m_{jj}$	8.450e-02	1.392e-01
$\Delta\eta(j, j)$	7.997e-02	6.007e-02
$\eta_{\mu\mu}$	7.929e-02	6.567e-02
$\|\Delta\phi(\mu\mu, jj) - \pi\|$	7.852e-02	1.028e-01
$p_{\mathrm{T}}(jj)$	7.454e-02	1.463e-01
$\Delta\phi(j, j)$	4.688e-02	1.189e-01

Table 5.2: Separation and importance using TMVA [87] for the different input variables of the VH hadronic BDT. The selected jets are denoted by j with the (sub) leading jet denoted as j_1 (j_2).

to background, the variable $\eta_{\mu\mu}$ is able to provide some additional separation power. The TMVA configuration and an overview of the separation power of the different BDT input variables is given in Tab. 5.1 and Tab. 5.2. The resulting separation power of the resulting BDT is shown in Fig. 5.4. Optimizing the overall cross section limit on $\mathrm{H} \to \mu\mu$ decays, the BDT output is then used to define three categories with a ggH enriched category containing events with a BDT output lower than 0.7 and two VH enriched categories for events with a BDT output greater/smaller than 0.8. The three BDT categories from lowest to highest BDT output feature a significance $\frac{VH}{\sqrt{B}}$ ($\frac{S}{\sqrt{B}}$) of 0.041 (0.225), 0.042 (0.083) and 0.071 (0.104) and purity $\frac{VH}{S}$ of 18%, 50% and 72% respectively. The partially blinded Di-Muon mass spectrum of all three categories for the 2018 dataset is shown in Fig. 5.5. Similar as for the cut-based approach, the expected 95% CL upper limits on the $\mathrm{H} \to \mu\mu$ are estimated corresponding to an early version of the $\mathrm{H} \to \mu\mu$ analysis. Only using the two VH enriched categories containing about 2.7 signal events or 0.3% of the signal events in the inclusive ggH category an expected upper limit of 14.88 $\times\sigma_{\mathrm{SM}}$ is found. Using all three categories and a total of 17.8 signal events or 2% of the signal event in the ggH category an expected upper limit of 7.47 can be achieved.

Considering the high expected background in the order of 5000 events compared to about 20 $\mathrm{H} \to \mu\mu$ signal events, both the results of the cut-based as well as the BDT approach, result in

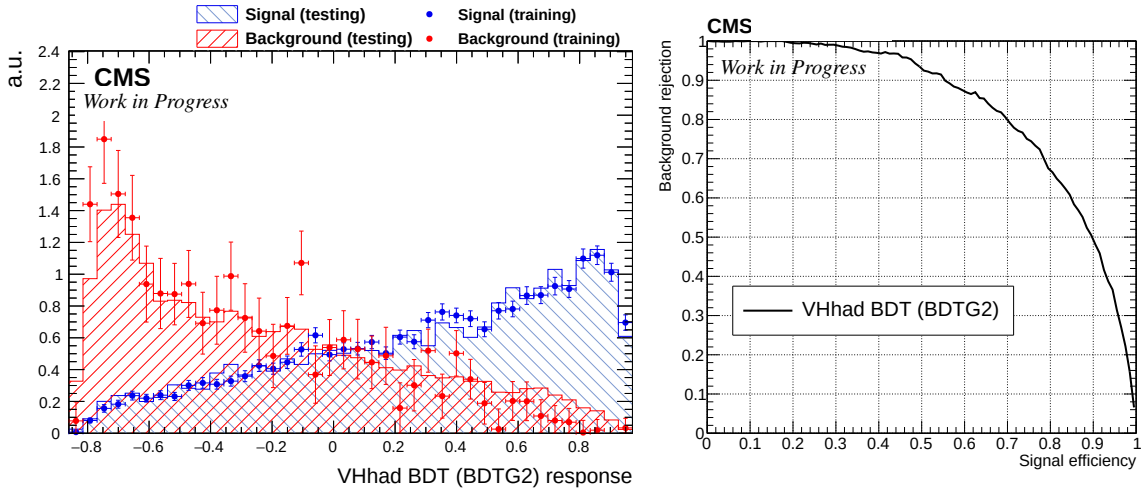

Figure 5.4: The output of the BDT trained for the VH hadronic selection on the left and the corresponding Receiver Operating Characteristic displaying the relation of signal selection efficiency and background rejection for different cuts on the BDT output. The BDT separating VH hadronic events from Z/γ^* background events, was trained and evaluated on simulated events corresponding to the 2016 LHC dataset. The simulated events used in the training correspond to an independent dataset not used in the calculation of expected upper limits.

respectable expected upper limits on σ of about 15-20 $\times\sigma_{SM}$ while utilizing only a small fraction of the overall signal. In the context of the CMS $H \to \mu\mu$ analysis, the optimized VH hadronic category would enter as a dedicated new category with a sensitivity about four times lower than the VH leptonic category. Future iterations of the analysis will have to decide if the described approach for a VH hadronic selection is to be expanded and a dedicated category should enter the analysis approach.

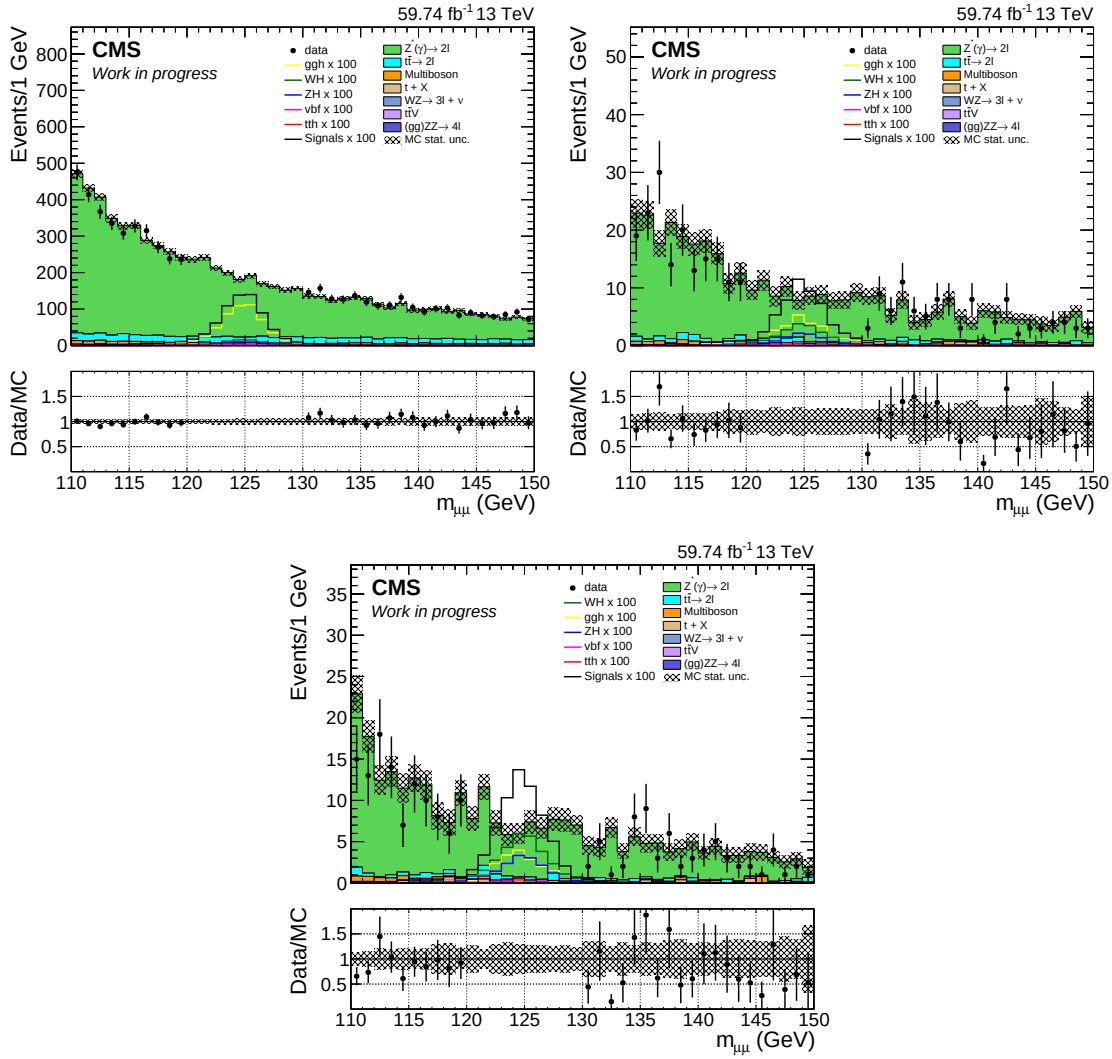

Figure 5.5: The distribution of $m_{\mu\mu}$ for the three regions of the VH hadronic BDT output, with events for a BDT output smaller than 0.7 on the left, between 0.7 and 0.8 in the center, and greater than 0.8 on the right. Data and simulated events shown correspond to the 2018 LHC dataset as recorded by CMS. The Di-Muon mass spectrum is blinded in the signal sensitive mass region between 120 GeV and 130 GeV. The shown uncertainty bands correspond to statistical uncertainties only.

6

The Di-Higgs Boson Analysis

As described in Sec. 2 the study of HH signatures allows for an analysis with a broad scope in particle physics. As the expected production rates especially for SM like physics scenarios are quite small and BSM physics can offer challenging final state signatures, the discovery potential of HH studies with the current LHC dataset of around $140\,\mathrm{fb}^{-1}$ per experiment for ATLAS and CMS was deemed small only a few years ago. Decent results were only expected at the high luminosity LHC [88] in the 2030s with a dataset of $3000\,\mathrm{fb}^{-1}$ or at the earliest at the end of the next LHC data taking period, with then a combined $\sqrt{(s)} = 13$ TeV dataset of $300\,\mathrm{fb}^{-1}$ per experiment.

As explained in the following however, current analyses have developed far and especially their combination is approaching the sensitivity needed to probe SM like HH production.

To maximize sensitivity with the current dataset, as many HH decay modes as possible must be studied. Fig. 6.1 shows the branching fraction of the most prominent HH decay modes as well as their planned experimental coverage by the CMS collaboration. Most analyses cover a single final state with at least one $\mathrm{H} \to \mathrm{b\bar{b}}$ decay, offering a high HH branching fraction of $\approx 58\,\%$ [5]. This thesis mainly contributed to the CMS $\mathrm{HH} \to$ Multilepton analysis [4]. The $\mathrm{HH} \to$ Multilepton analysis does not focus on a single HH decay channel but instead covers a set of HH decays with multiple leptons in the final state that do not contain a $\mathrm{H} \to \mathrm{b\bar{b}}$ decay. In doing so, several so far uncovered decay channels are combined in a single analysis.While this analysis has a lower HH branching fraction than others, the seven selected Multilepton final states offer very clean signatures with high selection efficiencies even at low particle energies in overall low background

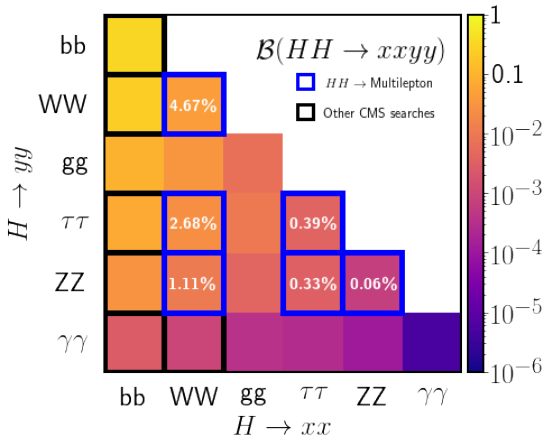

Figure 6.1: Overview of branching fractions ($\mathscr{B}$) for the most prominent HH decays as well as their planned experimental coverage in CMS analyses. The decay channels covered by the $\mathrm{HH} \to$ Multilepton analysis featured in this thesis are highlighted as well [14].

categories. As shown in this thesis, this leads to a sensitivity comparable to the three leading bbbb [89, 90], $\mathrm{bb}\gamma\gamma$ [91, 92], and $\mathrm{bb}\tau\tau$ [93, 94] analyses.
Sec. 6.1 gives an overview of the $\mathrm{HH} \rightarrow$ Multilepton analysis discussed in more detail in Sections Sec. 6.2-Sec. 6.6. The major contributions of this thesis to the $\mathrm{HH} \rightarrow$ Multilepton analysis are discussed in Sec. 6.5.1 and Sec. 6.6.1 covering the $3\ell + 1\tau_{\mathrm{h}}$ sub channel. The methodology of the signal extraction as well as the results and interpretation of the analysis are then presented in the following chapter Sec.7.

6.1 Analysis Overview

In Fig. 6.2 a potential HH candidate event for the $\mathrm{HH} \rightarrow$ Multilepton analysis is shown. It was found in the $3\ell + 1\tau_{\mathrm{h}}$ final state this thesis focuses on. The following sections will give an overview of the $\mathrm{HH} \rightarrow$ Multilepton analysis, explaining how that event was identified. Inspired by previous analyses covering multilepton final states such as the CMS $\mathrm{ttH} \rightarrow$Multilepton analysis [62], this analysis focuses on decay channels with two or more leptons[1] (ℓ) or hadronically decaying taus (τ_{h}) in the final state.
Seven analysis channels are defined:

- $0\ell + 4\tau_{\mathrm{h}}$
- 2ℓ(ss) + 0/1 τ_{h}
- $3\ell + 0\tau_{\mathrm{h}}$
- $1\ell + 3\tau_{\mathrm{h}}$
- $2\ell + 2\tau_{\mathrm{h}}$
- $3\ell + 1\tau_{\mathrm{h}}$
- 4ℓ

where 2ℓ(ss) denotes two same charge (sign) leptons. This covers most leptonic final states of the $\mathrm{HH} \rightarrow 4V$, $\mathrm{HH} \rightarrow 2V2\tau$ and $\mathrm{HH} \rightarrow 4\tau$ decay modes. The analysed data corresponds to the 2016-2018 LHC dataset with a luminosity of $138\,\mathrm{fb}^{-1}$ recorded at $\sqrt{s} = 13$ TeV by CMS. A set of single, double and triple lepton triggers as well as a Di-Tau trigger and a lepton-tau cross trigger are used. For the optimization of the analysis, the training of MVA methods as well as the background and signal modeling in the signal extraction, Monte Carlo event simulation (MC) is used. The dataset, the used triggers and MC methods are further described in Sec. 6.2.
To suppress background from misidentified hadronic taus as well as misidentified leptons as much as possible, this analysis makes use of the DeepTau algorithm (Sec. 3.2.11) and a dedicated prompt lepton MVA (Sec. 3.2.13). For the 2ℓ(ss) + 0/1 τ_{h} and $3\ell + 0\tau_{\mathrm{h}}$ channels, the presence of additional jets, reconstructed with the anti-kt algorithms (Sec. 3.2.10), and originating in hadronic W decays, is required. Jets from b-quarks are identified with the DeepJet algorithm (Sec. 3.2.12) and are vetoed in all channels to suppress top-quark related background processes such as $\mathrm{t\bar{t}}$ and ensure orthogonality to other HH analyses. The reconstruction of leptons, hadronic taus as well as jets and other event quantities is described further in Sec. 6.3. The event selection based on these object definitions is described in Sec. 6.5.
As most channels target final state signatures with high object multiplicities or uncommon signatures such as two leptons of same electric charge, the amount of genuine background with indistinguishable final state content (prompt background) is comparatively small. Instead back-

[1] Muons or electrons.

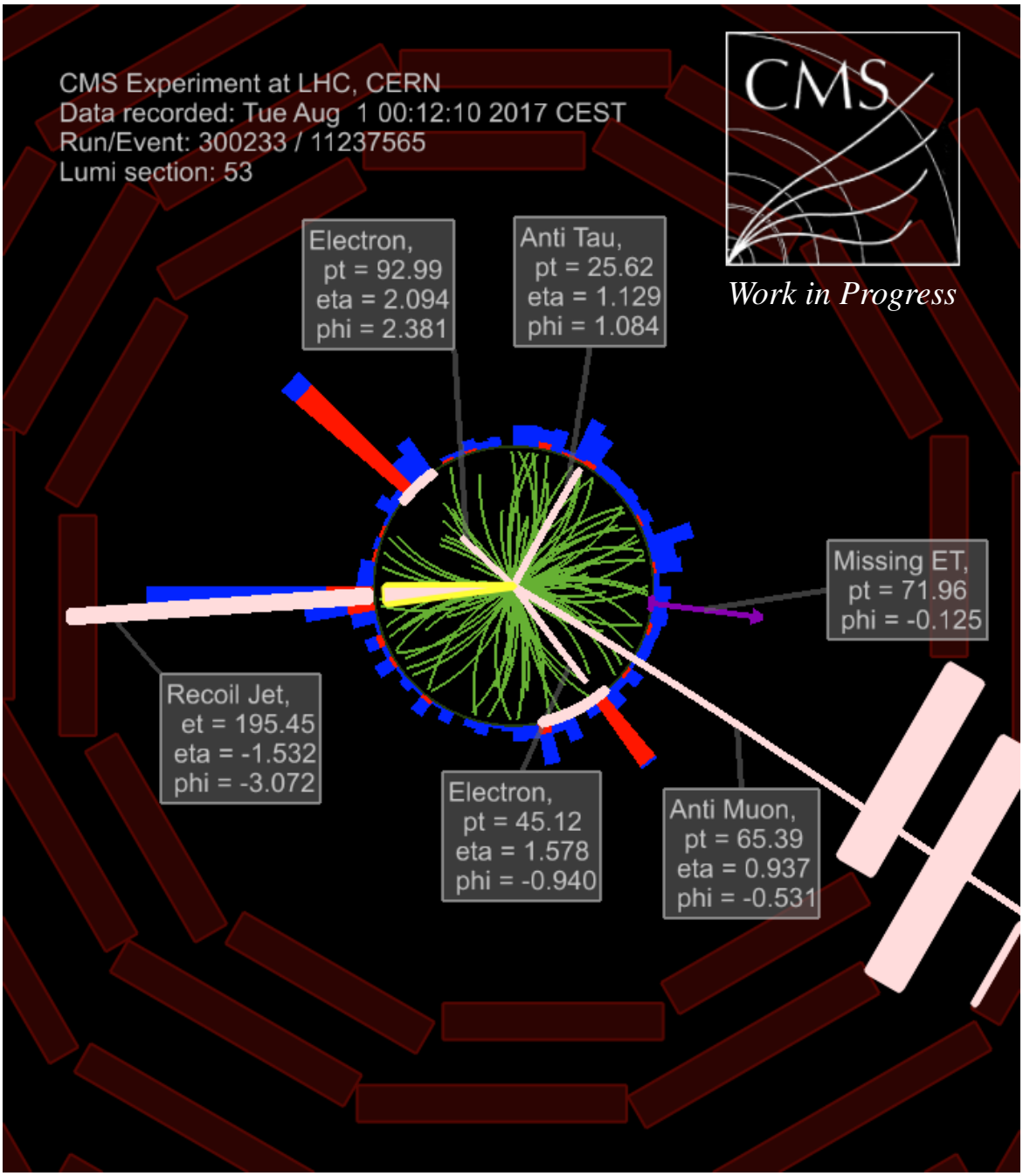

Figure 6.2: Event display of a potential HH candidate event observed in 2017 with the CMS experiment. The display shows three reconstructed leptons, two electrons and an anti-muon and one reconstructed hadronic tau with positive charge, all potentially originating from an HH $\rightarrow$ WWWW decay. The event also contains two additional jets of which the more higher energetic one recoiling against the potential HH system is shown.

grounds involving misidentified leptons or hadronic taus (fake background) or backgrounds with misidentified lepton charge (charge-flip background) become relevant. As these backgrounds are not well described in simulation, data driven background methods are used as described in Sec. 6.4.
For the signal extraction the output of a BDT aimed at separating signal and background events is used. Three different BDTs are used for spin-0 and spin-2 resonant as well as non-resonant signals. To ensure the best performance over the wide range of HH physics scenarios, the BDTs are parameterized in the resonant mass or a set of non-resonant benchmark scenarios. Details about the BDT training can be found in Sec. 6.6.
The signal extraction itself, systematic uncertainties and background validation as well as the results of the analysis are discussed in Sec. 7

6.2 Datasets and Event Simulation

The analysed dataset of 137.6 fb^{-1} (137.2 fb^{-1}) corresponds to proton-proton pp collision data at a center of mass energy of $\sqrt{s} = 13$ TeV with an average of about 30 pp collisions per bunch crossing. The data was taken during the Run 2 LHC data taking period, with 36.3 fb^{-1} (35.9 fb^{-1}), 41.5 fb^{-1} and 59.7 fb^{-1} of collected luminosity[2] in the years 2016, 2017 and 2018, respectively.
As described in Sec. 3.2.7, CMS makes use of a two level trigger system to select relevant data from the 40 million events per second present during the runtime of the LHC. This analysis uses a set of different multilepton, tau and lepton/tau cross triggers as listed in Sec. 6.2.1.
For the optimization of the analysis, training of MVA methods as well as background and signal modeling Monte Carlo event simulation is used. This includes a full detector simulation for the respective state of the detector in 2016, 2017 and 2018, a simulation of the proton remnants not participating in the hard interaction process (underlying event) as well as additional pp collisions happening during the same bunch crossing (pile up). The various stages of simulation, involved tools and the selected MC datasets are given in Sec. 6.2.2.
While the Monte Carlo simulation already includes effects such as detector response and pile-up effects[3] additional data to Monte Carlo corrections are applied to further improve the agreement of simulation and data. They are listed and discussed in Sec. 6.2.3.
For the signal modelling MC samples at different order of matrix element calculation are used. In non-resonant ggHH production, NLO MC samples for four different values of κ_λ as well as LO MC samples for 12 different benchmark coupling scenarios in the EFT parameter space and the SM are available. A reweighting procedure is introduced, reweighting the sum of the either the 4 NLO or the 13 LO MC samples to arbitrary points in the 5D EFT parameter space. This

[2] A newer calibration of the luminosity measurement places the 2016 luminosity about 0.4 fb^{-1} higher. This change would have an impact of 0.3 % of the total signal normalization and an negligible effect on the background prediction, where background modeled by simulation would be scaled upwards by 0.3 % while data-driven backgrounds are diminished. While the final signal extraction is performed on the newer luminosity estimate, the optimization/validation of the analysis was performed on the older estimate given in brackets. In plots showing the full Run 2 data this is indicated by labels 138fb^{-1}/137fb^{-1} for the new/old luminosity estimate.

[3] The effect of multiple pp interactions per bunch crossing.

Trigger	$0\ell+4\tau_h$	$1\ell+3\tau_h$	2ℓ(ss) + 0/1 τ_h	$2\ell+2\tau_h$	$3\ell+0\tau_h$	$3\ell+1\tau_h$	4ℓ
Double τ_h trigger	✓	✓	**X**	**X**	**X**	**X**	**X**
Lepton + τ_h cross trigger	**X**	✓	**X**	**X**	**X**	**X**	**X**
Single lepton trigger	**X**	✓	✓	✓	✓	✓	✓
Double lepton trigger	**X**	**X**	✓	✓	✓	✓	✓
Triple lepton trigger	**X**	**X**	**X**	**X**	✓	✓	✓

Table 6.1: HLT trigger categories used in the seven different sub-channels of the HH $\rightarrow$ Multilepton analysis.

allows not only for the study of the mentioned EFT benchmark scenarios but also additional parameter scans such as in the c_2 EFT coupling. By combining the samples of either all NLO or all LO samples, the available amount of simulated events for each scenario is increased. This provides the necessary statistics for the non-resonant BDT training, where the reweighted sum of the 13 LO MC samples is used. While the reweighting accounts for kinematic differences of the HH topology between LO and NLO, it cannot account for all LO to NLO effects, such as the modeling of initial-state or final-state radiation (ISR/FSR) motivating the use of the lower statistic NLO samples for the signal extraction as described in Sec. 7.2.

6.2.1 Triggers and Datasets

The choice of the different trigger categories for the different channels is summarized in Tab. 6.1. As depending on the triggers and lepton multiplicity, p_T thresholds and other quality criteria change, the combination of these three trigger categories yields a higher signal efficiency than, for instance, single lepton triggers on their own. A set of lepton-tau cross triggers is used for the $1\ell+3\tau_h$ channel, while both the $1\ell+3\tau_h$ and the $0\ell+4\tau_h$ also use double-tau triggers.
The actual HLT trigger paths corresponding to these categories for the three different years are given in the Appendix **A**. Within CMS every HLT trigger path corresponds to a different data sub stream / sub dataset. The actual datasets used are given in Tab. 8.2, Tab. 8.3 and Tab. 8.4 of the Appendix **B**. While one data event can fulfill multiple trigger paths, double counting is prevented by a prioritization of the different triggers allowing each event only to be taken from one data set.

6.2.2 Monte Carlo Simulation

Matrix element generators compute cross sections by numerically integrating Feynman integrals. While doing so they generate random variations of the hard interaction at the core of the desired process that can be used as a first step of event generation. As this can only describe the core event up to a certain order in the perturbative series, additional initial-state radiation, final-state radiation and the hadronization process of color charged particles are not directly calculated but modeled by a parton shower algorithm. These are phenomenological models tuned to experimental observations. In addition, parton distribution function of the colliding protons described in Sec. 2.5 enter the calculation.
Finally, events are run through a detector simulation, modelling the detector response used as input to the same event reconstruction as used for recorded data.
For the Monte Carlo event simulation in this analysis, events at leading order (LO) matrix el-

ement level are generated using MADGRAPH5_AMC@NLO [95]. Events at next-to-leading order (NLO) matrix element level are generated using either MADGRAPH5_AMC@NLO or POWHEG V2 [24, 96–110]. A few samples modelling single Higgs boson background processes where generated using the JHUGEN generator [111–117]. For the modelling of parton shower effects, hadronization and τ decays, PYTHIA [118] is used with the CUETP8M1, CUETP8M2 and CUETP8M2T4 tunes [119] used for the simulation of 2016 events and the CP5 tune [120] used for 2017 and 2018 simulated events. Both tunes are based on the MONASH tune [121].
For all samples NNPDF [35, 122–125] is used. Events generated with the CUETP8* tunes use the the NNPDF3.0 PDF set while samples generated with the CP5 tune the NNPDF3.1 PDF set. For the detector simulation, GEANT 4 is used [126].
Background events from single boson production (W, Z), Di-Boson production (WW, WZ, ZZ), triple-boson production (WWW, WWZ, WZZ, ZZZ, $\mathrm{WZ}\gamma$), processes including one or two top quarks ($\mathrm{t}, \mathrm{t\bar{t}}, \mathrm{t\bar{t}W}, \mathrm{t\bar{t}Z}, \mathrm{t\bar{t}WW}$) or single Higgs boson production ($\mathrm{ggH}, \mathrm{qqH}, \mathrm{tHq}, \mathrm{tHW}, \mathrm{t\bar{t}H}, \mathrm{WH}, \mathrm{ZH}$) are modelled by simulation. Where these processes contribute through leptons or hadronic taus from misidentified jets or through misidentified lepton charge, data driven background estimation (see Sec. 6.4) is used instead. Background from processes involving lepton pairs from photon conversions in detector material are modeled by simulation as well, using a combination of X+jets and dedicated $X + \gamma$ samples for singe boson and top production.
Some background processes are covered by multiple available MC datasets. Depending on the available amount of simulated events and the occurrence of negative event weights, different samples are used for the BDT training and the background modelling in the signal extraction.
For the simulation of signal, four different sets of MC events are used. For resonant HH production, a number of different mass points between 250 and 1000 GeV is covered both for a heavy spin-0 and a heavy spin-2 resonance decaying into a pair of SM Higgs bosons generated at LO. For non-resonant HH production, two sets of MC events are used in the ggHH production mode. Four different points in κ_λ produced at NLO matrix element precision are used exclusively for the signal extraction together with a set of signal samples for VBF like non-resonant HH production at LO. The second set of non-resonant ggHH samples is produced at LO matrix element accuracy and used for the training of MVA methods. All four sets of signal samples are generated exclusively for either the $\mathrm{HH} \to 4V$, $\mathrm{HH} \to 4\tau$ or $\mathrm{HH} \to 2V2\tau$ decay modes with V either being a W or a Z boson.
All samples, if not otherwise stated are normalized to their respective cross section at the highest order available for the given process. A full list of the MC event samples entering in this analysis including their cross section and whether or not they were used for the BDT training can be found in Appendix **C**.

6.2.3 Data to Monte Carlo Corrections

Additional data to Monte Carlo corrections are applied to the generated event samples from Sec. 6.2.2 to further improve agreement between data and simulation and take into account a variety of experimental and resolution effects. These include:

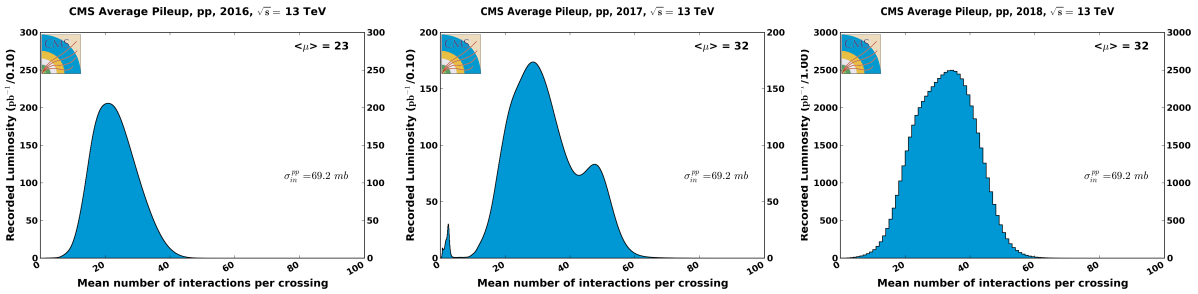

Figure 6.3: From left to right, the distribution of pileup events for the 2016, 2017 and 2018 data taking periods. The plots correspond to an inelastic pp cross section of 69.2 mb and correspond to an average amount of 23/32 and 32 proton-proton interactions per bunch crossing in 2016/2017 and 2018 [127].

1. **Pile-up reweighting:** As the amount of pileup interactions in simulation and data does not match, a reweighting corresponding to an inelastic pp cross section of 69.2 mb [127] is applied to simulated events. The expected pileup for this cross section can be seen in Fig. 6.3.

2. **Trigger efficiency:** The efficiency for events passing a given trigger is not perfectly described in simulation, especially for events close to the triggers threshold(s). To account for this scale factors (SF) are applied to reweight events by the ratio of the efficiency in data and simulation. For the 2ℓ(ss) + 0/1 τ_h, $2\ell+2\tau_h$, $3\ell+0\tau_h$, $3\ell+1\tau_h$ and the 4ℓ channel, SF from [62] are used. These SF are gained by measuring the efficiency in data and simulation on an orthogonal E_T^{miss} based trigger. The SF are measured separately for the ee, eμ and μμ case for 2ℓ events and inclusively for 3ℓ events. Events containing 4ℓ use the SF obtained for 3ℓ events. All SF are parameterized in cone-p_T[4] of the leading/subleading lepton. In case of the $0\ell+4\tau_h$ and $1\ell+3\tau_h$ channels, efficiency curves measured in $Z/\gamma^* \to ee$, $Z/\gamma^* \to \mu\mu$ and $Z/\gamma^* \to \tau\tau$ events using a tag-and-probe method are used. They are parameterized in p_T and η of the lepton and p_T, η, ϕ, decay mode and DeepTau working point of the τ_h. The efficiency in the $1\ell+3\tau_h$ case is then parameterized depending on the probability to pass the single lepton trigger ε_L, the lepton part of the lepton+tau cross-trigger ε_ℓ or the tau part of the lepton+tau ε_τ for the leading, sub-leading and third highest p_T τ_h as stated in equations Eq. 6.1 and Eq. 6.2.

$$\varepsilon = \begin{cases} \varepsilon_L - \min(\varepsilon_L, \varepsilon_\ell) \times \varepsilon_\tau & \text{if only the single lepton trigger fires} \\ (\varepsilon_\ell - \varepsilon_L) \times \varepsilon_\tau & \text{if only the cross-trigger fires} \\ \min(\varepsilon_L, \varepsilon_\ell) \times \varepsilon_\tau & \text{if both triggers fire} \end{cases} , \quad (6.1)$$

with

$$\varepsilon_\tau = \{1-(1-\varepsilon_{\tau 1})(1-\varepsilon_{\tau 2})(1-\varepsilon_{\tau 3}) . \quad (6.2)$$

In case of the $0\ell+4\tau_h$ channel the total efficiency is given as the product of the efficiencies of both parts of the double tau trigger.

3. **Identification and isolation efficiencies of electrons and muons:** To correct for differences in the lepton selection efficiency for passing the given lepton ID and isolation criteria,

[4] see Sec. 6.3

τ_h decay mode	2016	2017	2018
$h^\pm$	0.994 ± 0.010	1.007 ± 0.008	0.987 ± 0.011
$h^\pm + 1\pi^0$ and $h^\pm + 2\pi^0$	0.995 ± 0.009	0.998 ± 0.008	0.995 ± 0.009
$h^\pm h^\mp h^\pm$	1.000 ± 0.011	1.001 ± 0.009	0.988 ± 0.008
$h^\pm h^\mp h^\pm + 1\pi^0$	1.000 ± 0.011	0.999 ± 0.010	0.988 ± 0.008

Table 6.2: Scale factors for the τ_h energy scale as determined on $Z/\gamma^* \to \tau\tau \to \tau_h\mu$ events. The scale factors are given by the ratio of the energy scale in data and simulation and are then applied as a correction in simulated events.

scale factors, given by the ratio of the lepton selection efficiency on data and simulation are applied as a multiplicative event weight per lepton.

The efficiencies are measured separately for muons and electrons, both for passing the Loose lepton ID and Tight lepton IDs used in this analysis (see Sec. 6.3). The efficiencies were originally measured for the CMS $t\bar{t}H$ analysis [62] as a function of lepton $|\eta|$ and p_T using a tag-and-probe method on $Z/\gamma^* \to ee$ and $Z/\gamma^* \to \mu\mu$ events.

To reapply them for this analysis, a correction factor accounting for the looser working points (Sec. 6.3) in the prompt lepton MVA (Sec. 3.2.13) is calculated using the WZ control region (Sec. 7.3) by measuring the average of the original scale factor $SF^{avg}_{t\bar{t}H}$ and the corresponding average correction factor `corr` needed for a data to simulation ratio of one. The new Loose-Tight ID scale factors $SF_{HH}(p_T, |\eta|)$ are then given by:

$$SF_{HH}(p_T, |\eta|) = 1 - \left[(1 - SF_{t\bar{t}H}(p_T, |\eta|)) \frac{1 - \texttt{corr} \times SF^{avg}_{t\bar{t}H}}{1 - SF^{avg}_{t\bar{t}H}} \right] \tag{6.3}$$

4. τ_h **identification efficiency:** Similarly to leptons, the efficiency for τ_h to pass the Tight ID selection criteria in Sec. 6.3 have been measured in $Z/\gamma^* \to \tau\tau$ and the ratio of the efficiency in data and in simulation has been applied as a p_T and $|\eta|$ dependent scale factor. The scale factors have been determined centrally by the Tau POG[5] of the CMS collaboration and can be found in [128].

5. τ_h **energy scale:** The τ_h energy scale is measured by fitting the $m_{\tau_h\mu}$ mass in $Z/\gamma^* \to \tau\tau \to \tau_h\mu$ events. The energy scale is calculated separately for the different τ_h decay modes of the DeepTau τ_h identification described in Sec. 3.2.11, and is provided centrally by the Tau POG of the CMS collaboration. The ratio of the energy scale in data and in simulation is then used to calculate the scale factors given in Tab. 6.2 that are then applied to the τ_h energy in simulated events.

6. b**-tagging efficiency and miss-tag rates:** The efficiency for b-jets passing the given working points of the DeepJet discriminator described in Sec. 3.2.12 as well as the misidentification probability for light jets, slightly differs between data and simulation. For each jet a individual weight in dependence of the jets p_T, η, b-tagging score and original generator level flavour is derived. The final correction is then given by the product of all jet weights in the event [129].

[5] Physics Objects Group

7. **Jet Energy Scale and Jet Energy Resolution:** The energy of jets is calibrated such that both the jet energy scale (JES) as well as the jet energy resolution (JER) of data and simulation match. For this, Di-Jet and Z/γ^*+jets events are used to measure the jet energy response of the CMS detector as well as their p_T resolution. This procedure is described further in [130].

8. E_T^{miss} **corrections:** Differences in the scale and resolution of E_T^{miss} in data and simulation are accounted for by propagating data to simulation differences found in the JER and JES to the E_T^{miss} calculation. Within the CMS collaboration, this is typically referred to as "type-I" corrected PF E_T^{miss} and is validated in [131].
   Due to inhomogeneities in the detector, "type-I" corrected PF E_T^{miss} shows a sinusoidal modulation in ϕ. This is accounted for by applying a correction parameterized in the reconstructed number of vertices as measured on $\mathrm{Z} \to \mu\mu$ events to the p_x and p_y components of E_T^{miss}.

9. **Prefiring issue in ECAL trigger:** During 2016 and 2017, a timing problem with the ECAL trigger caused an efficiency loss in data by triggering events early. In case a sufficient amount of energy in the ECAL was deposited between $|\eta| = 2$ and $|\eta| = 3$ an event could trigger a readout for the previous bunch crossing. As the triggering of events in two consecutive bunch crossing is vetoed in the trigger system, events could thus veto themselves causing the loss of relevant data. As this effect is not present in simulation, the corresponding efficiency loss is corrected for by applying a weight based on an associated prefire probability [132].

10. $\mathrm{t\bar{t}}$ **reweighting:** The p_T spectrum of simulated $\mathrm{t\bar{t}}$ events is corrected to match the predictions of the higher order NNLO QCD calculations in [133] as the p_T spectrum produced by POWHEG is found to be more energetic than observed in data.

6.2.4 EFT benchmarks and signal reweighting

Definition of EFT benchmarks

As discussed in Sec. 2.3 this thesis studies BSM variations of non-resonant Di-Higgs boson production in an EFT context (HEFT) within a set of 5 EFT couplings. A study in more than 2-3 parameters facilitates a challenge on both the practical level, yielding a potentially very high number of signal scenarios, and on the interpretational level where assumptions need to be made on fixed parameters. This thesis instead focuses on a set of adequately chosen benchmark scenarios.

For this two sets of benchmarks are discussed as featured in [28] and [134]. To keep confusion at a minimal level, the 12 benchmark scenarios from the former are denoted as JHEP04BMX with X a number between 1 and 12. The seven benchmarks from the latter are denoted as JHEP03BMX with X a number between 1 and 7. The first set of benchmarks is the older of the two and was also used in the BDT training as described in Sec. 6.6. Therefore in cases where the JHEP03/JHEP04 part of the name is not specified, BMX refers to JHEP04BMX.

Both sets of benchmarks are selected using shape analysis techniques, clustering the different kinematic distributions in kinematic scenarios representative of the whole phase space. In the

Benchmark name	κ_λ	κ_t	c_2	c_g	c_{2g}
JHEP04BM1	7.5	1.0	-1.0	0.0	0.0
JHEP04BM2	1.0	1.0	0.5	-0.8	0.6
JHEP04BM3	1.0	1.0	-1.5	0.0	-0.8
JHEP04BM4	-3.5	1.5	-3.0	0.0	0.0
JHEP04BM5	1.0	1.0	0.0	0.8	-1.0
JHEP04BM6	2.4	1.0	0.0	0.2	-0.2
JHEP04BM7	5.0	1.0	0.0	0.2	-0.2
JHEP04BM8	15.0	1.0	0.0	-1.0	1.0
JHEP04BM8a	1.0	1.0	0.5	0.4	0.0
JHEP04BM9	1.0	1.0	1.0	-0.6	0.6
JHEP04BM10	10.0	1.5	-1.0	0.0	0.0
JHEP04BM11	2.4	1.0	0.0	1.0	-1.0
JHEP04BM12	15.0	1.0	1.0	0.0	0.0

Table 6.3: EFT benchmark scenarios as chosen in [28] using a cluster analysis on Di-Higgs mass and $\cos\theta^*$ distributions. JHEP04BM8a is taken from [20], as JHEP04BM8 does not yield representative kinematics for samples in cluster 8 on NLO accuracy level. As the coupling convention in [28] and [20] is slightly different for c_g and c_{2g}, JHEP04BM8a has been converted to the convention of [28].

JHEOP04 case this is done by comparing the Di-Higgs mass and $|\cos\theta^*|$ distributions for scenarios in the 5d EFT space and by clustering them together based on a likelihood test statistic, quantifying the shape difference of two distributions. The benchmark is then defined as the scenario within each cluster, that is most similar to all other samples within the cluster. The number of clusters is chosen by comparing the kinematic uniformity within each cluster for different numbers of clusters. This worsens visibly for less than 12 clusters. The 12 benchmark points in [28] where found using simulated pp collisions at leading order (LO) matrix level accuracy. When repeating the same clustering in next-to-leading order simulations in [20] similar results are achieved, with the kinematic distributions showing the same general features as observed at LO. Only the distribution for JHEP04BM8 does not yield kinematic distributions representative of cluster 8 on NLO. Therefore an additional benchmark point 8a (JHEP04BM8a) is defined, representing the cluster 8 kinematics more closely.
The couplings of the chosen JHEP04 benchmarks are given in Tab. 6.3. Di-Higgs mass distributions for all JHEP04 benchmark points except JHEP04BM8 are shown in Fig. 6.4 . The seven benchmark points in [134] are found by means of an unsupervised neural network approach, finding the number of seven clusters as optimal number of distinct shape types, with more than 7 clusters not yielding to any new distinct shape types. Among each cluster, the benchmark scenario is then defined as the scenario among the training input scenarios closest to the average of all scenarios in the cluster. In case of ambiguities, the scenario closest in y_t to the SM not exceeding a total cross section of $6.9\times\sigma_{SM}$, is chosen. The couplings of the chosen JHEP03 benchmarks are given in Tab. 6.4. Di-Higgs mass distributions for all JHEP03 benchmark points are shown in Fig. 6.5.

Non-resonant ggHH signal reweighting

In [135], a polynomial parametrization of the Di-Higgs boson cross section $\sigma_{HH}(\kappa_\lambda, \kappa_t, c_2, c_g, c_{2g})$

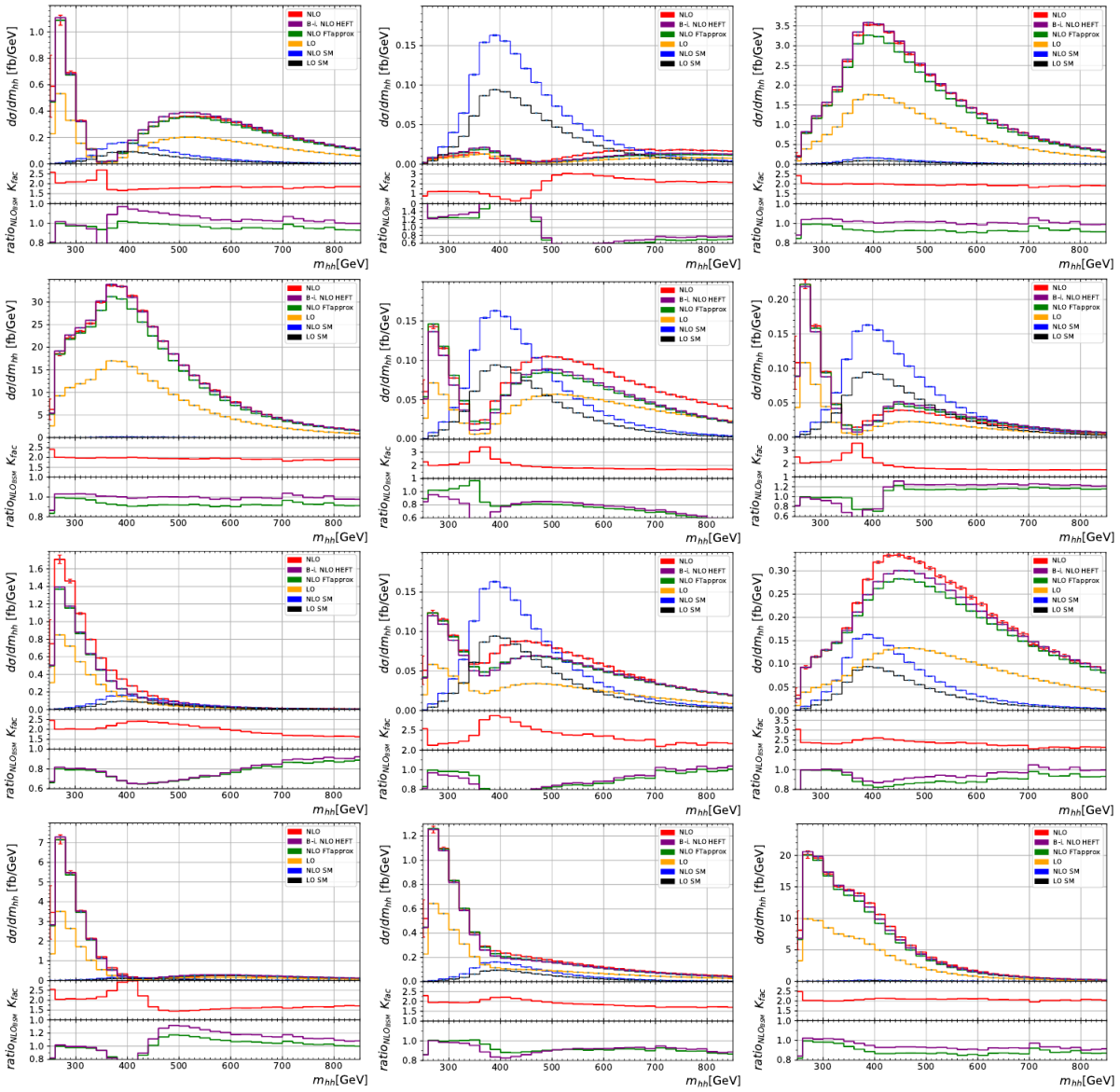

Figure 6.4: Differential ggHH production cross section in the Di-Higgs mass (m_{HH}) for the EFT benchmark scenarios and the SM as given in [20] at LO and different levels of NLO matrix element calculation [20].

Benchmark name	κ_λ	κ_t	c_2	c_g	c_{2g}
JHEP03BM1	3.94	0.94	$-\frac{1}{3}$	0.75	-1.0
JHEP03BM2	6.84	0.61	$\frac{1}{3}$	0.0	-1.0
JHEP03BM3	2.21	1.05	$-\frac{1}{3}$	0.75	-1.5
JHEP03BM4	2.79	0.61	$\frac{1}{3}$	-0.75	-0.5
JHEP03BM5	3.95	1.17	$-\frac{1}{3}$	0.25	-1.5
JHEP03BM6	5.68	0.83	$\frac{1}{3}$	-0.75	-1.0
JHEP03BM7	-0.10	0.94	1.0	0.25	-0.5

Table 6.4: EFT benchmark scenarios as chosen in [134] using a neural network based cluster analysis on Di-Higgs mass distributions. As the coupling convention in [28] and [134] is slightly different for c_g and c_{2g}, the coupling values have been converted to the convention of [28].

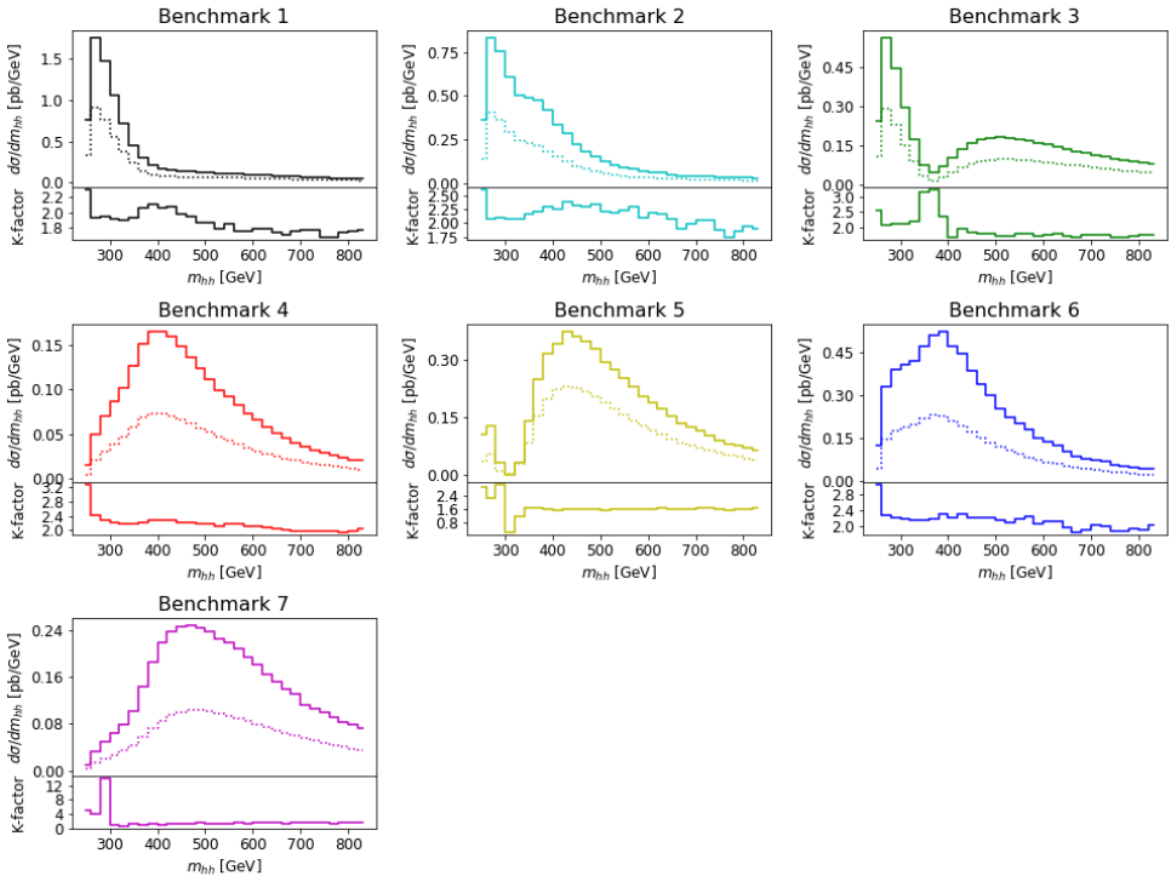

Figure 6.5: Differential ggHH production cross section in the Di-Higgs mass (m_{HH}) for the EFT benchmark scenarios as given in [134] at LO (dotted lines) and NLO (solid lines) matrix element calculation.

relative to the SM cross section $\sigma_{\mathrm{HH}}^{SM}$ is developed at LO matrix element level as:

$$R_{\mathrm{HH}}^{LO} = \frac{\sigma_{\mathrm{HH}}^{LO}(\kappa_\lambda, \kappa_t, c_2, c_{\mathrm{g}}, c_{2\mathrm{g}})}{\sigma_{\mathrm{HH}}^{SM,LO}} = A_1\kappa_{\mathrm{t}}^4 + A_2 c_2^2 + (A_3\kappa_{\mathrm{t}}^2 + A_4 c_{\mathrm{g}}^2)\kappa_\lambda^2 + A_5 c_{2\mathrm{g}}^2 + (A_6 c_2 + A_7\kappa_{\mathrm{t}}\kappa_\lambda)\kappa_{\mathrm{t}}^2$$
$$+(A_8\kappa_t\kappa_\lambda + A_9 c_{\mathrm{g}}\kappa_\lambda)c_2 + A_{10}c_2 c_{\mathrm{g}} + (A_{11}c_{\mathrm{g}}\kappa_\lambda A_{12}c_{2\mathrm{g}})\kappa_{\mathrm{t}}^2$$
$$+(A_{13}\kappa_\lambda c_{\mathrm{g}} + A_{14}c_{2\mathrm{g}})\kappa_{\mathrm{t}}\kappa_\lambda + A_{15}c_{\mathrm{g}}c_{2\mathrm{g}}\kappa_\lambda \quad (6.4)$$

This can easily be extended to a model, for the differential HH cross sections by rewriting R_{HH}^{LO} as:

$$R_{\mathrm{HH}}^{LO} = \frac{\sigma_{\mathrm{HH}}^{LO}(\kappa_\lambda, \kappa_t, c_2, c_{\mathrm{g}}, c_{2\mathrm{g}})}{\sigma_{\mathrm{HH}}^{SM,LO}} \frac{Frac_j}{Frac_j^{SM}} = Poly(A_i^j) \quad (6.5)$$

where $Frac_j$ and $Frac_j^{SM}$ are the fractions of events in an adequately binned differential distribution. The coupling dependent (differential) cross section can then be obtained by extracting the coefficients A_i^j in a likelihood fit to an ensemble of base scenarios distributed in the 5d EFT parameter space. In [135] these coefficients are extracted for a binning based on the Di-Higgs boson invariant mass m_{HH} and $|\cos\theta^*|$, the angle between the flight direction of either Higgs boson and the beam axis in the Di-Higgs boson rest frame. As these two variables completely define the kinematics of the HH system, the obtained differential cross section can be used for the

reweighting of non-resonant ggHH signal samples to any point in the 5d EFT parameter space. This has two advantages: first the studying of a multitude of different signal scenarios without having to generate every single one of them and secondly the enhancement of signal statistics by reweighting the sum of any existing signal sample. In [20] this approach is extended to NLO accuracy:

$$\begin{aligned}\frac{d_\sigma^{NLO}}{dm_{\mathrm{HH}}} = {} & A_1\kappa_\mathrm{t}^4 + A_2\kappa_\mathrm{t}^2\kappa_\lambda^2 + A_4 c_\mathrm{g}^2\kappa_\lambda^2 + A_5 c_{2\mathrm{g}}^2 + A_6 c_2\kappa_\mathrm{t}^2 + A_7\kappa_\mathrm{t}^3\kappa_\lambda \\ & + A_8 c_2\kappa_\mathrm{t}\kappa_\lambda + A_9 c_2 c_\mathrm{g}\kappa_\lambda + A_{10} c_2 c_{2\mathrm{g}} + A_{11}\kappa_\mathrm{t}^2 c_\mathrm{g}\kappa_\lambda + A_{12}\kappa_\mathrm{t}^2 c_{2\mathrm{g}} \\ & + A_{13}\kappa_\mathrm{t}\kappa_\lambda^2 c_\mathrm{g} + A_{14}\kappa_\mathrm{t}\kappa_\lambda c_{2\mathrm{g}} + A_{15} c_\mathrm{g}\kappa_\lambda c_{2\mathrm{g}} + A_{16}\kappa_\mathrm{t}^3 c_\mathrm{g} + A_{17}\kappa_\mathrm{t} c_2 c_\mathrm{g} \\ & + A_{18}\kappa_\mathrm{t} c_\mathrm{g}^2\kappa_\lambda + A_{19}\kappa_\mathrm{t} c_\mathrm{g} c_{2\mathrm{g}} + A_{20}\kappa_\mathrm{t}^2 c_\mathrm{g}^2 + A_{21} c_2 c_\mathrm{g}^2 + A_{22} c_\mathrm{g}^3\kappa_\lambda \\ & + A_{23} c_\mathrm{g}^2 c_{2\mathrm{g}}\end{aligned} \tag{6.6}$$

where the coefficients A are extracted in the invariant Di-Higgs boson mass spectrum. As the second reweighting only considers m_{HH} and not $|\cos\theta^*|$, custom coefficients have been extracted by CMS using the same NLO parametrization as in [20]. They can be found in [21]. The described reweighting of ggHH samples is used in this analysis in one of three different ways:

- The sum of the LO non-resonant ggHH samples was reweighted using the LO coefficients from [135] to be used in the BDT training described in Sec. 6.6.

- The final BDT training for the $3\ell + 0\tau_\mathrm{h}$ and the 2ℓ(ss) + 0/1 τ_h channels was performed using the reweighted sum of the LO non-resonant ggHH with the NLO coefficients in [21].

- The sum of all available NLO ggHH samples was reweighted using the NLO coefficients in [21] to be used in the signal extraction (see. Sec. 7.2) on the described EFT BM scenarios and for a scan on the EFT coupling parameter c_2.

These differences in the reweighting approach have mostly historical reasons, with the used approach representing the status of the CMS HH effort at the different steps of the analysis. The main differences between the different approaches is given by the softer m_{HH} spectrum in NLO compared to LO and the inclusion/absence of additional initial or final state radiation (ISR/FSR) in the core matrix element in NLO/LO simulation. ISR and FSR determine the overall boost of the HH system and modify the single Higgs boson p_T on top of the differences in m_{HH}. While these effects can have an influence on the kinematic distributions of the HH system at the order of 5-10%, the general kinematic properties remain unchanged resulting only in a slightly sub-optimal BDT training. The biggest effects are expected in the $3\ell + 0\tau_\mathrm{h}$ and the 2ℓ(ss) + 0/1 τ_h channels, where the use of differential NLO cross section mitigates some of the differences. Fig. 6.6 shows these differences for the visible Di-Higgs mass m_{HH}^{vis} in the $3\ell + 0\tau_\mathrm{h}$ channel given by the invariant mass of the three selected leptons and two AK4-jets. All approaches agree well in overall signal acceptance and yield. The main differences are in the tail of m_{HH}^{vis} where the genuine NLO signal as well as the NLO→NLO reweighted signal show a generally softer behaviour.

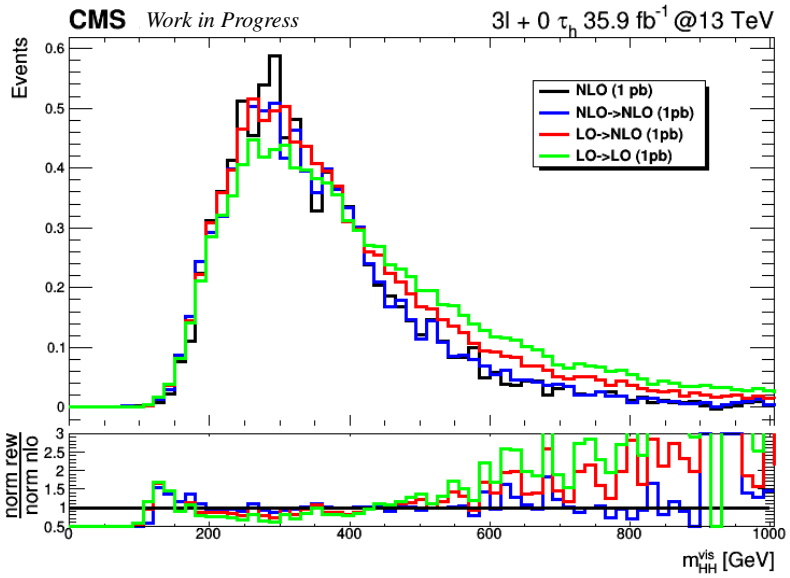

Figure 6.6: The visible Di-Higgs mass m_{HH}^{vis} in the $3\ell+0\tau_{\mathrm{h}}$ channel given by the invariant mass of the three selected leptons and two AK4-jets. The genuine SM NLO ggHH signal is compared to the reweighted sum of all NLO ggHH signal samples reweighted to SM NLO (NLO→NLO), the SM NLO reweighted sum of all LO ggHH signal samples (LO→NLO) and the SM LO reweighted sum of all LO ggHH signal samples (LO→LO). The NLO reweighting is based on the parametrization in [20] extending it to a reweighting in m_{HH} and $|\cos\theta^*|$ with custom coefficients in [21]. The LO reweighting is based on the parametrization and coefficients in [135]. All signal distributions are scaled for an inclusive ggHH cross section of 1 pb.

Phase space comparison of ggHH signal scenarios

As this thesis explores a multitude of physics scenarios with the two sets of EFT benchmarks, as well as parameter scans in κ_λ, κ_{t} and c_2, it is interesting to understand their connection and kinematic similarities for both, the interpretation of the final results and the optimization of the analysis. The latter is of particular importance, as the main feature of the non-resonant HH analysis is a parameterized BDT, using the 12 original JHEP04 benchmarks and the SM as input and target scenarios.

Parameter scans showing the kinetically closest benchmark scenario for different regions in the 5d EFT space are given in [135]. These are obtained by plotting the position of samples from the twelve clusters found in [135] on slices of the parameter space. Fig. 6.7 shows two of those parameter scans in κ_λ-κ_{t} and κ_{t}-c_2. It can be seen that scans in κ_λ outside of the SM and interference regions ($\kappa_\lambda = 1.0$ and $\kappa_\lambda = 2.45$), correspond to EFT benchmark scenarios like JHEP04BM7 and JHEP04BM12 with strong contributions in the low mass regime of m_{HH}. This makes sense, as with growing κ_λ the contribution of the triangle diagram is enhanced. For negative κ_λ, the interference between triangle and box diagram is constructive, explaining the mapping to JHEP04BM12 with a broader m_{HH} distribution compared to JHEP04BM7. For $\kappa_\lambda = 0$ the Di-Higgs boson kinematics are similar to those of JHEP04BM4 with a long tail in m_{HH} as favored for the box diagram. Variations in κ_{t} seem to have a smaller impact on the m_{HH} spectrum and the Di-Higgs boson kinematics in general, with increased $|\kappa_{\mathrm{t}}|$ leading to slightly increased contributions of the box diagram and therefore a slightly more energetic m_{HH} spectrum. This makes benchmarks JHEP04BM12, JHEP04BM4, and JHEP04BM7 good reference points for the kinematics present in a κ_λ scan and is used in Sec. 6.6 to verify the performance of the nonRes

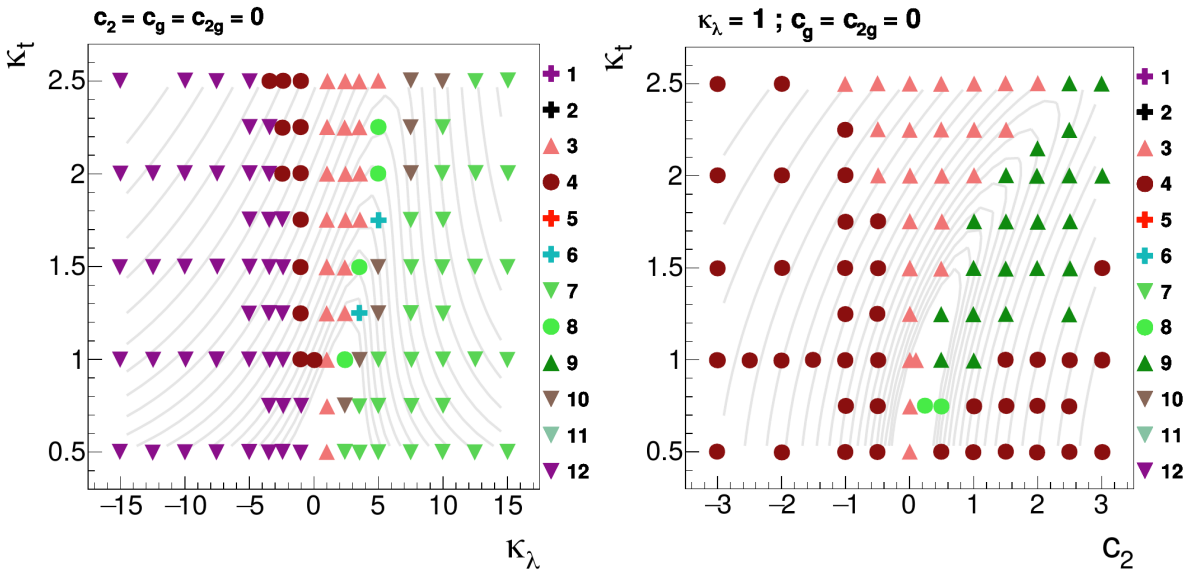

Figure 6.7: Distribution of points from the 12 clusters found in [135] in two slices of the 5d parameter space. The gray contours correspond to constant HH production cross sections.

JHEP03BM /JHEP04BM8a benchmark	closest JHEP04BM benchmark
JHEP03BM1	JHEP04BM11
JHEP03BM2	JHEP04BM11
JHEP03BM3	JHEP04BM5
JHEP03BM4	JHEP04BM3
JHEP03BM5	JHEP04BM9
JHEP03BM6	JHEP04BM3
JHEP03BM7	JHEP04BM9
JHEP04BM8a	JHEP04BM9

Table 6.5: Mapping of JHEP03 EFT benchmark scenarios [134] and the JHEP04BM8a benchmark [20] to the JHEP04 benchmark scenarios [28] using the metric in Eq. 6.7 on the differential NLO HH cross section as a function of m_{HH} [20, 21].

BDT among all desired Di-Higgs boson kinematics. As discussed in Sec. 7.2, the BDT output optimized on JHEP04BM7 is chosen for coupling scans as it allows a focus on the currently important regions in κ_λ.

For variations in c_2 the m_{HH} spectrum gets harder for high $|c_2|$ resulting in long tails towards high m_{HH} as present in benchmarks like JHEP04BM4, JHEP04BM3 or JHEP04BM9.

For comparisons between results on the JHEP04 and JHEP03 set of benchmarks and the choice of the ideal nonRes BDT output for the JHEP03 benchmarks and the JHEP04BM8a benchmark, a mapping between the two sets is useful as well. For this the differential NLO HH cross section in m_{HH} of the different benchmarks is compared by minimizing the following metric:

$$diff(s1,s2) = \sum_{i=0}^{bins} \left| \frac{N^{s1}_{events}(i) - N^{s2}_{events}(i)}{N^{s1}_{events}(i) + N^{s2}_{events}(i)} \right| \tag{6.7}$$

This yields the shown mapping of benchmarks in Tab. 6.5

6.3 Particle Reconstruction and Event Level Quantities

The general reconstruction of electrons, muons, taus, and jets within the CMS experiment is described in Sec. 3.2. On top of this, additional quality criteria are applied to define the analysis level objects used in the $\mathrm{HH} \rightarrow$ Multilepton analysis [4].

Electrons

Based on the basic electron reconstruction, three different electron identification IDs given in Tab. 6.6 are defined for this analysis. The Tight ID is used for the final event selection of events in the signal regions of the $1\ell + 3\tau_{\mathrm{h}}$, 2ℓ(ss) + 0/1 τ_{h}, $2\ell + 2\tau_{\mathrm{h}}$, $3\ell + 0\tau_{\mathrm{h}}$, $3\ell + 1\tau_{\mathrm{h}}$ and 4ℓ channel. The Fakeable electron ID together with the Tight electron ID is used for the estimation of background from misidentified leptons as described in Sec. 6.4. The Loose electron ID is used for low level event vetoes, such as background events containing a $\mathrm{Z} \rightarrow \ell\ell$ decay or the decays of low mass meson resonances. Additionally the Loose electron ID is also used to clean other collections such as jet and τ_{h} candidates from overlapping electron candidates.

The following describes the different electron requirements further: Electron reconstruction

Observable	Loose ID	Fakeable ID	Tight ID
Cone-p_{T}	> 7 GeV	> 10 GeV	> 10 GeV
$\lvert\eta\rvert$	< 2.5	< 2.5	< 2.5
$\lvert d_{xy}\rvert$	< 0.05 cm	< 0.05 cm	< 0.05 cm
$\lvert d_{z}\rvert$	< 0.1 cm	< 0.1 cm	< 0.1 cm
d/σ_d	< 8	< 8	< 8
I_{e}	$< 0.4 \times p_{\mathrm{T}}$	$< 0.4 \times p_{\mathrm{T}}$	$< 0.4 \times p_{\mathrm{T}}$
$\sigma_{i\eta i\eta}$	–	$<$ { 0.011 / 0.030 }[1]	$<$ { 0.011 / 0.030 }[1]
H/E	–	< 0.10	< 0.10
1/E - 1/p	–	> -0.04	> -0.04
Conversion rejection	–	✓	✓
Missing hits	≤ 1	$= 0$	$= 0$
EGamma POG MVA	>WP-loose	>WP-90 (>WP-loose)†	>WP-loose
Deep Jet of nearby jet	–	<WP-tight (<WP-medium)†	<WP-medium
Jet relative isolation[4]	–	< 0.7 (–) †	–
Prompt-e MVA	–	$< 0.30 (> 0.30)$	> 0.30

[1] Barrel / endcaps.
† For electrons failing (passing) the prompt-e MVA > 0.30 requirement

Table 6.6: Electron selection criteria for the Loose electron ID used for low level vetoes and cleaning between electrons, muons, jets and taus, the Tight electron ID used for the Event selection of signal region events in the $1\ell + 3\tau_{\mathrm{h}}$, 2ℓ(ss) + 0/1 τ_{h}, $2\ell + 2\tau_{\mathrm{h}}$, $3\ell + 0\tau_{\mathrm{h}}$, $3\ell + 1\tau_{\mathrm{h}}$ and 4ℓ channels and the Fakable electron ID used in the data driven background estimation of processes involving misidentified leptons (Sec. 6.4). The different selection criteria and variables are described in Sec. 6.3.

relies on the coverage of the CMS tracking system as well as the CMS ECAL allowing for an electron reconstruction up to $|\eta| = 2.5$. For this analysis, electrons with a p_{T} as low as 10 GeV are targeted. Therefore, instead of the normal electron p_{T}, a modified p_{T} variable labeled as cone-p_{T} is used in the definition of electrons and muons to avoid potential biases with the Fakable lepton ID definition and the data driven background estimation for misidentified leptons. In case the electrons fails the selected working point of the Prompt-e MVA, the cone-p_{T} is given by electron p_{T} and mini-isolation: cone-$p_{\mathrm{T}}{}^{e} = p_{\mathrm{T}}{}^{\mathrm{e}} + I_{\mathrm{e}}$ in case there is no jet closer than ΔR=0.4 or,

otherwise, by 0.9 times the lepton subtracted jet p_{T}. If the electron passes the selected Prompt-e MVA working point, the cone-$p_{\mathrm{T}}{}^{e}$ is given by the reconstructed electron $p_{\mathrm{T}}{}^{e}$.
Unlike leptons from hadron decays in jets, signal like electrons and muons are expected to be isolated from other particle candidates in the detector. To quantify this, the lepton isolation is defined by the scalar p_{T} sum of reconstructed particles in a cone of size R around the electron candidate. To take into account the effects of boosted event topologies and allow for electrons from events with high hadronic activity a p_{T} dependent cone size is used. To reduce the effect of pileup on the isolation efficiency, only charged particles from the electron production vertex are taken into account. A correction for the neutral pileup contribution based on the energy density ρ of neutral particles within the acceptance of the tracking detectors is applied. This "mini isolation" [136] is the defined as

$$I_{\ell} = \sum_{\text{charged}} p_{\mathrm{T}} + \max\left(0, \sum_{\text{neutrals}} p_{\mathrm{T}} - \rho \mathscr{A} \left(\frac{\mathrm{R}}{0.3}\right)^{2}\right) \tag{6.8}$$

with the sums running over all particles in a cone

$$\mathrm{R} = \begin{cases} 0.05 & \text{if } p_{\mathrm{T}} > 200\,\mathrm{GeV} \\ 10\,\mathrm{GeV}/p_{\mathrm{T}} & \text{if } 50 < p_{\mathrm{T}} < 200\,\mathrm{GeV} \\ 0.2 & \text{if } p_{\mathrm{T}} < 50\,\mathrm{GeV} \end{cases},$$

The neutral pileup correction is determined by the effective area $\mathscr{A}$ calculated as the correlation of I_{ℓ} and ρ.
For all electrons a mini isolation of $I_{\mathrm{e}} < 0.4 \times p_{\mathrm{T}}{}^{\mathrm{e}}$ is required.

General quality cuts on the distance of the reconstructed electron track to the matched primary vertex d_{xy} and d_z are applied, as well as quality cuts on the width of the corresponding electron cluster $\sigma_{i\eta i\eta}$, the energy ratio of HCAL and ECAL deposits H/E and the difference of the inverse cluster and track energy 1/E-1/p are applied. For Fakable ID and Tight ID electrons also requirements on conversion rejection and the number of missing tracker hits are applied.
Common to electron identification in CMS, a BDT based algorithm (EGamma POG MVA) [137] is used to separate electron from jets. Three working points WP-loose, WP-90 and WP-80 are defined corresponding to 98%, 90% and 80% signal efficiency respectively. For all three IDs, WP-loose electrons are required, as these possess the highest signal efficiency. In case of the Fakable electron ID, if the Prompt-e MVA requirement can not be satisfied, the EGamma POG MVA requirement is raised to WP-90.
Additional requirements on the closest jet are applied such as the DeepJet (Sec. 3.2.12) b-quark identification score and the jets relative isolation defined as the particle flow relative isolation [48] in case the jet is further away than ΔR=0.4 or as $\frac{p_{\mathrm{T}}{}^{jet}}{p_{\mathrm{T}}{}^{e}} - 1$ otherwise. Both cuts are tightened for the Fakable electron ID in case the Prompt-e requirement is failed.
Finally a cut on the Prompt-e lepton MVA described in Sec. 3.2.13) is applied. This recipe is based on the lepton selection in the CMS search for $t\bar{t}\mathrm{H}$ production with Multilepton final states [62] and is optimized for both the identification of low p_{T} electrons and the application of the Fake-Factor method for background prediction.

Muons

Similar to the electron selection described in the previous paragraph, three different muon identification IDs given in Tab. 6.7 are defined for this analysis. The Tight ID is used for the final event selection of events in all channels. The Fakeable muon ID together with the Tight muon ID is used for the estimation of background from misidentified leptons as described in Sec. 6.4. The Loose muon ID is used for low level event vetoes, such as background events containing a $Z \to \ell\ell$ decay or the decays of low mass meson resonances. Additionally, the Loose muon ID is also used to clean other collections such as jet and τ_h candidates with overlapping muon candidates.

For this analysis muons with a p_T as low as 10 GeV are targeted. Instead of the normal muon

Observable	Loose ID	Fakeable ID	Tight ID
p_T	> 5 GeV	> 10 GeV	> 10 GeV
$\lvert\eta\rvert$	< 2.4	< 2.4	< 2.4
$\lvert d_{xy}\rvert$	< 0.05 cm	< 0.05 cm	< 0.05 cm
$\lvert d_z\rvert$	< 0.1 cm	< 0.1 cm	< 0.1 cm
d/σ_d	< 8	< 8	< 8
I_μ	$< 0.4 \times p_T$	$< 0.4 \times p_T$	$< 0.4 \times p_T$
PF muon ID	>WP-loose	>WP-loose	>WP-medium
Deep Jet of nearby jet	–	<WP-interp. (<WP-medium)	<WP-medium
Jet relative isolation	–	<0.8 (–) †	–
Prompt-μ MVA	–	$< 0.5\,(> 0.5)$	> 0.5

† For muons failing (passing) the prompt-μ MVA > 0.50 requirement

Table 6.7: Muon selection criteria for the Loose muon ID used for low level vetoes and cleaning between electrons, muons, jets and taus, the Tight muon ID used for the Event selection of signal region events in all channels, and the Fakable muon ID used in the data driven background estimation of processes involving misidentified leptons (Sec. 6.4).

p_T, however, a modified p_T variable labeled as cone-p_T defined in the same way as the electron cone-p_T is used to avoid potential biases with the Fakable lepton ID definition in the data driven background estimation for misidentified leptons.

Similar as for electrons, a requirement on the mini isolation of $I_\mu < 0.4 \times {p_T}^\mu$ is added. General quality cuts on the distance of the reconstructed muon track to the matched primary vertex d_{xy}, d_z are applied.

Instead of the EGamma POG MVA for electrons, requirements on a different set of muon IDs (PF muon ID) are set. WP-loose muons are defined as particle flow (PF) muons that are tagged either as a global or as an arbitrated tracker muon as studied in [138]. For WP-medium muons, additional requirements on the quality of the muon track fit such as the χ^2 of the fit are applied. Additional requirements on the closest jet are applied. These include the DeepJet b-quark identification score and the relative isolation of jets. The latter is defined as the particle flow relative isolation [48] in case the jet is further away than ΔR=0.4 or as $\frac{{p_T}^{jet}}{{p_T}^\mu} - 1$ otherwise. Both cuts are tightened for the Fakable muon ID in case the Prompt-μ requirement failed.

Finally a cut on the Prompt-μ lepton MVA (Sec. 3.2.13) is applied. This recipe is based on the lepton selection in the CMS search for $t\bar{t}H$ production with Multilepton final states [62] and is optimized for both the identification of low p_T muons and the application of the Fake-Factor method for background prediction.

Hadronic Taus

The reconstruction of hadronic taus using the hadron + strips algorithm and the DeepTau algorithm is described in Sec. 3.2.11. Similar to the muon and electron identification in this analysis, two hadronic tau IDs are defined, with the Tight τ_h ID being used for the final event selection of events in the signal regions and a Fakable τ_h ID used in the data driven background estimation for events containing misidentified τ_h as described in Sec. 6.4.
Hadronic taus with a p_T as low as 20 GeV are reconstructed. Additional quality criteria on the distance of the reconstructed τ_h direction to the matched primary vertex d_{xy} and d_z are applied. These criteria are relatively loose compared to electrons or muons to account for the displaced secondary vertex of the τ decay due to the finite τ lifetime. For the separation against muons and electrons, the loosest available DeepTau working points, WP-VLoose and WP-VVVLoose, are used as they deliver the highest signal efficiency without increasing the τ_h misidentification rate significantly. Only in the $1\ell+3\tau_h$ and the $3\ell+1\tau_h$ channels, misidentified τ_h from $Z \to ee$ decays can contribute significantly. The data driven background estimation focuses on misidentified τ_h from jets wich is not being accounted for in the data driven background estimation. Therefore additional criteria are applied wich further discussed in Sec. 6.5. The definition of the Fakable τ_h ID and the Tight τ_h ID are summarized in Tab. 6.8.

Observable	Fakable ID	Tight ID
p_T	> 20 GeV	> 20 GeV
$\lvert\eta\rvert$	< 2.3	< 2.3
$\lvert d_{xy}\rvert$	< 1000 cm	< 1000 cm
$\lvert d_z\rvert$	< 0.2 cm	< 0.2 cm
DeepTau vs. jets	$>$ WP-VVLoose	WP-Medium
DeepTau vs. muons	$>$ WP-VLoose	$>$ WP-VLoose
DeepTau vs. electrons	$>$ WP-VVVLoose[1]	$>$ WP-VVVLoose[1]

Table 6.8: Selection criteria for the Tight ID hadronic taus used in the event selection of signal region and Fakable ID hadronic taus used in the data driven background estimation described in Sec. 6.4. In the $3\ell+1\tau_h$ and the $1\ell+3\tau_h$ channel, the DeepTau Working point ([1]) is raised to WP-VLoose.

Jets and b-jets

Jets are reconstructed using the anti-kT algorithm described in Sec. 3.2.10. Three types of jets are used in this analysis: AK4 jets, AK8 jets and b-tagged jets. The jets are mainly used for two purposes. The first one is to reconstruct hadronically decaying W bosons expected to leave either a pair of AK4 jets or a single merged AK8 jet.
The AK4 jets are required to have a $p_T > 25$ GeV and fulfill some additional quality criteria summarized in Tab. 6.9, Tab. 6.10 and Tab. 6.11 for 2016, 2017, and 2018, respectively. Central and forward AK4 jets are defined by $|\eta|$ with $|\eta| \leq 2.4$ and $2.4 < |\eta| \leq 5.0$, respectively.
Correspondingly AK8 jets are required to have a rather large $p_T > 100$ GeV motivated by the boosted nature of the two merged W boson decay products. The AK8 jets are further required to have a "subjetiness" parameter [139] $\tau_2/\tau_1 < 0.75$ and should contain two central AK4 sub-jets with $p_T > 20$ GeV as well as at least one tight ID lepton within $\Delta R < 1.2$ of the jet. The AK8 jets used in this analysis are only reconstructed in the central region $|\eta| < 2.4$, are only clustered from non-lepton PF candidates, and are thus referred to as lepton subtracted AK8 jets.

Criterion	$\lvert\eta\rvert \leq 2.7$	$\lvert\eta\rvert \leq 3.0$	$\lvert\eta\rvert > 3.0$
p_{T}	> 25 GeV	> 25 GeV	> 25 GeV
Neutral Hadron Fraction	< 0.99	< 0.98	-
Neutral EM Fraction	< 0.99	> 0.01	< 0.90
Number of Constituents	1	-	-
Charged Hadron Fraction	> 0 ($\lvert\eta\rvert < 2.4$)	-	-
Charged Multiplicity	> 0 ($\lvert\eta\rvert < 2.4$)	-	-
Charged EM Fraction	< 0.99 ($\lvert\eta\rvert < 2.4$)	-	-
Neutral Multiplicity	-	> 2	> 10

Table 6.9: Jet quality criteria for AK4 jet selection in 2016. The selection is based on the number (multiplicity) of charged/neutral objects within the jet candidate as well as the fraction of energy neutral/charged particles have left in the CMS ECAL (EM Fraction) and the CMS HCAL (Hadron Fraction).

Criterion	$\lvert\eta\rvert \leq 2.7$	$\lvert\eta\rvert \leq 3.0$	$\lvert\eta\rvert > 3.0$
p_{T}	> 25 GeV	> 25 GeV	> 25 GeV
Neutral Hadron Fraction	< 0.90	-	> 0.02
Neutral EM Fraction	< 0.90	> 0.02 and < 0.99	< 0.90
Number of Constituents	1	-	-
Charged Hadron Fraction	> 0 ($\lvert\eta\rvert < 2.4$)	-	-
Charged Multiplicity	> 0 ($\lvert\eta\rvert < 2.4$)	-	-
Neutral Multiplicity	-	> 2	> 10

Table 6.10: Jet quality criteria for AK4 jet selection in 2017. The selection is based on the number (multiplicity) of charged/neutral objects within the jet candidate as well as the fraction of energy neutral/charged particles have left in the CMS ECAL (EM Fraction) and the CMS HCAL (Hadron Fraction)

The second purpose for jets in this analysis is to identify and veto events containing b-quark induced jets either from top-quark decays or from $\mathrm{H} \to \mathrm{b\bar{b}}$ decays, ensuring orthogonality with respect to other HH analyses. b-tagged jets are defined as central AK4 jets passing either the DeepJet-L or DeepJet-M working points of the DeepJet algorithm detailed in Sec. 3.2.12.

E_T^{miss} and other quantities

Particles such as weakly interacting neutrinos can not be reconstructed by the particle detectors at collider experiments. They can, however, show up as a momentum imbalance in the $x-y$ plane

Criterion	$\lvert\eta\rvert \leq 2.6$	$2.6 < \lvert\eta\rvert \leq 2.7$	$2.7 < \lvert\eta\rvert \leq 3.0$	$3.0 < \lvert\eta\rvert \leq 5.0$
p_{T}	> 25 GeV	> 25 GeV	> 25 GeV	> 25 GeV
Neutral Hadron Fraction	< 0.90	< 0.9	-	> 0.02
Neutral EM Fraction	< 0.90	< 0.99	> 0.02 and < 0.99	< 0.90
Number of Constituents	1	-	-	-
Charged Hadron Fraction	> 0	-	-	-
Charged Multiplicity	> 0	> 0	-	-
Neutral Multiplicity	-	-	> 2	> 10

Table 6.11: Jet quality criteria for AK4 jet selection in 2018. The selection is based on the number (multiplicity) of charged/neutral objects within the jet candidate as well as the fraction of energy neutral/charged particles have left in the CMS ECAL (EM Fraction) and the CMS HCAL (Hadron Fraction)

where energy and momentum conservation is required. Based on this, the Missing Transverse Energy (MET) is defined as the negative transverse momentum of the sum of all reconstructed PF candidates, with E_T^{miss} and $\phi(E_T^{miss})$ given by the magnitude and ϕ direction of the resulting four vector sum.
$H_{\mathrm{T}}^{\mathrm{miss}}$ is defined in a similar fashion to E_T^{miss}, only considering the reconstructed central jets, electrons, muons and τ_{h} passing the Fakable ID. Only considering these reconstructed event level objects, reduces the dependence of $H_{\mathrm{T}}^{\mathrm{miss}}$ on pileup, while also reducing the corresponding resolution.
With a linear combination of E_T^{miss} and $H_{\mathrm{T}}^{\mathrm{miss}}$, energy resolution and pileup dependence can be balanced while reducing the contribution of "fake" MET from instrumentation effects compared to "genuine" MET, e.g. from neutrinos. This reduction has its origin in the reduced correlation of E_T^{miss} and $H_{\mathrm{T}}^{\mathrm{miss}}$ in events without a genuine source of E_T^{miss}. For this reason,

$$E_T^{miss}LD = 0.6 \times E_T^{miss} + 0.4 \times H_{\mathrm{T}}^{\mathrm{miss}} \tag{6.9}$$

is used to track the contribution of MET in this analysis. While $H_{\mathrm{T}}^{\mathrm{miss}}$ is the negative vectorial sum of the transverse momenta of all reconstructed event level object, HT tracks the overall energetic activity of an event, and is defined as the scalar sum of these momenta.

6.4 The Fake-Factor Method and Data-Driven Background Estimation

The high object multiplicities required in most of the sub channels of this analysis as well as the exotic charge requirement in the 2ℓ(ss) + 0/1 τ_{h} channel lead to channels low in genuine background with final states matching the required event signatures, making fake leptons an important source of background.
The object reconstruction algorithms within CMS are highly effective and feature high signal efficiency and small misidentification rate. Still, processes with a high cross section compared to signal or the genuine background processes entering the signal categories, can contribute with an additional misidentified lepton or τ_{h}. One example of this is the contribution of leptonically decaying WZ events in the $3\ell + 1\tau_{\mathrm{h}}$ channel, in which a jet can be misidentified as a τ_{h}. Here, the jet can be either a pileup jet or the result of initial or final state radiation. With a cross section of 4.43 pb [140] the WZ process contributes nearly as many fake background events as ZZ yields genuine background events, despite a cross section for leptonically decaying ZZ events that is about a factor four lower [140] and further reduced by about a factor three due to the restriction to at least one $\mathrm{Z} \to \tau\tau$ decay.
Therefore, while rare, the contribution of background events containing misidentified electrons, muons, and τ_{h} becomes one of the leading contributions to selected events in this analysis.

As the effects leading to misidentified e, μ, and τ_{h} are not well described in simulation, the corresponding background processes are modelled by a data driven approach schematically described in Fig. 6.8 that is known as the Fake-Factor (FF) method [141]. To avoid double counting, events

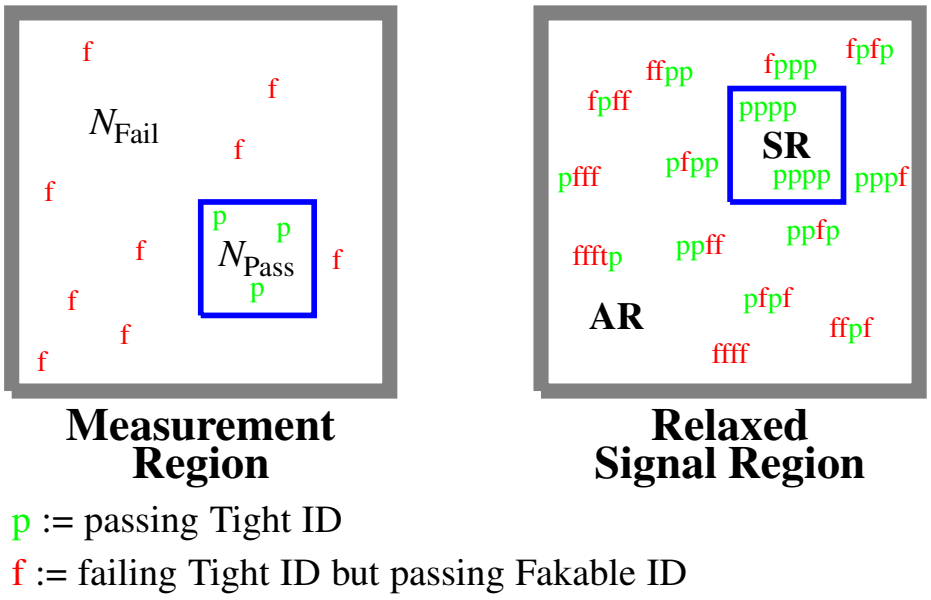

Figure 6.8: Schematic representation of the fake background estimation of the HH $\rightarrow$ Multilepton analysis. First, the probability f of a misidentified lepton or τ_h passing the corresponding Fakeable ID to also pass the Tight ID is measured in a measurement region as the ratio of objects passing (p) Tight ID criteria N_{Pass} and all Fakable objects passing and failing (f) the Tight ID criteria $N_{\text{Pass}} + N_{\text{Fail}}$ (left). These are then used to compute fake factors $F = \frac{f}{1-f}$ to calculate weights (Eq. 6.10) applied on an application region (AR) where at least one of the objects required for the signal region (SR), does only pass the Fakable ID but not the Tight ID criteria.

where the selected final state objects cannot be matched to objects at the generator level of the simulation are vetoed.

To model this fake background, first the probability f of a lepton or τ_h which passes the Fakable ID to also pass the corresponding Tight ID is determined in a measurement region (MR) where no genuine leptons/τ_h are expected.

These misidentification rates $f = \frac{N_{\text{Pass}}}{N_{\text{Pass}}+N_{\text{Fail}}}$ are determined separately for electrons, muons and τ_h and all three data taking years in bins of $|\eta|$ and (cone-)p_T.

For electrons and muons, the measurement is performed in events enriched in QCD multijet events, requiring exactly one lepton passing the Fakable ID in addition to at least one jet with $\Delta R > 0.7$ between jet and lepton. A set of single electron and muon triggers is used and offline jet and lepton p_T thresholds chosen to ensure full trigger efficiency. Events with genuine leptons are modeled by simulation and subtracted from data before extracting f.

For τ_h the measurement of f is performed on $Z/\gamma^* \rightarrow \mu\mu+$ jets events requiring a pair of oppositely charged Tight ID muons with a leading (subleading) $p_T > 25(15)$ GeV of the muons in a mass window $60 < m_{\mu\mu} < 120$ GeV with an additional τ_h passing the Fakable ID. The events are further enriched in $Z/\gamma^* \rightarrow \mu\mu$ events by vetoing events containing more than one DeepJet-L tagged or any DeepJet-M b-tagged jet in order to reduce the contribution of $t\bar{t}$ events. For the measurement of f events containing a τ_h from genuine τ_h, electron, or muon are subtracted using simulated data.

Based on the misidentification rates f from the measurement region, the fake background in the signal region (SR) is estimated by applying adequately chosen weights to events selected in an application region (AR). The AR is defined by loosening the lepton and τ_h ID of the correspond-

ing SR from Tight to Fakable and vetoing any SR events, i.e. events where all objects pass (p) the Tight ID criteria, therefore requiring at least one of the selected objects to fail (f) them.
The fake background events N^{fake} are then given depending on the number of required leptons and τ_h by one of the following sums:

$$
\begin{aligned}
N^{\text{fake}}_{\text{pp}} &= \sum_{\text{fp}} F_1 + \sum_{\text{pf}} F_2 - \sum_{\text{ff}} F_1 F_2 \\
N^{\text{fake}}_{\text{ppp}} &= \sum_{\text{fpp}} F_1 + \sum_{\text{pfp}} F_2 + \sum_{\text{ppf}} F_3 \\
&\quad - \sum_{\text{ffp}} F_1 F_2 - \sum_{\text{fpf}} F_1 F_3 - \sum_{\text{pff}} F_2 F_3 + \sum_{\text{fff}} F_1 F_2 F_3 \\
N^{\text{fake}}_{\text{pppp}} &= \sum_{\text{fppp}} F_1 + \sum_{\text{pfpp}} F_2 + \sum_{\text{ppfp}} F_3 + \sum_{\text{pppf}} F_4 \\
&\quad - \sum_{\text{ffpp}} F_1 F_2 - \sum_{\text{fpfp}} F_1 F_3 - \sum_{\text{fppf}} F_1 F_4 - \sum_{\text{pffp}} F_2 F_3 - \sum_{\text{pfpf}} F_2 F_4 - \sum_{\text{ppff}} F_3 F_4 \\
&\quad + \sum_{\text{fffp}} F_1 F_2 F_3 + \sum_{\text{ffpf}} F_1 F_2 F_4 + \sum_{\text{fpff}} F_1 F_3 F_4 + \sum_{\text{pfff}} F_2 F_3 F_4 - \sum_{\text{ffff}} F_1 F_2 F_3 F_4 \,. \qquad (6.10)
\end{aligned}
$$

Here the lepton indices (p,f) are ordered by p_T. This means that e.g. the sum $\sum_{\text{pfff}} F_2 F_3 F_4$ runs over events with a total number of four leptons and τ_h where the highest p_T objects passes the Tight ID criteria, where the remaining ones pass the Fakable ID but fail the Tight ID. The fake factors F_i are then given by the corresponding misidentification rate

$$F_i = \frac{f_i}{1 - f_i}. \qquad (6.11)$$

The sums run over all events in the AR region with the given number and p_T order of leptons/τ_h passing and failing the Tight ID criteria.
To ensure the validity of the method a closure test comparing the number of simulated events in the SR with that extrapolated from the AR to the SR is performed in the $3\ell + 0\tau_h$ and $2\ell(\text{ss}) + 0/1$ τ_h channels. This leads to only small differences in the order of $5 - 10\%$ between expected and extrapolated simulation events. The remaining non closure is applied as an additional normalization and shape uncertainty in these two channels. Additional normalization uncertainties on the fake background are applied in all channels as described in Sec. 7.1. Additionally the closure of data and background prediction is studied in a set of channel specific background control regions described in Sec. 7.3.

In the $2\ell(\text{ss}) + 0/1$ τ_h channel in addition to genuine and fake backgrounds, also events containing leptons with misidentified charge ("flips") can enter the SR. These originate for example from $Z/\gamma^* \to \ell\ell$ events with two leptons and two jets in the final state. As the charge flip of leptons is not well modelled in simulation, this charge flip background is estimated from data as well.
For this the charge flip rate of electrons and muons in $Z/\gamma^* \to \ell\ell$ events is determined comparing the Z boson mass peak in same sign and opposite sign lepton pairs in bins of $|\eta|$ and p_T.

The charge flip rates for muons is found to be negligible compared to electrons. The charge flip rates for electrons are applied as a multiplicative event weight to ee and eμ events in the charged flipped 2ℓ (OS) + 0/1 τ_h side band of the 2ℓ(ss) + 0/1 τ_h channel.

6.5 Event Selection

Based on the Multilepton signature of the leptonic decay channels in $\mathrm{HH} \to 4\mathrm{W}$, $\mathrm{HH} \to 2\mathrm{W}2\tau$ and $\mathrm{HH} \to 4\tau$ decays, seven channels are defined requiring a number of Tight ID leptons (ℓ) and Tight ID hadronic taus (τ_h). These channels are chosen to cover most of the leptonic W decay modes with the exception of final states with low object multiplicities and a high number of expected background events like the 2ℓ (OS) final state.
On top of the event reconstruction described in Sec. 6.3 an additional filter algorithm is applied rejecting events influenced by detector noise, calibration and beam halo[6] effects. A list of the Filter tags applied, commonly referred to as E_T^{miss} Filter, is given in Tab. 6.12 as reference. Common among all seven channels is the rejection of events involving b-tagged jets, reducing the number of background events from processes containing top quark decays as well as ensuring orthogonality to other HH analyses within CMS. This b-jet veto rejects all events with more than one DeepJet-L b−tagged jets or any DeepJet-M b−tagged jet.
Furthermore all channels involving two ore more leptons undergo up to three additional criteria:

- A veto against low mass meson resonances, as they are not covered well by the simulation.
- A veto against leptonic Z boson decays that are common to many background processes.
- A veto against leptonic $\mathrm{H} \to \mathrm{ZZ}$ decays reducing single Higgs boson background and ensuring orthogonality against the CMS $\mathrm{HH} \to \mathrm{bbZZ}$ analysis [142].

All these vetoes are performed on Loose ID lepton pairs. In the case of the low mass resonance any event with a Di-Lepton pair mass $m_{\ell\ell} < 12$ GeV is rejected. For the Z boson mass veto all

[6] The proton bunches circulating within the LHC have a small but finite size within the beam pipe. Beam halo refers to the proton expansion in the transverse plane.

Filter name	Used for data events	Used for simulated events
`Flag_goodVertices`	✓	✓
`Flag_globalSuperTightHalo2016Filter`	✓	✓
`Flag_HBHENoiseFilter`	✓	✓
`Flag_HBHENoiseIsoFilter`	✓	✓
`Flag_EcalDeadCellTriggerPrimitiveFilter`	(Only 17/18)	(Only 17/17)
`Flag_BadPFMuonFilter`	✓	✓
`Flag_ecalBadCalibReducedMINIAODFilter`†	✓	✓
`Flag_eeBadScFilter`	✓	–

Table 6.12: Event filters (E_T^{miss} filters) rejecting events influenced by detector noise, calibration and beam halo effects. The given names reflect CMS internal flags and are given for reference. The `Flag_eeBadScFilter` filter is only applied on simulated events while the `Flag_EcalDeadCellTriggerPrimitiveFilter` is only available in 2017 and 2018 data and simulation.

events with a same flavor opposite sign pair (SFOS) with an invariant mass in a 10 GeV mass window around the Z boson mass are vetoed. The $\mathrm{H} \to \mathrm{ZZ}$ veto is applied on events containing four leptons forming two SFOS pairs with a total invariant mass $m_{\ell\bar{\ell}\ell'\bar{\ell}'} < 140\,\mathrm{GeV}$.
Background from events with fake τ_h from misidentified electrons is not modelled by the data driven background estimation described in Sec. 6.4 and is not properly described by simulation. This can lead to disagreements between data and background prediction at low ${p_\mathrm{T}}^{\tau_\mathrm{h}}$ for both the $1\ell+3\tau_\mathrm{h}$ and the $3\ell+1\tau_\mathrm{h}$ channel. In the $2\ell+2\tau_\mathrm{h}$ channel no such discrepancies were observed as the main contribution of such fake τ_h events originates from $\mathrm{Z} \to \mathrm{ee}$ decays, where one electron is misreconstructed as a τ_h leading to final states with an odd number of leptons.
To resolve this issue, additional requirements are placed on the τ_h in both the $1\ell+3\tau_\mathrm{h}$ and the $3\ell+1\tau_\mathrm{h}$ channel:

- $3\ell+1\tau_\mathrm{h}$: As one of the main reasons for electron misidentification are dead regions or "cracks" between the subcomponents of the ECAL, events where the τ_h is compatible with passing through the main crack of the ECAL at $1.460 < |\eta| < 1.558$ are vetoed. Additionally the DeepTau working point for the discriminant against electrons is raised from WP-VVVLoose to WP-VLoose.

- $1\ell+3\tau_\mathrm{h}$: Due to the higher multiplicity of τ_h in the $1\ell+3\tau_\mathrm{h}$ channel, the same requirements cannot be applied without reducing signal efficiency. Therefore, as the main contribution of these fake τ_h comes from $\mathrm{Z} \to \mathrm{ee}$ decays, the "crack" cut in the $1\ell+3\tau_\mathrm{h}$ channel and the DeepTau vs. electrons WP-VLoose requirements are only applied on τ_h having an invariant mass with an oppositely charged electron close to the Z boson mass $m_\mathrm{Z} - 20\,\mathrm{GeV} < m^{\mathrm{OS}}_{\ell\tau_\mathrm{h}} < m_\mathrm{Z} + 10\,\mathrm{GeV}$.

After the described τ_h criteria are applied, no further disagreements between data and background prediction are observed as can be seen in Sec. 7.3. In addition to this general selection criteria, every channel was optimized separately with the final selection criteria described in the following two sections for the $3\ell+1\tau_\mathrm{h}$ channel in Sec. 6.5.1 and all other channels in Sec. 6.5.2.

6.5.1 The $3\ell+1\tau_\mathrm{h}$ channel

The $3\ell+1\tau_\mathrm{h}$ analysis focuses on the $\mathrm{HH} \to 2\mathrm{W}2\tau$ and $\mathrm{HH} \to 4\mathrm{W}$ tau decay modes. It requires exactly 3 Tight ID leptons and 1 Tight ID τ_h with a total electric charge sum of 0.
$\mathrm{H} \to \mathrm{WW}$ decays lead to one on-shell W and one off-shell W boson with the latter only having a mass of typically 40 GeV. This motivates the relatively low p_T thresholds for the selected leptons down to 10 GeV. Thresholds lower than the required 25/15/10 GeV for the leading, subleading and third highest p_T lepton would lead to higher contributions from fake background as well as complications with trigger requirements leaving little room for further optimization. A similar case can be made for the requirement on τ_h at $p_\mathrm{T} > 20$ GeV. Instead, the working points for the Prompt-lepton MVA used in the electron and muon reconstruction (Sec. 6.3) were optimized. It was found, that the working points used by the $\mathrm{t\bar{t}H}$ analysis, for which this MVA was developed, were too tight for some of the high object multiplicity channels in this analysis. For a consistent lepton ID use in all Multilepton channels, the working points where re-optimized for the relatively high statistics $3\ell+0\tau_\mathrm{h}$ channel to the values reported in Sec. 6.3. These where then used

Criterion	Value
Tight ID leptons	3
Lepton p_{T}	$>$ 25/15/10 GeV
Tight ID τ_{h}	≥ 1
Tau p_{T}	$>$ 20 GeV
deep Tau WP (vs Electrons)	WP-VLoose
Tau $\lvert\eta\rvert$ veto	$1.460 \leq \lvert\eta\rvert \geq 1.558$
Low mass resonance veto	any $m_{\ell\ell}^{\text{Loose ID}} < 12$ GeV
Z mass veto	any $\lvert m_{\ell\ell}^{\text{SFOS, Loose ID}}\rvert < 10$ GeV
b-jet Veto	any DeepJet-M or $>$ 1 DeepJet-L b-tag
Charge Sum	$Q(\tau_{\mathrm{h}}) + \sum_i Q(\ell_i) = 0$

Table 6.13: Event selection for the $3\ell + 1\tau_{\mathrm{h}}$ channel.

in all other channels as well.

The use of a lower working point on the DeepTau discrimination between τ_{h} and misidentified jets was studied as well. A looser working point than the commonly used Medium-WP leads to disagreements between data and background prediction, while the use of tighter working points leads to a reduction in signal efficiency. As described in the beginning of Sec. 6.5 the DeepTau working point against electrons is raised to WP-VLoose and an additional veto against taus compatible with passing through the ECAL crack around $1.460 < |\eta| < 1.558$ is applied to counter background events containing $\mathrm{ZZ} \to \mathrm{ee}$ decays.

As in other Multilepton channels the vetoes against low mass resonances as well as b-tagged jets and leptons from $\mathrm{Z} \to \ell\ell$ are applied. The selection criteria are summarized in Tab. 6.13. The given selection leads to a category with a very low expected background yield of about 55 events for the combined Run 2 dataset, which consist mostly out of genuine ZZ events and fake τ_{h} and fake lepton events from WZ, with smaller contributions from single Higgs boson production and other rare processes such as triple boson production as can be seen in Fig. 6.9 . Due to the low expected signal yield of about 0.2 SM events for the full Run 2 data taking period, further selection requirements as on an minimal amount of E_T^{miss}LD were omitted and corresponding variables with good signal to background separation where left to an event level BDT instead (see Sec. 6.6.1) which then is used in the signal extraction (see Sec. 7.2). Similarly sub categorization by the number of SFOS lepton pairs splitting the $3\ell + 1\tau_{\mathrm{h}}$ channel into a ZZ enriched NSFOS$>$ 1 and a fake background enriched NSFOS=0 region was considered, but the corresponding information was left to the BDT instead. This was done, as a splitting of the channel would place an additional challenge on the background prediction and the BDT training because of the limited statistics of the simulation and in the application region (Sec. 6.4). With an increased amount of data and simulated events however, such a sub categorization might gain interest again in the future. Then the application of two separate BDTs or neural network discriminators could focus on one singular background in each category instead of the combined ZZ and Fake background in the unsplit $3\ell + 1\tau$ channel.

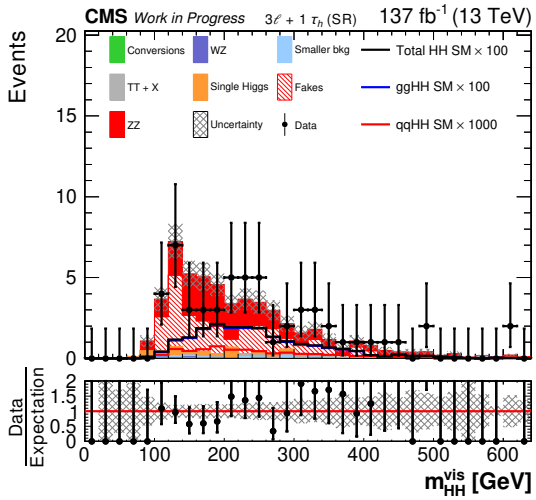

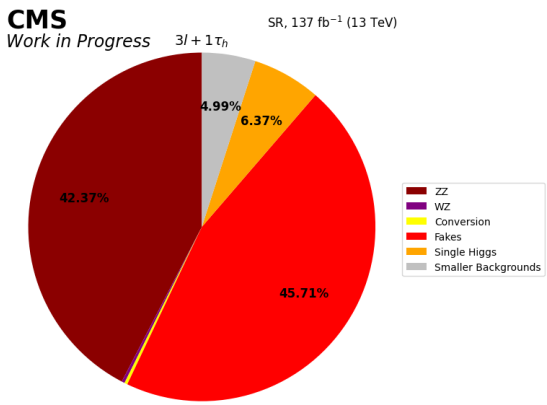

Figure 6.9: The distribution of the visible Di-Higgs mass given by the invariant mass of the three selected leptons and the hadronic tau for the full Run 2 dataset on the left. The right shows the relative contributions of the different backgrounds in a pie chart. The shown uncertainty band corresponds to statistical uncertainty contributions only. The SM expected $\mathrm{ggHH}/\mathrm{qqHH}$ signal is scaled by a factor of 100/1000 for better visibility.

Criterion	$0\ell+4\tau_h$	$1\ell+3\tau_h$	$2\ell+2\tau_h$
Tight ID leptons	0	1	2
Lepton p_T	–	$>20(15)$ GeV for an electron (muon)	25/15 GeV (leading/subleading lepton)
Tight ID τ_h	≥ 4	3	2
Tau p_T	40/40/20/20 GeV	$>40/30/20$ GeV	>20 GeV
τ_h $\lvert\eta\rvert$ veto + DeepTau vs. Ele WP-VLoose if $m_Z-20\,\mathrm{GeV}<m^{OS}_{\ell\tau_h}<m_Z+10\,\mathrm{GeV}$	$1.460\leq\lvert\eta\rvert\geq 1.558$	–	–
Low mass resonance veto	–	–	✓
Z mass veto	–	–	✓
b-jet Veto	✓	✓	✓
Charge Sum	$\sum Q(\tau_h)=0$	$\sum Q(\tau_h)+Q(\ell)=0$	$\sum Q(\tau_h)+Q(\ell)=0$

	4ℓ	$3\ell+0\tau_h$	$2\ell(\mathrm{ss})+0/1\ \tau_h$
Tight ID leptons	≥ 4	3	2
Lepton p_T	25/15/15/10 GeV	25/15/10 GeV	25/15 GeV
Tight ID τ_h	–	0	<1
number of jets	–	≥ 1 AK8 jet(s) or ≥ 1 AK4 jet(s)	≥ 1 AK8 jet(s) or ≥ 2 AK4 jet(s)
Low mass resonance veto	–	–	✓
Z mass veto	✓	✓	extended to SS ee pairs
b-jet Veto	✓	✓	✓
$H\to ZZ\to 4\ell$ Veto	✓	✓	✓
E_T^{miss}LD	–	$>45/30/0$ GeV for events with/without SFOS Fakable ID lepton pairs/ ≥ 4 AK4 jets	$>30/0$ for events without/with Tight ID muons
Charge Sum	$\sum Q(\text{leading } 4\ell)=0$	$\sum Q(\ell)=0$	$\sum Q(\tau_h)+Q(\ell)=0$

Table 6.14: Event selection for the $0\ell+4\tau_h$, $1\ell+3\tau_h$, $2\ell+2\tau_h$, $3\ell+0\tau_h$, 4ℓ and $2\ell(\mathrm{ss})+0/1\ \tau_h$ channels.

6.5.2 Other $\mathrm{HH}\to$ Multilepton Channels

The six other Multilepton channels $0\ell+4\tau_h$, $1\ell+3\tau_h$, $2\ell+2\tau_h$, $3\ell+0\tau_h$, 4ℓ and $2\ell(\mathrm{ss})+0/1\ \tau_h$ are defined in a similar fashion to the $3\ell+1\tau_h$ channel (Sec. 6.5.1) by requiring the specific amount of Tight ID final state objects and, where necessary, vetoing additional Tight ID leptons and τ_h to avoid overlap with other sub-channels.

In addition to these basic criteria, all channels follow the b-jet, $Z\to\ell\ell$, low mass resonance and $H\to ZZ\to 4\ell$ rejection criteria described in Sec. 6.5 where applicable.

Additionally the $3\ell+0\tau_h$ and $2\ell(\mathrm{ss})+0/1\ \tau_h$ require the presence of jets aiming at the presence of one (two) hadronically decaying W bosons. These two channels also place additional requirements on E_T^{miss}LD, motivated by the presence of neutrinos in the signal. The exact selection criteria, also including p_T thresholds are summarized in Tab. 6.14. The given selection results in six channels defined mostly by a mixture of Di-Boson ZZ and WZ as well as fake lepton/τ_h background (see Fig. 6.10). The expected event yields range between about 3 events in

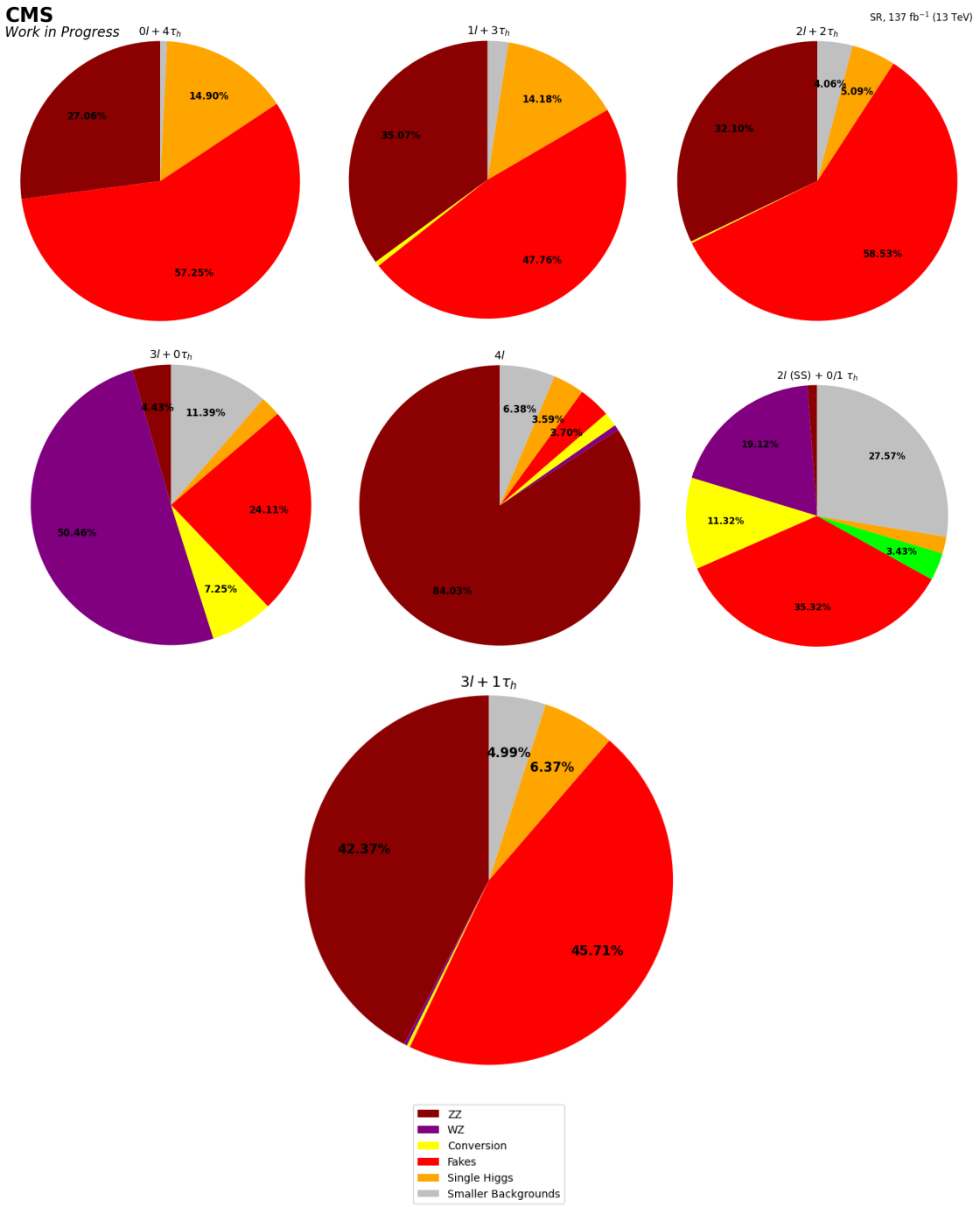

Figure 6.10: Background composition in the $0\ell + 4\tau_h$, $1\ell + 3\tau_h$, $2\ell + 2\tau_h$, $3\ell + 0\tau_h$, 4ℓ, 2ℓ(ss) + 0/1 τ_h, and $3\ell + 1\tau_h$ channels.

the $0\ell + 4\tau_h$ and about 10000 expected events in the 2ℓ(ss) + 0/1 τ_h channel. While all channels contain contributions from the $HH \to 4W$, $HH \to 2W2\tau$ and $HH \to 4\tau$ decay modes as well as smaller contributions from $HH \to 4Z$ and $HH \to 2Z2\tau$ decays, each signal is dominant in a different subset of channels allowing a good constraint of bosonic as well as fermionic Higgs boson decay modes.

This results, as shown in Sec. 7.4 and Sec. 7.5.1, in an advantage over other HH analysis with a high number of fermionic Higgs boson decays: for large values, the trilinear Higgs boson self-coupling κ_λ has a profound effect on the single Higgs boson branching fraction (see Sec. 2.3) reducing/enhancing the contribution of fermionic compared to bosonic decay modes for posi-

Process	2ℓ(ss) + 0/1 τ_h	$3\ell+0\tau_h$	4ℓ	$0\ell+4\tau_h$	$1\ell+3\tau_h$	$2\ell+2\tau_h$	$3\ell+1\tau_h$
SM HH $\to 4V$ ($\times 30$)	72.9 ± 1.6	33.0 ± 0.7	2.23 ± 0.11	0.26 ± 0.01	0.19 ± 0.02	0.16 ± 0.04	0.91 ± 0.05
SM HH $\to 2V2\tau$ ($\times 30$)	30.8 ± 0.7	11.9 ± 0.4	0.95 ± 0.07	0.07 ± 0.03	0.61 ± 0.14	3.94 ± 0.37	4.13 ± 0.24
SM HH $\to 4\tau$ ($\times 30$)	2.7 ± 0.1	1.0 ± 0.0	0.10 ± 0.01	1.32 ± 0.20	2.59 ± 0.28	2.30 ± 0.13	0.89 ± 0.05

Table 6.15: Expected SM signal yields for the seven different HH $\to$ Multilepton channels scaled by a factor of 30. The signals include both ggHH as well as qqHH production. The given uncertainties correspond to the complete sum of statistical and systematic uncertainties [4].

tive/negative κ_λ. Thus, while for other analysis the sensitivity for negative κ_λ is usually higher than for positive κ_λ, the sensitivity in the HH $\to$ Multilepton search is almost flat in κ_λ as a result of the interplay between the seven different channels. A table showing the signal composition in each of the seven sub channels is given in Tab. 6.15.

6.6 BDT Disciminants

The main separation between the various HH signals and the WZ, ZZ, Fake and other backgrounds is achieved by three different parameterized BDT discriminants for each of the seven channels. The output of the different BDT discriminants is then used in a binned maximum likelihood fit together with the control region distributions (Sec. 7.3) as described in Sec. 7.2.
To ensure a sufficient number of training events, the training is performed on simulated events only, taking any contribution of fake lepton/τ_h backgrounds from simulation instead of background events estimated from data. Further the lepton ID requirements are relaxed to the Loose lepton ID and the DeepTau working point against jets is relaxed from WP-Medium to WP-VVVLoose (**Training Region**). For backgrounds with multiple available datasets, the one with the fewer negative event weights is used for training and the other dataset is used in the signal extraction. Any remaining events with negative weights are removed from the set of training events gained in this manner. The background events are then re-scaled relatively to their expected event yields in the signal region. This ensures that every background is considered in the BDT training with regard to its relative contribution. Both signal and the sum of backgrounds are scaled to a total of 50000 events to give both of them the same importance in the training dataset. To avoid potential biases when applying the trained BDT on the rest of the background processes and signal in the signal extraction, the dataset is split by an unambiguous event number in even and odd events. Two separate sub-BDTs are trained for each discriminant with the BDT trained on the odd half of training events evaluated (test events) and latter being applied on the even number events and vice versa.
For the resonant spin-0 and spin-2 signal scenarios two different BDTs parameterized in the signal resonant mass $m_{gen,\mathrm{HH}}^{spinCase}$ are trained. For this, the background events are added multiple times in the training dataset, for each signal mass used. To aid the BDT especially for low $m_{gen,\mathrm{HH}}^{spinCase}$ with low signal acceptance, the BDT inputs are decorrelated from the signal input mass $m_{gen,\mathrm{HH}}^{spinCase}$. This is done by fitting the mass dependence of the mean $\bar{\mu}_{sig}$ of any appropriate non-integer BDT input variable in signal by a higher order polynomial and then dividing the given BDT input variable by the functional value of the polynomial for all events of the given mass. This essentially shifts the $m_{gen,\mathrm{HH}}^{spinCase}$ dependence of the signal events in a given variable into a $m_{gen,\mathrm{HH}}^{spinCase}$ depen-

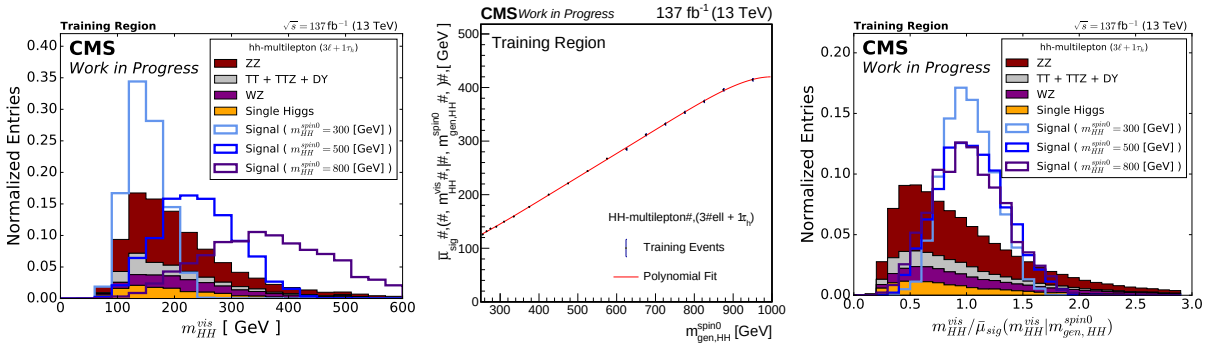

Figure 6.11: The visible Di-Higgs boson mass $m_{\mathrm{HH}}^{vis} = m(3\ell + 1\tau_{\mathrm{h}})$ in the $3\ell + 1\tau_{\mathrm{h}}$ channel (**left**) is decorrelated from the signal dependence on the generator Di-Higgs mass $m_{gen,\mathrm{HH}}$ (**right**) by fitting the mean $\bar{\mu}_{sig}$ of m_{HH}^{vis} in signal in dependence of the generator mass $m_{gen,\mathrm{HH}}$ (**center**) and dividing m_{HH}^{vis} by the functional value of this fit at the given $m_{gen,\mathrm{HH}}$ for all training events including background. The training events use a relaxed version of the $3\ell + 1\tau_{\mathrm{h}}$ signal region selection in Tab. 6.13 with the working point on the DeepTau discriminant against jets relaxed to WP-VVVLoose and only Loose ID requirements on the lepton. The same procedure is used for all non integer input variables of the resonant BDT training in all channels.

dence of the background, overlaying and thus maximizing the use of signal statistics as much as possible. To illustrate this, Fig. 6.11 shows one of the BDT inputs in the $3\ell + 1\tau_{\mathrm{h}}$ before and after the decorrelation as well as the corresponding polynomial fit of the variable mean for signal. For the analysis of non-resonant Di-Higgs boson production a similar approach is used. Here a single parameterized BDT (nonRes BDT) is trained on a set of 12 different EFT benchmark points and the SM with a "one-hot" encoded variable *nodeX* used as parametrization for the 13 different input scenarios. This means, that the EFT scenario is given by a 13 dimensional vector of 12 zeros and one one, with the one representing the active scenario. The signal samples are obtained by reweighting the LO non-resonant signal events according to the procedure described together with the EFT scenarios in Sec. 6.2.4. Similar to the resonant case, the background events are added multiple times to the training dataset for each of the 13 variants of the "one-hot" encoded variable for the physics scenario.
The optimization of each of the three BDTs is guided by the following algorithm:

- A set of physics inspired high level event variables as well as promising low level variables is chosen as the possible set of BDT input variables for each subchannel.
- Pairs of BDT input variables with a correlation higher than 0.8 on the whole dataset (signal + background) are trimmed, only keeping one of the variables .
- The BDT is trained iteratively, determining the importance of each input variable on the BDT input as described in Sec. 4.1. The lowest scoring variables are removed. This is repeated until the observed performance of the BDT measured by the integral of an Receiver-Operator-Curve (ROC) drops visibly compared to the previous iteration, finding the minimal viable set of BDT input variables. This reduction in input variables is performed to reduce the chance of overtraining and corresponding biases on the limited training dataset.
- The hyperparameters of the three BDTs constructed with `XGBOOST` as described in Sec. 4.1 are optimized using a particle swarm optimization (PSO) as described in Sec. 4.2. As this optimization balances the BDT performance against overtraining quantified by the

difference in the BDT performance on test and training events, a random event splitting instead of the even/odd event number splitting for the final BDT training is used. This is done to not choose hyperparameters that contain but simply hide a relevant amount of overtraining in the final BDT training.

Depending on the channel, the optimization procedure might slightly differ from the described approach, e.g. in cases where the chosen variables in the resonant spin-0 scenario yield a similar result in the resonant spin-2 BDT training as the spin-2 BDT variables chosen by the described algorithm, the variable choice might be simplified by using the spin-0 variables for both the spin-0 and the spin-2 training. Additionally, input variables and hyperparameters are also tweaked by hand on a case by case basis to ensure the stability and degree of optimization.

6.6.1 Optimization of the $3\ell + 1\tau_h$ Channel

The dominant signal in the $3\ell + 1\tau_h$ channel is given by $\mathrm{HH} \to \mathrm{WW}\tau\tau$ events with a sizeable contribution of $\mathrm{HH} \to \mathrm{WWWW}$ events. To separate these from the two main backgrounds ZZ production and fake background events (mostly from WZ production), a number of physics inspired variables are studied as discussed in the following.
Depending on the Di-Higgs mass m_{HH} and the boost of the HH system both in the resonant as well as the non-resonant case, the decay products of both Higgs bosons are collimated and the remnants of the two Higgs boson decays fly into opposite regions of the detector. This distinguishes the HH signal uniquely from Fake background events, as the direction of the fake lepton or τ_h is arbitrary to the rest of the event. Sadly, the event kinematics of ZZ events are quite similar to HH events with the collimated decay products of two Z bosons flying in opposite directions of the detector, with three small differences. One difference between the HH signal and ZZ events is of course given by the different mass of H and Z boson. Secondly, the Z boson decay products show a flavor connection as a Z boson can only decay in a pair of same flavored particles yielding for $\mathrm{Z} \to \ell\ell$ decays always to a pair of muons or electrons while an $\mathrm{H} \to \mathrm{WW} \to \ell\ell\nu\nu$ decay can also yield and electron + muon pair. Thirdly, the Higgs boson mass of about 125 GeV yields an on-shell W boson of about 80 GeV and an off-shell boson of about 40 GeV. This subsequently yields one higher and one lower energetic W boson decay product, while on the other hand, for an $\mathrm{Z} \to \ell\ell$ decay, there is no inherent energetic difference between the two produced leptons.
The main BDT input variables used in this channel are given by a kinematic pairing inspired by the above event information, labeled in the following as "smart pairing":

- The two Higgs bosons are each identified with an oppositely charged pair of leptons and a lepton and the τ_h
- These pairings are chosen such that the invariant mass of none of the pairs exceeds that of the Higgs boson at 125 GeV
- In case both or none of the possible pairings passes the Higgs boson mass criterion, both the leading lepton as well as the τ_h are paired with one of the subleading leptons

Decay	m_{HH}^{gen} cut	smart pairing	min($\Delta R(\ell\ell)$ pairing)	min($\Delta R(\ell\tau_{\mathrm{h}})$) pairing
$\mathrm{HH} \to \mathrm{WW}\tau\tau$	-	81.5%	88.3%	79.1%
	< 350 GeV	59.5%	69.4%	42.5%
	> 350 GeV	84.9%	91.2%	84.7%
$\mathrm{HH} \to \mathrm{WWWW}$	-	90.7%	94.8%	98.1%
	< 350 GeV	60.4%	70.8%	87.4%
	> 350 GeV	94.2%	97.6%	99.3%
$\mathrm{HH} \to \tau\tau\tau\tau$	-	77.9%	81.0%	77.6%
	< 350 GeV	51.8%	41.0%	38.8%
	> 350 GeV	82.1%	87.5%	83.8%

Table 6.16: Efficiency of the smart pair method to find the correct pairing of Higgs boson decay products compared to a pair finding based on minimizing the opening angle of the $\ell\ell$ (min($\Delta R(\ell\ell)$) or the $\ell\tau_{\mathrm{h}}$ (min($\Delta R(\ell\tau_{\mathrm{h}})$) pair. The efficiencies are given for the inclusive m_{HH} distribution and for events below or above a Di-Higgs mass of 350 GeV. All pairings yield similar pairing efficiencies with slightly higher values for the min($\Delta R(\ell\ell)$ pairing.

- If the leading lepton and the τ_{h} have the same charge, two possible pairings remain and the pair that maximizes the sum of the pairs p_{T}s, ${p_{\mathrm{T}}}^{pairs} = {p_{\mathrm{T}}}^{\ell\ell} + {p_{\mathrm{T}}}^{\ell\tau_{\mathrm{h}}}$ is chosen.

Here the pairing of leading lepton and subleading lepton is motivated by the on- and off-shell W bosons in the $\mathrm{H} \to \mathrm{WW}$ decay. Similarly a $\mathrm{H} \to \tau\tau \to \ell\tau_{\mathrm{h}}\nu$ decay motivates the pairing of the τ_{h} with a low p_{T} lepton, as the leptonically decaying τ produces an additional neutrino.
Similar arguments can be made for the $\mathrm{HH} \to \mathrm{WWWW}$ decay mode. This method identifies the correct pairing in about 82%/91%/78% of the cases in the $\mathrm{HH} \to \mathrm{WW}\tau\tau$ / $\mathrm{HH} \to \mathrm{WWWW}$ and $\mathrm{HH} \to \tau\tau\tau\tau$ decay modes.
Other pairing methods can be used as well, e.g. choosing the pairing where the opening angle of the lepton pair $\Delta R_{\ell\ell}$ or the opening angle of the lepton/τ_{h} pair $\Delta R_{\ell\tau_{\mathrm{h}}}$ is minimized. While the smart-pairing only yields comparable results to these pairing methods (see Tab. 6.16), the smart pairing does not use any angular or mass information. This has the big advantage of avoiding background sculpting, where the pair selection biases the background to look signal like. An example of this would be, that when the pairing that minimizes $\Delta R_{\ell\ell}$ is selected, both signal and background will tend to lower $\Delta R_{\ell\ell}$. A $\Delta R_{\ell\ell}$ neutral pairing on the other hand yields a distribution that is more flat in background, separating it better from the signal peaking at low $\Delta R_{\ell\ell}$.

The opening angles $\Delta R_{\ell\ell}^{smart}$ and $\Delta R_{\ell\tau_{\mathrm{h}}}^{smart}$ as well as the invariant masses $m_{\ell\ell}^{smart}$ and $m_{\ell\tau_{\mathrm{h}}}^{smart}$ in Fig. 6.12 show good separation and are included in all the BDT trainings. Other pair related variables such as the opening angels $\Delta\phi$ and $\Delta\eta$, the pairs total p_{T} as well as the p_{T} difference of the pair constituents were studied as well, but did not rank highly enough to be included in the BDTs.

As the main backgrounds in the $3\ell + 1\tau_{\mathrm{h}}$ channel are ZZ and WZ (+fake) production, several variables targeting Z bosons where studied. The probably strongest variable in the $3\ell + 1\tau_{\mathrm{h}}$ channel would be the number of SFOS lepton pairs, as it enables the near complete suppression of any Z boson related background. However, as also 2/3 of the signal contain at least one SFOS lepton pair, using this variable directly does not yield the best results. Instead, it is used in combination with another variable, the SFOS Di-Lepton mass closest to the Z-boson mass. While the Z boson veto greatly reduces background events with $\mathrm{Z} \to \ell\ell$ decays, the chosen mass window of 10 GeV around the Z boson mass is intentionally small, allowing for further optimization on the

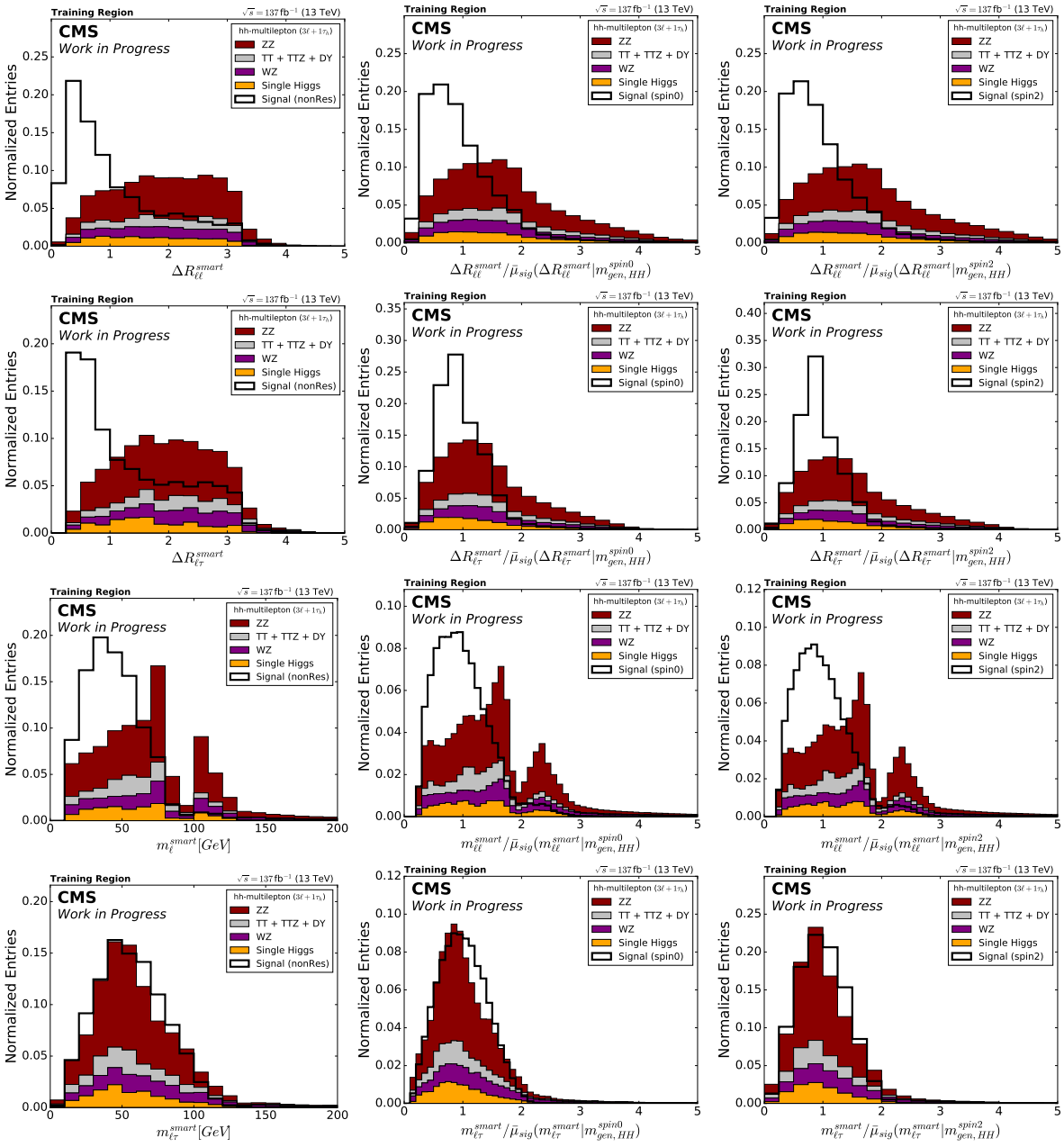

Figure 6.12: From top to bottom, the distributions of $\Delta R_{\ell\ell}^{smart}$, $\Delta R_{\ell\tau_h}^{smart}$, $m_{\ell\ell}^{smart}$ and $m_{\ell\tau_h}^{smart}$ as used in the $3\ell + 1\tau_h$ BDT training. The shown simulated events, correspond to a relaxed lepton and τ_h selection with Loose ID leptons and DeepTau vs. jets WP-VVVLoose τ_h. Contrary to other parts of this thesis, the shown simulated events also contain fake background events with wrongly identified leptons and τ_h. From left to right, the input distributions for the non-resonant, spin-0 and spin-2 BDT are shown. For the resonant spin-0 and spin-2 BDTs, the shown input distribution was decorrelated from the signal Di-Higgs mass dependence.

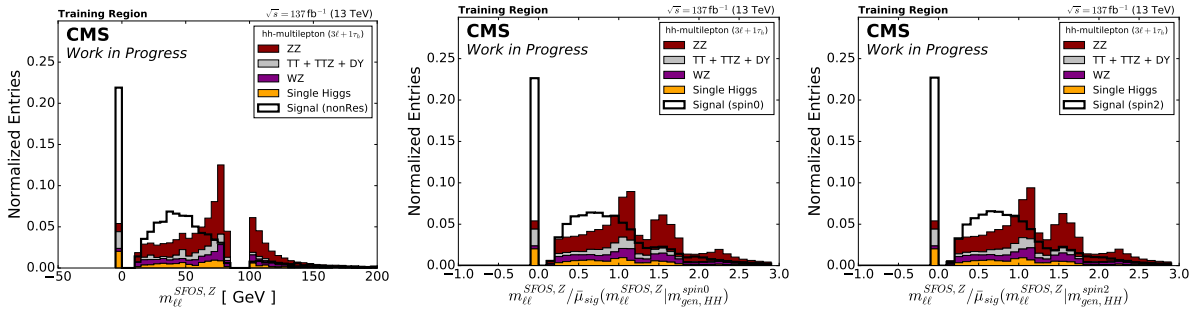

Figure 6.13: The distribution of $m_{\ell\ell}^{SFOS,Z}$, defined as the same-flavor opposite-sign Di-Lepton mass closest to m_Z in case an SFOS Di-Lepton pair exists and -1 otherwise. The shown simulated events correspond to a relaxed lepton and τ_h selection with Loose ID leptons and DeepTau vs. jets WP-VVVLoose τ_h as used in the BDT training. Contrary to other parts of this thesis, the shown simulated events also contain fake background events with wrongly identified leptons and τ_h. From left to right, the input distributions for the non-resonant, spin-0 and spin-2 BDT are shown. For the resonant spin-0 and spin-2 BDTs the shown input distribution was decorrelated from the signal Di-Higgs mass dependence.

$m_{\ell\ell}$ spectrum by the BDT. By defining $m_{\ell\ell}^{SFOS,Z}$ as the same flavor opposite sign Di-Lepton mass closes to m_Z in case an SFOS Di-Lepton pair exists and setting it to -1 otherwise, a variable is designed combining the remaining exclusion power of the Di-Lepton-mass spectrum and n_{SFOS}. Fig. 6.13 shows $m_{\ell\ell}^{SFOS,Z}$ as used in all three BDTs for the training dataset with an accumulation of signal at low masses and for n_{SFOS}=0.

Other Z boson related variables that were studied but not used are the transverse mass (Eq. 7.7) of E_T^{miss}, and an lepton/τ_h pair $m_T(E_T^{miss}, \ell\tau_h)$ aimed at $Z \to \tau\tau \to \ell\tau_h$ decays as well as the single Z boson mass of a kinematic fit[7] for a ZZ scenario.

The Di-Higgs mass spectrum is the driving kinematic quantity between any HH signal scenario and drives the differences between the different resonant masses and EFT scenarios. Therefore variables highly correlated to m_{HH} offer not only potential for signal to background separation but also information about the BDTs parameter dependence. In the τ_h dominated $0\ell+4\tau_h$, $1\ell+3\tau_h$ and $2\ell+2\tau_h$ channels a kinematic fit using `SVFit` [143] is used for the reconstruction of m_{HH}. This was tested for the $3\ell+1\tau_h$ channel as well, however as `SVFit` is heavily tailored on decays involving τ, the simpler visible HH mass m_{HH}^{vis} defined as the invariant mass of the three leptons and the τ_h providing similar results is used instead. The visible Di-Higgs mass is used in all three BDT trainings and can be seen in Fig. 6.14 for the training dataset. Other variables based on the HH system that were studied but not included contain the Di-Higgs boson p_T itself, and several projections of the Di-Higgs boson p_T e.g. parallel and orthogonal to the hadronic component of E_T^{miss} calculated by adding the p_x and p_y components of the $3\ell+1\tau_h$ system to the E_T^{miss}.

Another significant property of the signal is the high number of expected neutrinos compared to background as every W boson decay contains one, and every leptonic τ decay contains two neutrinos. This leads to an increased amount of E_T^{miss} for signal, making E_T^{miss}LD another promising BDT input variable as can be seen in Fig. 6.15. Also the WZ (+fake) background contains genuine E_T^{miss}, Therefore, variables such as the transverse mass between E_T^{miss} and one of the leptons, aiming at the reconstruction of the W boson decay and the opening angle $\Delta\phi(E_T^{miss}, \ell)$ between

[7] `SVFIT` [143]

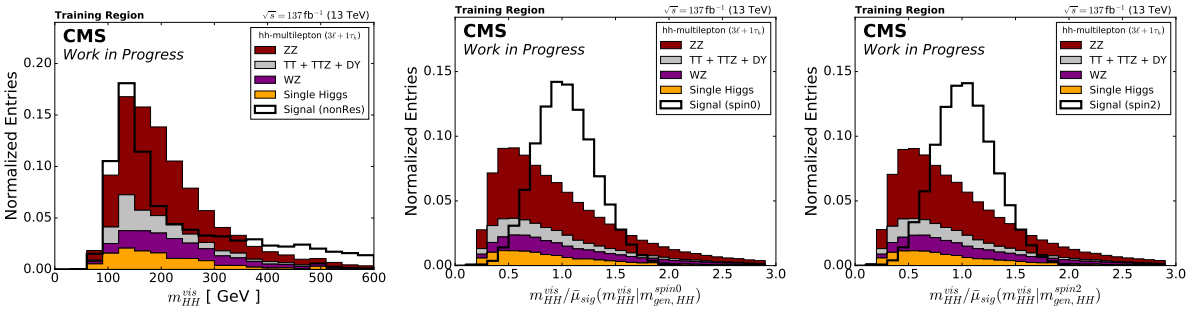

Figure 6.14: The distribution of the visible Di-Higgs mass m_{HH}^{vis}, defined as the invariant mass of the three leptons and the τ_{h}. The shown simulated events correspond to a relaxed lepton and τ_{h} selection with Loose ID leptons and DeepTau vs. jets WP-VVVLoose τ_{h} as used in the BDT training. Contrary to other parts of this thesis, the shown simulated events also contain fake background events with wrongly identified leptons and τ_{h}. From left to right, the input distributions for the non-resonant, spin-0 and spin-2 BDT are shown. For the resonant spin-0 and spin-2 BDTs the shown input distribution was decorrelated from the signal Di-Higgs mass dependence.

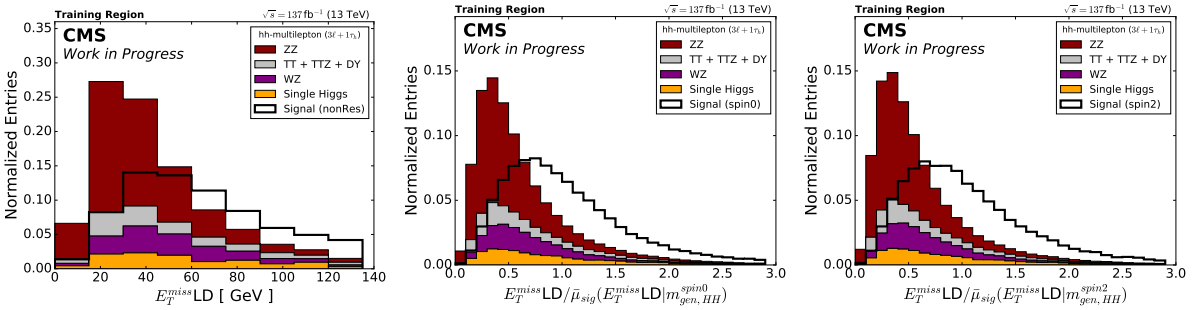

Figure 6.15: The distribution of E_T^{miss}LD as used in the $3\ell+1\tau_{\mathrm{h}}$ BDT training. The shown simulated events correspond to a relaxed lepton and τ_{h} selection with Loose ID leptons and DeepTau vs. jets WP-VVVLoose τ_{h}. Contrary to other parts of this thesis, the shown simulated events also contain fake background events with wrongly identified leptons and τ_{h}. From left to right, the input distributions for the non-resonant, spin-0 and spin-2 BDT are shown. For the resonant spin-0 and spin-2 BDTs the shown input distribution was decorrelated from the signal Di-Higgs mass dependence.

E_T^{miss} and lepton were tested. While yielding some separation power, they did not score high enough to be included in the final variable selection. The final variable used as BDT input in the nonRes BDT training is HT, tracking the general energy content or activity of an event. Non-resonant HH production in general shows a broader distribution than resonant production and a tail towards high m_{HH}, offering some signal to background separation at high HT as shown in Fig. 6.16. Other low level event variables such as single lepton/τ_{h} $p_{\mathrm{T}}/\eta/\phi$, the transverse mass of lepton/τ_{h} with E_T^{miss}, the number of electrons/muon/jets and the maximum impact parameter of the leptons were studied as well. With the latter being aimed at the identification of a lepton from a leptonic τ decay. None of these improved the BDT performance further. Overall the optimization of BDT input variables yielded 7 variables for both the resonant spin-0 and resonant spin-2 BDT training and 8 variables for the nonRes BDT training as summarized in Tab. 6.17. Control plots for the BDT training variables are shown in Sec. 7.3. Signal region distributions of all 8 variables are shown in the Appendix **D**. The BDT hyperparameters (Sec. 4.1) used in the three $3\ell+1\tau_{\mathrm{h}}$ BDT trainings are listed in Tab. 6.18. To account for the relatively low amount of available simulated signal, the depth and number of the used trees is kept relatively low. Despite this, the three BDTs are able to achieve a good performance as can be seen in Fig. 6.17 showing Receiver Operating Characteristic (ROC) for the BDT output as evaluated on the train-

BDT Input Features:

Variable	nonRes BDT	spin-0 BDT	spin-2 BDT	Description
$\Delta R_{\ell\ell}^{smart}$	✓	✓	✓	Opening angle $\Delta R = \sqrt{\Delta\eta^2 + \Delta\phi^2}$ of the smart paired Di-Lepton pair
$\Delta R_{\ell\tau_h}^{smart}$	✓	✓	✓	Opening angle $\Delta R = \sqrt{\Delta\eta^2 + \Delta\phi^2}$ of the smart paired Lepton/τ_h pair
$\Delta m_{\ell\ell}^{smart}$	✓	✓	✓	Invariant mass of the smart paired Di-Lepton pair
$\Delta m_{\ell\tau_h}^{smart}$	✓	✓	✓	Invariant mass of the smart paired Lepton/τ_h pair
$m_{\ell\ell}^{SFOS,Z}$	✓	✓	✓	Invariant Di-lepton mass of the SFOS pair closest to m_Z Set to -1 for NSFOS=0
m_{HH}^{vis}	✓	✓	✓	Visible Di-Higgs mass, invariant mass of the three leptons and the τ_h
E_T^{miss}LD	✓	✓	✓	Missing transverse energy $= 0.6 \times E_T^{miss} + 0.4 \times H_T^{miss}$
HT	✓	X	X	Event activity, the scalar p_T sum of all (Fakable) leptons/τ_h and jets in the event

BDT parametrization:

Variable	nonRes BDT	spin-0 BDT	spin-2 BDT	Description
$m_{gen,HH}^{spinCase}$	X	✓	✓	Generator level m_{HH} of resonant signal, used for BDT parametrization, set to each of the signal masses for every background event
$nodeX$	✓	X	X	Set of 13 BDT input variables used as 'one-hot' encoding for the EFT scenario of the non-resonant signal used as BDT parametrization Background is added for each signal configuration of $nodeX$

Table 6.17: Summary and description of the BDT input features and parametrization variables used in the $3\ell + 1\tau_h$ BDT training.

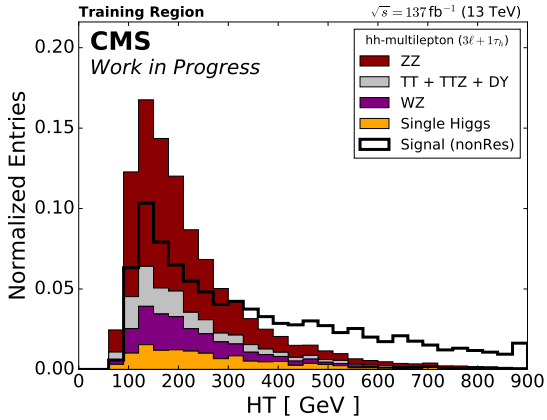

Figure 6.16: The distribution of HT as used in the $3\ell + 1\tau_h$ BDT training. The shown simulated events correspond to a relaxed lepton and τ_h selection with Loose ID leptons and DeepTau vs. jets WP-VVVLoose τ_h. Contrary to other parts of this thesis, the shown simulated events also contain fake background events with wrongly identified leptons and τ_h. From left to right, the input distributions for the non-resonant, spin-0 and spin-2 BDT are shown. For the resonant spin-0 and spin-2 BDTs the shown input distribution was decorrelated from the signal Di-Higgs mass dependence.

`XGBoost` Hyperparameter	nonRes BDT	spin-0 BDT	spin-2 BDT
n_estimators	115	129	71
subsample	0.8032	0.8269	0.8370
colsample_bytree	0.6841	1.0	0.8887
gamma	0.0	0.2957	3.8066
learning_rate	0.1642	0.4998	0.2911
max_depth	2	2	3
min_child_weight	205.97	474.38	405.65

Table 6.18: `XGBoost` Hyperparameters used in the $3\ell + 1\tau_h$ nonRes, spin-0 and spin-2 BDT trainings.

ing dataset. The same figure also shows ROC performances for different subsets of the training dataset, showing the higher performance of high mass scenarios in the resonant BDT trainings. This is expected as kinematic distributions such as the opening angles of the lepton and lepton/τ_h pairs show a clearer distinction for higher mass scenarios. The same effect can be seen partly in the non-resonant training as well, where EFT scenarios, such as BM7 with a softer distribution in m_{HH}, present a more challenging phase space for the BDT. In general, the performance of the resonant training is distinctly better than the nonRes BDT training as non-resonant HH production in general leads to a broad distribution in m_{HH} resulting in a wide range of different signal kinematics, more challenging to grasp. As can be seen by the ROC curves, the chosen hyperparameters are able to keep the amount of overtraining at an acceptable level. BDT outputs for example resonant mass and EFT scenarios are shown in Fig. 6.18, showing good agreement of training and validation events.

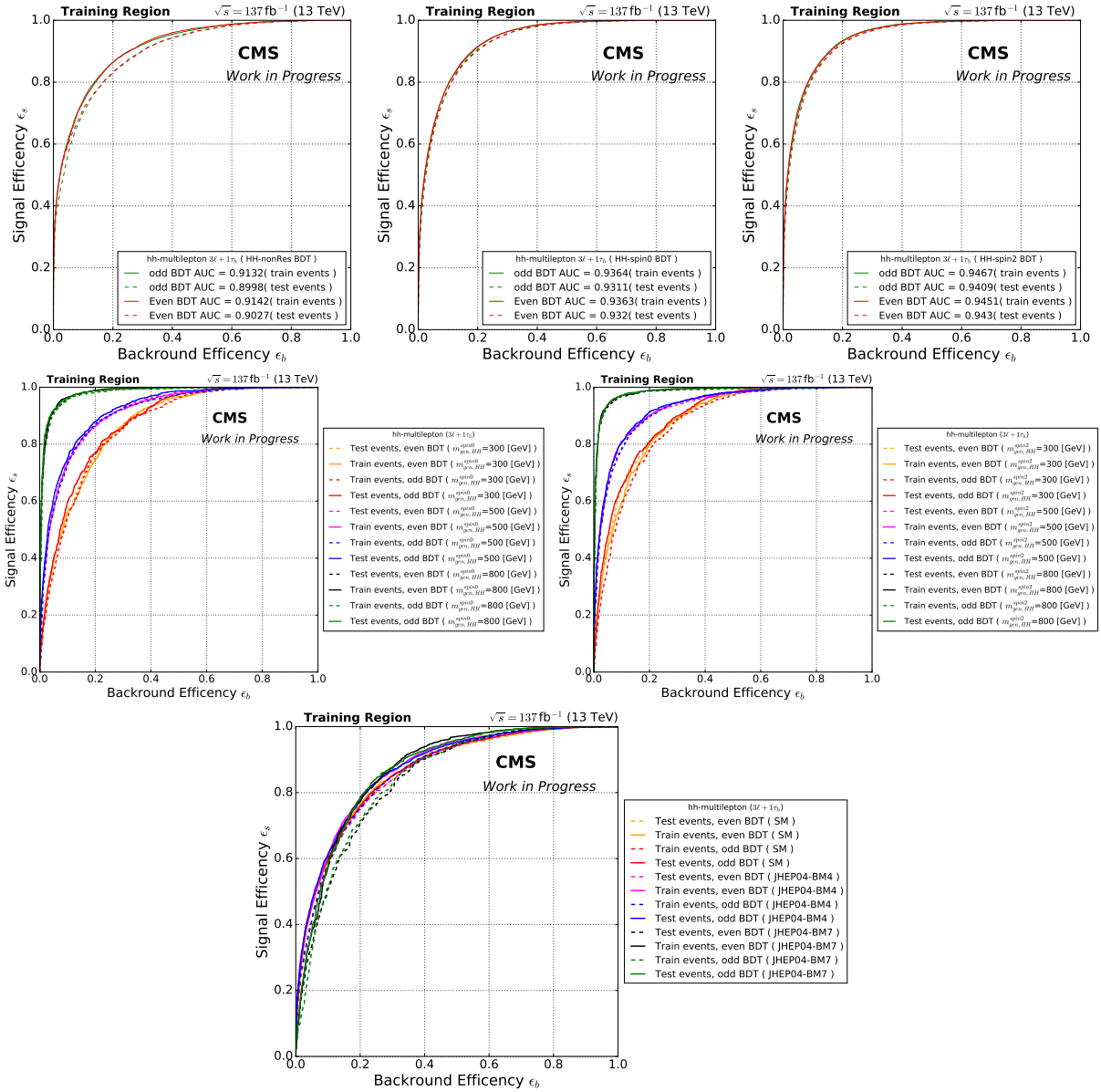

Figure 6.17: ROC curves for the $3\ell + 1\tau_h$ BDT training (top row). From left to right, they show the separation potential of the trained non-resonant, spin-0 and spin-2 BDTs on the BDT training dataset. Per BDT, two sub-BDTs are trained on the even and odd numbered halves of the training set and are applied (tested) on the corresponding other half. The lower two rows show ROC curves corresponding to exemplary mass points (middle row) and EFT scenarios (bottom row). The chosen EFT scenarios correspond to the SM, EFT BM7 with a soft m_{HH} spectrum and EFT BM4 covering similar kinematics as in a scenario of maximum interference between the triangle and box ggHH Feynman diagrams. For the resonant BDTs, the example mass points were chosen to cover the whole m_{HH} phase space. The amount of visible overtraining was found to be acceptable.

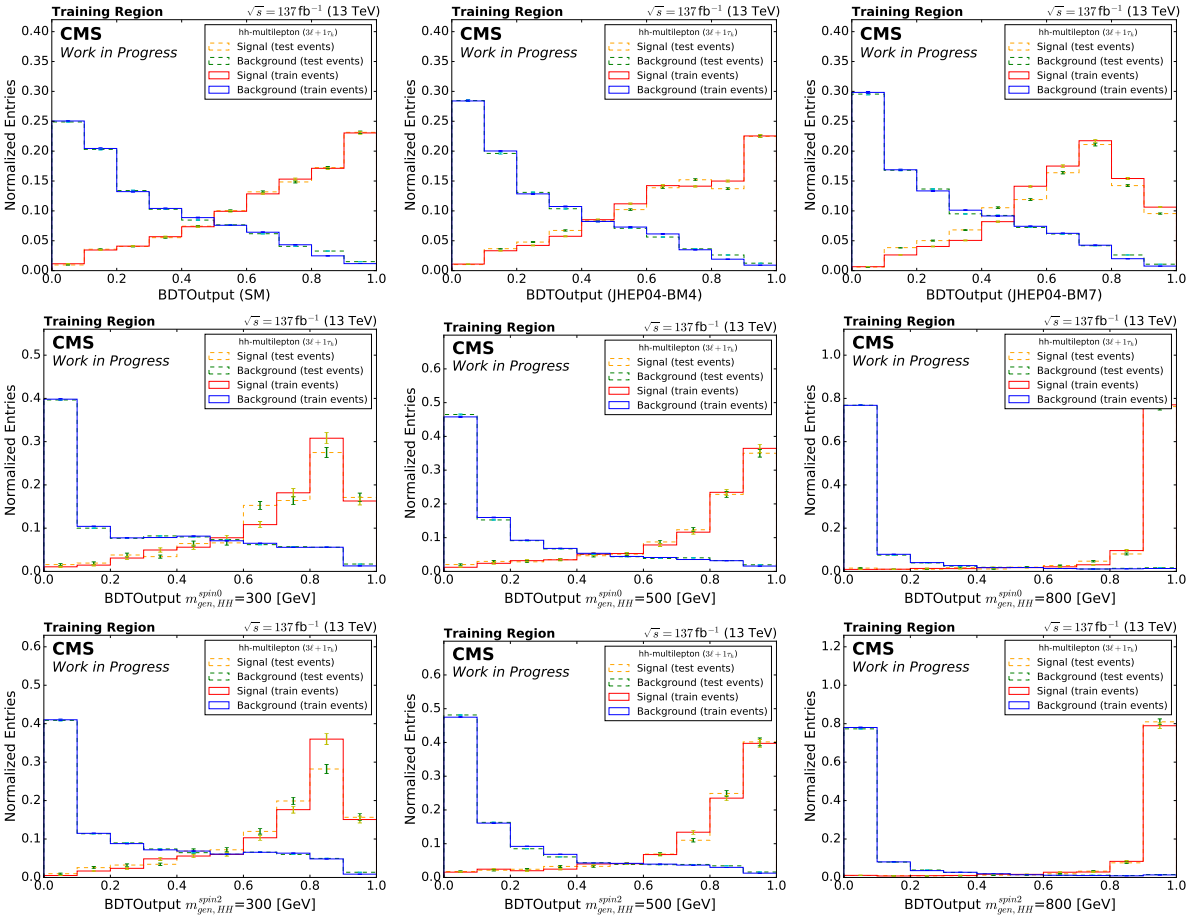

Figure 6.18: From top to bottom example BDT outputs on the BDT training dataset per BDT. Two sub-BDTs are trained on the even and odd numbered halves of the training set and are applied (tested) on the corresponding other half for the nonRes, spin-0 and spin-2 BDTs. The chosen EFT scenarios correspond to the SM, EFT BM7 with a soft m_{HH} spectrum and EFT BM4 covering similar kinematics as in a scenario of maximum interference between the triangle and box ggHH Feynman diagrams. For the resonant BDTs, the example mass points were chosen to cover the whole m_{HH} phase space. The amount of visible overtraining was found to be acceptable.

7

Results and Interpretation of the HH analysis

As discussed in Sec. 2.3 and Sec. 2.4 a diverse set of physics scenarios is tested in the presented analysis. For this thesis the following results are obtained:

- Limits on both the signal strength modifier r and the cross section of non-resonant SM like HH production
- Limit and likelihood scans in both the SM parameters κ_λ, κ_t, and c_{2V} as well as the EFT coupling parameter c_2, placing 1D as well as 2D limits on the coupling parameters
- Cross section limits on non-resonant ggHH production for the EFT benchmark scenarios in [28], [20], and [134]
- Cross section limits on both spin-0 and spin-2 resonant ggHH production.

For the results presented in Sec. 7.4 a binned maximum likelihood fit (Sec. 7.2) is performed on the BDT outputs described in the previous chapter as well as two control region distibrutions, described together with other background checks in Sec. 7.3. In this context a physics model used for scans of the various HH coupling parameters was developed and its implementation is discussed in Sec. 7.2.1. The fit includes several nuisance parameters representing systematic uncertainties described in Sec. 7.1. The final parts of this chapter discuss other ongoing HH searches in Sec. 7.5 as well as their combination with the HH $\rightarrow$ Multilepton analysis in Sec. 7.5.1. An outlook to possible future developments in HH is found in Sec. 7.6

7.1 Systematic Uncertainties

While the overall modelling of background processes works very well as can bee seen in Sec. 7.3, several experimental and theoretical effects contribute as sources of uncertainty, both on the yield as well as the kinematic properties of the considered background and signal processes. Most of the experimental effects correspond to the data to simulation corrections described in Sec. 6.2.3 and uncertainties on the data driven background estimation described in Sec. 6.4. These effects and the corresponding systematic uncertainties are treated as nuisance parameters in the signal extraction described in Sec. 7.2 and will be described further in the following.

Trigger efficiency:

As discussed in Sec. 6.2.3 the efficiency of simulated events to pass the trigger requirements described in Sec. 3.2.7 is not perfectly modelled. To account for this, the applied trigger scale factors are varied within their uncertainties. The resulting uncertainty models both variations in

the BDT/CR shapes as well as the expected event yields. The corresponding uncertainties are treated as uncorrelated among the different data taking years but are treated as correlated among the 2ℓ(ss) + 0/1 τ_h and $2\ell + 2\tau_h$ channels and among the $3\ell + 0\tau_h$, $3\ell + 1\tau_h$ and 4ℓ channels.

Uncertainties on the electrons, muons and τ_h reconstruction:

The uncertainty on the electron, muon and τ_h identification and isolation criteria have been measured separately in Z boson enriched regions for the Loose, Fakable and Tight ID leptons. These uncertainties are given as a function of p_T, $|\eta|$ and τ_h decay mode and thus describe both variations in the expected event yield as well as the BDT and CR shapes.

The τ_h energy scale described in Sec. 6.2.3 has an uncertainty of about 1% depending on the data taking year and the decay mode of the τ_h. As the τ_h energy scale affects both the selection efficiency of τ_h as well as the energy itself, this uncertainty leads to a variation in the expected event yield as well as the expected BDT and CR shapes. The uncertainties on the electron, muons and τ_h reconstruction are treated as correlated among different processes but uncorrelated across different data taking years.

Jet Energy Scale and Resolution:

As discussed in Sec. 6.2.3 jets within CMS undergo a calibration procedure in order to achieve matching JES and JER between simulation and data. Uncertainties on the scale and resolution of reconstructed jets are centrally measured for all CMS analysis using Di-Jet control regions and are common for most CMS analysis as described in [144]. Uncertainties on the JES are evaluated in a set of 11 different components, with 6 component correlated and 5 components uncorrelated among the different data taking years. The uncertainty on the jet JER is treated as uncorrelated among the different data taking years. For the application of the given uncertainties, the energy of reconstructed jets is varied according to the different uncertainty components and the events are reanalyzed resulting in both variations of the expected event yield as well as event kinematics varying the shape of the BDT and CR distributions.

As corrections in JER and JES are propagated to the calculation of E_T^{miss}, the corresponding uncertainties therefore yield an additional uncertainty on E_T^{miss} that is treated as uncorrelated among the different data taking years.

b-tagging rate and mistag rates:

The scale factors, applied for corrections of the b-tagging efficiency described in Sec. 6.2.3 come with three sources of uncertainties connected to impact of the JES uncertainties, the purity and the size of the event sample used for the scale factor extraction. The statistical part of these uncertainties is treated as uncorrelated across the different data taking years with the others treated as correlated among all three years.

Luminosity:

The uncertainties on the luminosity measurement [145–147] affect the overall normalization of the number of expected events. Uncorrelated uncertainties amount to 1%, 2% and 1.5% for the 2016, 2017 and 2018 data taking period respectively. Correlated uncertainties among all years corresponding to 0.6%, 0.9% and 2% and further correlated uncertainties for the data taking in 2017 and 2018 corresponding to 0.6% and 0.2% are applied.

Pileup:

To account for the uncertainty on the inelastic proton-proton interactions and therefore the num-

ber of PU interactions, the amount of PU interactions is varied by 5% and the analysis is repeated for the different conditions, leading to a small uncertainty treated as uncorrelated among the three data taking years.

Prefiring issue in the ECAL trigger

The uncertainty of the scale factors used to correct for the prefire issue described in Sec. 6.2.3 is accounted for and treated as uncorrelated among the two affected data taking years 2016 and 2017.

Uncertainties on the theory cross section:

The theory cross sections used in this analysis to normalize the signal and background processes are only known up to a certain degree. This uncertainty is dominated by the order of Feynman diagrams considered in the calculation, the choice of the scale of QCD interactions, the coupling strength of the strong interaction α_s, uncertainties on the proton PDF and the mass of the top-quark. The uncertainty on the total non-resonant ggHH signal production is discussed in Sec. 2.3. For SM non-resonant qqHH production, the total cross section amounts to $1.726^{+0.03}_{-0.04}(\text{QCD scale}) \pm 2.1\%(\alpha_s + \text{PDF})\,\text{fb}$ [148]. The uncertainties on the total signal cross section are applied when deriving limits on the signal strength modifier r (see. Sec. 7.2) and frozen when deriving limits on the signal cross section itself as described in Sec. 7.2. The uncertainties on the background cross section are treated in the following manner:

- Uncertainties arising from the uncertainty on the proton PDFs are correlated among processes with the same initial state, that means for example that the PDF uncertainty for $\mathrm{t\bar{t}}$ production is correlated with gluon induced ZZ production (ggZZ), but decorrelated from quark induced ZZ production (qqZZ). Processes involving Higgs boson production are decorrelated from other background processes.

- Uncertainties arising from the choice of the QCD scale are treated as correlated among processes with similar final states, for example, for all processes involving Di-Boson production.

- Uncertainties arising from α_s are correlated among all processes involving Higgs boson production and among all other processes.

This scheme corresponds to the recommendations used for all CMS HH analyses [149].

For both signal HH and single Higgs boson production, theoretical uncertainties on the Higgs boson branching fractions are placed, with an uncertainty of 1.65%, 1.54% and 1.54% for Higgs boson decays into $\tau\tau$, ZZ and WW respectively [14].

On top of normalization uncertainties corresponding to the QCD scale, α_s PDF and m_{t}, the uncertainty on the effect of missing higher orders in calculation is estimated by varying the renormalization (μ_R) and factorization scales (μ_F) between 0.5 and 2 times their nominal values under the constraint $0.5 \geq \mu_F/\mu_R < 2$ and taking the result as an uncertainty on the shape of the BDT output and CR distributions.

For the qqHH signal an additional uncertainty is applied on a model choice in the parton showering, corresponding to the application of the dipole recoil scheme in PYTHIA. As some of the background processes only contribute with very few events in most of the channels the contributions of triple-boson production, $\mathrm{W\gamma}$, $\mathrm{Z\gamma}$, $\mathrm{t\gamma}$, $\mathrm{t\bar{t}\gamma}$, tZq, qW, $\mathrm{t\bar{t}t\bar{t}}$, tttW, $\mathrm{t\bar{t}WZ}$ and $\mathrm{t\bar{t}ZZ}$ are

treated as a single combined background (Other) in the signal extraction and instead of assigning individual cross section uncertainties, a conservatively chosen 50% normalization uncertainty is assigned. Similarly the uncertainty on the normalization of conversion background is chosen to be 50% as well.

Uncertainty on the data-driven background estimation:

For the uncertainty on the data driven fake-background estimation, uncertainties on the measurement of the fake-rate (misidentification rate) f (see. Sec. 6.4) are propagated as an uncertainty on both the expected yield as well as the BDT and CR region shapes of the fake lepton background. As discussed in Sec. 6.4 a closure test is performed to check the validity of the fake background estimation by applying the method on simulated instead of data events. The closure of simulated events in the signal region with the prediction from simulated events in the AR is used as a shape and normalization uncertainty for the 2ℓ(ss) + 0/1 τ_h and $3\ell + 0\tau_h$ channels as well as the WZ and ZZ control regions. For the other lower statistics channels, this uncertainty is deemed negligible as it is expected to be much smaller than the statistical uncertainty on the fake background estimation. On top of this an additional normalization uncertainty is placed on the data driven background corresponding to a 20% uncertainty correlated among all data taking years and channels and a 20% uncertainty treated as uncorrelated among the different data taking years and channels. As the $1\ell + 3\tau_h$ and $3\ell + 1\tau_h$ channel use a slightly different τ_h ID than that used in measuring the fake factors, an additional 30% uncertainty is placed on the fake background in these channels.

For the charge flip background in the 2ℓ(ss) + 0/1 τ_h channel, a normalization uncertainty of 30% correlated among all data taking years is used.

7.2 Signal Extraction

For the signal extraction, the BDT output distributions in all seven Multilepton channels as well as two control region distributions for the prompt WZ and ZZ background (Sec. 7.3) are evaluated in a binned maximum likelihood fit, measuring the signal strength of the given signal scenario defined as $r = \frac{\sigma_{\mathrm{HH}}^{\mathbf{fit}}}{\sigma_{\mathrm{HH}}^{\mathrm{theo}}}$ with a profile likelihood test statistic [150]. The likelihood quantifying the probability finding the given data given the background (+ signal) model with and without the contribution of signal, is defined in terms of nuisance parameters θ, representing the different systematic uncertainties discussed in Sec. 7.1 in the modified frequentist approach [151]. Additional nuisance parameters taking into account statistical uncertainties on the prediction of signal and background approaches (MCStat) are taken into account using the approach described in [152].

The significance of the found best fit signal strength $\hat{r}$ is then given by the ratio of the likelihoods for a fit with freely floating r, resulting in the best fit signal strength $\hat{r}$ and a set of corresponding nuisance parameters $\hat{\theta}$ and a fit for the background only hypothesis with fixed $r = 0$ with

resulting nuisance parameters $\hat{\theta}_0$

$$-2\ln\left(\frac{\mathscr{L}(\text{data}|r=0,\hat{\theta}_0)}{\mathscr{L}(\text{data}|r=\hat{r},\hat{\theta}_0)}\right) \tag{7.1}$$

This definition is then used to place upper limits on r using the an asymptotic approximation [150] of the CL method [153, 154] defining a 95% confidence interval for r, excluding higher values with a 95% probability. As the amount of observed data is a statistical observable, in addition to the observed limits obtained as described above, expected limits are calculated as well using an Asimov dataset [150] based on the signal and background model. The expected significance/limit is given by the average over many toy datasets, thus providing a reliable estimator for comparing the sensitivity of different analyses.
The limits provided in this analysis are extracted using the `Higgs Combine` toolkit [155] common among all CMS Higgs analyses.
Limits on r can simply be converted into limits on signal cross section by multiplying the resulting upper limit on the signal strength r with the signal cross section the input signal model is normalized to. To place limits on coupling parameters κ such as on the trilinear Higgs boson self-coupling parameter κ_λ, the upper limit on r is scanned in the given parameter and the limit on κ is then given by the intersection of the limit on r with one, excluding all κ scenarios where values $r(\kappa) < 1$ are excluded. By including the coupling parameters in a physics model as described in Sec. 7.2.1, the coupling dependence can be included in the likelihood as well, allowing for the determination of best fit values and likelihood profiles in the given parameters.

Verifying the statistical model:

To test the validity of the signal + background model and its compatibility with the observed data two tests are performed. Firstly, to check the validity of the systematic model, the postfit values and uncertainties of the different likelihood nuisance parameters and their impact on the best fit $\hat{r}$ are estimated by fitting the nuisance parameter in question simultaneously with the parameter of interest (POI) r. This is both important to find out which uncertainties currently limit the sensitivity of the analysis as well as a sanity check of both the choice of prefit nuisance constraints as well as the fitting behaviour. Fig. 7.1 shows this for the 15 most important non MCStats nuisances. The whole list of (non MCStats) pulls and impacts can be found in the Appendix **E**. Tab. 7.1 summarizes the impact of different nuisance groups. As can be seen the impact of statistical uncertainties from data and the background prediction with 84% and 34% is quite high. This promises better results for the future as with more data and simulation these will automatically get lower. Due to the strong dependence on statistical uncertainties, the obtained results are also found to be relatively robust with respect to small changes in the systematics model or the ordering of fit parameters in the ML fit leading to fluctuations on the observed limits in r in $\mathscr{O}(1-2\%)$.

Secondly, a goodness of fit (gof) test is performed calculating a measure quantifying how well the given signal + background model can describe the data. The gof measure itself is calculated in the saturated model [156] a more generalized version of a $\chi^2 = 2\ln\mathscr{L}$ term. By comparing the gof statistics on data and a set of toy datasets generated for the signal + background model the stability and consistency of the model is tested. Distributions of the gof on data and toy data

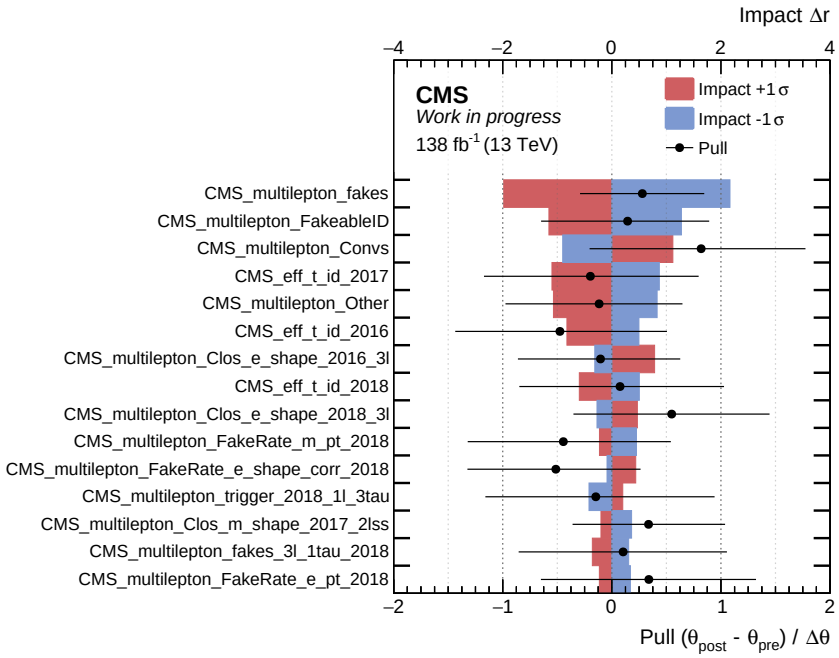

Figure 7.1: Pulls and impacts for the 15 most important nuisance parameters in the combined HH $\rightarrow$ Multilepton signal extraction fit with the JHEP04BM7 tuned nonRes BDT output in all seven Multilepton channels and the kinematic distributions in the WZCR and ZZCR for all three years using SM like non-resonant HH signal. These include uncertainties on the rate of the fake background, conversion background, other background category, uncertainties on the τ_h ID efficiency, the fake rate measurements and the MC closure of the fake background estimation.

Uncertainty group	Contribution to uncertainty on $\hat{r}$
Statistical uncertainty (Data)	84%
Nuisance parameters:	
MCStats	34%
Signal rate	21%
Data driven fake BG	21%
Background rate (Simulated BG)	11%
Other	$< 0.1\%$

Table 7.1: Impact of different uncertainties on the total uncertainty on the best fit signal strength modifier $\hat{r}$. The impact for the nuisance parameters is estimated by comparing the total uncertainty on $\hat{r}$ for a fit to an Asimov dataset with all nuisance parameters $\Delta\hat{r}_{\text{all}}$ with a fit where the corresponding group of nuisances is fixed $\Delta\hat{r}_{\text{w.o group X}}$ by subtracting the two uncertainties in quadrature and dividing by the total uncertainty, $\sqrt{(\Delta\hat{r}_{\text{all}})^2 - (\Delta\hat{r}_{\text{w.o group X}})^2}/\Delta\hat{r}_{\text{all}}$. The impact of the statistical uncertainty on the data in the SR is estimated by dividing the uncertainty obtained when freezing all nuisance parameters by the total uncertainty. The biggest uncertainties are given by the statistical uncertainty on the SR data, statistical uncertainties of the BG prediction, theoretical uncertainties on the signal rate (including single Higgs boson branching fractions), uncertainties on the data driven background estimation and the theoretical uncertainties on the background prediction taken from simulation. Compared to these, all other uncertainties including uncertainties from the lepton and τ_h reconstruction efficiency , pileup, b-tagging, JES and JER, E_T^{miss} and experimental issues like the prefiring issue are negligible and contribute with less than 0.1% of the total uncertainty.

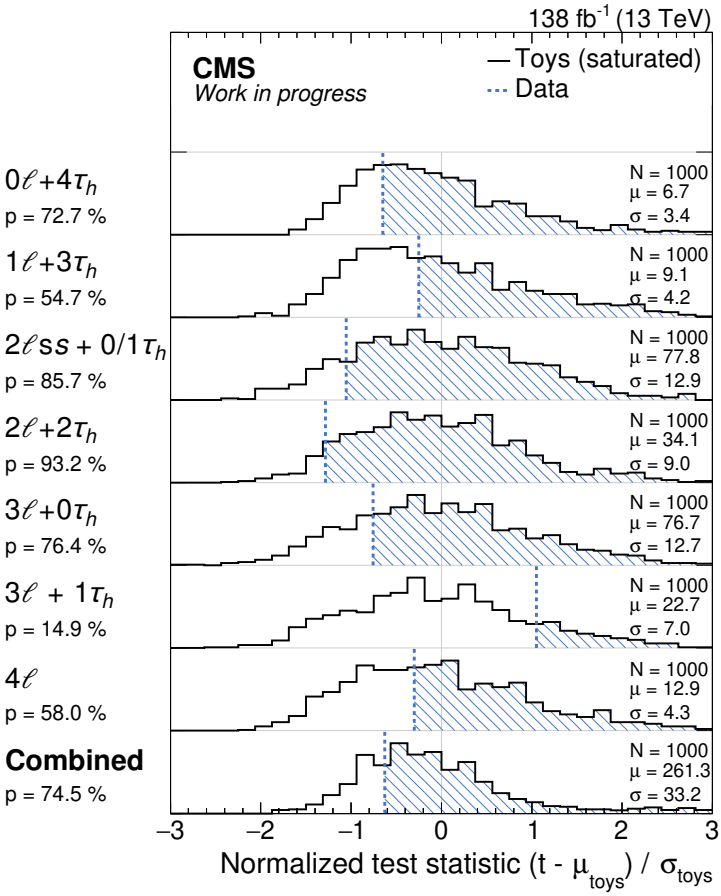

Figure 7.2: Distribution of the gof measure in the saturated model [156] for all seven event channels separately as well as their combination for the signal + background fit on data (dotted line) as well as a set of toy data sets generated from the expected signal and background distributions. The signal extraction corresponds to a fit of SM like signal on the JHEP04BM7 optimized nonRes BDT output. For the combined fit of all channels also the two control region distributions for the WZCR and ZZCR are included in the fit.

for the seven Multilepton channels as well as the combined Multilepton fit is shown in Fig. 7.2.

Choosing the right BDT output node:

The three parameterized BDTs trained in the context of the presented analysis allow for some freedom when choosing the BDT output node for the given signal scenario. The different choices used in the signal extraction are given and motivated in the following.

For the limits on resonant HH production the corresponding spin-0 or spin-2 BDT of the given channel is evaluated for the corresponding mass scenario. Similarly for the cross section limits on the EFT benchmarks in non-resonant HH production with the JHEP04 benchmark points, the nonRes BDT is evaluated for the given scenario. For the JHEP03 benchmarks and the JHEP04BM8a the BDT output is evaluated on the kinematically closest benchmark scenario as discussed in Sec. 6.2.4. For the presented parameter scans performed in κ_λ, κ_λ-κ_t, c_2, κ_λ-c_2 and κ_t-c_2 the choice of the BDT output is less obvious. As discussed in Sec. 6.2.4 scenarios with high κ_λ correspond to kinematically softer scenarios, suggesting the use of the JHEP04BM7 or JHEP04BM12 optimized BDT output. Indeed, as shown in Fig. 7.3, the choice of JHEP04BM7 compared to for instance the SM tuned BDT output was found to improve the cross section limit

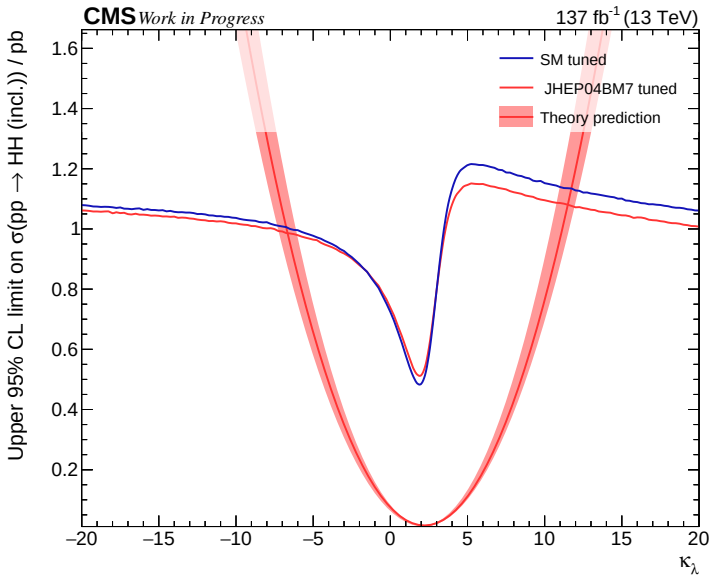

Figure 7.3: Expected (blinded) limits at 95% CL on the HH production cross section as a function of κ_λ for a fit involving all seven HH $\rightarrow$ Multilepton channels and the two control region distributions. Limits for a fit on the SM tuned nonRes BDT output as well as the JHEP04BM7 tuned nonRes BDT output is shown.

for high κ_λ by about 5-10% and the limit on κ_λ itself by 1-3% compared to a limit scan performed with the SM optimized BDT output. For scenarios around the SM where the m_{HH} is expected to be larger on average, the differences between different BDT nodes is found to be smaller. A similar trend is also observed for scans in c_2 where the on average larger m_{HH} would suggest the use of the JHEP04BM9 output, but only a small improvement is found. As the different parameter scans overlap, the choice of a single BDT output allows for more consistent results and therefore is favored. Therefore as the choice of the BDT output node has the strongest influence on scans in κ_λ, the JHEP04BM7 output is used for all coupling scans. For the limit on the SM signal strength modifier and cross section however the SM optimized node is used instead.

Optimizing the binning:

The choice of binning of the BDT output used for the signal extraction, has to balance the needs for a valid background estimation and for signal sensitivity. The high amount of available simulated events and events available for the estimation of fake- and flip backgrounds allows for a sensitivity optimized binning in the 2ℓ(ss) + 0/1 τ_{h}, $3\ell + 0\tau_{\mathrm{h}}$ and 4ℓ channels. For these channels the BDT output is binned based on quantiles of the signal, making the amount of signal constant across all bins and thus bringing out the signal peak with more bins in the high BDT score region. This results in only a few bins containing most of the background, allowing the constraint of background normalization with the rest of the bins containing a relatively high amount of signal increasing the overall sensitivity. The number of signal quantiles is chosen such that the relative statistical uncertainty of the summed Run 2 background prediction in each bin does not exceed 15% of the total background. The total number of quantiles is limited to a minimum of 5 and a maximum of 25.

For the remaining four channels the BDT is binned in quantiles of the background, ensuring a solid background prediction also in the high BDT score region. Here also a maximum relative

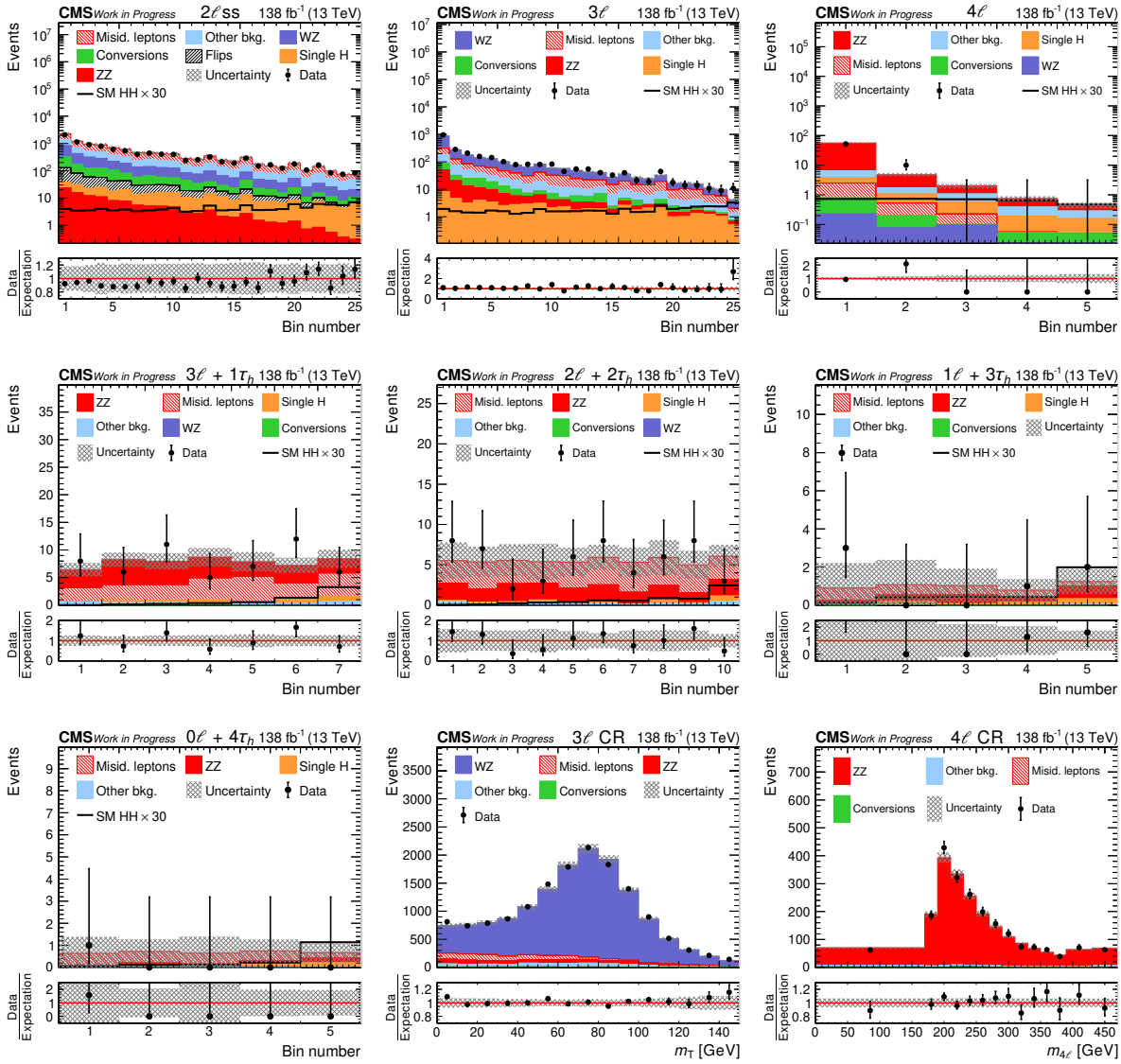

Figure 7.4: Distribution of the output for the JHEP04BM7 tuned nonRes BDT for all seven HH $\rightarrow$ Multilepton channels and the kinematic distributions for the two CR, from top-left to bottom right: the 2ℓ(ss) + 0/1 τ_h, $3\ell + 0\tau_h$, 4ℓ, $3\ell + 1\tau_h$, $2\ell + 2\tau_h$, $1\ell + 3\tau_h$ and the $0\ell + 4\tau_h$ channel followed by the WZCR and ZZCR control distributions . The plots show the Run 2 combination as a linear sum of the 2016, 2017 and 2018 prefit distributions for SM like ggHH + qqHH signal. The signal shown corresponds to 30$\times$ the SM signal strength.

per bin uncertainty per bin of 15% of the total background is chosen. For the $2\ell + 2\tau_h$ and the $3\ell + 1\tau_h$ channel this criterion is relaxed, requiring a relative per bin uncertainty of 15% on the background contributions covered by simulated events and a 50% criterion on the fake background contribution. This is done because the data driven fake background contribution contains a high number of negative event weights, yielding by construction a high statistical uncertainty even for a comparatively high amount of events in the background extrapolation.

Fig. 7.4 shows exemplary prefit distributions for the seven Multilepton channels and the two control regions. While all distributions enter the fit individually for each data taking year, the shown distributions correspond to the full Run 2 distributions obtained by adding the distributions for 2016, 2017 and 2018 for better visibility. Corresponding postfit distributions and yields for the different channels and years are given in Sec. 7.4.2. Postfit distributions for the individual years and a variety of signal scenarios can be found in the Appendix **F**.

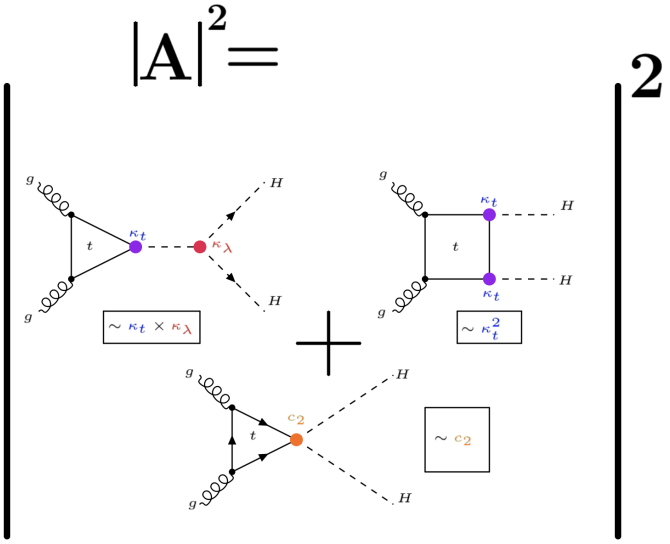

Figure 7.5: Illustration of the squared matrix element for non-resonant ggHH production involving SM like couplings and the EFT c_2 coupling. Feynman diagrams for the three involved processes at LO are shown.

7.2.1 Physics models and parameter scans

As discussed in Sec. 2.3 the measurement of the trilinear Higgs boson self-coupling λ and the coupling of the four point interaction between two Higgs bosons and two vector bosons c_{2V} is of particular interest for the study of non-resonant Di-Higgs boson production.
This motivates parameter scans in a set of SM like Higgs boson couplings $\kappa_\lambda, \kappa_t, c_V, c_{2V}$ to non-resonant Di-Higgs boson production in the ggHH and qqHH production modes. The facilitation of such a (multidimensional) scan is computationally challenging, especially when performed at a high granularity of scanned coupling points or along more than one axis of the parameter space. While an event based reweighting procedure as described in Sec. 6.2.4 allows the modulation of signal for all necessary coupling scenarios, the signal obtained in this manner would still need to pass through all steps of the analysis to obtain the necessary BDT outputs for the given scenario. As this would still be computationally not feasible a physics model was developed for CMS HH analyses [157]. The model uses the BDT output distributions (or any other distribution) of a chosen few scenarios in a linear combination, to reproduce the desired distribution for any given coupling scenario.
This thesis expands on this idea, developing a similar model expanding the default model for scans used for scans in κ_λ and κ_t to cover the EFT coupling parameter c_2 as well. As motivated in the discussion of the EFT parameters, the parameters κ_t and c_2 are inherently connected, motivating a focus on the reduced parameter space of κ_λ, κ_t and c_2.
As illustrated in Fig. 7.5 the matrix element determining the ggHH Di-Higgs boson production cross section at leading order, for a physics scenario involving the c_2 coupling is proportional to the sum of three Feynman diagrams. As in Sec. 2.3, the SM diagrams are labeled as the $\square$- and $\triangle$- diagram, respectively. The additional diagram involving the c_2 coupling is labeled as the X-diagram. Looking at Fig. 7.5, the $\triangle$ diagram is found to be proportional to $\kappa_t \times \kappa_\lambda$. For simplicity, the whole diagram can be written as $\kappa_\lambda \cdot \kappa_t \cdot \triangle$ with $\triangle$ absorbing all components of the $\triangle$ matrix element constant with respect to the couplings. Similarly the $\square$-diagram and X-diagram

can be written down as $\kappa_t^2 \cdot \square$ and $c_2 \cdot X$, respectively. With this, the ggHH matrix element can be written as:

$$\begin{aligned} |A|^2 = \kappa_\lambda^2 \cdot \kappa_t^2 \cdot |\triangle|^2 + \kappa_t^4 \cdot |\square|^2 + c_2^2 \cdot |X|^2 + \kappa_\lambda \cdot \kappa_t \cdot c_2 \cdot |\triangle^* X + X^* \triangle| \\ + \kappa_t^2 \cdot c_2 \cdot |\square^* X + X^* \square| + \kappa_t^3 \cdot \kappa_\lambda \cdot |\triangle^* \square + \square^* \triangle| \end{aligned} \tag{7.2}$$

Based on this, the cross section $\sigma \propto |A^2|$ can be expressed as:

$$\sigma(\kappa_\lambda, \kappa_t, c_2) = \mathbf{c}^T(\kappa_\lambda, \kappa_t, c_2) \cdot \mathbf{v} \tag{7.3}$$

with $\mathbf{c}^T(\kappa_\lambda, \kappa_t, c_2) = (\kappa_\lambda^2 \kappa_t^2,\ \kappa_t^4,\ c_2^2,\ c_2 \kappa_\lambda \kappa_t,\ c_2 \kappa_t^2,\ \kappa_t^3 \kappa_\lambda)$ a vector holding the coupling dependencies found in Eq. 7.2 and a vector $\mathbf{v}$ containing the coupling independent $\triangle, \square, X$ terms as well as any additional phase space related factors. The functional form found in Eq. 7.3 holds true for any order of matrix element calculation as long as the couplings remain unchanged. Equation Eq. 7.3 can not only be used for the total ggHH cross section but also for any differential cross section or kinematic distribution directly proportional to the cross section in general, with $\mathbf{v}$ absorbing any additional factors. For a reduced model with constant κ_λ and κ_t, everything can be reduced to three dimensions and $\mathbf{c}^T$ becomes $\mathbf{c}^T(c_2) = (1, c_2^2, c_2)$ with the 1 absorbing all now constant $\kappa_\lambda^n \kappa_t^m$ terms.
Assuming a scenario with three measured observables σ^a, σ^b, σ^c, according to Eq. 7.3 one can write:

$$\vec{\sigma} = \begin{pmatrix} \sigma^a \\ \sigma^b \\ \sigma^c \end{pmatrix} = \begin{pmatrix} c_1^a & c_2^a & c_3^a \\ c_1^b & c_2^b & c_3^b \\ c_1^c & c_2^c & c_3^c \end{pmatrix} \cdot \begin{pmatrix} v_1 \\ v_2 \\ v_3 \end{pmatrix} = \mathbf{C} \cdot \mathbf{v} \tag{7.4}$$

The vector $\mathbf{v}$ could now be found by solving the corresponding set of linear equations. An easier and more general way however is to use Eq. 7.3 substituting $\mathbf{v} = \mathbf{C}^{-1} \cdot \vec{\sigma}$ in Eq. 7.4 to arrive at:

$$\sigma(c_2) = \mathbf{c}^T(c_2) \cdot \mathbf{C}^{-1} \cdot \vec{\sigma} \tag{7.5}$$

or for the full κ_λ, κ_t, c_2 case at:

$$\sigma(\kappa_\lambda, \kappa_t, c_2) = \mathbf{c}^T(\kappa_\lambda, \kappa_t, c_2) \cdot \mathbf{C}^{-1} \cdot \vec{\sigma} \tag{7.6}$$

This allows the description of any cross section dependent distribution by a linear combination of adequately chosen input scenarios $\vec{\sigma}$ by calculating $\mathbf{c}^T$ for the target scenario and $\mathbf{C}^{-1}$ the inverted matrix of $\mathbf{c}^T$ from the input scenario couplings.

Choosing the input scenario basis:

As the physics model needs to be able to extrapolate any scenario by a linear combination of a given set of basic scenarios, the choice of a basis with kinetically diverse scenarios is advantageous. A valid basis is found, if the resulting matrix $\mathbf{C}$ is invertable. Mathematically, this can also be quantified in terms of the condition number [158], describing how well a matrix is (numerically) invertable and therefore how close it is to an ideal basis with a matrix of eigenvectors. Fig. 7.6 shows the differential ggHH cross section as inferred from the reweighting procedure in

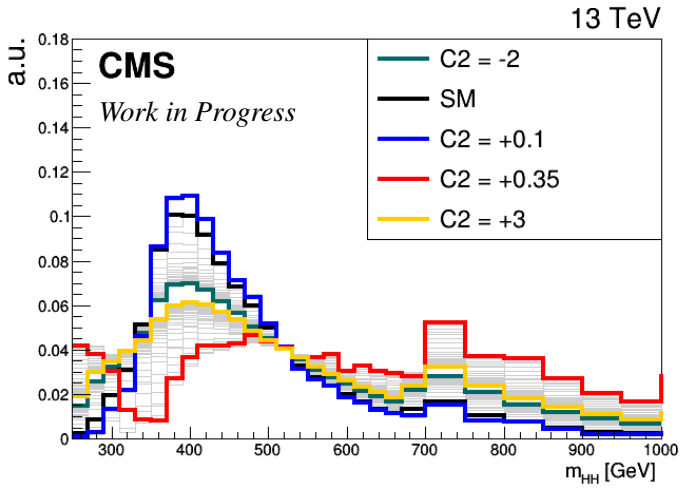

Figure 7.6: Differential ggHH cross section in the invariant Di-Higgs mass m_{HH} for different values of the EFT coupling c_2 in the range $-2 < c_2 < 3$. For this comparison all other couplings with an impact on Di-Higgs boson production are fixed to their SM value. For an easier comparison of the different kinematic scenarios, the cross section distributions are shown normalized to 1. The differential cross section is calculated as described in Sec. 6.2.4.

Sec. 6.2.4 for different values of c_2 in the range $-2 < c_2 < 3$. As can be seen in Fig. 7.6, the scenarios with the strongest kinematic differences correspond to (κ_λ, κ_t, c_2) $(1, 1, 0.35)$, $(1, 1, 0.1)$ and one of the scenarios at the edge of the presented scan, either $(1, 1, -2)$ or $(1, 1, 3)$ with all other scenarios in between these three (four) cases.

Therefore any combination of the scenarios $(1, 1, 0.35)$, $(1, 1, 0.1)$ and one of $(1, 1, -2)$ or $(1, 1, 3)$ will form a good basis of the c_2 part of the parameter space. As the SM is close to $(1, 1, 0.1)$ it can be used instead. For the κ_λ and κ_t part of the parameter space a set of four dedicated NLO ggHH samples also used in the "default" non EFT model is available. These correspond to the SM $(1, 1, 0)$, a scenario without the trilinear Higgs boson self-coupling corresponding to the $\square$ diagram $(0, 1, 0)$, a scenario corresponding to high κ_λ and the $\triangle$ diagram $(5, 1, 0)$ and a scenario representing the maximum interference between the $\square$ and $\triangle$ diagrams $(2.45, 1, 0)$. For the full description of κ_λ, κ_t and c_2 a total of six scenarios is needed. While the described scenarios are sufficient to separately describe variations in κ_λ-κ_t and c_2, no complete basis with an invertable matrix $\mathbf{C}$ is found. To solve this, a scenario describing contributions only from the $\square$ and X diagrams $(0, 1, 1)$ is found to complete the basis. The final basis of six scenarios is then found by choosing six of the described nine scenarios such that the samples contain the SM and the condition number is minimized. In the end the scenarios: $(0, 1, 0)$, $(1, 1, 0)$, $(2.45, 1, 0)$, $(0, 1, 1)$, $(1, 1, 0.35)$ and $(1, 1, 3)$ are used.

The default ggHH model used for non-EFT scans in the combination is similarly parameterized in κ_λ, κ_t with $\mathbf{c}^T = (\kappa_\mathrm{t}^4, \kappa_\lambda^2\kappa_\mathrm{t}^2, \kappa_\mathrm{t}^3\kappa_\lambda)$ using the ($\kappa_\lambda = 1$, $\kappa_\mathrm{t} = 1$), ($\kappa_\lambda = 5$, $\kappa_\mathrm{t} = 1$) and ($\kappa_\lambda = 2.45$, $\kappa_\mathrm{t} = 1$) scenarios.

Similarly to the ggHH signal, the qqHH signal is parameterized in κ_λ and the Higgs boson vector boson couplings c_V and c_{2V}. Here $\mathbf{c}^T = (c_V^2\kappa_\lambda^2, c_V^4, c_{2V}^2, c_V^3\kappa_\lambda, c_V c_{2V}\kappa_\lambda, c_V^2 c_{2V})$ and scenarios $(\kappa_\lambda, c_V, c_{2V}) = (1, 1, 1)$, $(0, 1, 1)$, $(2, 1, 1)$, $(1, 1, 0)$, $(1, 1, 2)$ and $(1, 1.5, 1)$ are used. Both the default and the c_2 EFT model are implemented in the `Inference` framework [159] used for parameter scans in all CMS HH analyses.

The ggHH input scenarios for both models are either generated at NLO accuracy or obtained using the NLO signal reweighting discussed in Sec. 6.2.4. For NNLO matrix element accuracy they are normalized to their NNLO cross section using the κ_λ dependent NLO/NNLO k factor and the κ_λ dependent cross section uncertainties described in Sec.2.3. Both single Higgs boson backgrounds as well as the HH signal are scaled according to the κ_λ dependence of the single Higgs branching fractions. Furthermore the scaling of the single Higgs boson processes also includes the κ_λ dependence of their production cross section. Both effects are discussed in Sec. 2.3.

7.3 Background Control Regions

For this analysis two types of control regions are defined:

- The WZ $\to 3\ell$ and ZZ $\to 4\ell$ control regions are used to constrain the two main prompt background processes and their related systematic uncertainties in the final signal extraction described in Sec. 7.2.
- A number of channel specific control regions are defined close to the signal region of the channel in question to check the overall modelling of backgrounds also in the various kinematic distributions used in the BDT based signal/background discrimination.

The following will describe the various control regions with a focus on the WZ $\to 3\ell$ and ZZ $\to 4\ell$ control regions as well as three control regions defined for the $3\ell + 1\tau_h$ channel.

WZ $\to 3\ell$ **control region**

Genuine WZ $\to 3\ell$ events are the main background in the $3\ell + 0\tau_h$ channel and have a sizeable contribution in the 2ℓ(ss) + 0/1 τ_h channel as well. The WZ $\to 3\ell$ control region (3ℓCR) is defined analogously to the $3\ell + 0\tau_h$ channel described in Sec. 6.5.2 by requiring 3ℓ passing the Tight ID criteria with a total charge sum of ± 1 and a $p_T > 25/15/10$ GeV for the leading/sub leading and third highest p_T lepton. Events containing any τ_h, any DeepJet-M b-tagged jet or more than one DeepJet-L b-tagged jet are vetoed. Events likely to contain a low mass meson resonance are vetoed by excluding events containing a Di-Lepton pair with a mass below 12 GeV. In contrast to the $3\ell + 0\tau_h$ channel the presence of a same flavor opposite sign lepton pair with a mass $|m_{\ell\ell}^{\text{SFOS}} - m_Z| < 10$ GeV is not vetoed but required. For the low mass veto as well as the inverted Z boson mass veto, Loose ID leptons are used. To account for the presence of a neutrino in the W decay, E_T^{miss}LD> 45 GeV is required. These selection criteria are summarized in Tab. 7.3.
For the signal extraction (Sec. 7.2) the visible mass edge of the W decay is calculated by finding the two same flavor opposite sign leptons with the closest Di-Lepton mass to m_Z and computing the transverse mass between E_T^{miss} and the remaining lepton ℓ^3:

$$m_T(E_T^{miss}, \ell^3) = \sqrt{(E_T^{miss} + E_T^{l3})^2 - ((E_x^{miss} + p_x^{l3})^2 + (E_y^{miss} + p_y^{l3})^2)} \tag{7.7}$$

with E_T^{l3} the transverse energy $E_T = E \cdot \frac{p_T}{|\vec{p}|}$ of ℓ^3, p_x^{l3}/p_y^{l3} the momentum of ℓ^3 in x/y direction, and E_x^{miss}/E_y^{miss} the components of E_T^{miss} in x/y direction. The post signal extraction fit

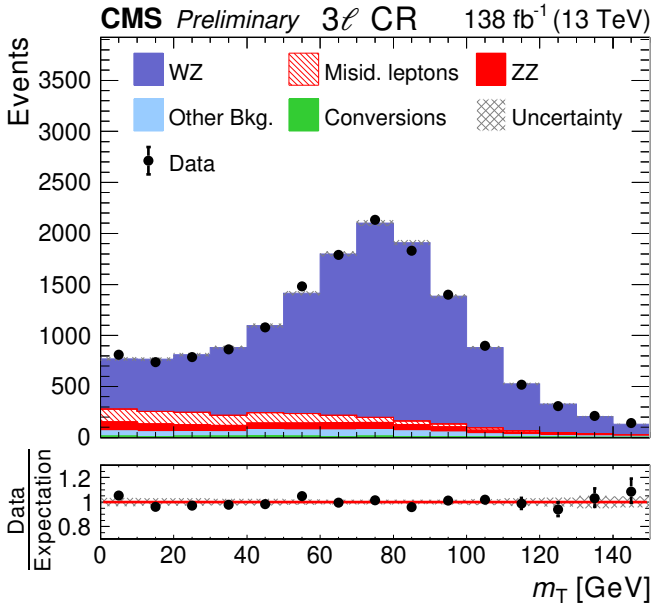

Figure 7.7: The distribution of the transverse mass between the vector of missing transverse energy and a the non Z boson tagged lepton $m_T(E_T^{miss}, \ell^3)$ for the 3ℓCR approximating the mass of the decaying W boson in the WZ decay. The plot shows shows the Run 2 combination as a sum of the 2016, 2017 and 2018 postfit distributions from the combined HH $\rightarrow$ Multilepton signal extraction. The dominant contribution comes from WZ production with only smaller contributions from other processes as listed in Tab. 7.2. (made public in [4])

Process	2016	2017	2018	Run2
WZ	3248.7±24.4	3873.2±33.1	5432.8±38.4	12554.7±56.3
ZZ	195.2±2.6	267.6±3.6	337.2±4.5	800.0±6.4
Fakes	160.7±13.5	423.1±27.0	322.2±23.1	906.0±38.0
Conversion	38.0±4.4	49.3±4.5	45.9±5.2	133.2±8.1
Other backgrounds	171.2±6.5	179.1±6.8	265.5±10.6	615.8±14.2
Total expected background	3813.8±28.3	4792.3±36.5	6403.6±43.8	15009.7±63.7
Data observed	3757	4813	6424	14994

Table 7.2: Post signal extraction (Sec. 7.2) yields in the WZ control region separately for 2016, 2017, 2018 as well as their Run 2 combination [4]. The given errors for all three years correspond to the full postfit uncertainty including all statistical as well as systematic uncertainties. The Run 2 uncertainties correspond to the quadratic sum of the uncertainties in all three years.

$m_T(E_T^{miss}, \ell^3)$ distribution for the combination of all three years can be seen in Fig. 7.7 with plots for the individual years in Appendix **F**. The distribution of $m_T(E_T^{miss}, \ell^3)$ shows as expected a peak around the W boson mass. A good agreement of data and background prediction within the given uncertainty bands is observed, proving that the dominant WZ background as well as the given lepton ID are well modelled within the context of this analysis. The post signal extraction fit event yields of data and background prediction for all three years are given in Tab. 7.2. In addition to its role in the signal extraction fit, the 3ℓCR is also used as a control region for the kinematic variables in the 2ℓ(ss) + 0/1 τ_h and $3\ell + 0\tau_h$ channels by requiring additional jets where necessary. No significant disagreements between data and background prediction where observed.

ZZ $\rightarrow 4\ell$ control region

Genuine decays of ZZ pairs into leptons and τ_h are the main background in the 4ℓ channel,

Criterion	3ℓCR	4ℓCR
Number of Tight ID leptons	3	4
Lepton p_{T}	$> 25/15/10$ GeV	$> 25/15/15/10$ GeV
Number of Tight ID τ_{h}	0	–
Low mass resonance veto	any $m_{\ell\ell}^{\text{Loose ID}} < 12$ GeV	any $m_{\ell\ell}^{\text{Loose ID}} < 12$ GeV
Z mass requirement	at least one $\lvert m_{\ell\ell}^{\text{SFOS, Loose ID}} \rvert < 10$ GeV	at least one $\lvert m_{\ell\ell}^{\text{SFOS, Loose ID}} \rvert < 10$ GeV
b-jet Veto	any DeepJet-M or > 1 DeepJet-L b-tag	any DeepJet-M or > 1 DeepJet-L b-tag
Charge Sum	$\lvert \sum_i Q(\ell_i) \rvert = 1$	$\lvert \sum_i Q(\ell_i) \rvert = 0$
Missing energy	E_T^{miss}LD> 45 GeV	–
$\mathrm{H} \to \mathrm{ZZ}$ veto	–	$m_{4\ell} < 140$ GeV and two SFOS pairs

Table 7.3: Selection criteria for the WZ and ZZ control regions.

Process	2016	2017	2018	Run2
ZZ	524.4±8.6	614.0±10.3	895.5±14.9	2033.9±20.0
Fakes	4.6±2.1	4.0±2.1	4.6±2.4	13.2±3.9
Conversion	0.9±0.1	1.0±0.1	1.0±0.1	2.9±0.1
Other backgrounds	15.6±0.7	16.7±0.8	26.4±1.3	58.7±1.6
Total expected background	545.5±5.5	635.7±6.9	927.4±9.6	2108.6±13.1
Data observed	582	620	916	2096

Table 7.4: Post signal extraction (Sec. 7.2) yields in the ZZ control region separately for 2016, 2017, 2018 as well as their Run 2 combination. The given errors for all three years correspond to the full postfit uncertainty including all statistical as well as systematic uncertainties. The Run 2 uncertainties correspond to the quadratic sum of the uncertainties in all three years.

one of the two main backgrounds in the $3\ell + 1\tau_{\mathrm{h}}$ channel, with further strong contributions in the $0\ell + 4\tau_{\mathrm{h}}$, $1\ell + 3\tau_{\mathrm{h}}$ and $2\ell + 2\tau_{\mathrm{h}}$ channel.

The ZZ control region (4ℓCR) is defined analogously to the 4ℓ channel by requiring at least 4 Tight ID leptons with a p_{T} higher than 25/15/15/10 GeV for the leading/sub-leading/third and fourth highest p_{T} lepton. The charge sum of these four leptons is required to be zero. Events containing any DeepJet-M b-tagged jet or more than one DeepJet-L b-tagged jet are vetoed. To avoid overlap with the $\mathrm{HH} \to \mathrm{bbZZ} \to \mathrm{bb}4\ell$ analysis [142] as well as to reduce contribution from single Higgs boson $\mathrm{H} \to \mathrm{ZZ} \to 4\ell$ production, events with two same flavor opposite sign pairs and a four lepton mass $m_{4\ell} < 140$ GeV are vetoed. Events likely to contain a low mass meson resonance are vetoed by excluding events containing a Di-Lepton pair with a mass below 12 GeV. In difference to the 4ℓ channel the presence of at least one same flavor opposite lepton pair with a mass $|m_{\ell\ell}^{\mathrm{SFOS}} - m_{\mathrm{Z}}| < 10$ GeV is required. For all mass veto as well as the inverted Z boson mass veto, loose ID leptons are used. These selection criteria are summarized in Tab. 7.3. For the signal extraction (Sec. 7.2) the four lepton mass $m_{4\ell}$ is used. The post signal extraction fit $m_{4\ell}$ distribution for the combination of all three years can be seen in Fig. 7.8 with plots for the individual years in Appendix **F**. The distribution of $m_{4\ell}$ shows as expected a peak around two times the Z boson mass. Very few events are observed below a threshold of 140 GeV, showing the veto on $\mathrm{H} \to \mathrm{ZZ} \to 4\ell$ events. A good agreement of data and background prediction within the given uncertainty bands is observed, proving that also the dominant ZZ background is well modelled within the context of this analysis. The post signal extraction fit event yields of data and background prediction for all three years are given in Tab. 7.4. In addition to its role in the signal extraction fit, the 4ℓCR is also used as control region for the studied kinematic variables in the 4ℓ channel. No significant disagreements between data and background prediction where observed.

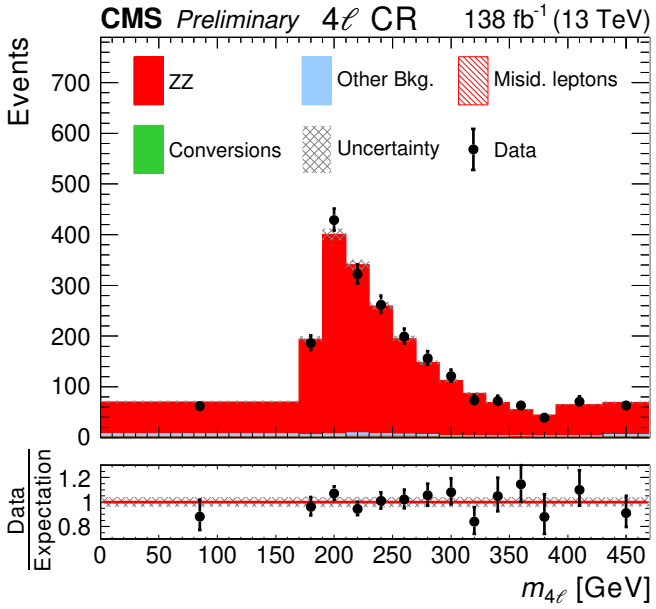

Figure 7.8: The distribution of the four lepton mass $m_{4\ell}$ in the ZZ CR. The plot shows shows the Run 2 combination as a sum of the 2016, 2017 and 2018 postfit distributions from the combined HH $\rightarrow$ Multilepton signal extraction (Sec. 7.2) [4]. The dominant contribution comes from ZZ production with only smaller contributions from other processes as listed in Tab. 7.4. (made public in [**CMS-PAS-HIG-21-002**]

$3\ell + 1\tau_h$ control regions

The $3\ell + 1\tau_h$ channel as described in Sec. 6.5.1 features fake τ_h events from WZ as well as ZZ $\rightarrow \ell\ell\tau\tau$ events as its two main background processes. The two dominant control regions of this analysis, the 3ℓCR and 4ℓCR, give no handle on the adequate modelling of the fake τ_h background component. While the general method for the fake background estimation has been used many times and is verified in the 2ℓ(ss) and 0/1 τ_h and $3\ell + 0\tau_h$ channels for this analysis, the MC closure test described in Sec. 6.4 mainly checks the method with regard to fake leptons, not for τ_h. On the other hand, while the global 4ℓCR covers the second major background ZZ, it does not provide a handle on the modelling and reconstruction of τ_h. Therefore the kinematic variables studied in the $3\ell + 1\tau_h$ channel (Sec. 6.6.1) as well as basic kinematic quantities such as the τ_h p_T are studied in three additional control regions. All of them are defined closely to the selection criteria of the $3\ell + 1\tau_h$ channel summarized in Tab. 6.13. Two fake enriched control regions are defined by inverting the charge sum criterion requiring $|Q(\tau_h) + \sum_i Q(\ell_i)| > 0$ ($3\ell + 1\tau_h$ **FakeCR**) or by inverting the b-jet veto requiring at least one DeepJet-M tagged or more than one DeepJet-L tagged jet ($3\ell + 1\tau_h$ **BCR**). In addition, for both of these control regions the veto for lepton pairs around the Z boson mass is dropped. The third control region ($3\ell + 1\tau_h$ **ZZCR**) enriched in ZZ decays is defined by inverting the Z boson mass veto, requiring at least one Loose ID same flavor opposite sign charge pair (SFOS) in the Z boson mass window $|m_{\ell\ell}^{\text{SFOS, Loose ID}} - m_Z| < 10$ GeV.

The general agreement of the background prediction and data can be seen in Fig. 7.9 showing distributions for the number of muons, the number of jets, E_T^{miss}LD and HT for the Run 2 combination of 2016, 2017 and 2018 data in the $3\ell + 1\tau_h$ control regions. While this shows that the modeling of the energy content and object multiplicities in the $3\ell + \tau_h$ phase space works well,

Process	2016	2017	2018	Run2
Fakes	13.06±1.82	13.81±1.89	19.54±2.25	46.41±3.45
ZZ	0.70±0.02	0.49±0.01	0.72±0.02	1.92±0.03
WZ	0.09±0.06	0.10±0.06	0.21±0.08	0.39±0.11
Single H	0.04±0.11	0.13±0.09	0.08±0.06	0.25±0.15
Conversion	0.07±0.04	0.04±0.03	−±−	0.11±0.05
$t\bar{t}+X$	0.01±0.01	−±−	0.03±0.01	0.04±0.01
Other Backgrounds	0.14±0.04	0.15±0.04	0.29±0.10	0.57±0.11
Total expected background	14.11±1.82	14.72±1.89	20.87±2.25	49.71±3.46
Data observed	14	16	21	51

Table 7.5: Expected and observed yields in the $3\ell + 1\tau_h$ FakeCR for the years 2016, 2017 and 2018 as well as their Run 2 combination. The given uncertainty corresponds to statistical uncertainty contributions only.

Process	2016	2017	2018	Run2
ZZ	36.89±0.12	41.69±0.10	63.15±0.21	141.73±0.27
Fakes	10.64±1.80	14.19±2.06	24.77±2.70	49.60±3.84
Single H	2.20±0.67	2.83±0.79	0.22±0.06	5.28±1.03
$t\bar{t}+X$	1.08±0.07	1.00±0.05	1.85±0.10	3.92±0.13
WZ	0.07±0.04	0.04±0.04	0.09±0.06	0.20±0.09
Conversion	-0.02±0.03	0.03±0.03	−±−	0.01±0.03
Other Backgrounds	1.53±0.18	1.58±0.22	2.17±0.33	5.28±0.44
Total expected background	52.39±1.93	61.35±2.22	92.23±2.73	205.98±4.01
Data observed	69	77	86	232

Table 7.6: Expected and observed yields in the $3\ell + 1\tau_h$ ZZCR for the years 2016, 2017 and 2018 as well as their Run 2 combination. The given uncertainty corresponds to statistical uncertainty contributions only.

Process	2016	2017	2018	Run2
ZZ	1.39±0.02	1.80±0.02	2.66±0.05	5.85±0.06
Fakes	5.78±1.27	7.90±1.40	8.24±1.49	21.91±2.41
Single H	2.08±0.17	2.25±0.17	3.73±0.18	8.07±0.31
$t\bar{t}+X$	6.15±0.16	8.23±0.14	12.49±0.26	26.87±0.33
WZ	−±−	−±−	0.02±0.02	0.02±0.02
Conversion	0.01±0.01	0.05±0.04	−±−	0.06±0.04
Other Backgrounds	0.20±0.05	0.50±0.09	0.57±0.09	1.28±0.14
Total expected background	15.60±1.30	20.74±1.43	27.71±1.53	64.05±2.46
Data observed	18	20	29	67

Table 7.7: Expected and observed yields in the $3\ell + 1\tau_h$ BCR for the years 2016, 2017 and 2018 as well as their Run 2 combination. The given uncertainty corresponds to statistical uncertainty contributions only.

the modelling of leptons and especially τ_h is also of particular concern. As the estimation of fake background in this analysis (Sec. 6.4) focuses on misidentified jets and does not model τ_h fakes from misidentified electrons for example in $ZZ \to \ell\ell ee$ decays, in the past, disagreements between background prediction and data have been observed at low ${p_T}^{\tau_h}$ for looser tau selection criteria (see Sec. 6.3). As seen in Fig. 7.10 showing the τ_h p_T, η, ϕ and charge for the Run 2 combination of 2016, 2017 and 2018 data, the current τ_h selection criteria lead to a good agreement between data and background expectation in all three $3\ell + 1\tau_h$ control regions. Fig. 7.13, Fig. 7.11 and Fig. 7.15 display the p_T, η and ϕ of electrons and muons for the Run 2 combination of 2016, 2017 and 2018 data in the three $3\ell + 1\tau_h$ control regions, showing that also the leptons at their relatively low p_T threshold down to 10 GeV are well modelled. Data and background prediction agree within $5 - 15\%$.

Other control regions

Similar as for the $3\ell + 1\tau_h$ channel, a fake control region is defined for the $2\ell + 2\tau_h$ channel by inverting the charge sum criterion and dropping the Z boson mass veto of the channel selection criteria described in Sec. 6.5.2. Therefore events with two Tight ID leptons with $p_T > 25/15$ GeV and two Tight ID τ_h with an invariant same flavor opposite sign Di-Lepton mass in a 10 GeV mass window around the Z boson mass and a neutral charge sum $\sum_i Q(\ell_i) + \sum_i Q(\tau_{h i})$ are selected. Events containing a low mass meson resonance are excluded. Events containing more than one DeepJet-L or any DeepJet-M b-tagged jet are vetoed as well. The observed and expected yields for this $2\ell + 2\tau_h$ FakeCR are summarized in Tab. 7.9. Exemplary plots for the $2\ell + 2\tau_h$FakeCR showing the visible Di-Higgs mass m_{HH}^{vis}, the invariant mass of both selected leptons and taus can be seen in Fig. 7.16. Data and background prediction agree within 10%. To verify the modelling of background events from photon conversion, a dedicated control region (ConversionCR) is defined by selecting $\mu^-\mu^+e$ events with E_T^{miss}LD < 45 GeV where the electron fails either the conversion rejection or has one lost hit in the tracker. The $\mu^-\mu^+$ pair is required to have a mass compatible with the Z boson mass $|m_{\mu^-\mu^+} - m_Z| < 10$ GeV targeting $\mu^-\mu^+\gamma$ events. As in the $3\ell + 0\tau_h$ channel a veto of events with more than one DeepJet-L or any DeepJet-M b-tagged jet is applied and the selected leptons are required to have a $p_T > 25/15/10$ GeV for the leading, subleading and third highest p_T lepton. Expected and observed yields for this control region are given in Tab. 7.10. Fig. 7.17 shows a plot of the invariant three lepton mass in the ConversionCR. Data and background prediction agree within 10%.

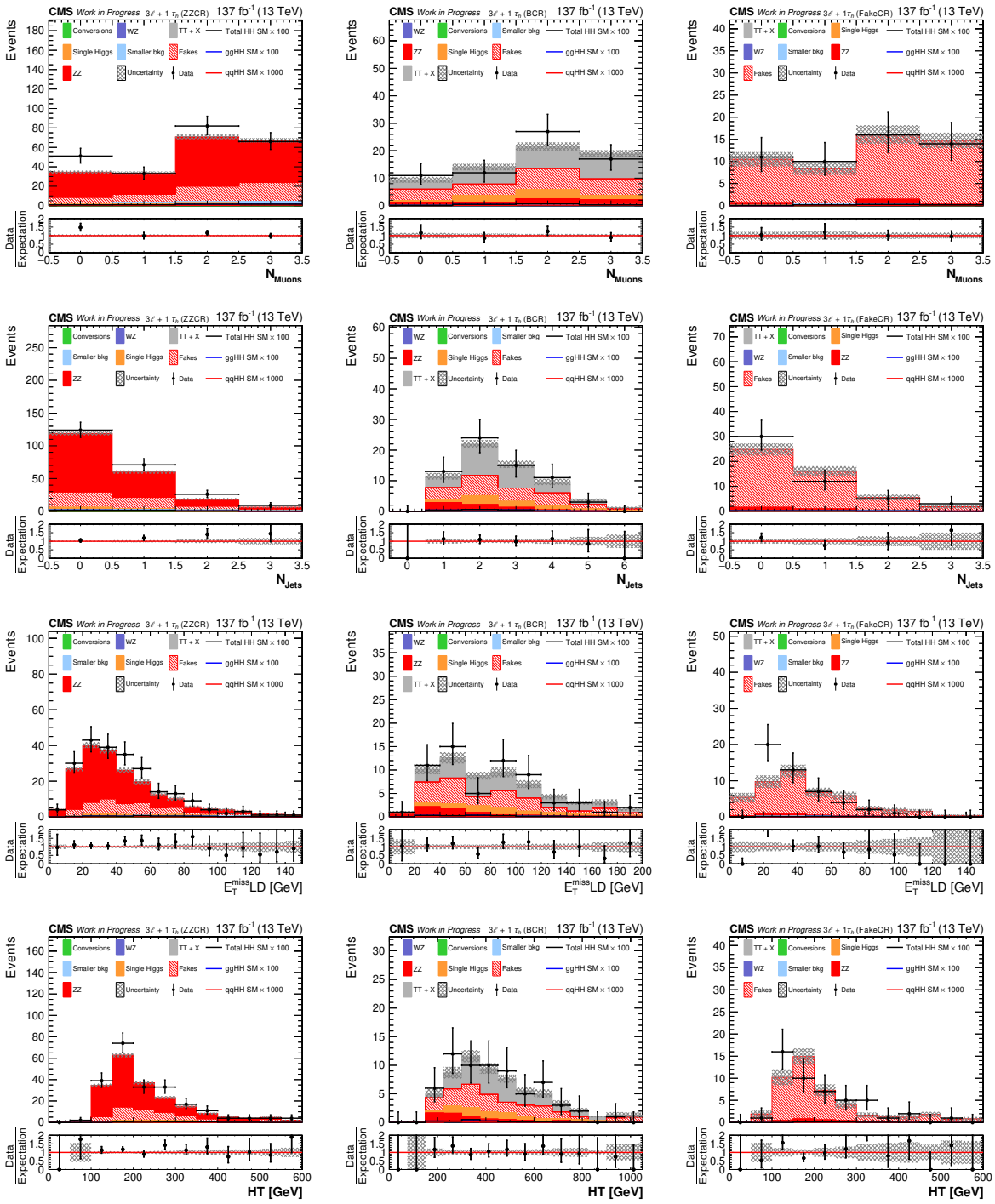

Figure 7.9: Distributions of the number of muons, the number of jets, E_T^{miss}LD and HT in the $3\ell + 1\tau_h$ ZZCR (left), the $3\ell + 1\tau_h$ BCR (center) and the $3\ell + 1\tau_h$ FakeCR (right) as defined in Tab. 7.8. The distributions are shown for Run 2 combination of the 2016, 2017 and 2018 dataset. The shown uncertainty bands corresponds to statistical uncertainty contributions only.

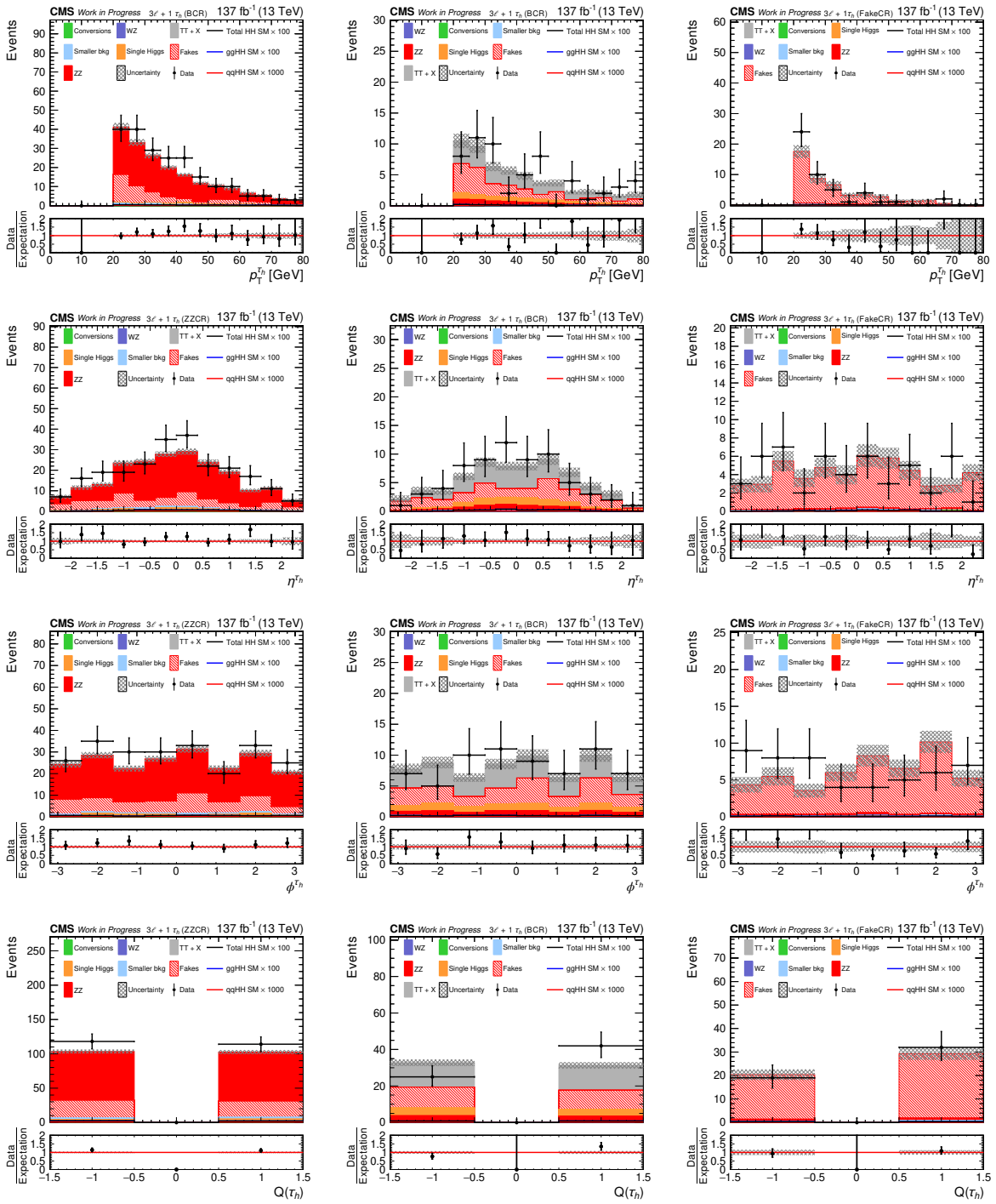

Figure 7.10: Distributions of p_T, η, ϕ and charge of the τ_h in the $3\ell + 1\tau_h$ ZZCR (left), the $3\ell + 1\tau_h$ BCR (center) and the $3\ell + 1\tau_h$ FakeCR (right) as defined in Tab. 7.8. The distributions are shown for Run 2 combination of the 2016, 2017 and 2018 dataset.The shown uncertainty bands corresponds to statistical uncertainty contributions only.

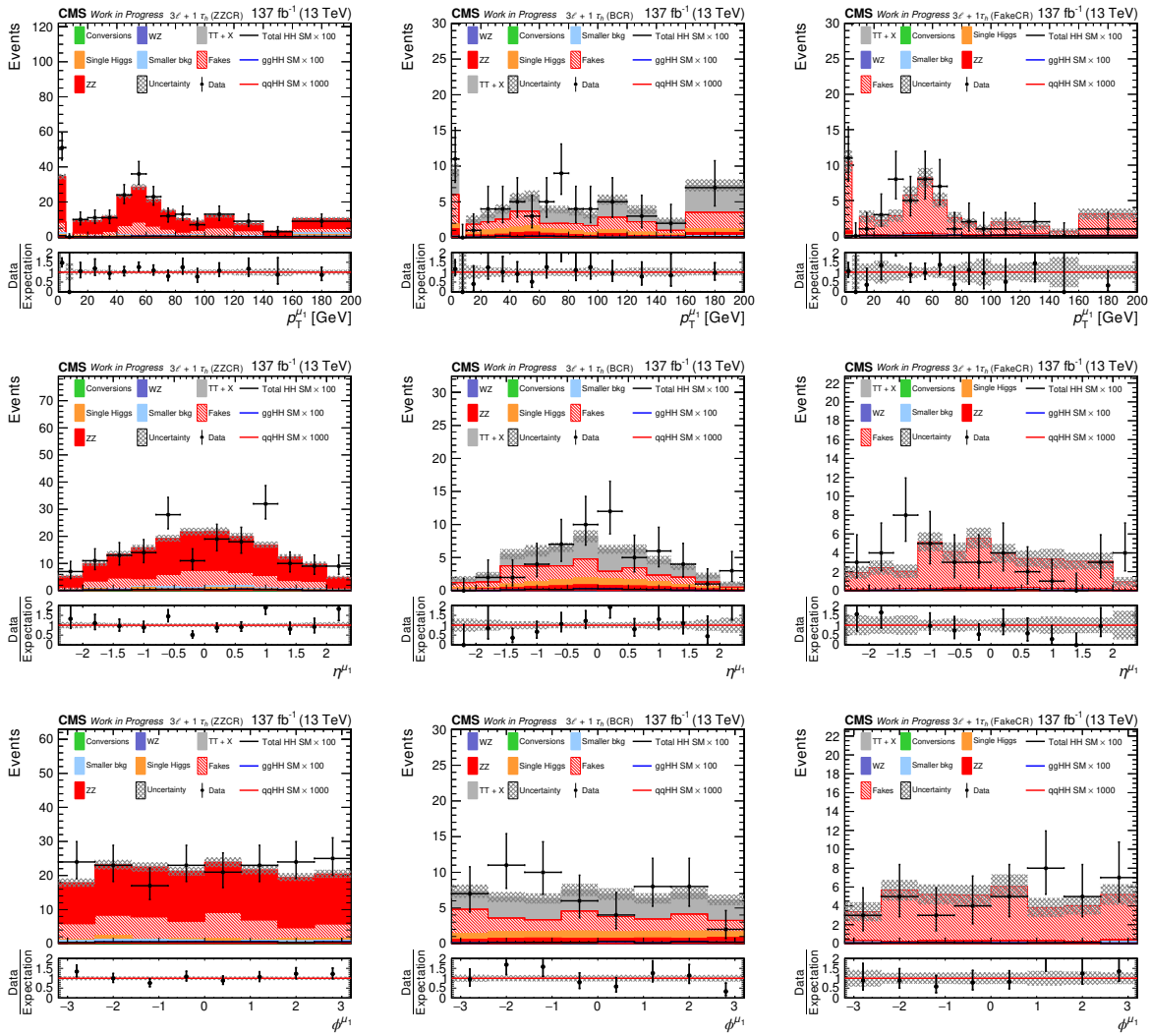

Figure 7.11: Distributions of p_T, η and ϕ for the leading muon in the $3\ell + 1\tau_h$ ZZCR (left), the $3\ell + 1\tau_h$ BCR (center) and the $3\ell + 1\tau_h$ FakeCR (right) as defined in Tab. 7.8. The distributions are shown for Run 2 combination of the 2016, 2017 and 2018 dataset.The shown uncertainty bands corresponds to statistical uncertainty contributions only.

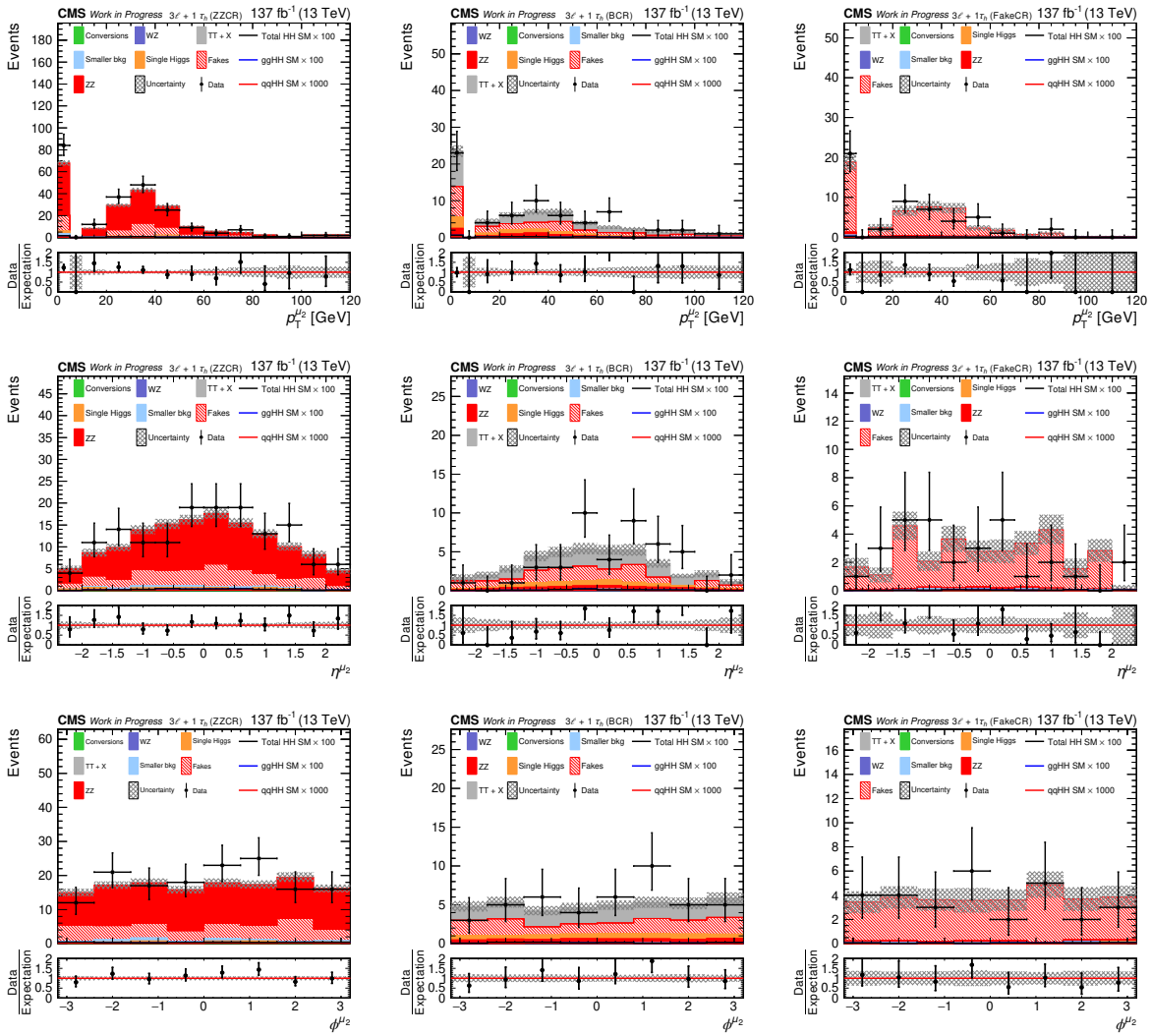

Figure 7.12: Distributions of p_T, η and ϕ for the subleading muon in the $3\ell + 1\tau_h$ ZZCR (left), the $3\ell + 1\tau_h$ BCR (center) and the $3\ell + 1\tau_h$ FakeCR (right) as defined in Tab. 7.8. The distributions are shown for Run 2 combination of the 2016, 2017 and 2018 dataset. The shown uncertainty bands corresponds to statistical uncertainty contributions only.

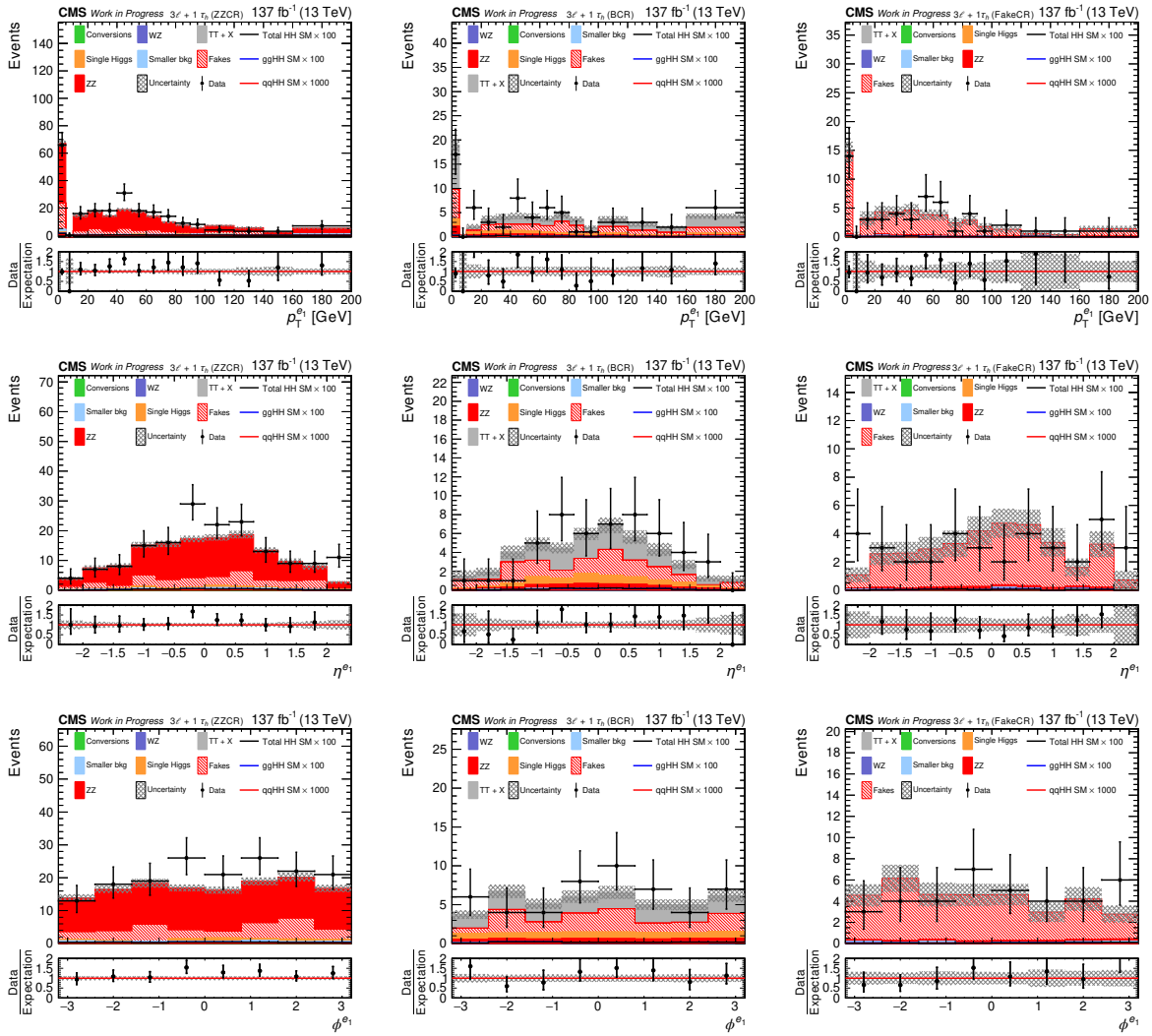

Figure 7.13: Distributions of p_T, η and ϕ for the leading electron in the $3\ell + 1\tau_h$ ZZCR (left), the $3\ell + 1\tau_h$ BCR (center) and the $3\ell + 1\tau_h$ FakeCR (right) as defined in Tab. 7.8. The distributions are shown for Run 2 combination of the 2016, 2017 and 2018 dataset. The shown uncertainty bands corresponds to statistical uncertainty contributions only.

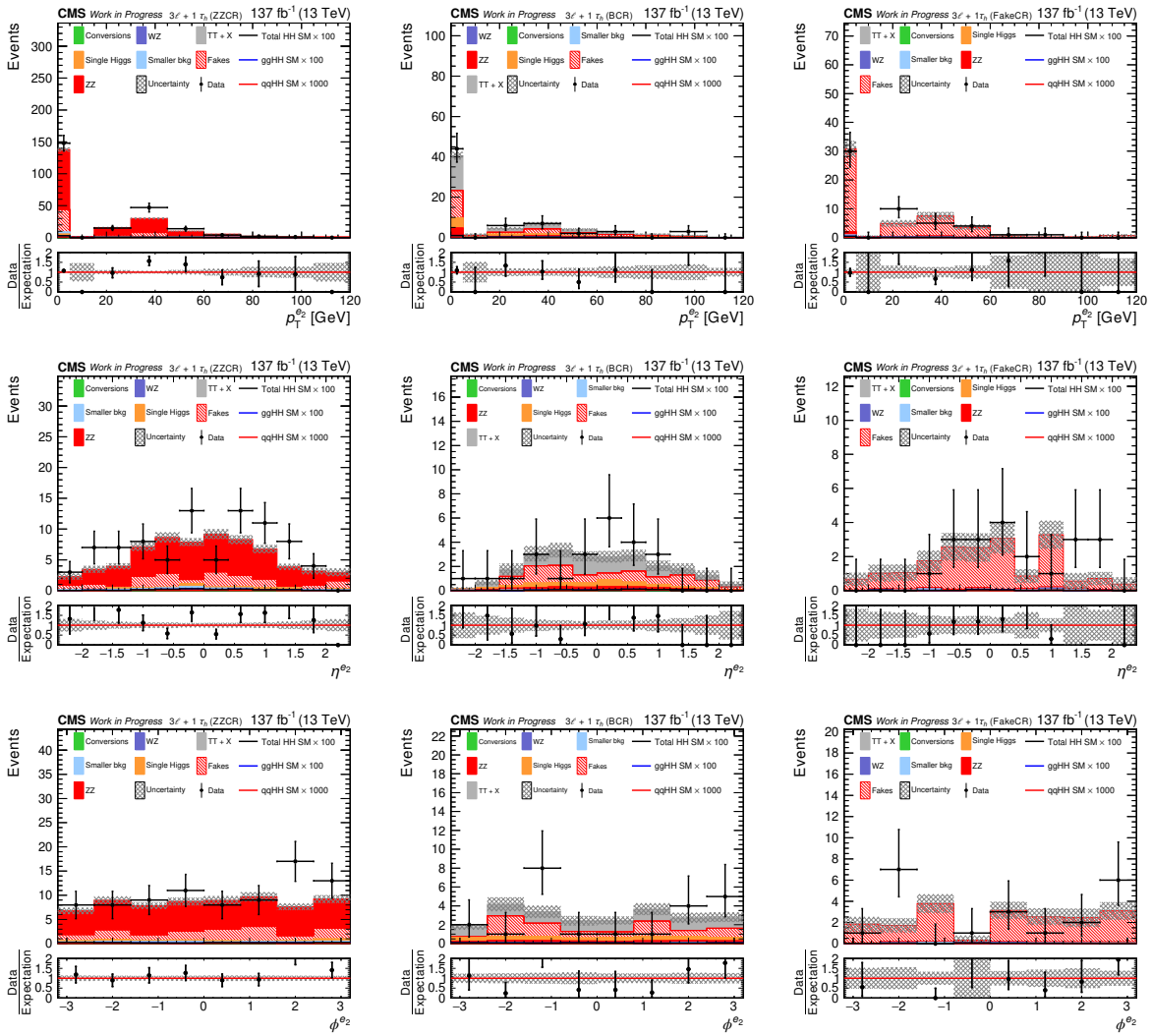

Figure 7.14: Distributions of p_T, η and ϕ for the subleading electron in the $3\ell + 1\tau_h$ ZZCR (left), the $3\ell + 1\tau_h$ BCR (center) and the $3\ell + 1\tau_h$ FakeCR (right) as defined in Tab. 7.8. The distributions are shown for Run 2 combination of the 2016, 2017 and 2018 dataset. The shown uncertainty bands corresponds to statistical uncertainty contributions only.

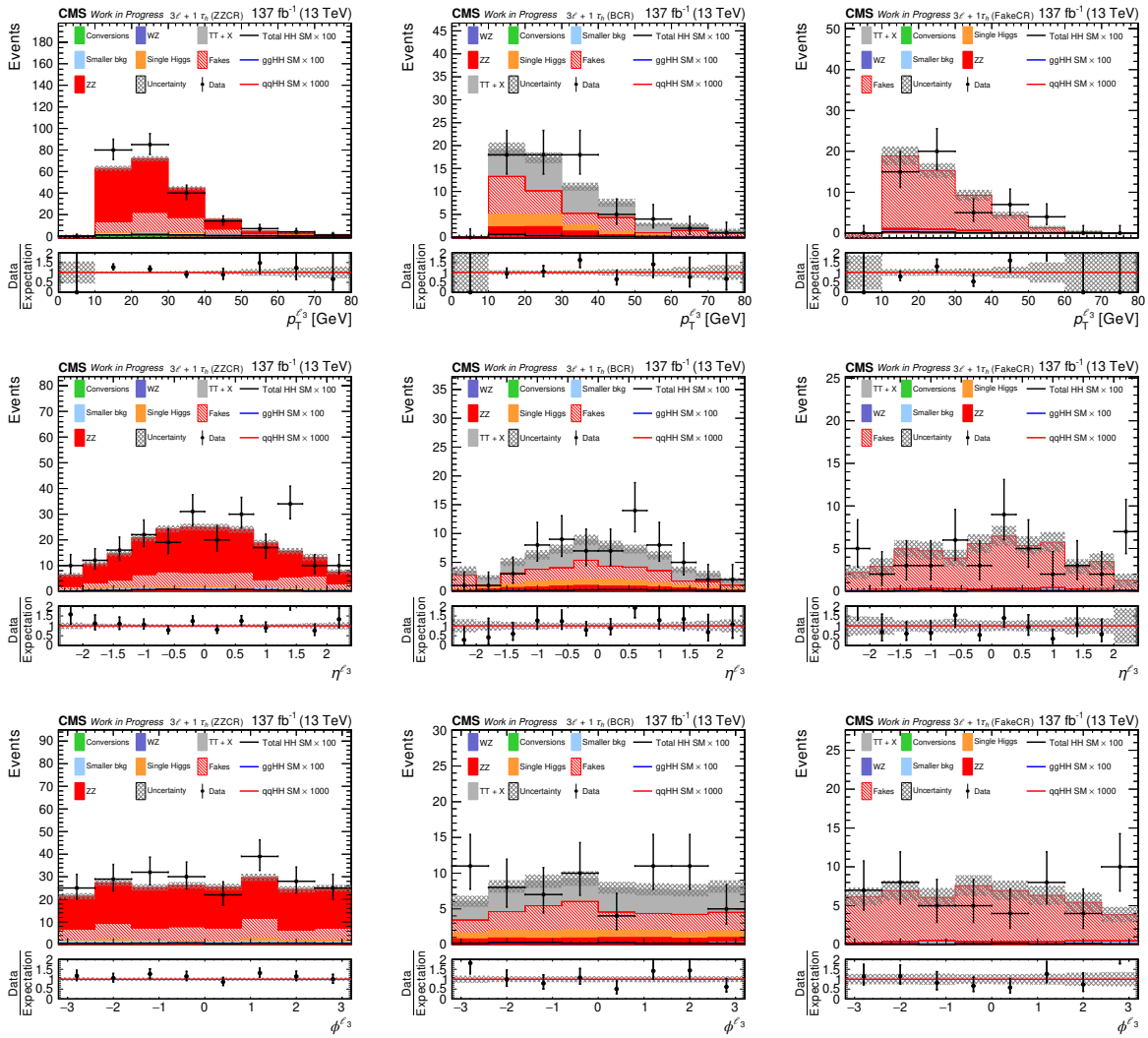

Figure 7.15: Distributions of p_{T}, η and ϕ for the lepton with the third highest p_{T} in the $3\ell+1\tau_{\mathrm{h}}$ ZZCR (left), the $3\ell+1\tau_{\mathrm{h}}$ BCR (center) and the $3\ell+1\tau_{\mathrm{h}}$ FakeCR (right) as defined in Tab. 7.8. The distributions are shown for Run 2 combination of the 2016, 2017 and 2018 dataset. The shown uncertainty bands corresponds to statistical uncertainty contributions only.

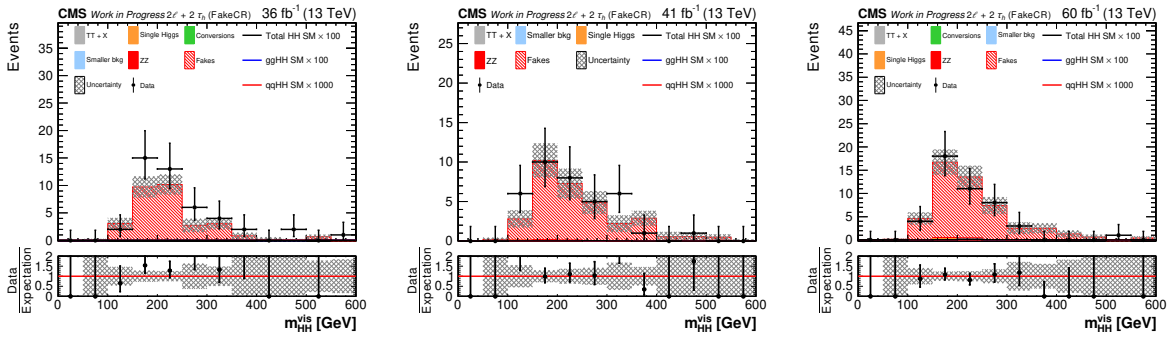

Figure 7.16: Distribution of the visible Di-Higgs mass m_{HH}^{vis}, the invariant mass of both selected leptons and taus for the $2\ell+2\tau_{\mathrm{h}}$FakeCR. The distributions are shown for the 2016, 2017 and 2018 datasets. The shown uncertainty bands corresponds to statistical uncertainty contributions only.

Table 7.8: Selection criteria for the three control regions used for the $3\ell + 1\tau_h$ channel. The fake enriched $3\ell + 1\tau_h$BCR and $3\ell + 1\tau_h$FakeCR as well as the ZZ dominated $3\ell + 1\tau_h$ ZZCR are all obtained by inverting one of the selection criteria of the $3\ell + 1\tau_h$ channel described in Sec. 6.5.1 and summarized in Tab. 6.13. The changed criteria, the Z boson mass requirement, the b-tag and the lepton + τ_h charge requirement are marked in red for the given CR.

Criterion	$3\ell + 1\tau_h$ZZCR	$3\ell + 1\tau_h$BCR	$3\ell + 1\tau_h$FakeCR
Tight ID leptons	3	3	3
Lepton p_T	$>$ 25/15/10 GeV	$>$ 25/15/10 GeV	$>$ 25/15/10 GeV
Tight ID τ_h	≥ 1	≥ 1	≥ 1
Tau p_T	$>$ 20 GeV	$>$ 20 GeV	$>$ 20 GeV
deep Tau WP (vs Electrons)	WP-VLoose	WP-VLoose	WP-VLoose
Tau $\lvert\eta\rvert$ veto	$1.460 \leq \lvert\eta\rvert \geq 1.558$	$1.460 \leq \lvert\eta\rvert \geq 1.558$	$1.460 \leq \lvert\eta\rvert \geq 1.558$
Low mass resonance veto	any $m_{\ell\ell}^{\text{Loose ID}} < 12$ GeV	any $m_{\ell\ell}^{\text{Loose ID}} < 12$ GeV	any $m_{\ell\ell}^{\text{Loose ID}} < 12$ GeV
Z mass requirement	at least one $\lvert m_{\ell\ell}^{\text{SFOS, Loose ID}} - m_Z\rvert < 10$ GeV	-	-
b-jet Veto	any DeepJet-M or >1 DeepJet-L b-tag	no DeepJet-M or <2 DeepJet-L b-tag	any DeepJet-M or >1 DeepJet-L b-tag
Charge Sum	$Q(\tau_h) + \sum_i Q(\ell_i) = 0$	$Q(\tau_h) + \sum_i Q(\ell_i) = 0$	$\lvert Q(\tau_h) + \sum_i Q(\ell_i)\rvert > 0$

Process	2016	2017	2018	Run2
Fakes	29.71±3.37	31.81±3.82	48.55±4.70	110.07±6.93
ZZ	0.40±0.01	0.35±0.01	0.52±0.02	1.28±0.02
Single H	0.01±0.01	0.09±0.08	0.54±0.24	0.65±0.26
$t\bar{t}+X$	−±−	−±−	0.01±0.01	0.02±0.01
Conversion	0.02±0.02	−±−	0.05±0.03	0.07±0.04
Other Backgrounds	0.04±0.02	0.05±0.02	0.05±0.03	0.15±0.04
Total expected background	30.19±3.37	32.3±3.82	49.72±4.70	112.22±6.93
Data observed	45	37	45	127

Table 7.9: Expected and observed yields in the $2\ell+2\tau_h$FakeCR for the years 2016, 2017 and 2018 as well as their Run 2 combination. The given uncertainty corresponds to statistical uncertainty contributions only.

Process	2016	2017	2018	Run2
Fakes	64.6±8.2	46.1±7.7	61.0±9.6	171.7±14.8
ZZ	20.4±0.1	11.3±0.1	21.6±0.1	53.2±0.2
WZ	40.5±1.2	22.9±1.1	40.1±1.2	103.6±2.0
Single H	1.05±0.34	0.44±0.25	0.99±0.36	2.48±0.55
$t\bar{t}+X$	0.11±0.02	0.07±0.01	0.11±0.02	0.29±0.04
Conversion	179.9±13.4	105.0±8.1	138.9±12.6	423.8±20.1
Other Backgrounds	13.7±4.0	6.0±2.2	11.0±4.8	30.7±6.6
Total expected background	320.2±16.3	191.6±11.4	273.9±16.5	785.7±25.9
Data observed	284	179	247	710

Table 7.10: Expected and observed yields in the ConversionCR for the years 2016, 2017 and 2018 as well as their Run 2 combination. The given uncertainty corresponds to statistical uncertainty contributions only.

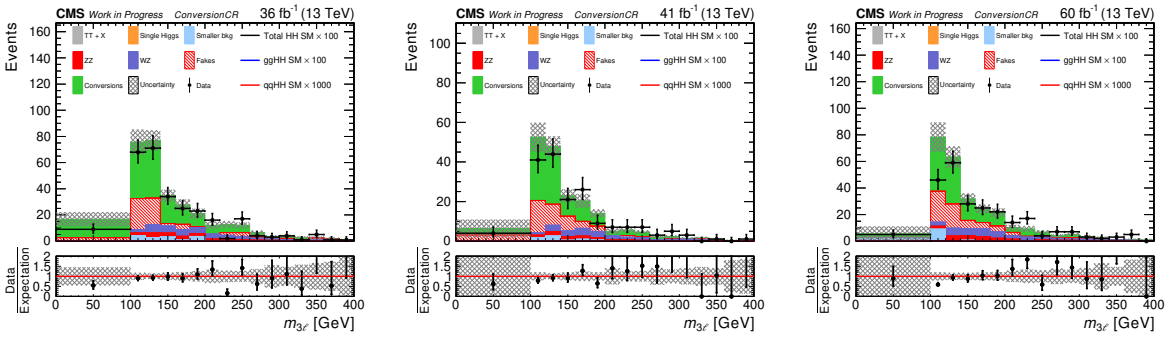

Figure 7.17: Distribution of the three lepton mass $m_{\mu^-\mu^+e}$ in the ConversionCR. The distributions are shown for the 2016, 2017 and 2018 datasets. The shown uncertainty bands corresponds to statistical uncertainty contributions only.

7.4 Results of the HH → Multilepton Analysis

In the following the results of the HH → Multilepton analysis on both resonant HH as well as non resonant HH production are discussed as made public in [4] . Sec. 7.4.1 presents the results for the $3\ell + 1\tau_h$ channel while Sec. 7.4.2 shows the results for the combination of all seven Multilepton channels.
The presented results are also planned to be published with slight modification in [160].

7.4.1 Results of the $3\ell + 1\tau_h$ channel

Fig. 7.18 shows a postfit BDT output distribution in the $3\ell + 1\tau_h$ channel for a combined fit on all HH → Multilepton channels and the two control regions as discussed in Sec. 7.2. No significant deviation from the background hypothesis is found. Within the most signal enriched bin, 6 events are found of which two exceed a BDT score of 0.85. One of these is shown in Fig. 6.2 at the beginning of Sec. 6.

The cross section limits on resonant ggHH production as extracted in the $3\ell + 1\tau_h$ channel are shown in Fig. 7.19 and Fig. 7.20 for heavy spin-0 and spin-2 resonances. In the mass range 250 GeV-1 TeV, no deviation from the background only hypothesis can be observed. Overall the limits for the spin-2 case are found to be slightly stronger than for the spin-0 case. Production cross sections for a new heavy resonance decaying into a pair of Higgs bosons can be excluded in the range of 2.8 pb-440 fb depending on the mass of the heavy resonance. The limits at higher masses are stronger due to the correspondingly higher signal acceptance and better BDT performance. Despite this, the overall mass dependence of the limits in the $3\ell + 1\tau_h$ channel is quite small compared to other channels (see Sec. 7.4.2) and analyses (see Sec. 7.5.1). This makes the $3\ell + 1\tau_h$ channel an important contributor for low mass scenarios.

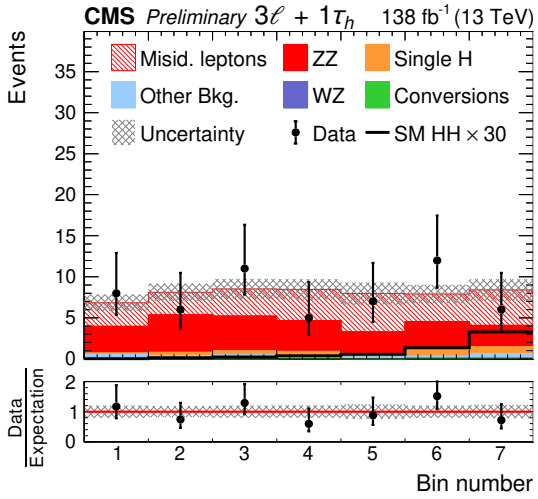

Figure 7.18: Distribution of the output for the JHEP04BM7 tuned $3\ell + 1\tau_h$ nonRes BDT. The binning is chosen such that the background prediction is approximately flat. The plot shows the Run 2 combination as a linear sum of the 2016, 2017 and 2018 postfit distributions from the combined fit to all HH → Multilepton channels and the two CR distributions for SM like ggHH + qqHH signal. For better visibility, the signal shown corresponds to 30 × the SM signal strength while the best fit value for the signal strength modifier corresponds to $\hat{r} = \sigma/\sigma_{\text{theo}} = 1.96^{+10.57}_{-9.98}$. (made public in [4])

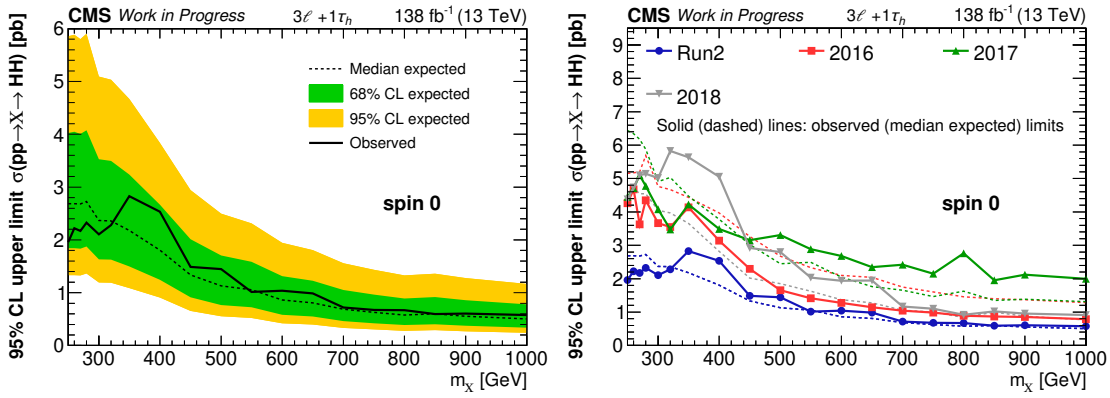

R

Figure 7.19: Expected and observed cross section limits at 95% confidence level (CL) on resonant HH production for a heavy spin-0 resonance in the mass range 250 GeV - 1 TeV. **Left:** The full Run 2 data collected in the $3\ell+1\tau_h$ channel **Right:** the data collected in the 2016, 2017 and 2018 separately compared to the Run 2 result.

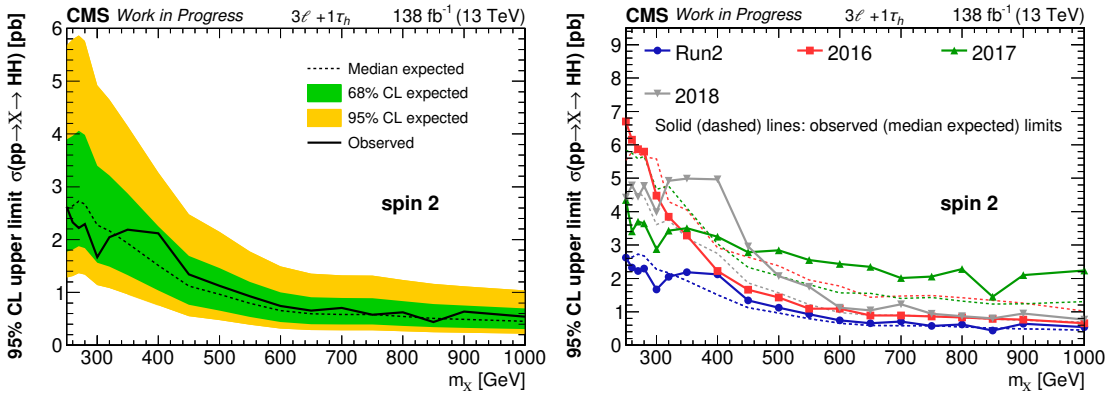

Figure 7.20: Expected and observed cross section limits at 95% confidence level (CL) on resonant HH production for a heavy spin-2 resonance in the mass range 250 GeV - 1 TeV. **Left:** For the full Run 2 data collected in the $3\ell+1\tau_h$ channel. **Right:** For the data collected in the 2016, 2017 and 2018 separately compared to the Run 2 result.

Fig. 7.21 shows the limit on SM like non-resonant HH production. For the limit on the corresponding cross section, theoretical uncertainties on the SM HH cross section are frozen, yielding an observed (expected) 95% confidence level (CL) upper limit on the total HH cross section for SM kinematics of 1.40 pb (1.92 pb). The observed (expected) limit on the SM HH production rate is $45.2 \times \sigma_{\mathrm{HH}}^{\mathrm{SM}}$ ($63.0 \times \sigma_{\mathrm{HH}}^{\mathrm{SM}}$).

Fig. 7.22 shows the 95% CL upper limit on the non-resonant HH production cross section and signal strength modifier $r = \sigma_{\mathrm{HH}}/\sigma_{\mathrm{HH}}^{\mathrm{theo}}$ as a function of κ_λ. Overall cross section limits between about 3 pb for high κ_λ scenarios and 2 pb for κ_λ scenarios in the interference region are extracted. The slightly lower performance for high κ_λ is expected as these correspond to a softer m_{HH} mass spectrum where both signal acceptance and BDT performance are lower. Similar as for the limits on resonant HH, the limits for different κ_λ are very uniform, delivering comparatively strong limits in the difficult high $|\kappa_\lambda|$ regime. From the limit on r, the observed (expected) 95% CL limit on the Higgs boson trilinear self-coupling modifier κ_λ is found to be $-13.00 < \kappa_\lambda < 16.75$ ($-12.91 < \kappa_\lambda < 16.93$).

In the SM the ggHH production cross section depends both on the trilinear Higgs boson self-coupling modifier κ_λ as well as the coupling between Higgs boson and top quark κ_t. Fig. 7.23 shows a two dimensional limit scan in κ_λ-κ_t. Both the limits on κ_λ and κ_t as well as their best fit value are found to be in agreement with the SM.

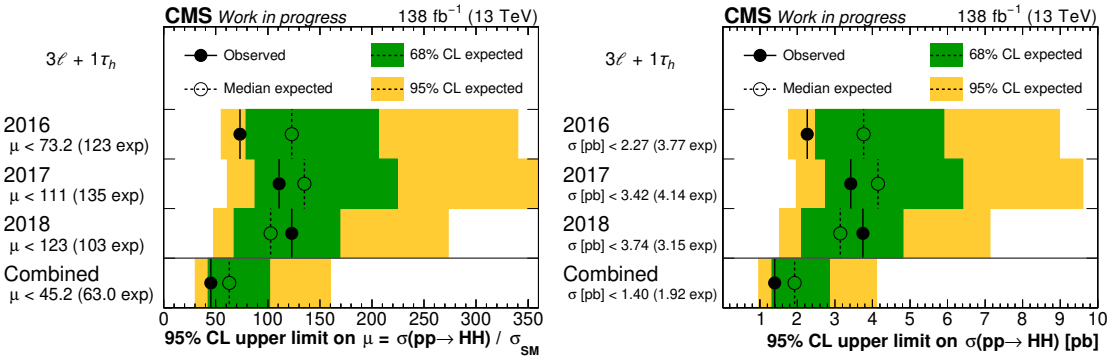

Figure 7.21: Limits on SM like HH production in the $3\ell + 1\tau_h$ channel for the years 2016, 2017 and 2018 as well as their combination. **Left:** The 95% confidence level (CL) upper limit on the signal strength modifier $r = \sigma(pp \to \mathrm{HH})/\sigma_{\mathrm{SM}}$. **Right:** The limit on the corresponding HH production cross section. For the cross section limit, theoretical uncertainties on σ_{SM} are frozen. For both limits the SM tuned output of the $3\ell + 1\tau_h$ nonRes BDT is used.

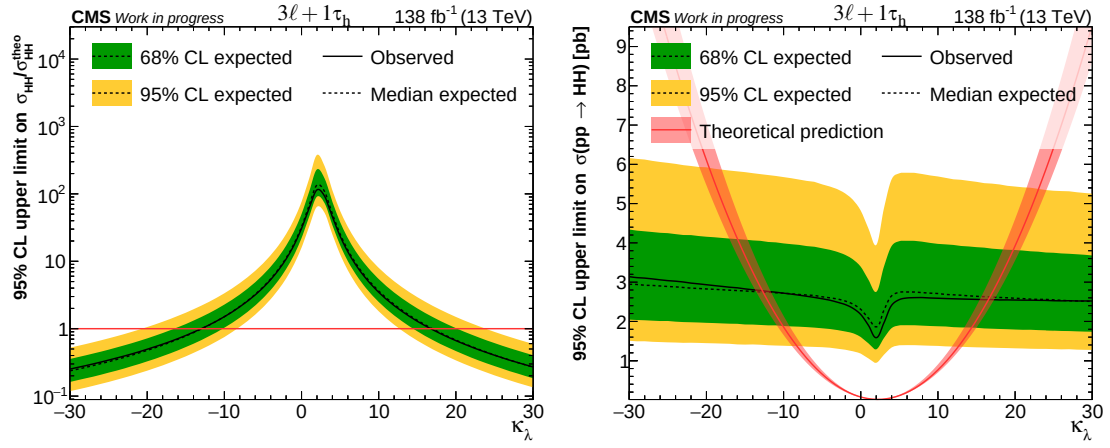

Figure 7.22: **Left:** The 95% CL upper limit on the HH signal strength modifier $r = \sigma_{\mathrm{HH}}/\sigma^{\mathrm{theo}}_{\mathrm{HH}}$ (μ). The intersection of the limit with the line at one correspond to the observed (expected) limit on κ_λ of $-13.00 < \kappa_\lambda < 16.75$ ($-12.91 < \kappa_\lambda < 16.93$). **Right:** The HH production cross section(on the right) as a function of κ_λ. For the cross section limit, theoretical uncertainties on σ_{theo} are frozen. For both limits the JHEP04BM7 tuned output of the $3\ell + 1\tau_h$ nonRes BDT is used.

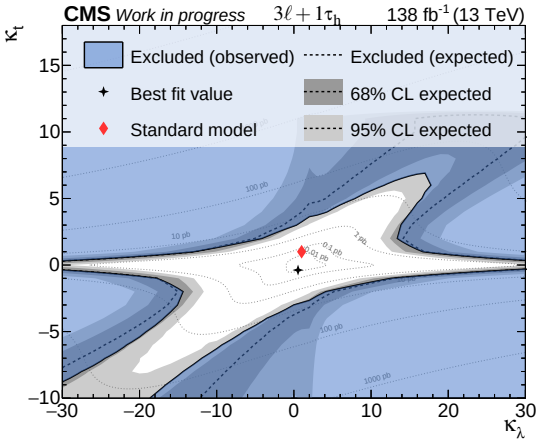

Figure 7.23: Limit at 95% CL on non-resonant HH production in the κ_λ-κ_t space for the $3\ell + 1\tau_h$ channel . The coupling point ($\kappa_\lambda = 1$, $\kappa_t = 1$) corresponding to the standard model as well as the best fit value for κ_λ, κ_t is shown as well. For reference the theory cross section is given in contour lines. For this scan, the JHEP04BM7 tuned output of the $3\ell + 1\tau_h$ nonRes BDT is used.

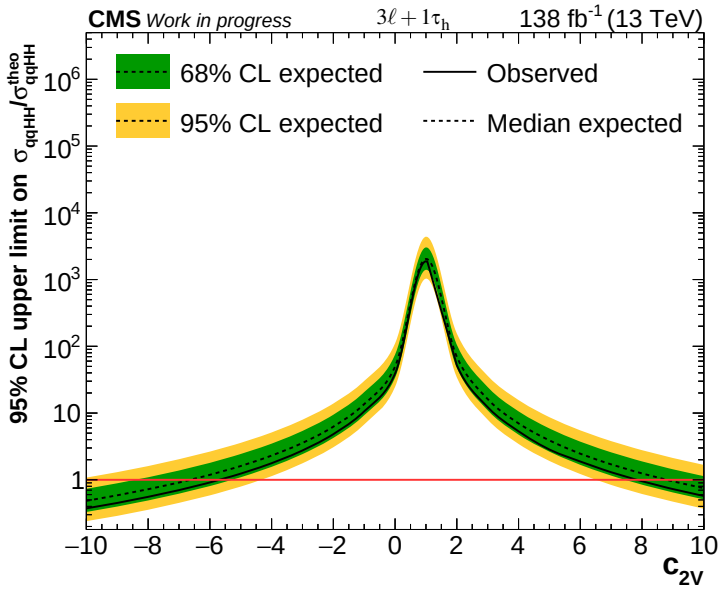

Figure 7.24: The 95% CL limits in the $3\ell + 1\tau_h$ channel on the coupling strength modifier for non-resonant qqHH production $r_{\mathrm{qqHH}} = \sigma_{\mathrm{qqHH}}/\sigma^{\mathrm{theo}}_{\mathrm{qqHH}}$ for different values of the coupling c_{2V}. The intersection of the limit with the line at one corresponds to the observed (expected) limit on c_{2V} of $-5.73 < c_{2V} < 7.86$ ($-6.68 < c_{2V} < 8.83$).

Fig. 7.24 shows the 95% CL limits on the coupling strength modifier for non-resonant qqHH production $r_{\mathrm{qqHH}} = \sigma_{\mathrm{qqHH}}/\sigma^{\mathrm{theo}}_{\mathrm{qqHH}}$ for different values of the coupling c_{2V}. As described in previous sections, the presented analysis is not very sensitive to this VBF like HH production and the observed (expected) limits on r_{qqHH} for SM like qqHH production is found to be 1880 $\times\sigma^{\mathrm{SM}}_{\mathrm{qqHH}}$ (2036 $\times\sigma^{\mathrm{SM}}_{\mathrm{qqHH}}$) and an observed (expected) 95% CL limit on c_{2V} of $-5.73 < c_{2V} < 7.86$ ($-6.68 < c_{2V} < 8.83$) can be placed.

Limits at 95% CL on the ggHH production cross section for the different EFT BM scenarios discussed in Sec. 6.2.4 are shown in Fig. 7.25 and Fig. 7.26 for both the JHEP04 and JHEP03 set of benchmark points. Overall cross section limits in the range between 734 fb and 2.6 pb are found. Only a small dependence of the limit strength on the different physics cases is found, underlining the importance of this channel for more difficult BM scenarios like JHEP04BM7

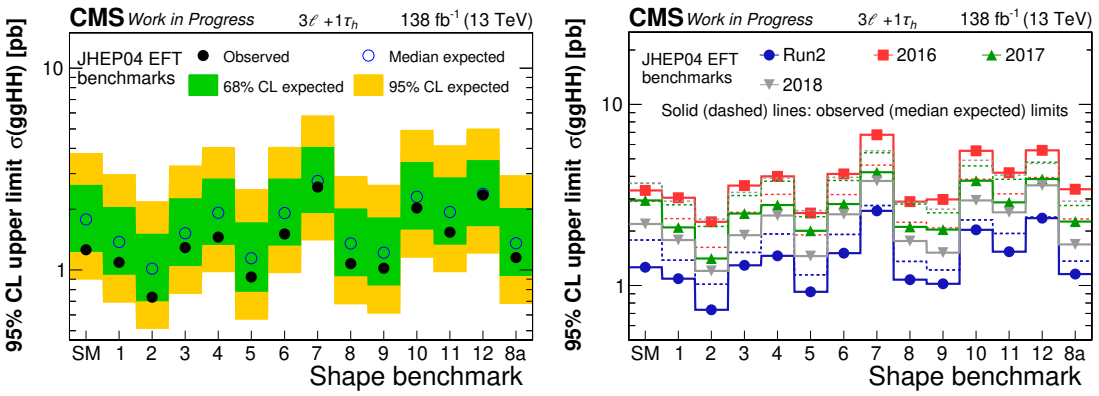

Figure 7.25: Limits for the $3\ell + 1\tau_h$ channel at 95% CL on the ggHH production cross section for the EFT benchmark scenarios features in [28] (JHEP04BM1-12) and [20] (JHEP04BM8a) as discussed in Sec. 6.2.4. **Left:** For the full Run 2 data collected in the $3\ell + 1\tau_h$ channel. **Right:**For the data collected in the 2016, 2017 and 2018 separately compared to the Run 2 result.

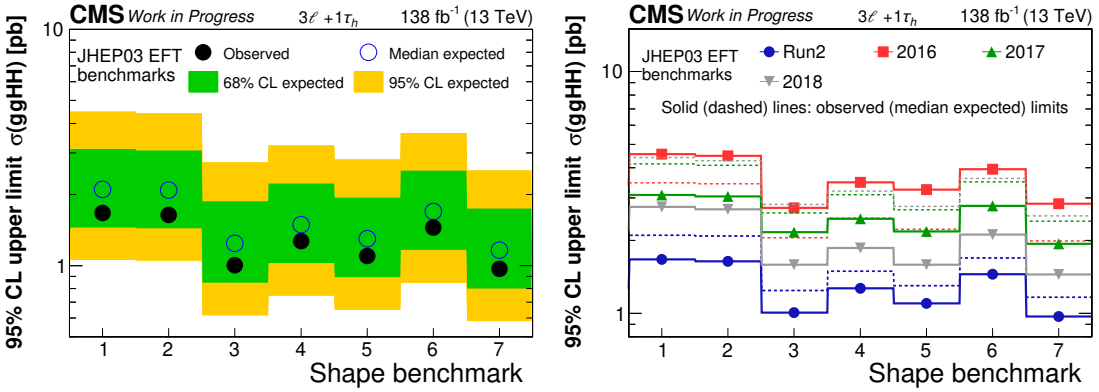

Figure 7.26: Limits for the $3\ell + 1\tau_h$ channel at 95% CL on the ggHH production cross section for the EFT benchmark scenarios features in [134] as discussed in Sec. 6.2.4. **Left:** For the full Run 2 data collected in the $3\ell + 1\tau_h$ channel. **Right:**For the data collected in the 2016, 2017 and 2018 separately compared to the Run 2 result.

corresponding to a soft m_{HH} spectrum.

As discussed in Sec. 7.2.1 a physics model is developed for limit scans in the EFT coupling parameter c_2. Fig. 7.27 shows the 95% CL upper limit on the HH production cross section and signal strength modifier $r = \sigma_{\mathrm{HH}}/\sigma_{\mathrm{HH}}^{\mathrm{theo}}$ as a function of c_2. Overall the cross section limits are very similar across the displayed range in c_2 and vary between about 1.5 pb for high c_2 scenarios and 2 pb for scenarios with small c_2. The slightly higher performance for high c_2 is expected as these correspond to a more energetic m_{HH} mass spectrum. From the limit on r, the observed (expected) 95% CL limit on the Higgs boson EFT coupling parameter c_2 is found to be $-1.79 < c_2 < 2.21$ ($-1.95 < c_2 < 2.39$).

Fig. 7.28 shows two dimensional limit scans in c_2-κ_{t} and c_2-κ_λ. The limits on κ_λ, κ_{t} and c_2 as well as their best fit value are found to be in agreement with the SM.

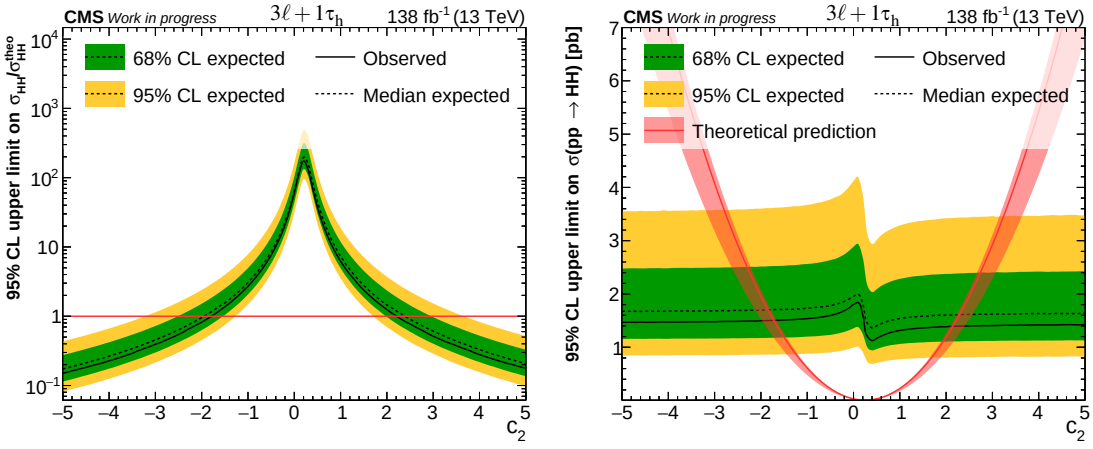

Figure 7.27: **Left:** The 95% CL upper limit on the HH signal strength modifier $r = \sigma_{HH}/\sigma_{HH}^{theo}$ (μ). The intersection of the limit with the line at one corresponds to the observed (expected) limit on c_2 of $-1.79 < c_2 < 2.21$ ($-1.95 < c_2 < 2.39$). **Right:** The HH production cross section as a function of c_2. For the cross section limit, theoretical uncertainties on σ_{theo} are frozen. For both limits the JHEP04BM7 tuned output of the $3\ell + 1\tau_h$ nonRes BDT is used.

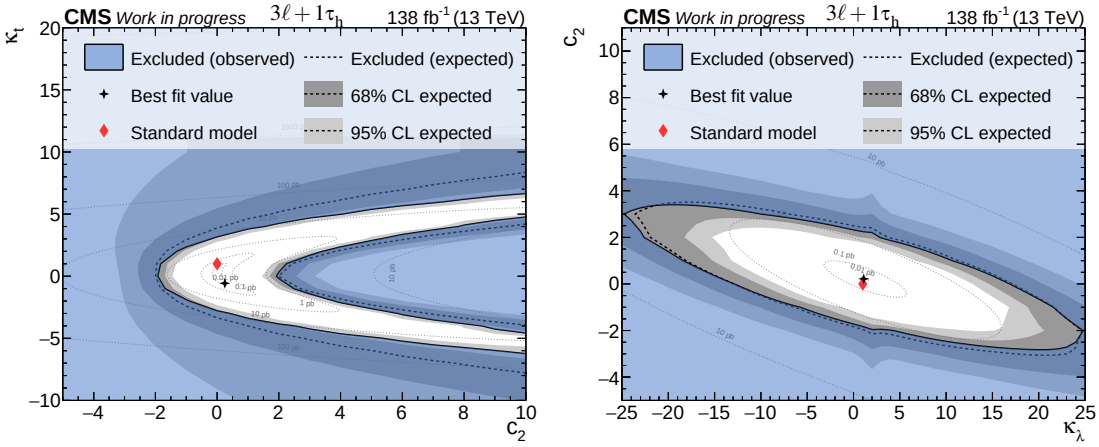

Figure 7.28: **Left:** Limit at 95% CL on non-resonant HH production in the c_2-κ_t space for the $3\ell + 1\tau_h$ channel. **Right:** Limit at 95% CL on non-resonant HH production in the κ_λ-κ_t space for the $3\ell + 1\tau_h$ channel. The coupling point ($c_2 = 0$, $\kappa_t = 1$, $\kappa_\lambda = 1$) corresponding to the Standard Model as well as the best fit values for the given coupling combination are shown as well. For reference the theory cross section is given in contour lines. For these scans, the JHEP04BM7 tuned output of the $3\ell + 1\tau_h$ nonRes BDT is used.

7.4.2 Results for the $\mathrm{HH} \rightarrow$ Multilepton combination

The following presents the $\mathrm{HH} \rightarrow$ Multilepton results as also reported in [4].
Fig. 7.29 shows postfit BDT distributions for a combined fit with SM like $\mathrm{ggHH} + \mathrm{qqHH}$ signal to the JHEP04BM7 tuned nonRes BDT output of all seven channels and the two CR distributions. The displayed signal corresponds to 30 times the SM signal strength. The best fit signal strength for the given scenario is $\hat{r} = 1.96^{+10.57}_{-9.98}$. While the 2ℓ(ss) + 0/1 τ_h and the $3\ell + 0\tau_\mathrm{h}$ channel show a small excess in the high BDT score region, no significant deviation from the background only or the SM hypothesis is found. The corresponding postfit event yields for the signal regions can be found in Tab. 7.11. More postfit distributions split by data taking year can be found in Appendix **F**. Upper limits at 95% CL on resonant ggHH production for the combination of all seven
$\mathrm{HH} \rightarrow$ Multilepton event channels and the two control regions as well as for the individual channels are shown in Fig. 7.30 and Fig. 7.31 for heavy spin-0 and spin-2 resonances in the mass range 250 GeV-1 TeV. A small $\mathcal{O}$(1.5-2) σ excess is observed for high mass scenarios mostly originating from the 2ℓ(ss) + 0/1 τ_h and $3\ell + 0\tau_\mathrm{h}$ channels. The access is visible over a rather large mass range, which can be explained by the rather broad Di-Higgs mass resolution of the $\mathrm{HH} \rightarrow$ Multilepton event channels and the subsequent high correlation of BDT outputs for close by mass scenarios ($\mathcal{O}$(100-200 GeV)). Overall the limits for the spin-2 case are found to be slightly stronger than for the spin-0 case. Production cross sections for a new heavy resonance decaying into a pair of Higgs bosons can be excluded in the range of 1 pb-200 fb depending on the mass of the heavy resonance. The overall mass dependence especially for the $3\ell + 1\tau_\mathrm{h}$ and 4ℓ channels is quite small compared to other channels and analyses. This makes the $\mathrm{HH} \rightarrow$ Multilepton analysis an important contributor for low mass scenarios.
Fig. 7.32 shows the limit on SM like non-resonant HH production. For the limit on the corresponding cross section, theoretical uncertainties on the SM HH cross section are frozen, thus the observed (expected) 95% confidence level (CL) upper limit on the total HH cross section for SM kinematics amounts to 659 fb (598 fb) while the observed (expected) limit on the SM HH production rate correspond to 21.8 $\times \sigma^{\mathrm{SM}}_{\mathrm{HH}}$ (19.6 $\times \sigma^{\mathrm{SM}}_{\mathrm{HH}}$). The strongest individual limit is observed in the $3\ell + 1\tau_\mathrm{h}$ channel, while the best sensitivity for SM like production is given by the $3\ell + 0\tau_\mathrm{h}$ and $1\ell + 3\tau_\mathrm{h}$ channels.
Fig. 7.33 shows the 95% CL upper limit on the HH production cross section and signal strength modifier $r = \sigma_{\mathrm{HH}}/\sigma^{\mathrm{theo}}_{\mathrm{HH}}$ as a function of κ_λ. Overall cross section limits between about 1 pb for high $|\kappa_\lambda|$ scenarios and 500 fb for κ_λ scenarios in the $\square$-$\triangle$ interference region are extracted. Similar as for the result in the $3\ell + 1\tau_\mathrm{h}$ channel, the slightly lower performance for high κ_λ is expected as these values correspond to a less energetic m_{HH} mass spectrum. From the limit on r, the observed (expected) 95% CL limit on the Higgs boson trilinear self-coupling modifier κ_λ is found to be $-6.98 < \kappa_\lambda < 11.17$ ($-6.98 < \kappa_\lambda < 11.73$). Fig. 7.34 shows a comparison of the limits on r and σ for the seven different channels and their combination. The overall most sensitive channel is found to be $3\ell + 0\tau_\mathrm{h}$ with strong contributions from $3\ell + 1\tau_\mathrm{h}$ at highly positive κ_λ and $1\ell + 3\tau_\mathrm{h}$ at highly negative κ_λ. The strongest observed limit over most of the κ_λ range is given by $3\ell + 1\tau_\mathrm{h}$. Depending on the contribution of fermionic and bosonic Higgs boson decays, the branching fraction scaling described in Sec. 2.3 leads to a tilt of the mostly flat cross

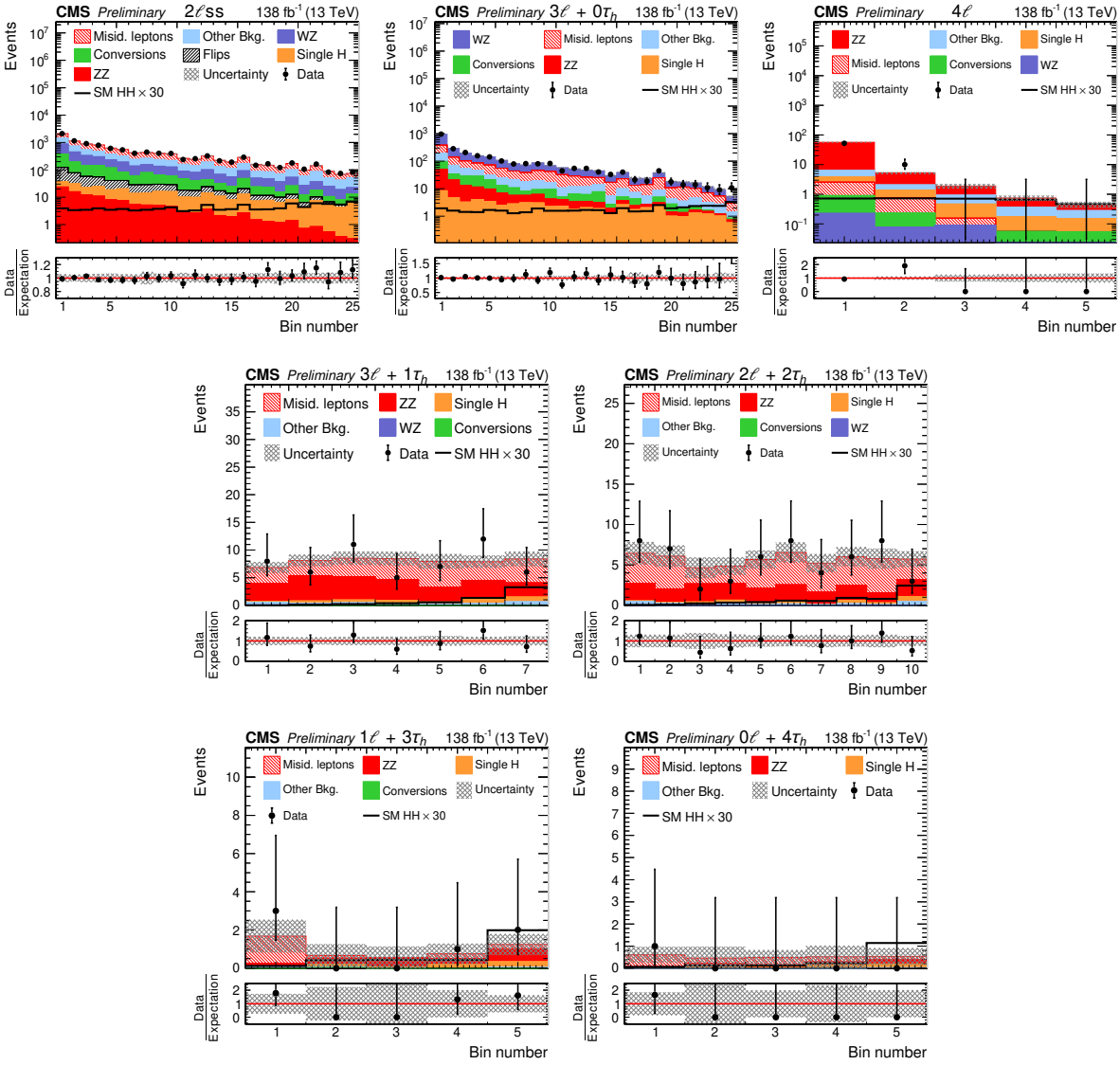

Figure 7.29: Distribution of the output for the JHEP04BM7 tuned nonRes BDT for all seven HH $\rightarrow$ Multilepton channels, from top-left to bottom right: the 2ℓ(ss) + 0/1 τ_h, $3\ell+0\tau_h$, 4ℓ, $3\ell+1\tau_h$, $2\ell+2\tau_h$, $1\ell+3\tau_h$, and the $0\ell+4\tau_h$ channel. The binning is chosen such that for the 2ℓ(ss) + 0/1 τ_h, $3\ell+0\tau_h$, and 4ℓ channel (top row) the signal is approximately flat and for the other channels the background is flat. The plots show the Run 2 combination as a linear sum of the 2016, 2017 and 2018 postfit distributions from the combined fit to all HH $\rightarrow$ Multilepton channels and the two CR distributions for SM like ggHH + qqHH signal. For better visibility, the shown corresponds to 30 $\times$ the SM signal strength while the best fit value for the signal strength modifier corresponds to $\hat{r} = \hat{\sigma}/\sigma_{SM} = 1.96^{+10.57}_{-9.98}$. (made public in [4])

Process	2ℓ(ss) + 0/1 τ_h	$3\ell + 0\tau_h$	4ℓ
SM HH $\to VVVV$ ($\times 30$)	72.9 ± 1.6	33.0 ± 0.7	2.23 ± 0.11
SM HH $\to VV\tau\tau$ ($\times 30$)	30.8 ± 0.7	11.9 ± 0.4	0.95 ± 0.07
SM HH $\to \tau\tau\tau\tau$ ($\times 30$)	2.7 ± 0.1	1.0 ± 0.0	0.10 ± 0.01
WZ	2013.7 ± 17.2	1323.0 ± 11.7	0.44 ± 0.06
ZZ	122.6 ± 0.5	110.2 ± 0.8	54.76 ± 1.59
Conversion	1001.9 ± 60.8	145.5 ± 11.4	0.89 ± 0.35
Fakes	3952.0 ± 81.3	668.4 ± 25.8	2.28 ± 1.02
Flips background	366.4 ± 17.8	< 0.1	< 0.01
Single Higgs	215.5 ± 2.2	61.6 ± 0.6	2.42 ± 0.32
Other backgrounds	2671.9 ± 72.2	292.1 ± 10.5	3.97 ± 0.22
Total expected background	10344.0 ± 86.1	2600.8 ± 31.2	64.77 ± 1.74
Data	10344	2621	62

Process	$0\ell + 4\tau_h$	$1\ell + 3\tau_h$	$2\ell + 2\tau_h$	$3\ell + 1\tau_h$
SM HH $\to VVVV$ ($\times 30$)	0.26 ± 0.01	0.19 ± 0.02	0.16 ± 0.04	0.91 ± 0.05
SM HH $\to VV\tau\tau$ ($\times 30$)	0.07 ± 0.03	0.61 ± 0.14	3.94 ± 0.37	4.13 ± 0.24
SM HH $\to \tau\tau\tau\tau$ ($\times 30$)	1.32 ± 0.20	2.59 ± 0.28	2.30 ± 0.13	0.89 ± 0.05
WZ	< 0.01	< 0.01	0.02 ± 0.01	0.16 ± 0.01
ZZ	0.70 ± 0.05	1.91 ± 0.12	18.56 ± 0.41	24.29 ± 0.33
Conversion	< 0.01	0.02 ± 0.03	0.10 ± 0.05	0.14 ± 0.02
Fakes	1.49 ± 0.94	2.01 ± 1.42	33.36 ± 3.75	25.14 ± 3.12
Single Higgs	0.38 ± 0.13	0.76 ± 0.25	2.86 ± 0.50	3.80 ± 0.19
Other backgrounds	0.02 ± 0.02	0.12 ± 0.04	2.11 ± 0.22	2.66 ± 0.13
Total expected background	2.59 ± 0.96	4.82 ± 1.45	57.00 ± 3.81	56.20 ± 3.23
Data	1	6	55	55

Process	3ℓCR	4ℓCR
WZ	12554.7 ± 56.3	< 0.1
ZZ	800.0 ± 6.4	2033.9 ± 20.0
Conversion	133.2 ± 8.1	2.9 ± 0.1
Fakes	906.0 ± 38.0	13.2 ± 3.9
Other backgrounds	615.8 ± 14.2	58.7 ± 1.6
Total expected background	15009.7 ± 63.7	2108.6 ± 13.1
Data	14994	2096

Table 7.11: Event yields for each of the seven HH $\to$ Multilepton event channels and the two WZ and ZZ control regions. The HH signal corresponds to 30 times the SM expectation for the sum of ggHH and qqHH. The yields and uncertainties for the different backgrounds correspond to the complete Run 2 expectation obtained by summing the postfit event yields for the 2016, 2017 and 2018 data taking periods. (made public in [4])

section limits either towards positive κ_λ as in the HH $\to$ 4W dominated 2ℓ(ss) + 0/1 τ_h channel, or negative κ_λ in case of the HH $\to 4\tau$ dominated $1\ell + 3\tau_h$ channel.

Fig. 7.35 shows a two dimensional limit scan in κ_λ-κ_t. Both the limits on κ_λ and κ_t as well as their best fit value are found to be in agreement with the SM.

Fig. 7.36 shows the 95% CL limits on the coupling strength modifier for non-resonant qqHH production $r_{\mathrm{qqHH}} = \sigma_{\mathrm{qqHH}}/\sigma^{\mathrm{theo}}_{\mathrm{qqHH}}$ for different values of the coupling c_{2V}. As described in previous sections, the presented analysis is not very sensitive to this VBF like HH production

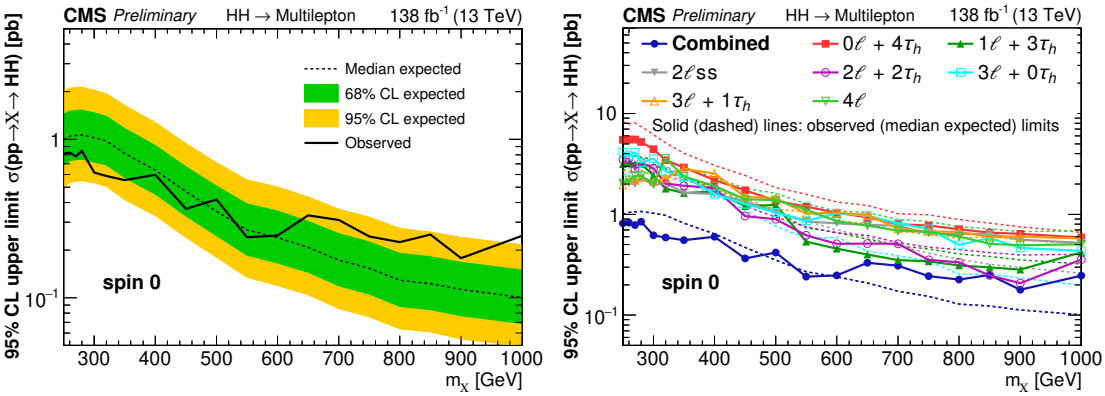

Figure 7.30: Expected and observed cross section limits at 95% CL on resonant ggHH production for a heavy spin-0 resonance in the mass range 250 GeV - 1 TeV. **Left:** For the full Run 2 data collected in the combination of all seven event channels and the two control regions. **Right:** For the data collected in the individual event channels separately, and compared to the combined Run 2 HH → Multilepton result. (made public in [4])

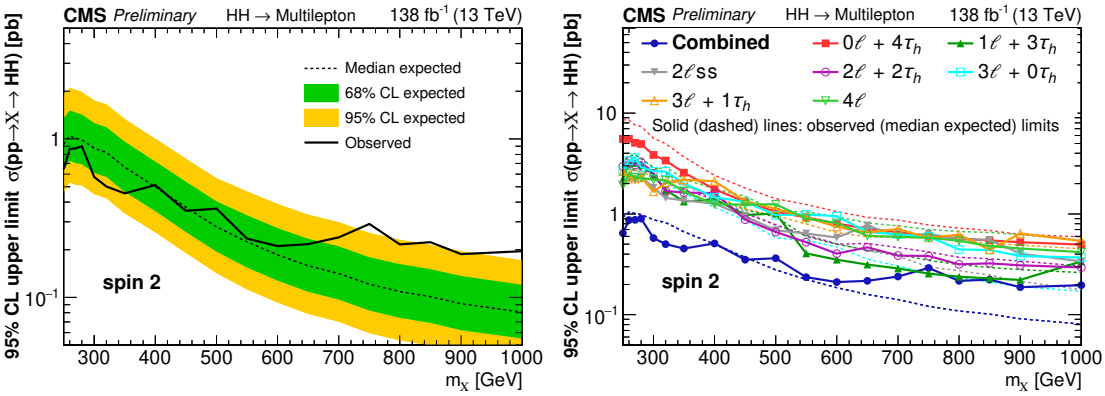

Figure 7.31: Expected and observed cross section limits at 95% CL on resonant ggHH production for a heavy spin-2 resonance in the mass range 250 GeV - 1 TeV. **Left:** For the full Run 2 data collected in the combination of all seven event channels and the two control regions. **Right:** For the data collected in the individual event channels separately, and compared to the combined Run 2 HH → Multilepton result. (made public in [4])

and the observed (expected) limits on r_{qqHH} for SM like qqHH production is found to be 360 $\times\sigma^{\mathrm{SM}}_{\mathrm{qqHH}}$ (496 $\times\sigma^{\mathrm{SM}}_{\mathrm{qqHH}}$) and an observed (expected) 95% CL limit on c_{2V} of $-3.42 < c_{2V} < 5.56$ ($-2.73 < c_{2V} < 4.83$) can be placed. The displayed sensitivity is mostly delivered by the higher statistics 2ℓ(ss) + 0/1 τ_{h} and $3\ell + 0\tau_{\mathrm{h}}$ channels.

Limits at 95% CL on the ggHH production cross section for the different EFT BM scenarios discussed in Sec. 6.2.4 are shown in Fig. 7.37 and Fig. 7.38 for both the JHEP04 and JHEP03 set of benchmark points. An overview is also given in Tab. 7.12. Overall cross section limits in the range between 200 fb and 1.2 pb are found.

Fig. 7.39 shows the 95% CL upper limit on the HH production cross section and signal strength modifier $r = \sigma_{\mathrm{HH}}/\sigma^{\mathrm{theo}}_{\mathrm{HH}}$ as a function of the EFT coupling parameter c_2. Overall the cross section limits are very similar across the displayed range in c_2 and very between about 1.5 pb for high c_2 scenarios and 2 pb for scenarios with vanishing c_2. The slightly higher performance for high c_2 is expected as these correspond to a more energetic m_{HH} mass spectrum. As scenarios corresponding to higher values of c_2 correspond to a more energetic m_{HH} spectrum, this measurement takes most of its sensitivity from the 2ℓ(ss) + 0/1 τ_{h} and $3\ell + 0\tau_{\mathrm{h}}$ that also for resonant HH provide the best sensitivity at high masses. From the limit on r, the observed (expected)

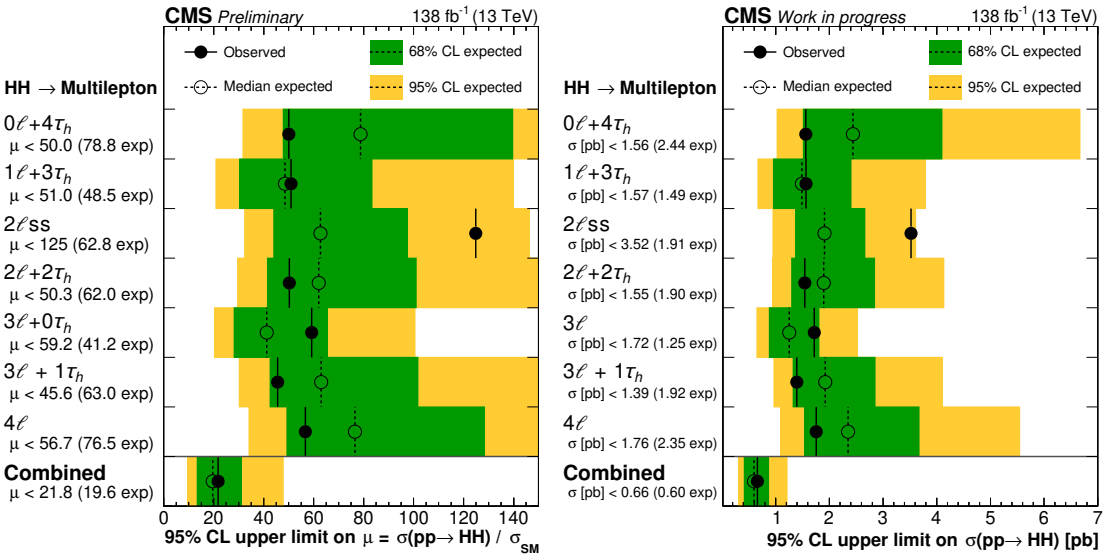

Figure 7.32: Limits on SM like HH production for the different HH $\rightarrow$ Multilepton event channels as well as their combination. **Left:** The 95% confidence level (CL) upper limit on the signal strength modifier $\mu = r = \sigma(\mathrm{pp} \rightarrow \mathrm{HH})/\sigma_{\mathrm{SM}}$. **Right:** The limit on the corresponding HH production cross section. For the cross section limit, theoretical uncertainties on σ_{SM} are frozen. For both limits the SM tuned output of the nonRes BDT is used. (left figure made public in[4])

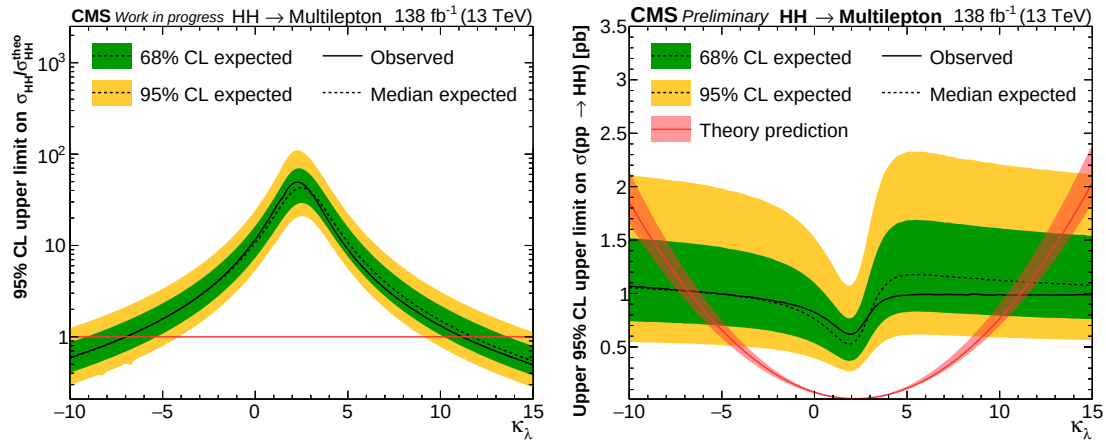

Figure 7.33: **Left:** The 95% CL upper limit on the HH signal strength modifier $r = \sigma(\mathrm{pp} \rightarrow \mathrm{HH})/\sigma_{\mathrm{SM}}$. The intersection of the limit with the line at one corresponds to the observed (expected) limit on κ_λ of $-6.98 < \kappa_\lambda < 11.17$ ($-6.98 < \kappa_\lambda < 11.73$). **Right:** The HH production cross section as a function of the trilinear Higgs boson self-coupling κ_λ for the combination of all HH $\rightarrow$ Multilepton channels. For the cross section limit, theoretical uncertainties on $\sigma_{\mathrm{HH}}^{\mathrm{theo}}$ are frozen. For both limits the JHEP04BM7 tuned output of the nonRes BDT is used. (right figure made public in [4])

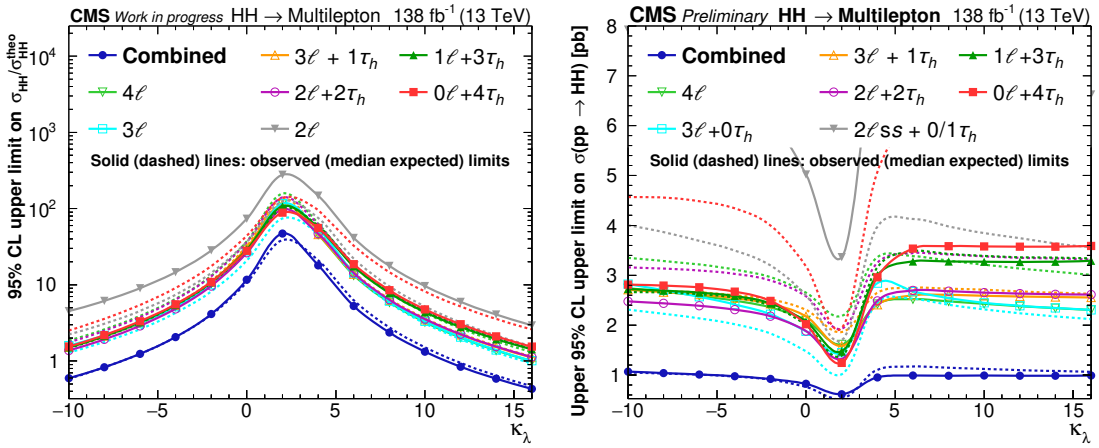

Figure 7.34: **Left:** The 95% CL upper limit on the HH signal strength modifier $r = \sigma_{\mathrm{HH}}/\sigma_{\mathrm{HH}}^{\mathrm{theo}}$ for the individual HH → Multilepton channels and their combination. **Right:** The HH production cross section as a function of the trilinear Higgs boson self-coupling κ_λ for the individual HH → Multilepton channels and their combination. For the cross section limit, theoretical uncertainties on $\sigma_{\mathrm{HH}}^{\mathrm{theo}}$ are frozen. For both limits the JHEP04BM7 tuned output of the nonRes BDT is used. (right figure made public in [4])

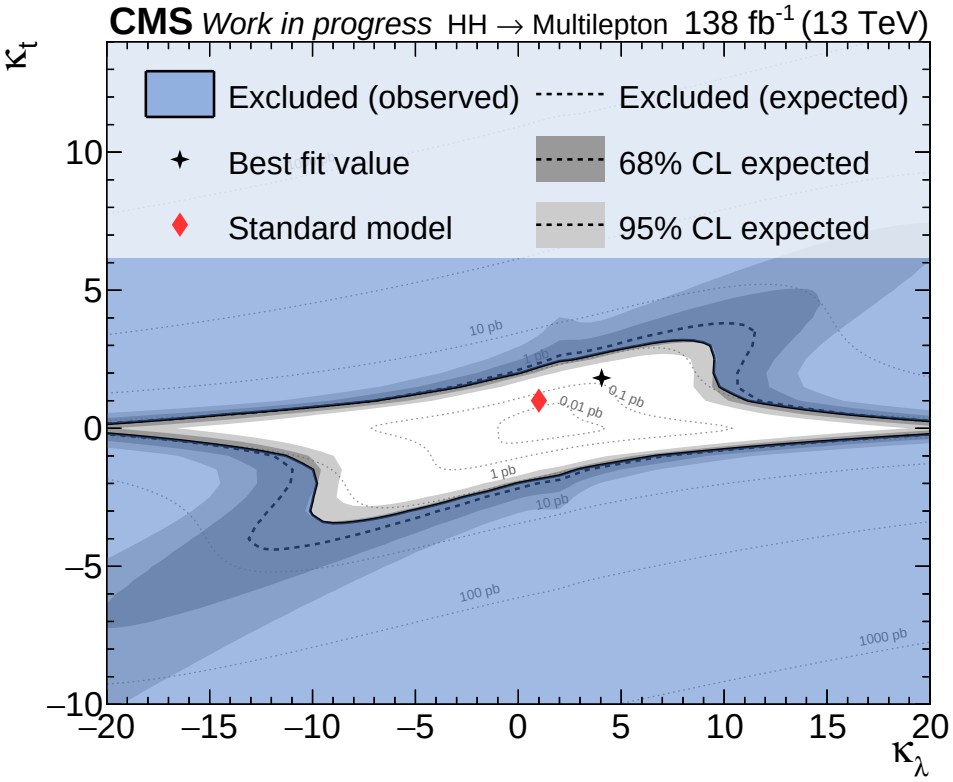

Figure 7.35: Limit at 95% CL on non-resonant HH production in the κ_λ-κ_t space. Shown is the result of the combination of all seven HH → Multilepton channels . The coupling point ($\kappa_\lambda = 1$, $\kappa_t = 1$) corresponding to the Standard Model as well as the best fit value for κ_λ, κ_t is shown as well. For reference the theory cross section is given in contour lines. For this scan, the JHEP04BM7 tuned output of the nonRes BDT is used.

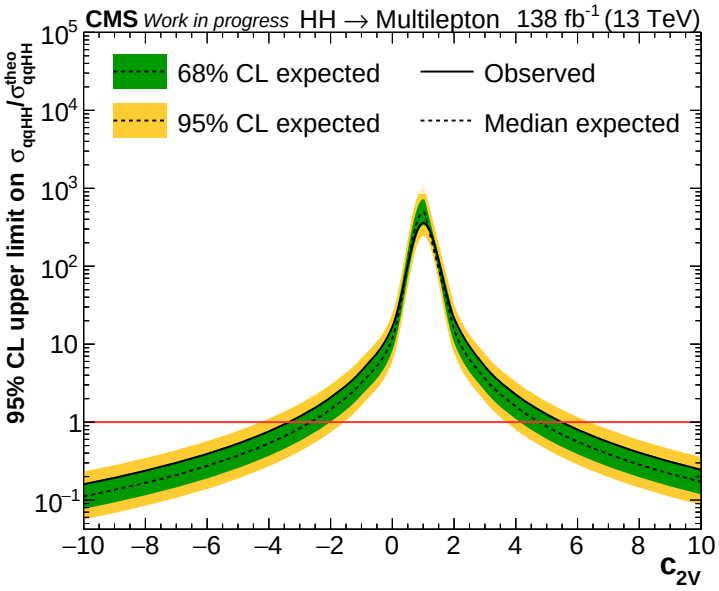

Figure 7.36: The 95% CL limits on the coupling strength modifier for non-resonant qqHH production $r_{\mathrm{qqHH}} = \sigma_{\mathrm{qqHH}}/\sigma^{\mathrm{theo}}_{\mathrm{qqHH}}$ for different values of the coupling c_{2V}. The intersection of the limit with the line at one corresponds to the observed (expected) limit on c_{2V} of $-3.42 < c_{2V} < 5.56$ ($-2.73 < c_{2V} < 4.83$).

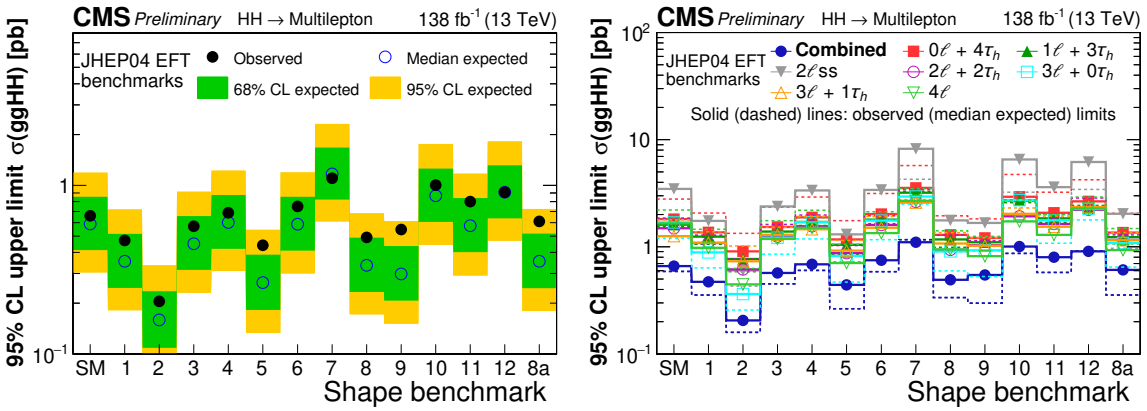

Figure 7.37: Upper limits at 95% CL on the ggHH production cross section for the EFT benchmark scenarios features in [28] (JHEP04BM1-12) and [20] (JHEP04BM8a) as discussed in Sec. 6.2.4. **Left:** For the combination of all HH → Multilepton channels. **Right:** For the individual channels as well as their combination. (made public in [4])

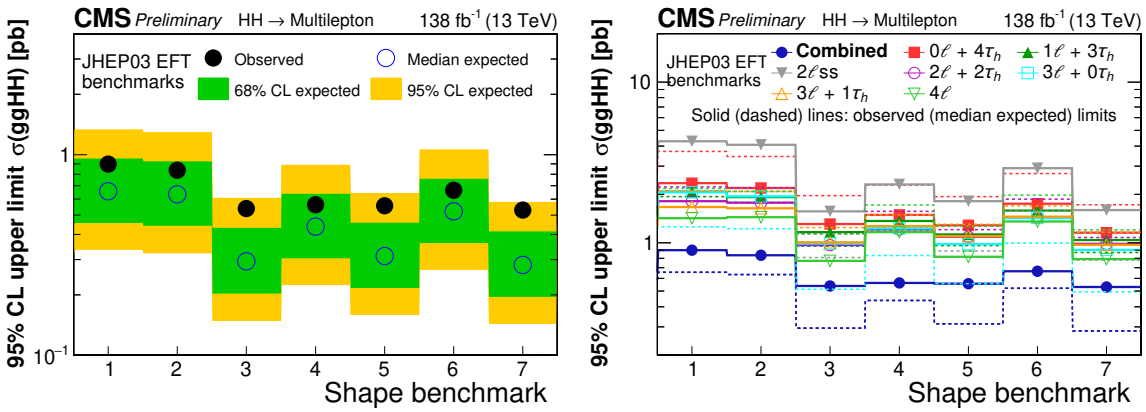

Figure 7.38: Upper limits at 95% CL on the ggHH production cross section for the EFT benchmark scenarios features in [134] as discussed in Sec. 6.2.4. **Left:** For the combination of all HH → Multilepton channels. **Right:** For the individual channels as well as their combination. (made public in [4])

Benchmark	Obs. (Exp.) limit
JHEP04 BM1	471 fb (354 fb)
JHEP04 BM2	205 fb (159 fb)
JHEP04 BM3	571 fb (451 fb)
JHEP04 BM4	687 fb (604 fb)
JHEP04 BM5	442 fb (265 fb)
JHEP04 BM6	750 fb (588 fb)
JHEP04 BM7	1102 fb (1168 fb)
JHEP04 BM8	491 fb (336 fb)
JHEP04 BM9	547 fb (298 fb)
JHEP04 BM10	1005 fb (867 fb)
JHEP04 BM11	801 fb (576 fb)
JHEP04 BM12	910 fb (910 fb)
JHEP04 BM8a	611 fb (354 fb)

Benchmark	Obs. (Exp.) limit
JHEP03 BM1	898 fb (656 fb)
JHEP03 BM2	837 fb (635 fb)
JHEP03 BM3	539 fb (294 fb)
JHEP03 BM4	563 fb (438 fb)
JHEP03 BM5	557 fb (313 fb)
JHEP03 BM6	665 fb (521 fb)
JHEP03 BM7	530 fb (282 fb)

Table 7.12: Observed (expected) 95% CL limits on the ggHH production cross section for the twelve EFT benchmark scenarios from [28], the additional EFT benchmark scenario 8a from [20] and the seven EFT benchmark scenarios from [134]. The given limits correspond to the combination of all seven channels. (made public in [4])

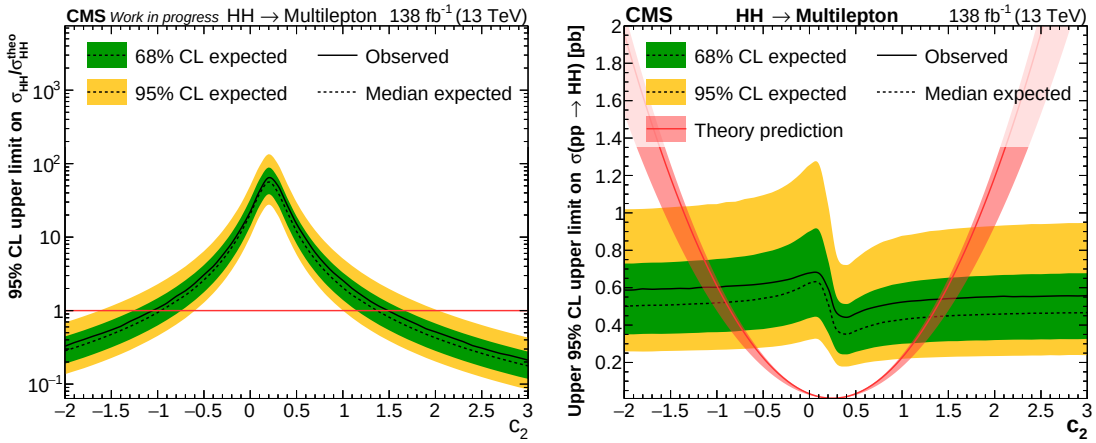

Figure 7.39: **Left:** The 95% CL upper limit on the HH signal strength modifier $r = \sigma_{\mathrm{HH}}/\sigma_{\mathrm{HH}}^{\mathrm{theo}}$. The intersection of the limit with the line at one corresponds to the observed (expected) limit on c_2 of $-1.06 < c_2 < 1.49$ ($-0.97 < c_2 < 1.37$). **Right:** The HH production cross section as a function of the EFT coupling parameter c_2. For the cross section limit, theoretical uncertainties on $\sigma_{\mathrm{HH}}^{\mathrm{theo}}$ are frozen. For both limits the JHEP04BM7 tuned output of the nonRes BDT is used. (right figure made public in [4])

95% CL limit on the Higgs boson EFT coupling parameter c_2 is found to be $-1.06 < c_2 < 1.49$ ($-0.97 < c_2 < 1.37$). Fig. 7.40 shows a two dimensional limit scan in c_2-κ_{t}. The limits on κ_{t} and c_2 as well as their best fit value are found to be in agreement with the SM.

7.5 Comparison to other HH results

The presented HH → Multilepton analysis is the first ever analysis targeting the HH → 4τ and HH → 2W2τ decay modes and the first analysis by CMS targeting HH → 4W decays. The most similar analysis so far was published by the ATLAS collaboration in 2018 targeting HH → 4W decays by analysing the ATLAS 2016 dataset of 36.1 fb^{-1} [161]. The ATLAS analysis features a cut based approach in a total of 9 event channels targeting Multilepton decays into 2 same sign leptons, three leptons and four leptons. Further subcategoriztion is performed by lepton flavor and the number of opposite sign same flavor lepton pairs. Similar to the CMS HH → Multilepton analysis, background contributions from prompt backgrounds are modeled by simulation while background contributions from misidentified leptons and charge flipped leptons are estimated from data. While the object selection and general event selection are similar, instead of a BDT based approach, the event selection is tightened on four channel specific variables with a good separation of signal and background events. In general, this makes the selection in the ATLAS HH → 4W analysis more restrictive compared to the CMS HH → Multilepton analysis. For the ATLAS 2ℓ(ss) channel a total event yield of 57 events in 2016 is found, compared to the 2978 events that the CMS analysis features for the approximately same luminosity. In general the background composition is very similar to the CMS Multilepton analysis with the 4ℓ phase space dominated by ZZ background and the 2ℓ and 3ℓ background consisting of mostly prompt lepton backgrounds like WZ with strong contributions from lepton fakes. Observed (expected) limits at 95% CL on the SM signal strength modifier of 160 (120) are placed. These compare to an observed (expected) limit of 40.5(40.4) in the HH → Multilepton analysis for the same luminosity. A dedicated comparison of resonant limits for both analysis using only the corre-

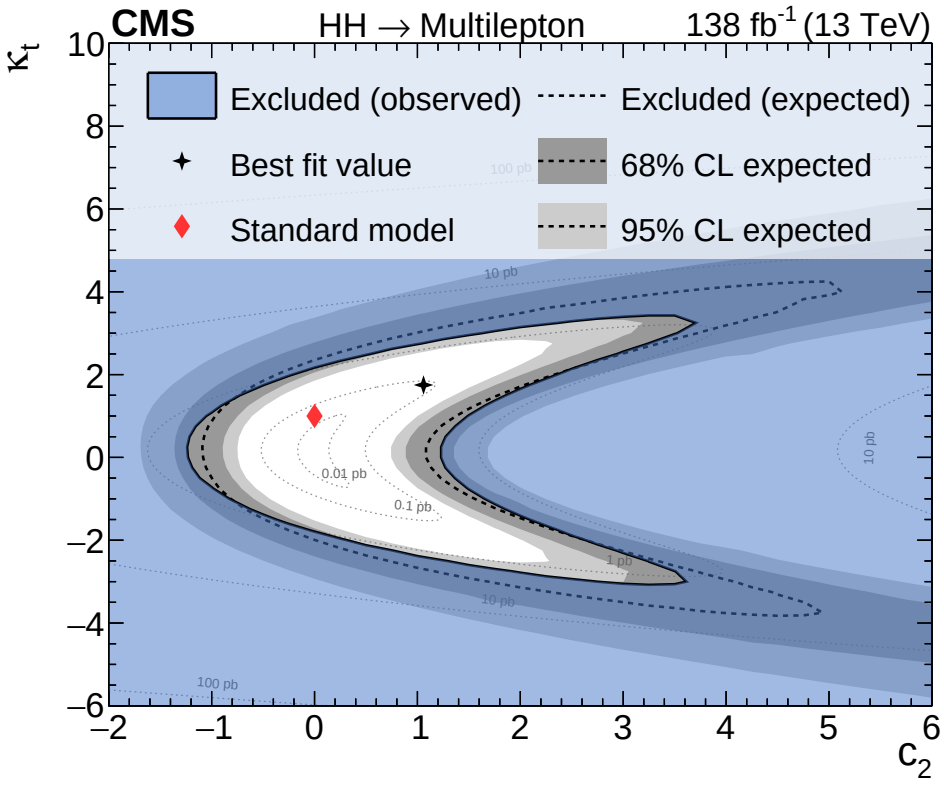

Figure 7.40: Limit at 95% CL on non-resonant HH production in the c_2-κ_t space. Shown is the result of all seven HH → Multilepton channels. The coupling point ($c_2 = 0$, $\kappa_t = 1$, $\kappa_\lambda = 1$) corresponding to the Standard Model as well as the best fit value for the given coupling combination is shown as well. For reference the theory cross section is given in contour lines. For this scan, the JHEP04BM7 tuned output of the nonRes BDT is used. (made public in [4])

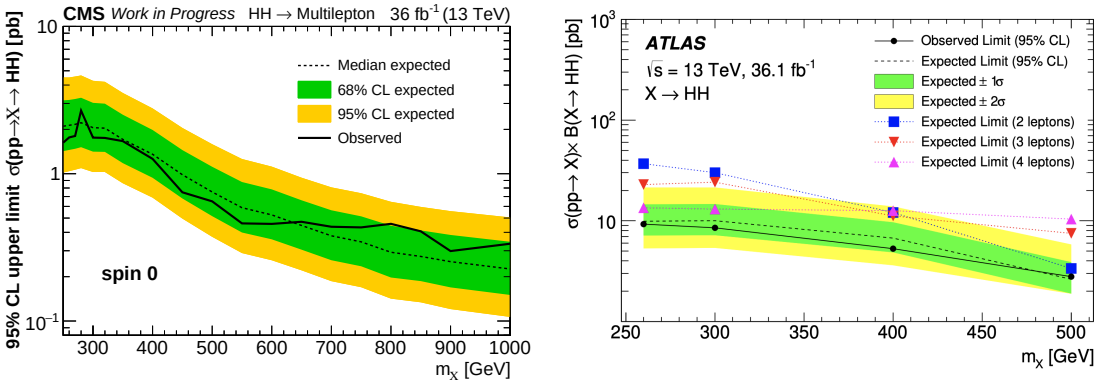

Figure 7.41: Comparison of upper cross section limits at 95% CL achieved for the CMS HH → Multilepton analysis made public in [4] on the left and the ATLAS HH → 4W analysis pb published in [161]. For both results, only the data collected in 2016 is used.

sponding 2016 CMS dataset of approximately 36 fb^{-1} is shown in Fig. 7.41. Both results place the CMS HH → Multilepton at a sensitivity about four to five times higher than the ATLAS HH → 4W analysis. Ignoring smaller differences in detector performance and resolution, a factor of up to 2 can be attributed to the inclusion of more HH signal processes like HH → WWττ and HH → ττττ not considered in the ATLAS analysis. This leaves a factor of about 2-3 to the inclusion of more phase space in the study of decay modes involving hadronic taus as well as the use of multivariate analysis techniques in all 7 event channels.

The latest combination results for HH are given in [162] (ATLAS) and [163] (CMS) for the 2016

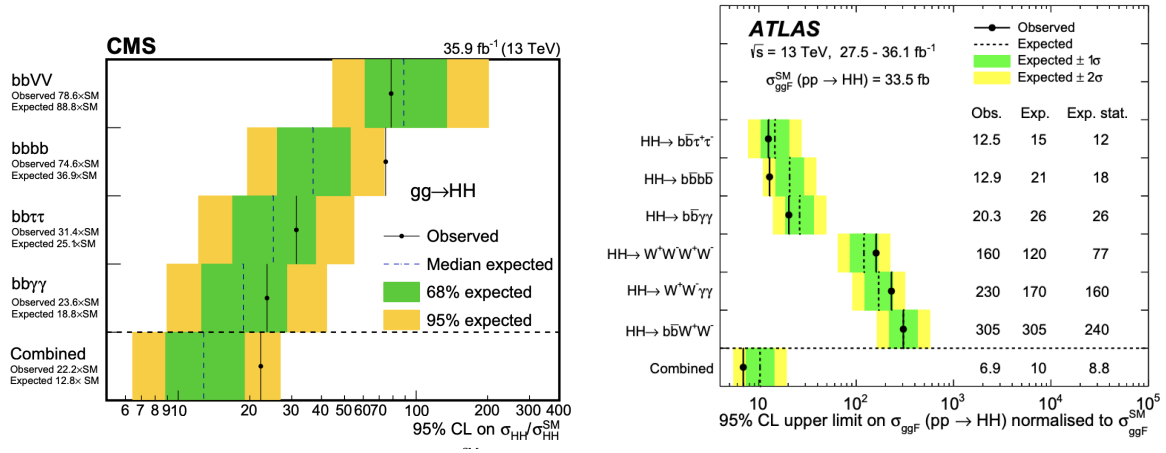

Figure 7.42: Upper limits at 95 % CL on the signal strength modifier $r = \sigma_{\mathrm{HH}}/\sigma_{\mathrm{HH}}^{\mathrm{SM}}$ for SM like non-resonant HH production for different analyses using the 2016 datasets of CMS and ATLAS with $35.9\,\mathrm{fb}^{-1}$ for CMS and $27.5-36.1\,\mathrm{fb}^{-1}$ for ATLAS, respectively. Both results for individual analysis as well as their combination within each collaboration are shown as published in [162, 163]. The HH $\rightarrow$ Multilepton analysis presented in this thesis was not yet available at the time of the 2016 combinations.

datasets, respectively. Fig. 7.42 shows the 95% CL upper limits on the SM signal strength modifier. The best individual results in both experiments have been achieved by analysis covering the HH $\rightarrow$ bbbb, HH $\rightarrow$ bbττ and HH $\rightarrow$ bbγγ final states. Both experiments place limits on SM like non-resonant production at about $10-12\times\sigma_{\mathrm{SM}}$ or about two times the sensitivity in the CMS HH $\rightarrow$ Multilepton search. The latter is in its sensitivity most comparable to the 2016 CMS and ATLAS searches covering the HH $\rightarrow$ bbγγ final state. Regarding limits on the trilinear Higgs boson self-coupling, both publications place the observed (expected) 95% CL upper limits at $-11.8<\kappa_\lambda<18.8$ ($-7.1<\kappa_\lambda<13.6$) for the CMS combination and $-5<\kappa_\lambda<12.0$ ($-5.8<\kappa_\lambda<12.0$) for the ATLAS combination. This places the CMS HH $\rightarrow$ Multilepton analysis at about the same or even slightly better sensitivity on κ_λ than the ATLAS and CMS combinations for the 2016 datasets. The cross section limits on non-resonant HH production for both combinations as a function of κ_λ is shown in Fig. 7.43. Fig. 7.44 shows upper limits at 95% CL on resonant HH production for the CMS and ATLAS combination of analyses for the 2016 datasets. The sensitivity for both experiments at low masses is comparable to that of the CMS HH $\rightarrow$ Multilepton analysis with limits in the order of 1 pb. At higher masses the cross section limits of the two combinations are about a factor of 5 (2 expected) times stronger, with limits of about 40 fb at a resonant mass of 1 TeV compared to about 200 fb (80 fb expected).

7.5.1 Recent Results and Di-Higgs Boson Analysis Prospects

More recent results for non-resonant HH production utilizing the full luminosity of the LHC 2016-2018 Run 2 data taking period of about $140\,\mathrm{fb}^{-1}$ have been released for the bbbb [164] (qqHH only), bbττ [165], bbγγ [166], and bb$\ell\nu\ell\nu$ [167] final states by the ATLAS collaboration and the bbbb [90] and bbγγ [92] final states by the CMS collaboration. An overview of these results can be found in Tab. 7.13. With limits in the order of $5\times\sigma_{SM}$ or better, the CMS results for the bbbb and bbγγ and ATLAS results for the bbγγ and bbττ final states, place the so far strongest limits on non-resonant HH production and promise together with the upcoming results

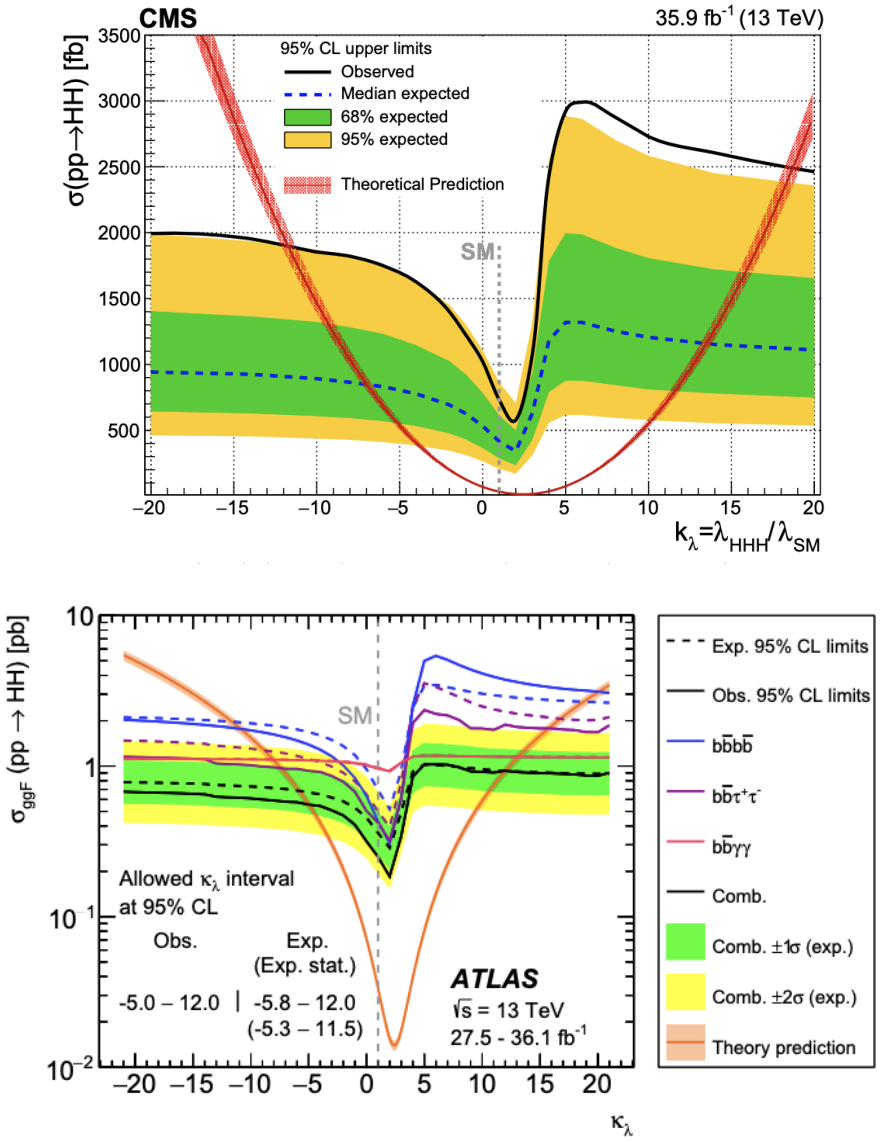

Figure 7.43: Upper limits at 95 % CL on the cross section for non-resonant HH production as a function of the trilinear HH self-coupling modifier κ_λ for a combination of analyses in the bbbb, bbγγ and bbττ final states for the CMS collaboration on the top and the ATLAS collaboration on the bottom. The CMS combination results also contains the bbVV final state. The theory cross section expectation for variations in κ_λ is shown as well. For the ATLAS analyses, also the results of the individual channels are shown. All results correspond to the 2016 datasets of CMS and ATLAS with 35.9 fb^{-1} for CMS and 27.5 – 36.1 fb^{-1} for ATLAS, respectively [162, 163].

Experiment	luminosity [fb^{-1}]	decay mode	limit σ/σ_{SM} [exp.]	allowed κ_λ [exp.])
ATLAS	36.1	4W →Multilepton	160 (120)	-
ATLAS	27.5-36.1	Combination	6.9 [10]	(-5.0)-12.0 [(-5.8)-12.0]
CMS	35.9	Combination	22.2 [12.8]	(-11.8)-18.8 [(-7.1)-13.6]
ATLAS	139	bbττ	4.7 [3.9]	-
ATLAS	139	bbbb	4.1 [5.5]	(-1.5)-6.7 [(-2.4)-7.7]
ATLAS	139	bb$\ell\nu\ell\nu$	40 (29)	-
CMS	137	bbγγ	7.7 [5.2]	(-3.3)-8.5 [(-2.5)-8.2]
CMS	138	bbbb	3.6 [7.3]	(-2.3)-9.4 [(-5.0)-12.0]
CMS	137	Multilepton	22.3 [19.8]	(-7.3)-11.4 [(-7.0)-11.8]

Table 7.13: Overview of results on non-resonant HH production for the ATLAS HH → 4W analysis [161], the CMS and ATLAS combinations of 2016 results [162, 163] as well as the most recent Run 2 results from ATLAS [165–167] and CMS [90, 92] compared to the results of the CMS HH → Multilepton analysis [4]. All limits correspond to 95% CL.

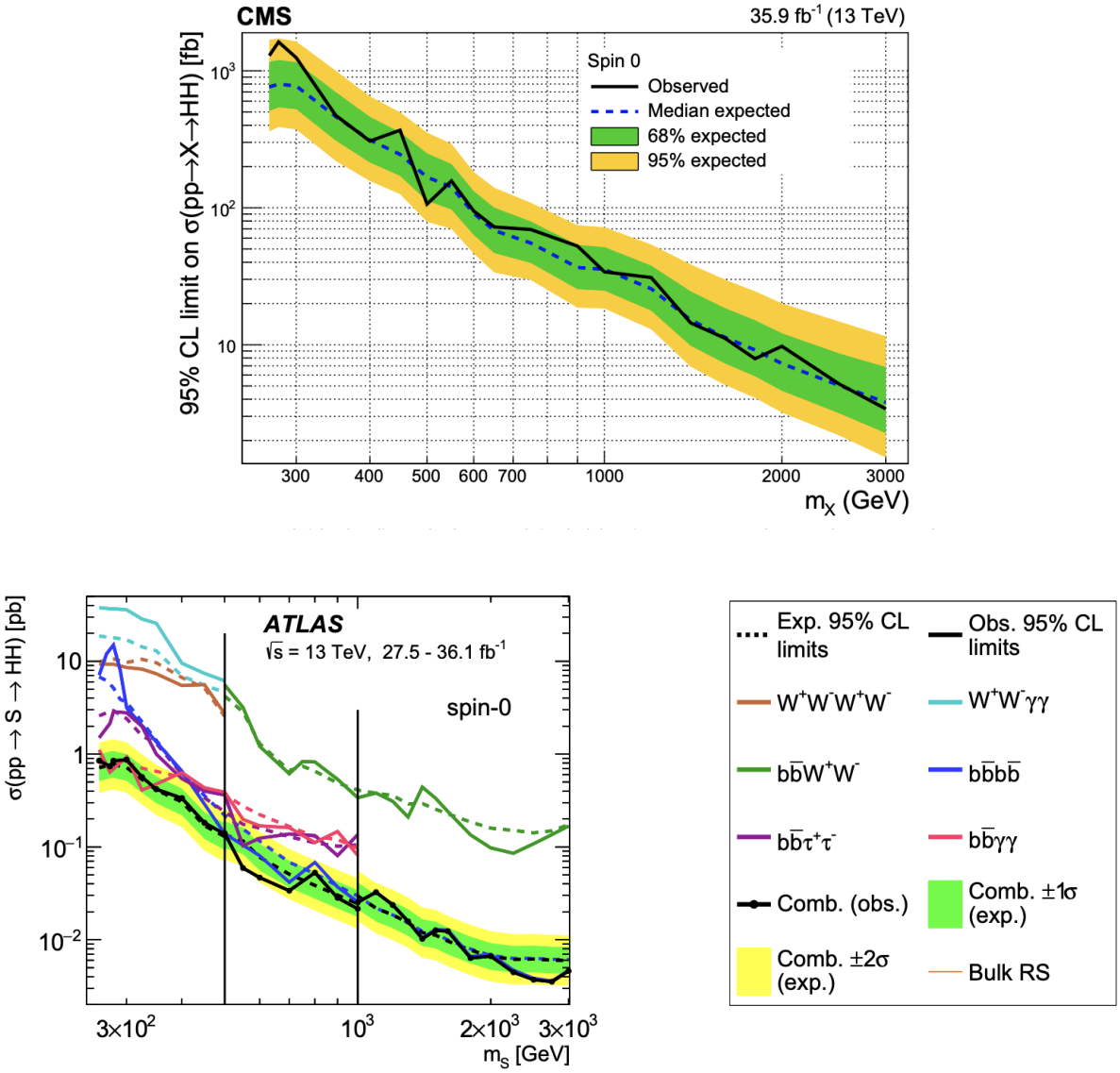

Figure 7.44: Upper limits at 95 % CL on the cross section for resonant HH production as a function of the mass of the new resonance χ (S) for the combination of analyses in the bbbb, $\mathrm{bb}\gamma\gamma$, $\mathrm{bb}\tau\tau$ and $\mathrm{bb}VV$ final states for the CMS collaboration on the top and the bbbb, $\mathrm{bb}\gamma\gamma$, $\mathrm{bb}\tau\tau$, bbWW, WWWW and $\mathrm{WW}\gamma\gamma$ final states for the ATLAS collaboration on the bottom. For the ATLAS analyses, also the results of the individual channels are shown. All results correspond to the hypothesis of a heavy spin-0 resonance and use the 2016 datasets of CMS and ATLAS with $35.9\,\mathrm{fb}^{-1}$ for CMS and $27.5-36.1\,\mathrm{fb}^{-1}$ for ATLAS, respectively [162, 163].

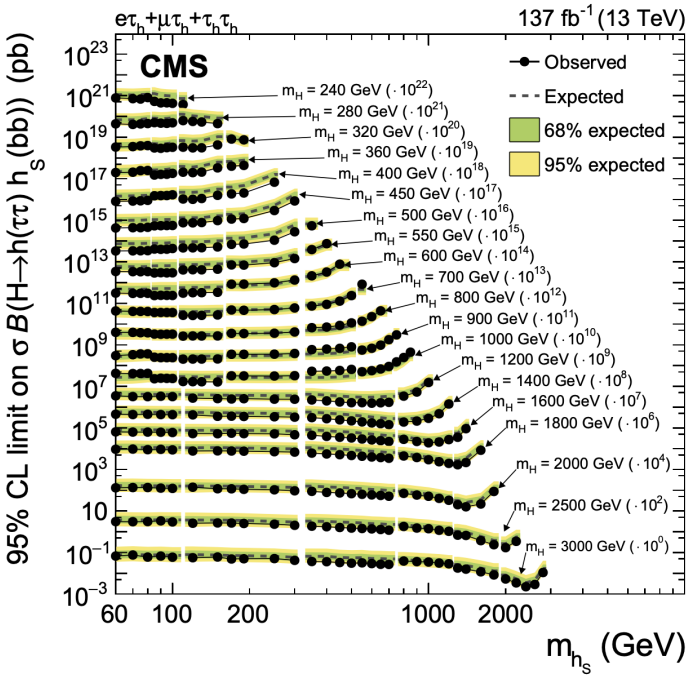

Figure 7.45: Upper cross section limits at 95% CL on resonant $\mathrm{H} \to hh_s$ production in the $\mathrm{bb}\tau\tau$ final state for different masses of a new heavy resonance H in the range of 240 GeV to 3 TeV decaying into a SM Higgs boson h and a second new resonance h_S of variable mass between 60 GeV and 2 TeV. To display results for all mass scenarios simultaneously the cross section limits for different masses of the heavy resonance H have been scaled by an adequate factor as given in the figure. For $m_{h_s} = 125$ GeV results corresponding to resonant production of two SM Higgs bosons are obtained [94].

in other HH final states a result, that previously was unexpected for the current luminosity. For the trilinear Higgs boson self-coupling, it is apparent that while in the limit on SM like HH production in the CMS $\mathrm{HH} \to$ Multilepton analysis is about a factor of 3-4 less sensitive than the leading bbbb and $\mathrm{bb}\gamma\gamma$ and $\mathrm{bb}\tau\tau$ analyses, the results for BSM HH production, especially at high κ_λ are comparable and highly significant. The limits on κ_λ are highly asymmetric with stronger bounds on negative κ_λ promising an exclusion of $\kappa_\lambda = 0$ in the not so distant future. For the next data taking period it might even be possible to reach sensitivity approaching standard model like HH production.

The latest results for resonant HH production are presented in the CMS analysis studying the $\mathrm{bb}\tau\tau$ final state with the full Run 2 luminosity [94]. Limits are placed on $\chi \to \mathrm{HH}_s$ production[1] for different values of resonant masses m_χ and m_{H_s}. They are shown in Fig. 7.45. For $m_{\mathrm{H}_s} =$ 125 GeV results comparable to the results of the $\mathrm{HH} \to$ Multilepton analysis are given. In the low mass regime around m_χ =250 GeV the presented cross section limits are found to be around 100 fb for decays into a b-quark pair and an τ pair corresponding to an upper limit on the $\chi \to \mathrm{HH}$ cross section of about 1.4 pb assuming SM Higgs boson branching fractions. For intermediate mass scenarios with m_χ =500 GeV, upper cross section limits in the order of 10 fb are found, corresponding to an upper limit on the $\chi \to \mathrm{HH}$ cross section of about 140 fb. Finally for high mass scenarios with $m_\chi = 1$ TeV cross section limits around 5 fb corresponding to limits on the $\chi \to \mathrm{HH}$ cross section of 70 fb are placed. This is comparable to the cross section limits achieved

[1] A different labeling/naming scheme is used in the $\mathrm{bb}\tau\tau$ analysis with H instead of χ, h instead of H and h_s instead of H_s.

in the CMS $\mathrm{HH} \rightarrow$ Multilepton analysis where (expected) limits in the order of 900 fb - 200 fb (1 pb-80 fb) are placed over the same mass range.

7.6 Prospects and Outlook

As discussed in previous sections, the current CMS $\mathrm{HH} \rightarrow$ Multilepton analysis is predominantly limited by both the available amount of data and the availability of simulated events both for the optimisation of multivariate analysis methods as well as the modelling of background. Higher amounts of both simulated and recorded events will not only reduce the statistical uncertainties and improve the quality of the data driven background estimation but will also allow for a more sophisticated analysis. This can be, for example, in the form of further subcategorization both by lepton flavor and the amount of same flavor opposite sign lepton pairs. Both quantities have a strong influence on the contribution of background containing either prompt leptons or fake lepton background and thus will allow a stronger focus on the individual background processes. In the higher statistics channels also a stronger focus on qqHH production is possible, either by the introduction of new event categories or the usage of MVA methods with multiclassification. In analyses that are statistically limited, the usual gain with luminosity follows a square root law, as the sensitivity of an analysis can be usually approximated by the significance $S/\sqrt{S+B}$ with the number of expected signal events S and the statistical error of the total expected event yield $\sqrt{S+B}$. As this does however not take into account indirect improvements in both background prediction and analysis optimization available with more event statistics, the $\mathrm{HH} \rightarrow$ Multilepton analysis profits over proportionally from additional data, so that an almost linear gain can be expected. Since the main strength of the presented analysis compared to analyses targeting other final states lies in the constraint of HH production at low m_{HH} and subsequently high (positive) κ_λ the expected impact of the analysis on the overall HH effort will remain high at least for the next data taking period of the LHC. However, as limits on the lower boundary of κ_λ are approaching 0 and the limits for SM like non-resonant production are approaching the sensitivity needed to constrain SM HH production, the long term impact of the presented analysis will decrease beyond that time frame and will mostly remain relevant in the search for BSM EFT scenarios and searches for resonant HH production.
In general the amount of available HH results and BSM interpretations as shown in this thesis is only ever increasing. In addition to the possible discovery of either SM or BSM like HH in the not so distant future, analyses will start becoming sensitive to the measurement of differential distributions allowing to constrain BSM effects even further. Without exaggeration it can be said that the age of HH measurements has now really begun and interesting times are ahead.

8

Summary and Conclusion

This thesis presented the search for rare Higgs boson production phenomena at the LHC using data of the CMS experiment with proton-proton collision data collected in the years 2016-2018 with a total luminosity of $137-138\,\text{fb}^{-1}$ at a center of mass energy of $\sqrt{s}=13$ TeV.
The main topic of this thesis is the CMS $\mathrm{HH}\rightarrow$ Multilepton analysis [4] where both results for non-resonant and resonant HH production where obtained. It focuses in particular on:

- the analysis of the $3\ell+1\tau_{\mathrm{h}}$ final state.
- the combination of all seven multilepton final states.
- the interpretation of results in resonant production of Higgs boson pairs through the decay of a heavy spin-0 or spin-2 resonance.
- the interpretation of results for Standard Model like non-resonant Higgs boon pair production with modified trillinear Higgs boson self-coupling, modified Top-Yukava coupling and modified $VV\mathrm{HH}$ quartic coupling.
- the interpretation of results in a 5 dimensional EFT parameter space.

The $\mathrm{HH}\rightarrow$ Multilepton analysis was performed in seven different decay channels with different multiplicities of electrons, muons and hadronic taus in the final state. For each channel a set of three different parameterized BDTs was trained separating HH signal for the non-resonant and resonant spin-0 or spin-2 HH production and the channel specific background processes. The signal extraction is performed simultaneously on the adequately binned output of said BDT for all seven channels and additionally kinematic distributions in two control regions, for the 2016, 2017 and 2018 LHC datasets of the CMS experiment. For the description of signal processes as well as background processes containing prompt leptons simulated event samples are used. For background processes involving misidentified leptons or τ_{h} and charge flip backgrounds, data driven methods such as the Fake-Factor method are used. For non-resonant HH production the observed (expected) bound on the trilinear Higgs boson self-coupling modifier obtained by this analysis can be placed at $-6.98<\kappa_{\lambda}<11.17$ ($-6.98<\kappa_{\lambda}<11.73$) and the observed (expected) upper limit at 95% CL on SM like HH production can be set at $21.8\times\sigma^{\mathrm{SM}}_{\mathrm{HH}}$ ($19.6\times\sigma^{\mathrm{SM}}_{\mathrm{HH}}$). Limits on the upper cross section for non-resonant ggHH for a variety of EFT benchmarks are set as well in a range between 200 fb and 1.2 pb. An observed (expected) limit on the EFT coupling parameter c_2 describing the point interaction of two top quarks and two Higgs bosons of $-1.06<c_2<1.49$ ($-0.97<c_2<1.37$) can be set as well. For resonant production limits in the mass range $250\,\text{GeV}<m_{\chi}<1000\,\text{GeV}$ for both a new boson of spin-0 or spin-2

decaying into a pair of SM Higgs boson have been obtained and range between 1 pb to 200 fb. In comparison to other analyses the presented $\mathrm{HH} \rightarrow$ Multilepton analysis shows particular strong sensitivity for scenarios with a low Di-Higgs boson invariant mass or scenarios of high (positive) κ_λ. Within the $\mathrm{HH} \rightarrow$ Multilepton analysis this is especially true for the $3\ell + 1\tau_\mathrm{h}$ channel with a sensitivity on the HH cross section of about 3 pb-600 fb depending on the physics case and a relatively strong limit on the Higgs boson trilinear self-coupling modifier of $-13.00 < \kappa_\lambda < 16.75$ ($-12.91 < \kappa_\lambda < 16.93$).
In addition to the main focus of this thesis on the study of HH processes, smaller contributions where made to the CMS $\mathrm{H} \rightarrow \mu\mu$ analysis [4] which was able to claim the first evidence for the coupling between the Higgs boson and muons. The contribution to the $\mathrm{H} \rightarrow \mu\mu$ analysis was centered around a feasibility study for a dedicated category aiming at Higgs boson production in association with hadronically decaying vector bosons. Both a cut based approach as well as BDT based approach were studied. While a dedicated $V\mathrm{H}$ hadronic category did not enter the current iteration of the $\mathrm{H} \rightarrow \mu\mu$ analysis, it shows promise and the presented study will serve as input for future iterations of the analysis.

Conclusion

The Run 2 data taking period was an exciting time for particle physics in general and Higgs boson physics in particular. The presented thesis could make contributions to two of the most interesting Higgs boson analyses, establishing the coupling of Higgs bosons to second generation fermions and putting strong constrains on the Higgs boson trilinear self-coupling and the production of Di-Higgs boson pairs. Both analyses feature extremely rare signals, showing the high levels of precision the LHC experiments are able to achieve with the current level of analysis techniques assisted by modern multivariate analysis tools that enable a surprisingly high sensitivity for the current amount of collected data. With this level of sensitivity, the prospects for future data taking are better than ever and the time of Higgs boson precision and Di-Higgs boson measurements has now truly begun!

Literature

[1] Serguei Chatrchyan et al. “Observation of a New Boson at a Mass of 125 GeV with the CMS Experiment at the LHC”. In: *Phys. Lett. B* 716 (2012), pp. 30–61. DOI: 10.1016/j.physletb.2012.08.021. arXiv: 1207.7235 [hep-ex].

[2] Georges Aad et al. “Observation of a new particle in the search for the Standard Model Higgs boson with the ATLAS detector at the LHC”. In: *Phys. Lett. B* 716 (2012), pp. 1–29. DOI: 10.1016/j.physletb.2012.08.020. arXiv: 1207.7214 [hep-ex].

[3] Albert M Sirunyan et al. “Evidence for Higgs boson decay to a pair of muons”. In: *JHEP* 01 (2021), p. 148. DOI: 10.1007/JHEP01(2021)148. arXiv: 2009.04363 [hep-ex].

[4] *Search for Higgs boson pairs decaying to WWWW, WW$\tau\tau$, and $\tau\tau\tau\tau$ in proton-proton collisions at $\sqrt{s} = 13$ TeV*. Tech. rep. Geneva: CERN, 2022. URL: http://cds.cern.ch/record/2799151.

[5] P.A. Zyla et al. “Review of Particle Physics”. In: *PTEP* 2020.8 (2020), p. 083C01. DOI: 10.1093/ptep/ptaa104.

[6] Laurent Canetti, Marco Drewes, and Mikhail Shaposhnikov. “Matter and Antimatter in the Universe”. In: *New J. Phys.* 14 (2012), p. 095012. DOI: 10.1088/1367-2630/14/9/095012. arXiv: 1204.4186 [hep-ph].

[7] Sebastian Bruggisser, Thomas Konstandin, and Geraldine Servant. “CP-violation for Electroweak Baryogenesis from Dynamical CKM Matrix”. In: *JCAP* 11 (2017), p. 034. DOI: 10.1088/1475-7516/2017/11/034. arXiv: 1706.08534 [hep-ph].

[8] Edvige Corbelli and Paolo Salucci. “The Extended Rotation Curve and the Dark Matter Halo of M33”. In: *Mon. Not. Roy. Astron. Soc.* 311 (2000), pp. 441–447. DOI: 10.1046/j.1365-8711.2000.03075.x. arXiv: astro-ph/9909252.

[9] Edward L. Wright. “Dark matter in the light of COBE”. In: *Astrophysics Symposium on Dark Matter: Critique of the Sources of Dark Matter in the Universe*. Feb. 1994. arXiv: astro-ph/9408002.

[10] Konstantin T. Matchev and Scott D. Thomas. “Higgs and Z boson signatures of supersymmetry”. In: *Phys. Rev. D* 62 (2000), p. 077702. DOI: 10.1103/PhysRevD.62.077702. arXiv: hep-ph/9908482.

[11] Abdelhak Djouadi. “The Anatomy of electro-weak symmetry breaking. II. The Higgs bosons in the minimal supersymmetric model”. In: *Phys. Rept.* 459 (2008), pp. 1–241. DOI: 10.1016/j.physrep.2007.10.005. arXiv: hep-ph/0503173.

[12] Mark Thomson. *Modern Particle Physics*. Cambridge University Press, 2013. DOI: 10.1017/CBO9781139525367.

[13] John Ellis. “Higgs Physics”. In: *2013 European School of High-Energy Physics*. Dec. 2013. DOI: 10.5170/CERN-2015-004.117. arXiv: 1312.5672 [hep-ph].

[14] D. de Florian et al. “Handbook of LHC Higgs Cross Sections: 4. Deciphering the Nature of the Higgs Sector”. In: 2/2017 (Oct. 2016). DOI: 10.23731/CYRM-2017-002. arXiv: 1610.07922 [hep-ph].

[15] J. Alison et al. “Higgs Boson Pair Production at Colliders: Status and Perspectives”. In: *Double Higgs Production at Colliders Batavia, IL, USA, September 4, 2018-9, 2019*. Ed. by B. Di Micco et al. 2019. arXiv: 1910.00012 [hep-ph]. URL: https://lss.fnal.gov/archive/2019/conf/fermilab-conf-19-468-e-t.pdf.

[16] R. Frederix et al. “Higgs pair production at the LHC with NLO and parton-shower effects”. In: *Phys. Lett. B* 732 (2014), pp. 142–149. DOI: 10.1016/j.physletb.2014.03.026. arXiv: 1401.7340 [hep-ph].

[17] Massimiliano Grazzini et al. “Higgs boson pair production at NNLO with top quark mass effects”. In: *JHEP* 05 (2018), p. 059. DOI: 10.1007/JHEP05(2018)059. arXiv: 1803.02463 [hep-ph].

[18] J. Baglio et al. “$gg \to HH$: Combined uncertainties”. In: *Phys. Rev. D* 103.5 (2021), p. 056002. DOI: 10.1103/PhysRevD.103.056002. arXiv: 2008.11626 [hep-ph].

[19] The LHC Higgs Cross section group. *LHC Higgs Cross Section HH Sub-group (a.k.a LHC-HH)*. 2021. URL: {https://twiki.cern.ch/twiki/bin/view/LHCPhysics/LHCHWGHH}.

[20] G. Buchalla et al. “Higgs boson pair production in non-linear Effective Field Theory with full m_t-dependence at NLO QCD”. In: *JHEP* 09 (2018), p. 057. DOI: 10.1007/JHEP09(2018)057. arXiv: 1806.05162 [hep-ph].

[21] Peter Mandrik for the CMS Collaboration. *NLO HH reweight coefficents*. Github, commit 7abd19a. 2021. URL: https://github.com/pmandrik/VSEVA/blob/master/HHWWgg/reweight/pm_pw_NLO_Ais_13TeV_V2.txt.

[22] S. Amoroso et al. “Les Houches 2019: Physics at TeV Colliders: Standard Model Working Group Report”. In: *11th Les Houches Workshop on Physics at TeV Colliders: PhysTeV Les Houches*. Mar. 2020. arXiv: 2003.01700 [hep-ph].

[23] Georges Aad et al. “Combined Measurement of the Higgs Boson Mass in pp Collisions at $\sqrt{s} = 7$ and 8 TeV with the ATLAS and CMS Experiments”. In: *Phys. Rev. Lett.* 114 (2015), p. 191803. DOI: 10.1103/PhysRevLett.114.191803. arXiv: 1503.07589 [hep-ex].

[24] G. Heinrich et al. “Probing the trilinear Higgs boson coupling in di-Higgs production at NLO QCD including parton shower effects”. In: *JHEP* 06 (2019), p. 066. DOI: 10.1007/JHEP06(2019)066. arXiv: 1903.08137 [hep-ph].

[25] Giuseppe Degrassi et al. “Probing the Higgs self coupling via single Higgs production at the LHC”. In: *JHEP* 12 (2016), p. 080. DOI: 10.1007/JHEP12(2016)080. arXiv: 1607.04251 [hep-ph].

[26] Fabio Maltoni et al. “Trilinear Higgs coupling determination via single-Higgs differential measurements at the LHC”. In: *Eur. Phys. J. C* 77.12 (2017), p. 887. DOI: 10.1140/epjc/s10052-017-5410-8. arXiv: 1709.08649 [hep-ph].

[27] Fady Bishara, Roberto Contino, and Juan Rojo. "Higgs pair production in vector-boson fusion at the LHC and beyond". In: *Eur. Phys. J. C* 77.7 (2017), p. 481. DOI: 10.1140/epjc/s10052-017-5037-9. arXiv: 1611.03860 [hep-ph].

[28] Alexandra Carvalho et al. "Higgs Pair Production: Choosing Benchmarks With Cluster Analysis". In: *JHEP* 04 (2016), p. 126. DOI: 10.1007/JHEP04(2016)126. arXiv: 1507.02245 [hep-ph].

[29] Nathaniel Craig, Jamison Galloway, and Scott Thomas. "Searching for Signs of the Second Higgs Doublet". In: (May 2013). arXiv: 1305.2424 [hep-ph].

[30] Dao Thi Nhung et al. "Higher Order Corrections to the Trilinear Higgs Self-Couplings in the Real NMSSM". In: *JHEP* 11 (2013), p. 181. DOI: 10.1007/JHEP11(2013)181. arXiv: 1306.3926 [hep-ph].

[31] Christoph Englert et al. "Exploring the Higgs portal". In: *Phys. Lett. B* 703 (2011), pp. 298–305. DOI: 10.1016/j.physletb.2011.08.002. arXiv: 1106.3097 [hep-ph].

[32] Jose M. No and Michael Ramsey-Musolf. "Probing the Higgs Portal at the LHC Through Resonant di-Higgs Production". In: *Phys. Rev. D* 89.9 (2014), p. 095031. DOI: 10.1103/PhysRevD.89.095031. arXiv: 1310.6035 [hep-ph].

[33] Lisa Randall and Raman Sundrum. "A Large mass hierarchy from a small extra dimension". In: *Phys. Rev. Lett.* 83 (1999), pp. 3370–3373. DOI: 10.1103/PhysRevLett.83.3370. arXiv: hep-ph/9905221.

[34] King-man Cheung. "Phenomenology of radion in Randall-Sundrum scenario". In: *Phys. Rev. D* 63 (2001), p. 056007. DOI: 10.1103/PhysRevD.63.056007. arXiv: hep-ph/0009232.

[35] Richard D. Ball et al. "Parton distributions from high-precision collider data". In: *Eur. Phys. J. C* 77.10 (2017), p. 663. DOI: 10.1140/epjc/s10052-017-5199-5. arXiv: 1706.00428 [hep-ph].

[36] S. Chatrchyan et al. "The CMS Experiment at the CERN LHC". In: *JINST* 3 (2008), S08004. DOI: 10.1088/1748-0221/3/08/S08004.

[37] Lyndon Evans. "The LHC machine". In: *PoS* EPS-HEP2009 (2009), p. 004. DOI: 10.22323/1.084.0004.

[38] Dariusz Gora. "The Pierre Auger Observatory: review of latest results and perspectives". In: *Universe* 4.11 (2018), p. 128. DOI: 10.3390/universe4110128. arXiv: 1811.00343 [astro-ph.IM].

[39] Christopher W. Walter. "The Super-Kamiokande Experiment". In: (Feb. 2008), pp. 19–43. DOI: 10.1142/9789812771971_0002. arXiv: 0802.1041 [hep-ex].

[40] The ATLAS Collaboration. "The ATLAS Experiment at the CERN Large Hadron Collider". In: 3.08 (2008), S08003–S08003. DOI: 10.1088/1748-0221/3/08/s08003. URL: https://doi.org/10.1088/1748-0221/3/08/s08003.

[41] The LHCb Collaboration. “The LHCb Detector at the LHC”. In: 3.08 (2008), S08005–S08005. DOI: 10.1088/1748-0221/3/08/s08005. URL: https://doi.org/10.1088/1748-0221/3/08/s08005.

[42] The ALICE Collaboration. “The ALICE experiment at the CERN LHC”. In: 3.08 (2008), S08002–S08002. DOI: 10.1088/1748-0221/3/08/s08002. URL: https://doi.org/10.1088/1748-0221/3/08/s08002.

[43] Esma Anais Mobs. “The CERN accelerator complex. Complexe des accélérateurs du CERN”. In: (2016). General Photo. URL: https://cds.cern.ch/record/2225847.

[44] Oliver Sim Brüning et al. *LHC Design Report*. CERN Yellow Reports: Monographs. Geneva: CERN, 2004. DOI: 10.5170/CERN-2004-003-V-1. URL: https://cds.cern.ch/record/782076.

[45] J. T. Boyd. “LHC Run-2 and Future Prospects”. In: *2019 European School of High-Energy Physics*. Jan. 2020. arXiv: 2001.04370 [hep-ex].

[46] CMS group of the Universität Zürich. *Picture of the cms_coordinate_system*. 2017. URL: https://wiki.physik.uzh.ch/cms/_detail/latex:cms_coordinate_system.png?id=latex\%3Atikz.

[47] CMS group of the Universität Zürich. *How to draw diagrams in LaTeX with TikZ*. 2021. URL: https://wiki.physik.uzh.ch/cms/latex:tikz.

[48] A.M. Sirunyan et al. “Particle-flow reconstruction and global event description with the CMS detector”. In: *Journal of Instrumentation* 12.10 (2017), P10003–P10003. ISSN: 1748-0221. DOI: 10.1088/1748-0221/12/10/p10003. URL: http://dx.doi.org/10.1088/1748-0221/12/10/P10003.

[49] The Tracker Group of the CMS Collaboration. *The CMS Phase-1 Pixel Detector Upgrade*. 2020. arXiv: 2012.14304 [physics.ins-det].

[50] CMS HCAL/ECAL Collaborations. “The CMS barrel calorimeter response to particle beams from 2 to 350 GeV/c”. In: *Eur. Phys. J. C* 60.3 (2009), pp. 359–373. DOI: 10.1140/epjc/s10052-009-0959-5. URL: https://doi.org/10.1140/epjc/s10052-009-0959-5.

[51] Matteo Cacciari, Gavin P Salam, and Gregory Soyez. “The anti-ktjet clustering algorithm”. In: *Journal of High Energy Physics* 2008.04 (2008), 063–063. ISSN: 1029-8479. DOI: 10.1088/1126-6708/2008/04/063. URL: http://dx.doi.org/10.1088/1126-6708/2008/04/063.

[52] A.M. Sirunyan et al. “Performance of the CMS muon detector and muon reconstruction with proton-proton collisions at $\sqrt{s}$=13 TeV”. In: *Journal of Instrumentation* 13.06 (2018), P06015–P06015. ISSN: 1748-0221. DOI: 10.1088/1748-0221/13/06/p06015. URL: http://dx.doi.org/10.1088/1748-0221/13/06/P06015.

[53] V. Khachatryan et al. “The CMS trigger system”. In: *Journal of Instrumentation* 12.01 (2017), P01020–P01020. ISSN: 1748-0221. DOI: 10.1088/1748-0221/12/01/p01020. URL: http://dx.doi.org/10.1088/1748-0221/12/01/P01020.

[54] CMS Collaboration. “Performance of τ-lepton reconstruction and identification in CMS”. In: *Journal of Instrumentation* 7.01 (2012), P01001–P01001. ISSN: 1748-0221. DOI: 10.1088/1748-0221/7/01/p01001. URL: http://dx.doi.org/10.1088/1748-0221/7/01/P01001.

[55] “Reconstruction and identification of τ lepton decays to hadrons and $\nu\tau$ at CMS”. In: *Journal of Instrumentation* 11.01 (2016), P01019–P01019. ISSN: 1748-0221. DOI: 10.1088/1748-0221/11/01/p01019. URL: http://dx.doi.org/10.1088/1748-0221/11/01/P01019.

[56] A.M. Sirunyan et al. “Performance of reconstruction and identification of τ leptons decaying to hadrons and $\nu\tau$ in pp collisions at $\sqrt{s}$=13 TeV”. In: *Journal of Instrumentation* 13.10 (2018), P10005–P10005. ISSN: 1748-0221. DOI: 10.1088/1748-0221/13/10/p10005. URL: http://dx.doi.org/10.1088/1748-0221/13/10/P10005.

[57] “Performance of the DeepTau algorithm for the discrimination of taus against jets, electron, and muons”. In: (2019). URL: https://cds.cern.ch/record/2694158.

[58] Andrea Cardini. *Tau identification exploiting deep learning techniques*. ICHEP 2020 | Prague conference. July 2020. URL: https://indico.cern.ch/event/868940/contributions/3813676/.

[59] Armen Tumasyan et al. “Identification of hadronic tau lepton decays using a deep neural network”. In: (Jan. 2022). arXiv: 2201.08458 [hep-ex].

[60] Emil Bols et al. “Jet Flavour Classification Using DeepJet”. In: *JINST* 15.12 (2020), P12012. DOI: 10.1088/1748-0221/15/12/P12012. arXiv: 2008.10519 [hep-ex].

[61] “Performance of b tagging algorithms in proton-proton collisions at 13 TeV with Phase 1 CMS detector”. In: (2018). URL: http://cds.cern.ch/record/2627468.

[62] Albert M Sirunyan et al. “Measurement of the Higgs boson production rate in association with top quarks in final states with electrons, muons, and hadronically decaying tau leptons at $\sqrt{s} = 13$ TeV”. In: *Eur. Phys. J. C* 81.4 (2021), p. 378. DOI: 10.1140/epjc/s10052-021-09014-x. arXiv: 2011.03652 [hep-ex].

[63] W. Adam et al. “The DAQ and control system for the CMS Phase-1 pixel detector upgrade”. In: *JINST* 14.10 (2019), P10017. DOI: 10.1088/1748-0221/14/10/P10017.

[64] T. Lange on behalf of the CMS pixel online team. *Measurement and optimization of the soft-error-recovery rates in the Phase-1 pixel detector*. Tech. rep. 2020.

[65] Federico De Guio. “The CMS data quality monitoring software: experience and future prospects”. In: *J. Phys. Conf. Ser.* 513 (2014). Ed. by D. L. Groep and D. Bonacorsi, p. 032024. DOI: 10.1088/1742-6596/513/3/032024.

[66] Tianqi Chen and Carlos Guestrin. “XGBoost: A Scalable Tree Boosting System”. In: *Proceedings of the 22nd ACM SIGKDD International Conference on Knowledge Discovery and Data Mining*. KDD ’16. San Francisco, California, USA: Association for Computing Machinery, 2016, 785–794. ISBN: 9781450342322. DOI: 10.1145/2939672.2939785. URL: https://doi.org/10.1145/2939672.2939785.

[67] xgboost developers. *Introduction to Boosted Trees - XGboost Tutorials*. 2021. URL: https://xgboost.readthedocs.io/en/latest/tutorials/model.html.

[68] J. Kennedy and R. Eberhart. "Particle swarm optimization". In: *Proceedings of ICNN'95 - International Conference on Neural Networks*. Vol. 4. 1995, 1942–1948 vol.4. DOI: 10.1109/ICNN.1995.488968.

[69] Laurits Tani et al. "Evolutionary algorithms for hyperparameter optimization in machine learning for application in high energy physics". In: *Eur. Phys. J. C* 81.2 (2021), p. 170. DOI: 10.1140/epjc/s10052-021-08950-y. arXiv: 2011.04434 [hep-ex].

[70] Albert M Sirunyan et al. "Observation of the Higgs boson decay to a pair of τ leptons with the CMS detector". In: *Phys. Lett. B* 779 (2018), pp. 283–316. DOI: 10.1016/j.physletb.2018.02.004. arXiv: 1708.00373 [hep-ex].

[71] Albert M Sirunyan et al. "Observation of $t\bar{t}H$ production". In: *Phys. Rev. Lett.* 120.23 (2018), p. 231801. DOI: 10.1103/PhysRevLett.120.231801. arXiv: 1804.02610 [hep-ex].

[72] A. M. Sirunyan et al. "Observation of Higgs boson decay to bottom quarks". In: *Phys. Rev. Lett.* 121.12 (2018), p. 121801. DOI: 10.1103/PhysRevLett.121.121801. arXiv: 1808.08242 [hep-ex].

[73] A. M. Sirunyan et al. "Measurements of Higgs boson properties in the diphoton decay channel in proton-proton collisions at $\sqrt{s} = 13$ TeV". In: *JHEP* 11 (2018), p. 185. DOI: 10.1007/JHEP11(2018)185. arXiv: 1804.02716 [hep-ex].

[74] Albert M. Sirunyan et al. "Measurements of properties of the Higgs boson decaying to a W boson pair in pp collisions at $\sqrt{s} = 13$ TeV". In: *Phys. Lett. B* 791 (2019), p. 96. DOI: 10.1016/j.physletb.2018.12.073. arXiv: 1806.05246 [hep-ex].

[75] Albert M Sirunyan et al. "Measurements of properties of the Higgs boson decaying into the four-lepton final state in pp collisions at $\sqrt{s} = 13$ TeV". In: *JHEP* 11 (2017), p. 047. DOI: 10.1007/JHEP11(2017)047. arXiv: 1706.09936 [hep-ex].

[76] Albert M Sirunyan et al. "Combined measurements of Higgs boson couplings in proton–proton collisions at $\sqrt{s} = 13\,\text{TeV}$". In: *Eur. Phys. J. C* 79.5 (2019), p. 421. DOI: 10.1140/epjc/s10052-019-6909-y. arXiv: 1809.10733 [hep-ex].

[77] Morad Aaboud et al. "Cross-section measurements of the Higgs boson decaying into a pair of τ-leptons in proton-proton collisions at $\sqrt{s} = 13$ TeV with the ATLAS detector". In: *Phys. Rev. D* 99 (2019), p. 072001. DOI: 10.1103/PhysRevD.99.072001. arXiv: 1811.08856 [hep-ex].

[78] Morad Aaboud et al. "Observation of $H \to b\bar{b}$ decays and VH production with the ATLAS detector". In: *Phys. Lett. B* 786 (2018), pp. 59–86. DOI: 10.1016/j.physletb.2018.09.013. arXiv: 1808.08238 [hep-ex].

[79] M. Aaboud et al. "Observation of Higgs boson production in association with a top quark pair at the LHC with the ATLAS detector". In: *Phys. Lett. B* 784 (2018), pp. 173–191. DOI: 10.1016/j.physletb.2018.07.035. arXiv: 1806.00425 [hep-ex].

[80] Morad Aaboud et al. "Measurements of gluon-gluon fusion and vector-boson fusion Higgs boson production cross-sections in the $H \to WW^* \to e\nu\mu\nu$ decay channel in pp collisions at $\sqrt{s} = 13$ TeV with the ATLAS detector". In: *Phys. Lett. B* 789 (2019), pp. 508–529. DOI: 10.1016/j.physletb.2018.11.064. arXiv: 1808.09054 [hep-ex].

[81] Morad Aaboud et al. "Measurement of the Higgs boson coupling properties in the $H \to ZZ^* \to 4\ell$ decay channel at $\sqrt{s}$ = 13 TeV with the ATLAS detector". In: *JHEP* 03 (2018), p. 095. DOI: 10.1007/JHEP03(2018)095. arXiv: 1712.02304 [hep-ex].

[82] Morad Aaboud et al. "Measurements of Higgs boson properties in the diphoton decay channel with 36 fb^{-1} of pp collision data at $\sqrt{s} = 13$ TeV with the ATLAS detector". In: *Phys. Rev. D* 98 (2018), p. 052005. DOI: 10.1103/PhysRevD.98.052005. arXiv: 1802.04146 [hep-ex].

[83] Georges Aad et al. "Combined measurements of Higgs boson production and decay using up to 80 fb^{-1} of proton-proton collision data at $\sqrt{s} = 13$ TeV collected with the ATLAS experiment". In: *Phys. Rev. D* 101.1 (2020), p. 012002. DOI: 10.1103/PhysRevD.101.012002. arXiv: 1909.02845 [hep-ex].

[84] J R Andersen et al. "Handbook of LHC Higgs Cross Sections: 3. Higgs Properties". In: (July 2013). Ed. by S Heinemeyer et al. DOI: 10.5170/CERN-2013-004. arXiv: 1307.1347 [hep-ph].

[85] Albert M Sirunyan et al. "A measurement of the Higgs boson mass in the diphoton decay channel". In: *Phys. Lett. B* 805 (2020), p. 135425. DOI: 10.1016/j.physletb.2020.135425. arXiv: 2002.06398 [hep-ex].

[86] *Jet algorithms performance in 13 TeV data*. Tech. rep. Geneva: CERN, 2017. URL: https://cds.cern.ch/record/2256875.

[87] Andreas Hocker et al. "TMVA - Toolkit for Multivariate Data Analysis". In: (Mar. 2007). arXiv: physics/0703039.

[88] O. Aberle et al. *High-Luminosity Large Hadron Collider (HL-LHC): Technical design report*. CERN Yellow Reports: Monographs. Geneva: CERN, 2020. DOI: 10.23731/CYRM-2020-0010. URL: https://cds.cern.ch/record/2749422.

[89] Albert M Sirunyan et al. "Search for nonresonant Higgs boson pair production in the $b\bar{b}b\bar{b}$ final state at $\sqrt{s} = 13$ TeV". In: *JHEP* 04 (2019), p. 112. DOI: 10.1007/JHEP04(2019)112. arXiv: 1810.11854 [hep-ex].

[90] *Search for Higgs boson pair production in the four b quark final state*. Tech. rep. Geneva: CERN, 2021. URL: https://cds.cern.ch/record/2771912.

[91] Albert M Sirunyan et al. "Search for Higgs boson pair production in the $\gamma\gamma b\bar{b}$ final state in pp collisions at $\sqrt{s} = 13$ TeV". In: *Phys. Lett. B* 788 (2019), pp. 7–36. DOI: 10.1016/j.physletb.2018.10.056. arXiv: 1806.00408 [hep-ex].

[92] Albert M Sirunyan et al. "Search for nonresonant Higgs boson pair production in final states with two bottom quarks and two photons in proton-proton collisions at $\sqrt{s}$ = 13 TeV". In: *JHEP* 03 (2021), p. 257. DOI: 10.1007/JHEP03(2021)257. arXiv: 2011.12373 [hep-ex].

[93] Albert M Sirunyan et al. "Search for Higgs boson pair production in events with two bottom quarks and two tau leptons in proton–proton collisions at $\sqrt{s}$ =13TeV". In: *Phys. Lett. B* 778 (2018), pp. 101–127. DOI: 10.1016/j.physletb.2018.01.001. arXiv: 1707.02909 [hep-ex].

[94] Armen Tumasyan et al. "Search for a heavy Higgs boson decaying into two lighter Higgs bosons in the $\tau\tau$bb final state at 13 TeV". In: (June 2021). arXiv: 2106.10361 [hep-ex].

[95] J. Alwall et al. "The automated computation of tree-level and next-to-leading order differential cross sections, and their matching to parton shower simulations". In: *Journal of High Energy Physics* 2014.7 (2014). ISSN: 1029-8479. DOI: 10.1007/jhep07(2014)079. URL: http://dx.doi.org/10.1007/JHEP07(2014)079.

[96] Paolo Nason. "A New method for combining NLO QCD with shower Monte Carlo algorithms". In: *JHEP* 11 (2004), p. 040. DOI: 10.1088/1126-6708/2004/11/040. arXiv: hep-ph/0409146.

[97] Stefano Frixione, Paolo Nason, and Carlo Oleari. "Matching NLO QCD computations with Parton Shower simulations: the POWHEG method". In: *JHEP* 11 (2007), p. 070. DOI: 10.1088/1126-6708/2007/11/070. arXiv: 0709.2092 [hep-ph].

[98] Simone Alioli et al. "A general framework for implementing NLO calculations in shower Monte Carlo programs: the POWHEG BOX". In: *JHEP* 06 (2010), p. 043. DOI: 10.1007/JHEP06(2010)043. arXiv: 1002.2581 [hep-ph].

[99] Tom Melia et al. "W+W-, WZ and ZZ production in the POWHEG BOX". In: *JHEP* 11 (2011), p. 078. DOI: 10.1007/JHEP11(2011)078. arXiv: 1107.5051 [hep-ph].

[100] Paolo Nason and Giulia Zanderighi. "W^+W^- , WZ and ZZ production in the POWHEG-BOX-V2". In: *Eur. Phys. J. C* 74.1 (2014), p. 2702. DOI: 10.1140/epjc/s10052-013-2702-5. arXiv: 1311.1365 [hep-ph].

[101] John M. Campbell et al. "Top-Pair Production and Decay at NLO Matched with Parton Showers". In: *JHEP* 04 (2015), p. 114. DOI: 10.1007/JHEP04(2015)114. arXiv: 1412.1828 [hep-ph].

[102] Simone Alioli, Sven-Olaf Moch, and Peter Uwer. "Hadronic top-quark pair-production with one jet and parton showering". In: *JHEP* 01 (2012), p. 137. DOI: 10.1007/JHEP01(2012)137. arXiv: 1110.5251 [hep-ph].

[103] Simone Alioli et al. "NLO single-top production matched with shower in POWHEG: s- and t-channel contributions". In: *JHEP* 09 (2009). [Erratum: JHEP 02, 011 (2010)], p. 111. DOI: 10.1088/1126-6708/2009/09/111. arXiv: 0907.4076 [hep-ph].

[104] Emanuele Re. "Single-top Wt-channel production matched with parton showers using the POWHEG method". In: *Eur. Phys. J. C* 71 (2011), p. 1547. DOI: 10.1140/epjc/s10052-011-1547-z. arXiv: 1009.2450 [hep-ph].

[105] Rikkert Frederix, Emanuele Re, and Paolo Torrielli. "Single-top t-channel hadroproduction in the four-flavour scheme with POWHEG and aMC@NLO". In: *JHEP* 09 (2012), p. 130. DOI: 10.1007/JHEP09(2012)130. arXiv: 1207.5391 [hep-ph].

[106] Simone Alioli et al. "NLO Higgs boson production via gluon fusion matched with shower in POWHEG". In: *JHEP* 04 (2009), p. 002. DOI: 10.1088/1126-6708/2009/04/002. arXiv: 0812.0578 [hep-ph].

[107] Paolo Nason and Carlo Oleari. "NLO Higgs boson production via vector-boson fusion matched with shower in POWHEG". In: *JHEP* 02 (2010), p. 037. DOI: 10.1007/JHEP02(2010)037. arXiv: 0911.5299 [hep-ph].

[108] Ken Mimasu, Veronica Sanz, and Ciaran Williams. "Higher Order QCD predictions for Associated Higgs production with anomalous couplings to gauge bosons". In: *JHEP* 08 (2016), p. 039. DOI: 10.1007/JHEP08(2016)039. arXiv: 1512.02572 [hep-ph].

[109] G. Heinrich et al. "NLO predictions for Higgs boson pair production with full top quark mass dependence matched to parton showers". In: *JHEP* 08 (2017), p. 088. DOI: 10.1007/JHEP08(2017)088. arXiv: 1703.09252 [hep-ph].

[110] Gudrun Heinrich et al. "A non-linear EFT description of $gg \to HH$ at NLO interfaced to POWHEG". In: *JHEP* 10 (2020), p. 021. DOI: 10.1007/JHEP10(2020)021. arXiv: 2006.16877 [hep-ph].

[111] Yanyan Gao et al. "Spin Determination of Single-Produced Resonances at Hadron Colliders". In: *Phys. Rev. D* 81 (2010), p. 075022. DOI: 10.1103/PhysRevD.81.075022. arXiv: 1001.3396 [hep-ph].

[112] Sara Bolognesi et al. "On the spin and parity of a single-produced resonance at the LHC". In: *Phys. Rev. D* 86 (2012), p. 095031. DOI: 10.1103/PhysRevD.86.095031. arXiv: 1208.4018 [hep-ph].

[113] Ian Anderson et al. "Constraining Anomalous HVV Interactions at Proton and Lepton Colliders". In: *Phys. Rev. D* 89.3 (2014). Ed. by Norman A. Graf, Michael E. Peskin, and Jonathan L. Rosner, p. 035007. DOI: 10.1103/PhysRevD.89.035007. arXiv: 1309.4819 [hep-ph].

[114] Andrei V. Gritsan et al. "Constraining anomalous Higgs boson couplings to the heavy flavor fermions using matrix element techniques". In: *Phys. Rev. D* 94.5 (2016), p. 055023. DOI: 10.1103/PhysRevD.94.055023. arXiv: 1606.03107 [hep-ph].

[115] Andrei V. Gritsan et al. "New features in the JHU generator framework: constraining Higgs boson properties from on-shell and off-shell production". In: *Phys. Rev. D* 102.5 (2020), p. 056022. DOI: 10.1103/PhysRevD.102.056022. arXiv: 2002.09888 [hep-ph].

[116] Till Martini et al. "Probing the CP structure of the top quark Yukawa coupling: Loop sensitivity versus on-shell sensitivity". In: *Phys. Rev. D* 104.5 (2021), p. 055045. DOI: 10.1103/PhysRevD.104.055045. arXiv: 2104.04277 [hep-ph].

[117] Jeffrey Davis et al. "Constraining anomalous Higgs boson couplings to virtual photons". In: (Sept. 2021). arXiv: 2109.13363 [hep-ph].

[118] Torbjörn Sjöstrand et al. “An introduction to PYTHIA 8.2”. In: *Computer Physics Communications* 191 (2015), 159–177. ISSN: 0010-4655. DOI: 10.1016/j.cpc.2015.01.024. URL: http://dx.doi.org/10.1016/j.cpc.2015.01.024.

[119] Vardan Khachatryan et al. “Event generator tunes obtained from underlying event and multiparton scattering measurements”. In: (2015). arXiv: 1512.00815 [hep-ex].

[120] A. M. Sirunyan et al. “Extraction and validation of a new set of CMS PYTHIA8 tunes from underlying-event measurements”. In: *The European Physical Journal C* 80.1 (2020). DOI: 10.1140/epjc/s10052-019-7499-4. URL: https://doi.org/10.1140/epjc/s10052-019-7499-4.

[121] Peter Skands, Stefano Carrazza, and Juan Rojo. “Tuning PYTHIA 8.1: the Monash 2013 tune”. In: *Eur. Phys. J.* C 74.8 (2014), p. 3024. DOI: 10.1140/epjc/s10052-014-3024-y. arXiv: 1404.5630 [hep-ph].

[122] R. D. Ball et al. “Parton distributions for the LHC Run II”. In: *JHEP* 04 (2015), p. 040. DOI: 10.1007/JHEP04(2015)040. arXiv: 1410.8849 [hep-ph].

[123] Jon Butterworth et al. “PDF4LHC recommendations for LHC Run II”. In: *J. Phys. G* 43 (2016), p. 023001. DOI: 10.1088/0954-3899/43/2/023001. arXiv: 1510.03865 [hep-ph].

[124] Juan Rojo et al. “The PDF4LHC report on PDFs and LHC data: results from Run I and preparation for Run II”. In: *Journal of Physics G: Nuclear and Particle Physics* 42.10 (2015), p. 103103. ISSN: 1361-6471. DOI: 10.1088/0954-3899/42/10/103103. eprint: 1507.00556. URL: http://dx.doi.org/10.1088/0954-3899/42/10/103103.

[125] A. Accardi et al. “A critical appraisal and evaluation of modern PDFs”. In: *The European Physical Journal C* 76.8 (2016). ISSN: 1434-6052. DOI: 10.1140/epjc/s10052-016-4285-4. eprint: 1603.08906. URL: http://dx.doi.org/10.1140/epjc/s10052-016-4285-4.

[126] S. Agostinelli et al. “GEANT4—a simulation toolkit”. In: *Nucl. Instrum. Meth.* A 506 (2003), p. 250. DOI: 10.1016/S0168-9002(03)01368-8.

[127] The CMS Collaboration. *Public CMS Luminosity Information*. URL: https://twiki.cern.ch/twiki/bin/view/CMSPublic/LumiPublicResults.

[128] The CMS Collaboration. *Tau ID scale factors*. URL: https://github.com/cms-tau-pog/TauIDSFs.

[129] Serguei Chatrchyan et al. “Identification of b-Quark Jets with the CMS Experiment”. In: *JINST* 8 (2013), P04013. DOI: 10.1088/1748-0221/8/04/P04013. arXiv: 1211.4462 [hep-ex].

[130] The CMS collaboration. “Determination of jet energy calibration and transverse momentum resolution in CMS”. In: 6.11 (2011), P11002–P11002. DOI: 10.1088/1748-0221/6/11/p11002. URL: https://doi.org/10.1088/1748-0221/6/11/p11002.

[131] *Performance of missing energy reconstruction in 13 TeV pp collision data using the CMS detector*. Tech. rep. Geneva: CERN, 2016. URL: http://cds.cern.ch/record/2205284.

[132] Laurent Thomas. "L1 pre-firing in 2016 and 2017 data". Cross POG Forum. 2018. URL: https://indico.cern.ch/event/764279/contributions/3175800/attachments/1734412/2811545/prefiring_2.pdf.

[133] Michal Czakon et al. "Top-pair production at the LHC through NNLO QCD and NLO EW". In: *JHEP* 10 (2017), p. 186. DOI: 10.1007/JHEP10(2017)186. arXiv: 1705.04105 [hep-ph].

[134] Matteo Capozi and Gudrun Heinrich. "Exploring anomalous couplings in Higgs boson pair production through shape analysis". In: *JHEP* 03 (2020), p. 091. DOI: 10.1007/JHEP03(2020)091. arXiv: 1908.08923 [hep-ph].

[135] Alexandra Carvalho et al. "On the reinterpretation of non-resonant searches for Higgs boson pairs". In: *JHEP* 02 (2021), p. 049. DOI: 10.1007/JHEP02(2021)049. arXiv: 1710.08261 [hep-ph].

[136] Keith Rehermann and Brock Tweedie. "Efficient Identification of Boosted Semileptonic Top Quarks at the LHC". In: *JHEP* 03 (2011), p. 059. DOI: 10.1007/JHEP03(2011)059. arXiv: 1007.2221 [hep-ph].

[137] Vardan Khachatryan et al. "Performance of Electron Reconstruction and Selection with the CMS Detector in Proton-Proton Collisions at $\sqrt{s}$ = 8 TeV". In: *JINST* 10.06 (2015), P06005. DOI: 10.1088/1748-0221/10/06/P06005. arXiv: 1502.02701 [physics.ins-det].

[138] Serguei Chatrchyan et al. "Performance of CMS Muon Reconstruction in pp Collision Events at $\sqrt{s} = 7$ TeV". In: *JINST* 7 (2012), P10002. DOI: 10.1088/1748-0221/7/10/P10002. arXiv: 1206.4071 [physics.ins-det].

[139] Jesse Thaler and Ken Van Tilburg. "Identifying Boosted Objects with N-subjettiness". In: *JHEP* 03 (2011), p. 015. DOI: 10.1007/JHEP03(2011)015. arXiv: 1011.2268 [hep-ph].

[140] Rafael Coelho Lopes De Sa et al. "About the normalization of diboson samples for Run2". PH Generator meeting. 2015. URL: https://indico.cern.ch/event/439995/contributions/1094416/attachments/1143460/1638648/diboson_final.pdf.

[141] Albert M Sirunyan et al. "Evidence for associated production of a Higgs boson with a top quark pair in final states with electrons, muons, and hadronically decaying τ leptons at $\sqrt{s} = 13$ TeV". In: *JHEP* 08 (2018), p. 066. DOI: 10.1007/JHEP08(2018)066. arXiv: 1803.05485 [hep-ex].

[142] *Search for nonresonant Higgs boson pair production in the 4 leptons plus 2 b jets final state in proton-proton collisions at $\sqrt{s} = 13$ TeV*. Tech. rep. Geneva: CERN, 2020. URL: https://cds.cern.ch/record/2725691.

[143] Lorenzo Bianchini et al. “Reconstruction of the Higgs mass in events with Higgs bosons decaying into a pair of τ leptons using matrix element techniques”. In: *Nucl. Instrum. Meth. A* 862 (2017), pp. 54–84. DOI: 10.1016/j.nima.2017.05.001. arXiv: 1603.05910 [hep-ex].

[144] Vardan Khachatryan et al. “Jet energy scale and resolution in the CMS experiment in pp collisions at 8 TeV”. In: *JINST* 12.02 (2017), P02014. DOI: 10.1088/1748-0221/12/02/P02014. arXiv: 1607.03663 [hep-ex].

[145] Albert M Sirunyan et al. “Precision luminosity measurement in proton-proton collisions at $\sqrt{s} = 13$ TeV in 2015 and 2016 at CMS”. In: *Eur. Phys. J. C* 81.9 (2021), p. 800. DOI: 10.1140/epjc/s10052-021-09538-2. arXiv: 2104.01927 [hep-ex].

[146] “CMS luminosity measurement for the 2017 data-taking period at $\sqrt{s} = 13$ TeV”. In: (2018).

[147] “CMS luminosity measurement for the 2018 data-taking period at $\sqrt{s} = 13$ TeV”. In: (2019).

[148] Frédéric A. Dreyer and Alexander Karlberg. “Vector-Boson Fusion Higgs Pair Production at N^3LO”. In: *Phys. Rev. D* 98.11 (2018), p. 114016. DOI: 10.1103/PhysRevD.98.114016. arXiv: 1811.07906 [hep-ph].

[149] Marcel Rieger for the CMS Collaboration. *Naming conventions for the full run 2 HH combination*. Gitlab, commit 0022cc2a. 2021. URL: https://gitlab.cern.ch/hh/naming-conventions.

[150] Glen Cowan et al. “Asymptotic formulae for likelihood-based tests of new physics”. In: *Eur. Phys. J. C* 71 (2011). [Erratum: Eur.Phys.J.C 73, 2501 (2013)], p. 1554. DOI: 10.1140/epjc/s10052-011-1554-0. arXiv: 1007.1727 [physics.data-an].

[151] *Procedure for the LHC Higgs boson search combination in Summer 2011*. Tech. rep. Geneva: CERN, 2011. URL: https://cds.cern.ch/record/1379837.

[152] Roger J. Barlow and Christine Beeston. “Fitting using finite Monte Carlo samples”. In: *Comput. Phys. Commun.* 77 (1993), pp. 219–228. DOI: 10.1016/0010-4655(93)90005-W.

[153] Alexander L. Read. “Presentation of search results: The CL(s) technique”. In: *J. Phys. G* 28 (2002). Ed. by M. R. Whalley and L. Lyons, pp. 2693–2704. DOI: 10.1088/0954-3899/28/10/313.

[154] Thomas Junk. “Confidence level computation for combining searches with small statistics”. In: *Nucl. Instrum. Meth. A* 434 (1999), pp. 435–443. DOI: 10.1016/S0168-9002(99)00498-2. arXiv: hep-ex/9902006.

[155] CMS Collaboration. *Combine - Statistical analysis software tools for CMS*. URL: https://cms-analysis.github.io/HiggsAnalysis-CombinedLimit/.

[156] R. Cousins. “Generalization of Chisquare Goodness-ofFit Test for Binned Data Using Saturated Models , with Application to Histograms”. In: 2013.

[157] M. Rieger, L. Cadamuro and F. Monti for the CMS Collaboration. *Custom HH physics model implementing gluon gluon fusion (ggf / gghh), vector boson fusion (vbf / qqhh) and V boson associated production (vhh) modes.* CERN gitlab, commit c79f9714. 2021. URL: https://gitlab.cern.ch/hh/tools/inference/-/blob/master/dhi/models/hh_model.py.

[158] Encyclopedia of Mathematics. *Condition number.* URL: http://encyclopediaofmath.org/index.php?title=Condition_number\&oldid=50975.

[159] L. Cadamuro, . Carvalho, P.Fackeldey, B.Fischer, T. Lange, D. Noll, M. Rieger and L.Wang for the CMS Collaboration. *HH Inference Tools*. 2021. URL: https://cms-hh.web.cern.ch/tools/inference/.

[160] The CMS collaboration. "Search for Higgs boson pairs decaying to WWWW, WW$\tau\tau$, and $\tau\tau\tau\tau$ in proton-proton collisions at $\sqrt{s} = 13$ TeV". In: *JHEP* (2022). [To be published].

[161] Morad Aaboud et al. "Search for Higgs boson pair production in the $WW^{(*)}WW^{(*)}$ decay channel using ATLAS data recorded at $\sqrt{s} = 13$ TeV". In: *JHEP* 05 (2019), p. 124. DOI: 10.1007/JHEP05(2019)124. arXiv: 1811.11028 [hep-ex].

[162] Georges Aad et al. "Combination of searches for Higgs boson pairs in pp collisions at $\sqrt{s} =$13 TeV with the ATLAS detector". In: *Phys. Lett. B* 800 (2020), p. 135103. DOI: 10.1016/j.physletb.2019.135103. arXiv: 1906.02025 [hep-ex].

[163] Albert M Sirunyan et al. "Combination of searches for Higgs boson pair production in proton-proton collisions at $\sqrt{s} = 13$ TeV". In: *Phys. Rev. Lett.* 122.12 (2019), p. 121803. DOI: 10.1103/PhysRevLett.122.121803. arXiv: 1811.09689 [hep-ex].

[164] Georges Aad et al. "Search for the $HH \to b\bar{b}b\bar{b}$ process via vector-boson fusion production using proton-proton collisions at $\sqrt{s} = 13$ TeV with the ATLAS detector". In: *JHEP* 07 (2020). [Erratum: JHEP 01, 145 (2021), Erratum: JHEP 05, 207 (2021)], p. 108. DOI: 10.1007/JHEP07(2020)108. arXiv: 2001.05178 [hep-ex].

[165] *Search for resonant and non-resonant Higgs boson pair production in the $b\bar{b}\tau^+\tau^-$ decay channel using 13 TeV pp collision data from the ATLAS detector*. Tech. rep. Geneva: CERN, 2021. URL: https://cds.cern.ch/record/2777236.

[166] *Search for Higgs boson pair production in the two bottom quarks plus two photons final state in pp collisions at $\sqrt{s} = 13$ TeV with the ATLAS detector*. Tech. rep. Geneva: CERN, 2021. URL: https://cds.cern.ch/record/2759683.

[167] Georges Aad et al. "Search for non-resonant Higgs boson pair production in the $bb\ell\nu\ell\nu$ final state with the ATLAS detector in pp collisions at $\sqrt{s} = 13$ TeV". In: *Phys. Lett. B* 801 (2020), p. 135145. DOI: 10.1016/j.physletb.2019.135145. arXiv: 1908.06765 [hep-ex].

[168] *How to work with files for Good Luminosity Sections in JSON format*. URL: https://twiki.cern.ch/twiki/bin/view/CMSPublic/SWGuideGoodLumiSectionsJSONFile.

[169] Simone Alioli et al. “ZZ production in gluon fusion at NLO matched to parton-shower”. In: *Phys. Rev. D* 95.3 (2017), p. 034042. DOI: 10.1103/PhysRevD.95.034042. arXiv: 1609.09719 [hep-ph].

[170] Michal Czakon and Alexander Mitov. “Top++: A Program for the Calculation of the Top-Pair Cross-Section at Hadron Colliders”. In: *Comput. Phys. Commun.* 185 (2014), p. 2930. DOI: 10.1016/j.cpc.2014.06.021. arXiv: 1112.5675 [hep-ph].

[171] P. Kant et al. “HatHor for single top-quark production: Updated predictions and uncertainty estimates for single top-quark production in hadronic collisions”. In: *Computer Physics Communications* 191 (2015), 74–89. ISSN: 0010-4655. DOI: 10.1016/j.cpc.2015.02.001. URL: http://dx.doi.org/10.1016/j.cpc.2015.02.001.

[172] M. Aliev et al. “HATHOR – HAdronic Top and Heavy quarks crOss section calculatoR”. In: *Computer Physics Communications* 182.4 (2011), 1034–1046. ISSN: 0010-4655. DOI: 10.1016/j.cpc.2010.12.040. URL: http://dx.doi.org/10.1016/j.cpc.2010.12.040.

[173] Izaak Neutelings. “Drell-Yan + jets cross section @ NNLO”. PH Generator meeting. 2018. URL: https://indico.cern.ch/event/746829/contributions/3138541/attachments/1717905/2772129/Drell-Yan_jets_crosssection.pdf.

[174] Izaak Neutelings. “Updated NNLO Drell-Yan + jets cross section”. PH Generator meeting. 2019. URL: https://indico.cern.ch/event/841566/contributions/3565385/attachments/1914850/3185933/Drell-Yan_jets_crosssection_September2019_update.pdf.

List of Figures

List of Tables

Declaration on Oath/ Eiderstattliche Versicherung

Hiermit versichere ich an Eides statt, die vorliegende Dissertationsschrift selbst verfasst und keine anderen als die angegebenen Hilfsmittel und Quellen benutzt zu haben.

.....	.....
Ort, Datum	Unterschrift

Appendix

Appendix A HLT Trigger Paths ($HH \rightarrow$ Multilepton)

Category	HLT path	Used in 16/17/18
Double τ_h triggers	HLT_DoubleMediumIsoPFTau35_Trk1_eta2p1_Reg	✓ / X / X
	HLT_DoubleMediumCombinedIsoPFTau35_Trk1_eta2p1_Reg	✓/ X / X
	HLT_DoubleMediumChargedIsoPFTau35_Trk1_eta2p1_Reg	X / ✓ / X
	HLT_DoubleTightChargedIsoPFTau35_Trk1_TightID_eta2p1_Reg	X /✓/✓
	HLT_DoubleMediumChargedIsoPFTau40_Trk1_TightID_eta2p1_Reg	X / ✓/ ✓
	HLT_DoubleTightChargedIsoPFTau40_Trk1_eta2p1_Reg	X / ✓ / ✓
	HLT_DoubleMediumChargedIsoPFTauHPS35_Trk1_eta2p1_Reg	X / X / ✓
Single lepton triggers	HLT_Ele25_eta2p1_WPTight_Gsf	✓ / X / X
	HLT_Ele27_WPTight_Gsf	✓ / X / X
	HLT_Ele27_eta2p1_WPLoose_Gsf	✓ / X / X
	HLT_Ele32_WPTight_Gsf	X / ✓ / ✓
	HLT_Ele35_WPTight_Gsf	X/✓/X
	HLT_IsoMu22	✓ / X / X
	HLT_IsoTkMu22	✓ / X / X
	HLT_IsoMu22_eta2p1	✓ / X / X
	HLT_IsoTkMu22_eta2p1	✓ / X / X
	HLT_IsoMu24	✓ / ✓ / ✓
	HLT_IsoTkMu24	✓ / X / X
	HLT_IsoMu27	X / ✓ / X
Lepton+τ_h cross−triggers	HLT_Ele24_eta2p1_WPLoose_Gsf_LooseIsoPFTau20	✓ / X / X
	HLT_Ele24_eta2p1_WPLoose_Gsf_LooseIsoPFTau20_SingleL1	✓ / X / X
	HLT_Ele24_eta2p1_WPLoose_Gsf_LooseIsoPFTau30	✓ / X / X
	HLT_Ele24_eta2p1_WPTight_Gsf_LooseChargedIsoPFTau30_eta2p1_CrossL1	X / ✓ / ✓
	HLT_Ele24_eta2p1_WPTight_Gsf_LooseChargedIsoPFTauHPS30_eta2p1_CrossL1	X / X / ✓
	HLT_IsoMu19_eta2p1_LooseIsoPFTau20_SingleL1	✓ / X / X
	HLT_IsoMu20_eta2p1_LooseChargedIsoPFTau27_eta2p1_CrossL1	X / ✓ / ✓
	HLT_IsoMu20_eta2p1_LooseChargedIsoPFTauHPS27_eta2p1_CrossL1	X / X / ✓
Double lepton triggers	HLT_Ele23_Ele12_CaloIdL_TrackIdL_IsoVL_DZ	✓ / X / X
	HLT_Ele23_Ele12_CaloIdL_TrackIdL_IsoVL	X / ✓ / ✓
	HLT_Mu17_TrkIsoVVL_Mu8_TrkIsoVVL	✓ / X / X
	HLT_Mu17_TrkIsoVVL_Mu8_TrkIsoVVL_DZ	✓ / X / X
	HLT_Mu17_TrkIsoVVL_TkMu8_TrkIsoVVL	✓ / X / X
	HLT_Mu17_TrkIsoVVL_TkMu8_TrkIsoVVL_DZ	✓ / X / X
	HLT_Mu17_TrkIsoVVL_Mu8_TrkIsoVVL_DZ_Mass8	X / ✓ / X
	HLT_Mu17_TrkIsoVVL_Mu8_TrkIsoVVL_DZ_Mass3p8	X / ✓ / ✓
	HLT_Mu8_TrkIsoVVL_Ele23_CaloIdL_TrackIdL_IsoVL	✓ / X / X
	HLT_Mu8_TrkIsoVVL_Ele23_CaloIdL_TrackIdL_IsoVL_DZ	✓ / ✓ / ✓
	HLT_Mu23_TrkIsoVVL_Ele8_CaloIdL_TrackIdL_IsoVL	✓ / X / X
	HLT_Mu23_TrkIsoVVL_Ele8_CaloIdL_TrackIdL_IsoVL_DZ	✓ / X / X
	HLT_Mu8_TrkIsoVVL_Ele23_CaloIdL_TrackIdL_IsoVL_DZ	✓ / ✓ / X
	HLT_Mu12_TrkIsoVVL_Ele23_CaloIdL_TrackIdL_IsoVL_DZ	✓ / ✓ / X
	HLT_Mu23_TrkIsoVVL_Ele12_CaloIdL_TrackIdL_IsoVL	✓ / ✓ / X
	HLT_Mu23_TrkIsoVVL_Ele12_CaloIdL_TrackIdL_IsoVL_DZ	X / ✓ / X
Triple lepton triggers	HLT_Ele16_Ele12_Ele8_CaloIdL_TrackIdL	✓ / ✓ / ✓
	HLT_TripleMu_12_10_5	✓ / ✓ / ✓
	HLT_Mu8_DiEle12_CaloIdL_TrackIdL	✓ / ✓ / ✓
	HLT_DiMu9_Ele9_CaloIdL_TrackIdL	✓ / X / X
	HLT_DiMu9_Ele9_CaloIdL_TrackIdL_DZ	X / ✓ / ✓

Table 8.1: HLT trigger paths used in the $HH \rightarrow$ Multilepton analysis. The corresponding trigger category mapping the different trigger to the seven analysis sub channel as given in Tab. 6.1 and weather the trigger path was used (✓) or not used (**X**) in a given data taking year 16/17/18 is given as well.

Appendix B List of datasets ($HH \rightarrow$ Multilepton)

Data stream	Dataset name	LHC run number	Integrated luminosity (fb^{-1})
SingleElectron	/SingleElectron/Run2016B-17Jul2018_ver2-v1/MINIAOD[1]	273150–275376	5.75
	/SingleElectron/Run2016C-17Jul2018-v1/MINIAOD[1]	275656–276283	2.57
	/SingleElectron/Run2016D-17Jul2018-v1/MINIAOD[1]	276315–276811	4.24
	/SingleElectron/Run2016E-17Jul2018-v1/MINIAOD[1]	276831–277420	4.02
	/SingleElectron/Run2016F-17Jul2018-v1/MINIAOD[1]	277932–278808	3.10
	/SingleElectron/Run2016G-17Jul2018-v1/MINIAOD[1]	278820–280385	7.58
	/SingleElectron/Run2016H-17Jul2018-v1/MINIAOD[1]	281613–284044	8.65
SingleMuon	/SingleMuon/Run2016B-17Jul2018_ver2-v1/MINIAOD[1]	273150–275376	5.75
	/SingleMuon/Run2016C-17Jul2018-v1/MINIAOD[1]	275656–276283	2.57
	/SingleMuon/Run2016D-17Jul2018-v1/MINIAOD[1]	276315–276811	4.24
	/SingleMuon/Run2016E-17Jul2018-v1/MINIAOD[1]	276831–277420	4.02
	/SingleMuon/Run2016F-17Jul2018-v1/MINIAOD[1]	277932–278808	3.10
	/SingleMuon/Run2016G-17Jul2018-v1/MINIAOD[1]	278820–280385	7.58
	/SingleMuon/Run2016H-17Jul2018-v1/MINIAOD[1]	281613–284044	8.65
DoubleEG	/DoubleEG/Run2016B-17Jul2018_ver2-v1/MINIAOD[1]	273150–275376	5.75
	/DoubleEG/Run2016C-17Jul2018-v1/MINIAOD[1]	275656–276283	2.57
	/DoubleEG/Run2016D-17Jul2018-v1/MINIAOD[1]	276315–276811	4.24
	/DoubleEG/Run2016E-17Jul2018-v1/MINIAOD[1]	276831–277420	4.02
	/DoubleEG/Run2016F-17Jul2018-v1/MINIAOD[1]	277932–278808	3.10
	/DoubleEG/Run2016G-17Jul2018-v1/MINIAOD[1]	278820–280385	7.58
	/DoubleEG/Run2016H-17Jul2018-v1/MINIAOD[1]	281613–284044	8.65
DoubleMuon	/DoubleMuon/Run2016B-17Jul2018_ver2-v1/MINIAOD[1]	273150–275376	5.75
	/DoubleMuon/Run2016C-17Jul2018-v1/MINIAOD[1]	275656–276283	2.57
	/DoubleMuon/Run2016D-17Jul2018-v1/MINIAOD[1]	276315–276811	4.24
	/DoubleMuon/Run2016E-17Jul2018-v1/MINIAOD[1]	276831–277420	4.02
	/DoubleMuon/Run2016F-17Jul2018-v1/MINIAOD[1]	277932–278808	3.10
	/DoubleMuon/Run2016G-17Jul2018-v1/MINIAOD[1]	278820–280385	7.58
	/DoubleMuon/Run2016H-17Jul2018-v1/MINIAOD[1]	281613–284044	8.65
MuonEG	/MuonEG/Run2016B-17Jul2018_ver2-v1/MINIAOD[1]	273150–275376	5.75
	/MuonEG/Run2016C-17Jul2018-v1/MINIAOD[1]	275656–276283	2.57
	/MuonEG/Run2016D-17Jul2018-v1/MINIAOD[1]	276315–276811	4.24
	/MuonEG/Run2016E-17Jul2018-v2/MINIAOD[1]	276831–277420	4.02
	/MuonEG/Run2016F-17Jul2018-v1/MINIAOD[1]	277932–278808	3.10
	/MuonEG/Run2016G-17Jul2018-v1/MINIAOD[1]	278820–280385	7.57
	/MuonEG/Run2016H-17Jul2018-v1/MINIAOD[1]	281613–284044	8.65
Tau	/Tau/Run2016B-17Jul2018_ver2-v1/MINIAOD[1]	273150–275376	5.75
	/Tau/Run2016C-17Jul2018-v1/MINIAOD[1]	275656–276283	2.57
	/Tau/Run2016D-17Jul2018-v1/MINIAOD[1]	276315–276811	4.24
	/Tau/Run2016E-17Jul2018-v1/MINIAOD[1]	276831–277420	4.02
	/Tau/Run2016F-17Jul2018-v1/MINIAOD[1]	277932–278808	3.10
	/Tau/Run2016G-17Jul2018-v1/MINIAOD[1]	278820–280385	7.58
	/Tau/Run2016H-17Jul2018-v1/MINIAOD[1]	281613–284044	8.65

[1] Cert_271036-284044_13TeV_23Sep2016ReReco_Collisions16_JSON.txt

Table 8.2: 2016 CMS datasets used in the $HH \rightarrow$ Multilepton analysis. The corresponding data stream, the range of LHC run numbers and the gathered luminosity per data set are given as well. From the given run range, only validated runs (good-run) with verified data quality according to the indicated json file are used [168].

Data stream	Dataset name	LHC run number	Integrated luminosity (fb^{-1})
SingleElectron	/SingleElectron/Run2017B-31Mar2018-v1/MINIAOD[1]	297047–299329	4.79
	/SingleElectron/Run2017C-31Mar2018-v1/MINIAOD[1]	299368–302029	9.63
	/SingleElectron/Run2017D-31Mar2018-v1/MINIAOD[1]	302030–302663	4.25
	/SingleElectron/Run2017E-31Mar2018-v1/MINIAOD[1]	303818–304797	9.31
	/SingleElectron/Run2017F-31Mar2018-v1/MINIAOD[1]	305040–306460	13.54
SingleMuon	/SingleMuon/Run2017B-31Mar2018-v1/MINIAOD[1]	297047–299329	4.79
	/SingleMuon/Run2017C-31Mar2018-v1/MINIAOD[1]	299368–302029	9.63
	/SingleMuon/Run2017D-31Mar2018-v1/MINIAOD[1]	302031–302663	4.25
	/SingleMuon/Run2017E-31Mar2018-v1/MINIAOD[1]	303824–304797	9.31
	/SingleMuon/Run2017F-31Mar2018-v1/MINIAOD[1]	305040–306462	13.54
DoubleEG	/DoubleEG/Run2017B-31Mar2018-v1/MINIAOD[1]	297047–299329	4.79
	/DoubleEG/Run2017C-31Mar2018-v1/MINIAOD[1]	299368–302029	9.63
	/DoubleEG/Run2017D-31Mar2018-v1/MINIAOD[1]	302030–302663	4.25
	/DoubleEG/Run2017E-31Mar2018-v1/MINIAOD[1]	303818–304797	9.31
	/DoubleEG/Run2017F-31Mar2018-v1/MINIAOD[1]	305040–306460	13.54
DoubleMuon	/DoubleMuon/Run2017B-31Mar2018-v1/MINIAOD[1]	297047–299329	4.79
	/DoubleMuon/Run2017C-31Mar2018-v1/MINIAOD[1]	299368–302029	9.63
	/DoubleMuon/Run2017D-31Mar2018-v1/MINIAOD[1]	302031–302663	4.25
	/DoubleMuon/Run2017E-31Mar2018-v1/MINIAOD[1]	303824–304797	9.31
	/DoubleMuon/Run2017F-31Mar2018-v1/MINIAOD[1]	305040–306462	13.54
MuonEG	/MuonEG/Run2017B-31Mar2018-v1/MINIAOD[1]	297047–299329	4.79
	/MuonEG/Run2017C-31Mar2018-v1/MINIAOD[1]	299368–302029	9.63
	/MuonEG/Run2017D-31Mar2018-v1/MINIAOD[1]	302031–302663	4.25
	/MuonEG/Run2017E-31Mar2018-v1/MINIAOD[1]	303824–304797	9.31
	/MuonEG/Run2017F-31Mar2018-v1/MINIAOD[1]	305040–306460	13.54
Tau	/Tau/Run2017B-31Mar2018-v1/MINIAOD[1]	297047–299329	4.79
	/Tau/Run2017C-31Mar2018-v1/MINIAOD[1]	299368–302029	9.63
	/Tau/Run2017D-31Mar2018-v1/MINIAOD[1]	302031–302663	4.25
	/Tau/Run2017E-31Mar2018-v1/MINIAOD[1]	303824–304797	9.31
	/Tau/Run2017F-31Mar2018-v1/MINIAOD[1]	305040–306460	13.53

[1] Cert_294927-306462_13TeV_EOY2017ReReco_Collisions17_JSON_v1.txt

Table 8.3: 2017 CMS datasets used in the HH $\rightarrow$ Multilepton analysis. The corresponding data stream, the range of LHC run numbers and the gathered luminosity per data set are given as well. From the given run range, only validated runs (good-run) with verified data quality according to the indicated json file are used [168].

Data stream	Dataset name	LHC run number	Integrated luminosity (fb^{-1})
SingleMuon	/SingleMuon/Run2018A-17Sep2018-v2/MINIAOD[1]	315257–316995	14.03
	/SingleMuon/Run2018B-17Sep2018-v1/MINIAOD[1]	317080–319310	7.06
	/SingleMuon/Run2018C-17Sep2018-v1/MINIAOD[1]	319337–320065	6.90
	/SingleMuon/Run2018D-22Jan2019-v2/MINIAOD[1]	320500–325175	31.74
EGamma	/EGamma/Run2018A-17Sep2018-v2/MINIAOD[1]	315257–316995	14.03
	/EGamma/Run2018B-17Sep2018-v1/MINIAOD[1]	317080–319310	7.06
	/EGamma/Run2018C-17Sep2018-v1/MINIAOD[1]	319337–320065	6.90
	/EGamma/Run2018D-22Jan2019-v2/MINIAOD[1]	320413–325175	31.74
DoubleMuon	/DoubleMuon/Run2018A-17Sep2018-v2/MINIAOD[1]	315257–316995	14.03
	/DoubleMuon/Run2018B-17Sep2018-v1/MINIAOD[1]	317080–319310	7.06
	/DoubleMuon/Run2018C-17Sep2018-v1/MINIAOD[1]	319337–320065	6.90
	/DoubleMuon/Run2018D-PromptReco-v2/MINIAOD[1]	320500–325175	31.74
MuonEG	/MuonEG/Run2018A-17Sep2018-v1/MINIAOD[1]	315257–316995	14.03
	/MuonEG/Run2018B-17Sep2018-v1/MINIAOD[1]	317080–319310	7.06
	/MuonEG/Run2018C-17Sep2018-v1/MINIAOD[1]	319337–320065	6.90
	/MuonEG/Run2018D-PromptReco-v2/MINIAOD[1]	320500–325175	31.74
Tau	/Tau/Run2018A-17Sep2018-v1/MINIAOD[1]	315257–316995	14.01
	/Tau/Run2018B-17Sep2018-v1/MINIAOD[1]	317080–319310	7.06
	/Tau/Run2018C-17Sep2018-v1/MINIAOD[1]	319337–320065	6.90
	/Tau/Run2018D-PromptReco-v2/MINIAOD[1]	320497–325175	31.74

[1] Cert_314472-325175_13TeV_17SeptEarlyReReco2018ABC_PromptEraD_Collisions18_JSON.txt

Table 8.4: 2018 CMS datasets used in the HH $\rightarrow$ Multilepton analysis. The corresponding data stream, the range of LHC run numbers and the gathered luminosity per data set are given as well. From the given run range, only validated runs (good-run) with verified data quality according to the indicated json file are used [168].

MC background samples 2016

Table 8.5: List of of MC samples used to estimate and model Di-Boson backgrounds for events gathered in 2016. The cross section used for each sample is given, where available cross sections from higher order calculation are used. Some cross section are directly extracted from the corresponding MC sample as the cross section is computed during matrix event generation, this indicated by labels for the usage of MADGRAPH5_AMC@NLO: **[M]**, POWHEG V2: **[POW]** and PYTHIA: **[PY]** (see Sec. 6.2.2). Additionaly the usage in signal extraction and the training of ml methods is given.

Process	CMS internal sample name	Cross section [pb]	ml-training	signal ext.
ZZ	/ZZTo4L_13TeV_powheg_pythia8/[1]	1.26 [140]	✓	✓
	/ZZTo4L_13TeV_powheg_pythia8_ext1/[2]	1.26 [140]	✓	✓
	/GluGluToContinToZZTo4tau_13TeV_MCFM701_pythia8/[2]	0.00349 [169]	✓	✓
	/GluGluToContinToZZTo4mu_13TeV_MCFM701_pythia8/[2]	0.00349 [169]	✓	✓
	/GluGluToContinToZZTo4e_13TeV_MCFM701_pythia8/[2]	0.00349 [169]	✓	✓
	/GluGluToContinToZZTo2e2tau_13TeV_MCFM701_pythia8/[2]	0.00698 [169]	✓	✓
	/GluGluToContinToZZTo2e2mu_13TeV_MCFM701_pythia8/[2]	0.00698 [169]	✓	✓
	/GluGluToContinToZZTo2mu2tau_13TeV_MCFM701_pythia8/[2]	0.00698 [169]	✓	✓
WZ	/WZTo3LNu_TuneCUETP8M1_13TeV-amcatnloFXFX-pythia8/[2]	4.43 [140]	X	✓
	/WZTo3LNu_mllmin01_13TeV-powheg-pythia8/[2]	4.43 [140][5]	✓	X
	/WZTo3LNu_mllmin01_13TeV-powheg-pythia8_ext1/[3]	4.43 [140][5]	✓	X
	/WZTo3LNu_TuneCUETP8M1_13TeV-powheg-pythia8/[4]	4.43 [140]	✓	X
	/WZTo2L2Q_13TeV_amcatnloFXFX_madspin_pythia8/[2]	5.6 [140]	X	✓
WW	/WWTo2L2Nu_13TeV-powheg/[2]	12.2 [140]	X	✓
	/WWTo2L2Nu_DoubleScattering_13TeV-pythia8/[2]	0.223 **[PY]**	X	✓
	/WpWpJJ_EWK-QCD_TuneCUETP8M1_13TeV-madgraph-pythia8/[1]	0.0493×10^{-2} **[M,PY]**	X	✓
Wγ	/WGToLNuG_01J_5f_TuneCUETP8M1_13TeV-amcatnloFXFX-pythia8/[2]	1.92×10^{1} **[M,PY]**	X	✓
Zγ	/ZGTo2LG_TuneCUETP8M1_13TeV-amcatnloFXFX-pythia8/[4]	1.24×10^{1} **[M,PY]**	X	✓

[1] RunIISummer16MiniAODv3-PUMoriond17_94X_mcRun2_asymptotic_v3-v1/MINIAODSIM

[2] RunIISummer16MiniAODv3-PUMoriond17_94X_mcRun2_asymptotic_v3-v2/MINIAODSIM

[3] RunIISummer16MiniAODv3-PUMoriond17_94X_mcRun2_asymptotic_v3_ext1-v2/MINIAODSIM

[4] RunIISummer16MiniAODv3-PUMoriond17_94X_mcRun2_asymptotic_v3_ext1-v1/MINIAODSIM

[5] A cut of $m_{\ell\ell} > 4$ GeV was applied at the LHE level so that the same NLO cross section can be used as for the other WZ samples.

Table 8.6: List of of MC samples used to estimate and model top-quark related backgrounds for events gathered in 2016. The cross section used for each sample is given, where available cross sections from higher order calculation are used. Some cross section are directly extracted from the corresponding MC sample as the cross section is computed during matrix event generation, this indicated by labels for the usage of MADGRAPH5_AMC@NLO: **[M]**, POWHEG V2: **[POW]** and PYTHIA: **[PY]** (see Sec. 6.2.2). Additionally the usage in signal extraction and the training of ml methods is given.

Process	CMS internal sample name	Cross section [pb]	ml-training	signal ext.
$t\bar{t}$+jets	/TTTo2L2Nu_TuneCP5_PSweights_13TeV-powheg-pythia8/[1]	88.4 [5, 170]	✓	✓
	/TTToSemiLeptonic_TuneCP5_PSweights_13TeV-powheg-pythia8/[1]	365.25 [5, 170]	✓	✓
	/TTToHadronic_TuneCP5_PSweights_13TeV-powheg-pythia8/[1]	377.85 [5, 170]	✓	✓
$t\bar{t}+\gamma+$ jets	/TTGJets_TuneCUETP8M1_13TeV-amcatnloFXFX-madspin-pythia8/[3,4]	4.215 **[M,PY]**	X	✓
$t\bar{t}W$	/TTWJetsToLNu_TuneCUETP8M1_13TeV-amcatnloFXFX-madspin-pythia8/[5]	0.196 [14, 171, 172]	X	✓
	/ttWJets_13TeV_madgraphMLM/[5]	0.6008 [14]	✓	✓
$t\bar{t}Z$	/TTZToLL_M-1to10_TuneCUETP8M1_13TeV-madgraphMLM-pythia8/[1]	8.22×10^{-2} [5, 14]	X	✓
	/TTZToLLNuNu_M-10_TuneCUETP8M1_13TeV-amcatnlo-pythia8/[5,6]	2.81×10^{-1} [5, 14]	X	✓
	/ttZJets_13TeV_madgraphMLM-pythia8/[1]	2.81×10^{-1} [5, 14]	✓	X
$t\bar{t}WW$	/TTWW_TuneCUETP8M2T4_13TeV-madgraph-pythia8/[2]	0.006981 **[M,PY]**	X	✓
Single top quark	/ST_s-channel_4f_leptonDecays_13TeV-amcatnlo-pythia8_TuneCUETP8M1/[1]	3.364 [171, 172]	X	✓
	/ST_s-channel_4f_leptonDecays_13TeV_PSweights-amcatnlo-pythia8/[1]	3.364 [171, 172]	X	✓
	/ST_t-channel_top_4f_inclusiveDecays_13TeV-powhegV2-madspin-pythia8_TuneCUETP8M1/[1]	136.02 [171, 172]	X	✓
	/ST_t-channel_antitop_4f_inclusiveDecays_13TeV-powhegV2-madspin-pythia8_TuneCUETP8M1/[1]	80.95 [171, 172]	X	✓
	/ST_t-channel_antitop_4f_inclusiveDecays_13TeV_PSweights-powhegV2-madspin/[1]	80.95 [171, 172]	X	✓
	/ST_tW_top_5f_inclusiveDecays_13TeV-powheg-pythia8_TuneCUETP8M1/[2]	35.85 [171, 172]	X	✓
	/ST_tW_antitop_5f_inclusiveDecays_13TeV-powheg-pythia8_TuneCUETP8M1/[2]	35.85 [171, 172]	X	✓
	/ST_tWll_5f_LO_13TeV-MadGraph-pythia8/[5]	0.01096 **[M,PY]**	X	✓
Single top quark $+\gamma+$ jets	/TGJets_leptonDecays_13TeV_amcatnlo_madspin_pythia8/[3]	1.018 **[M,PY]** X	✓	
Single top quark $+Z$	/tZq_ll_4f_13TeV-amcatnlo-pythia8/[2]	0.07358 **[M,PY]**	X	✓
	/tZq_ll_4f_PSweights_13TeV-amcatnlo-pythia8/[1]	0.07358 **[M,PY]**	X	✓
$t\bar{t}t\bar{t}$	/TTTT_TuneCUETP8M1_13TeV-amcatnlo-pythia8/[7]	8.21×10^{-3} **[M,PY]**	X	✓

[1] RunIISummer16MiniAODv3-PUMoriond17_94X_mcRun2_asymptotic_v3-v1/MINIAODSIM

[2] RunIISummer16MiniAODv3-PUMoriond17_94X_mcRun2_asymptotic_v3_ext1-v1/MINIAODSIM

[3] RunIISummer16MiniAODv3-PUMoriond17_94X_mcRun2_asymptotic_v3-v2/MINIAODSIM

[4] RunIISummer16MiniAODv3-PUMoriond17_94X_mcRun2_asymptotic_v3_ext1-v2/MINIAODSIM

[5] RunIISummer16MiniAODv3-PUMoriond17_94X_mcRun2_asymptotic_v3_ext2-v1/MINIAODSIM

[6] RunIISummer16MiniAODv3-PUMoriond17_94X_mcRun2_asymptotic_v3_ext3-v1/MINIAODSIM

Table 8.7: List of of MC samples used to estimate and model the DY and W+ jets backgrounds for events gathered in 2016. The cross section used for each sample is given, where available cross sections from higher order calculation are used. Some cross section are directly extracted from the corresponding MC sample as the cross section is computed during matrix event generation, this indicated by labels for the usage of MADGRAPH5_AMC@NLO: **[M]**, POWHEG V2: **[POW]** and PYTHIA: **[PY]** (see Sec. 6.2.2). Additionally the usage in signal extraction and the training of ml methods is given. Datasets marked with (†) are also utilized in the measurement of lepton charge misidentification.

Process	CMS internal sample name	Cross section [pb]	ml-training	signal ext.
$Z/\gamma \to \ell\ell$	/DYJetsToLL_M-10to50_TuneCUETP8M1_13TeV-madgraphMLM-pythia8/[1]	18610.0 [173]	✓	✓
	/DYJetsToLL_M-50_TuneCUETP8M1_13TeV-madgraphMLM-pythia8/[2,3] (†)	6077.22 [174]	✓	X
	/DY1JetsToLL_M-50_TuneCUETP8M1_13TeV-madgraphMLM-pythia8/[4] (†)	998.61 **[M,PY]**	✓	X
	/DY2JetsToLL_M-50_TuneCUETP8M1_13TeV-madgraphMLM-pythia8/[1] (†)	349.25 **[M,PY]**	✓	X
	/DY3JetsToLL_M-50_TuneCUETP8M1_13TeV-madgraphMLM-pythia8/[1] (†)	127.52 **[M,PY]**	✓	X
	/DY4JetsToLL_M-50_TuneCUETP8M1_13TeV-madgraphMLM-pythia8/[1] (†)	50.039 **[M,PY]**	✓	X
	/DYJetsToLL_M-50_HT-70to100_TuneCUETP8M1_13TeV-madgraphMLM-pythia8[1] (†)	167.33 **[M,PY]**	✓	X
	/DYJetsToLL_M-50_HT-100to200_TuneCUETP8M1_13TeV-madgraphMLM-pythia8[1,2] (†)	183.53 **[M,PY]**	✓	X
	/DYJetsToLL_M-50_HT-200to400_TuneCUETP8M1_13TeV-madgraphMLM-pythia8/[1,2] (†)	55.411 **[M,PY]**	✓	X
	/DYJetsToLL_M-50_HT-400to600_TuneCUETP8M1_13TeV-madgraphMLM-pythia8/[1,2] (†)	7.9592 **[M,PY]**	✓	X
	/DYJetsToLL_M-50_HT-600to800_TuneCUETP8M1_13TeV-madgraphMLM-pythia8/[1] (†)	2.0041 **[M,PY]**	✓	X
	/DYJetsToLL_M-50_HT-800to1200_TuneCUETP8M1_13TeV-madgraphMLM-pythia8/[1] (†)	0.92367 **[M,PY]**	✓	X
	/DYJetsToLL_M-50_HT-1200to2500_TuneCUETP8M1_13TeV-madgraphMLM-pythia8/[1] (†)	0.22025 **[M,PY]**	✓	X
	/DYJetsToLL_M-50_HT-2500toInf_TuneCUETP8M1_13TeV-madgraphMLM-pythia8/[1] (†)	0.004007 **[M,PY]**	✓	X
	/DYJetsToLL_M-50_TuneCUETP8M1_13TeV-amcatnloFXFX-pythia8/[5]	6077.22 [174]	X	✓
	/DYToLL_0J_13TeV-amcatnloFXFX-pythia8/[6,7]	4843.6 **[M,PY]**	X	✓
	/DYToLL_1J_13TeV-amcatnloFXFX-pythia8/[6,7]	897.8 **[M,PY]**	X	✓
	/DYToLL_2J_13TeV-amcatnloFXFX-pythia8/[2,8]	335.8 **[M,PY]**	X	✓
W+jets	/WJetsToLNu_TuneCUETP8M1_13TeV-madgraphMLM-pythia8/[1,3]	61526.7 **[M,PY]**	✓	✓
	/W1JetsToLNu_TuneCUETP8M1_13TeV-madgraphMLM-pythia8/[8]	9442.49 **[M,PY]**	✓	✓
	/W2JetsToLNu_TuneCUETP8M1_13TeV-madgraphMLM-pythia8/[1,2]	3252.49 **[M,PY]**	✓	✓
	/W3JetsToLNu_TuneCUETP8M1_13TeV-madgraphMLM-pythia8/[1,2]	1153.42 **[M,PY]**	✓	✓
	/W4JetsToLNu_TuneCUETP8M1_13TeV-madgraphMLM-pythia8/[1,5]	634.05 **[M,PY]**	✓	✓
	/WJetsToLNu_HT-70To100_TuneCUETP8M1_13TeV-madgraphMLM-pythia8/[1]	1504.92 **[M,PY]**	✓	✓
	/WJetsToLNu_HT-100To200_TuneCUETP8M1_13TeV-madgraphMLM-pythia8/[1,2,3]	1625.08 **[M,PY]**	✓	✓
	/WJetsToLNu_HT-200To400_TuneCUETP8M1_13TeV-madgraphMLM-pythia8/[1,2]	477.96 **[M,PY]**	✓	✓
	/WJetsToLNu_HT-400To600_TuneCUETP8M1_13TeV-madgraphMLM-pythia8/[1,2]	67.441 **[M,PY]**	✓	✓
	/WJetsToLNu_HT-600To800_TuneCUETP8M1_13TeV-madgraphMLM-pythia8/[1,2]	15.096 **[M,PY]**	✓	✓
	/WJetsToLNu_HT-800To1200_TuneCUETP8M1_13TeV-madgraphMLM-pythia8/[1,2]	6.3626 **[M,PY]**	✓	✓
	/WJetsToLNu_HT-1200To2500_TuneCUETP8M1_13TeV-madgraphMLM-pythia8/[1,2]	1.2658 **[M,PY]**	✓	✓
	/WJetsToLNu_HT-2500ToInf_TuneCUETP8M1_13TeV-madgraphMLM-pythia8/[1,2]	0.009405 **[M,PY]**	✓	✓

[1] RunIISummer16MiniAODv3-PUMoriond17_94X_mcRun2_asymptotic_v3-v2/MINIAODSIM

[2] RunIISummer16MiniAODv3-PUMoriond17_94X_mcRun2_asymptotic_v3_ext1-v2/MINIAODSIM

[3] RunIISummer16MiniAODv3-PUMoriond17_94X_mcRun2_asymptotic_v3_ext2-v2/MINIAODSIM

[4] RunIISummer16MiniAODv3-PUMoriond17_94X_mcRun2_asymptotic_v3-v1/MINIAODSIM

[5] RunIISummer16MiniAODv3-PUMoriond17_94X_mcRun2_asymptotic_v3_ext2-v1/MINIAODSIM

[6] RunIISummer16MiniAODv3-PUMoriond17_94X_mcRun2_asymptotic_v3_ext1-v1/MINIAODSIM

[7] RunIISummer16MiniAODv3-PUMoriond17_backup_94X_mcRun2_asymptotic_v3-v2/MINIAODSIM

[8] RunIISummer16MiniAODv3-PUMoriond17_94X_mcRun2_asymptotic_v3-v1/MINIAODSIM

Table 8.8: List of of MC samples used to estimate and model the triple boson backgrounds for events gathered in 2016. The cross section used for each sample is given, where available cross sections from higher order calculation are used. Some cross section are directly extracted from the corresponding MC sample as the cross section is computed during matrix event generation, this indicated by labels for the usage of MADGRAPH5_AMC@NLO: **[M]**, POWHEG V2: **[POW]** and PYTHIA: **[PY]** (see Sec. 6.2.2). Additionally the usage in signal extraction and the training of ml methods is given.

Process	CMS internal sample name	Cross section [pb]	ml-training	signal ext.
WWW	`/WWW_4F_TuneCUETP8M1_13TeV-amcatnlo-pythia8/`[1]	2.09×10^{-1} **[M,PY]**	X	✓
WWZ	`/WWZ_TuneCUETP8M1_13TeV-amcatnlo-pythia8/`[1]	1.68×10^{-1} **[M,PY]**	X	✓
WZZ	`/WZZ_TuneCUETP8M1_13TeV-amcatnlo-pythia8/`[1]	5.70×10^{-2} **[M,PY]**	X	✓
ZZZ	`/ZZZ_TuneCUETP8M1_13TeV-amcatnlo-pythia8/`[1]	1.47×10^{-2} **[M,PY]**	X	✓
WZγ	`/WZG_TuneCUETP8M1_13TeV-amcatnlo-pythia8/`[2]	4.35×10^{-2} **[M,PY]**	X	✓

[1] `RunIISummer16MiniAODv3-PUMoriond17_94X_mcRun2_asymptotic_v3-v2/MINIAODSIM`

[1] `RunIISummer16MiniAODv3-PUMoriond17_94X_mcRun2_asymptotic_v3-v1/MINIAODSIM`

Table 8.9: List of of MC samples used to estimate and model the single Higgs boson backgrounds for events gathered in 2016. The cross section used for each sample is given, where available cross sections from higher order calculation are used. Some cross section are directly extracted from the corresponding MC sample as the cross section is computed during matrix event generation, this indicated by labels for the usage of MADGRAPH5_AMC@NLO: **[M]**, POWHEG V2: **[POW]** and PYTHIA: **[PY]** (see Sec. 6.2.2). Additionally the usage in signal extraction and the training of ml methods is given.

Process	CMS internal sample name	Cross section [pb]	ml-training	signal ext.
$W/Z+H$	/VHToNonbb_M125_13TeV_amcatnloFXFX_madspin_pythia8/[1]	9.42×10^{-1} [14]	✓	✓
	/ZH_HToBB_ZToLL_M125_13TeV_powheg_pythia8/[2]	5.2×10^{-2} [14]	✓	✓
	/ZHToTauTau_M125_13TeV_powheg_pythia8/[1]	5.54×10^{-2} [14]	✓	✓
ggH	/GluGluHToTauTau_M125_13TeV_powheg_pythia8/[3]	3.05 [14]	✓	✓
	/GluGluHToZZTo4L_M125_13TeV_powheg2_JHUgenV6_pythia8/[4]	1.30×10^{-2} [5, 14]	✓	✓
	/GluGluHToWWToLNuQQ_M125_13TeV_powheg_JHUGenV628_pythia8/[2]	4.56 [5, 14]	✓	✓
	/GluGluHToWWTo2L2Nu_M125_13TeV_powheg_JHUgen_pythia8/[1]	1.10 [5, 14]	✓	✓
	/GluGluHToMuMu_M-125_TuneCP5_PSweights_13TeV_powheg_pythia8/[4]	1.06×10^{-2} [14]	✓	✓
	/GluGluHToBB_M125_13TeV_amcatnloFXFX_pythia8/[1,2]	2.83×10^{1} [14]	✓	✓
	/GluGluHToGG_M125_13TeV_amcatnloFXFX_pythia8/[5]	1.10×10^{-1} [14]	✓	✓
qqH	/VBFHToTauTau_M125_13TeV_powheg_pythia8/[1]	2.37×10^{-1} [14]	✓	✓
	/VBF_HToZZTo4L_M125_13TeV_powheg2_JHUgenV6_pythia8/[1]	1.01×10^{-3} [5, 14]	✓	✓
	/VBFHToWWToLNuQQ_M125_13TeV_powheg_JHUGenV628_pythia8/[2]	3.55×10^{-1} [5, 14]	✓	✓
	/VBFHToWWTo2L2Nu_M125_13TeV_powheg_JHUgenv628_pythia8/[1]	8.59×10^{-2} [5, 14]	✓	✓
	/VBFHToMuMu_M-125_TuneCP5_PSweights_13TeV_powheg_pythia8/[4]	8.23×10^{-4} [14]	✓	✓
	/VBFHToBB_M-125_13TeV_powheg_pythia8_weightfix/[2,4]	2.20 [14]	✓	✓
	/VBFHToGG_M125_13TeV_amcatnlo_pythia8/[5,6]	8.58×10^{-3} [14]	✓	✓
ttWH	/TTWH_TuneCUETP8M2T4_13TeV-madgraph-pythia8/[2]	1.58×10^{-3} [14]	X	✓
$t\bar{t}ZH$	/TTZH_TuneCUETP8M2T4_13TeV-madgraph-pythia8/[2]	1.54×10^{-3} [14]	X	✓
tHq	/THQ_ctcvcp_HIncl_M125_TuneCP5_13TeV-madgraph-pythia8/[7]	2.31×10^{-2} **[M,PY]**	✓	✓
tHW	/THW_ctcvcp_HIncl_M125_TuneCP5_13TeV-madgraph-pythia8/[7]	5.09×10^{-3} **[M,PY]**	✓	✓
ttH	/ttHJetToNonbb_M125_13TeV_amcatnloFXFX_madspin_pythia8_mWCutfix/[6]	2.12×10^{-1} [14]	✓	✓

[1] RunIISummer16MiniAODv3-PUMoriond17_94X_mcRun2_asymptotic_v3-v2/MINIAODSIM

[2] RunIISummer16MiniAODv3-PUMoriond17_94X_mcRun2_asymptotic_v3_ext1-v1/MINIAODSIM

[3] RunIISummer16MiniAODv3-PUMoriond17_94X_mcRun2_asymptotic_v3-v3

[4] RunIISummer16MiniAODv3-PUMoriond17_94X_mcRun2_asymptotic_v3-v1/MINIAODSIM

[5] RunIISummer16MiniAODv3-PUMoriond17_94X_mcRun2_asymptotic_v3_ext2-v2/MINIAODSIM

[6] RunIISummer16MiniAODv3-PUMoriond17_94X_mcRun2_asymptotic_v3_ext1-v2/MINIAODSIM

[7] RunIISummer16MiniAODv3-PUMoriond17_94X_mcRun2_asymptotic_v3-v1/MINIAODSIM

MC background samples 2017

Table 8.10: List of of MC samples used to estimate and model Di-Boson backgrounds for events gathered in 2017. The cross section used for each sample is given, where available cross sections from higher order calculation are used. Some cross section are directly extracted from the corresponding MC sample as the cross section is computed during matrix event generation, this indicated by labels for the usage of MADGRAPH5_AMC@NLO: **[M]**, POWHEG V2: **[POW]** and PYTHIA: **[PY]** (see Sec. 6.2.2). Additionaly the usage in signal extraction and the training of ml methods is given.

Process	CMS internal sample name	Cross section [pb]	ml-training	signal ext.
ZZ	`/ZZTo4L_13TeV_powheg_pythia8/`[1,2,3]	1.26 [140]	✓	✓
	`/GluGluToContinToZZTo4tau_13TeV_MCFM701_pythia8/`[4,5]	0.00349 [169]	✓	✓
	`/GluGluToContinToZZTo4mu_13TeV_MCFM701_pythia8/`[3,5,6]	0.00349 [169]	✓	✓
	`/GluGluToContinToZZTo4e_13TeV_MCFM701_pythia8/`[3,5,6]	0.00349 [169]	✓	✓
	`/GluGluToContinToZZTo2e2tau_13TeV_MCFM701_pythia8/`[5,7]	0.00698 [169]	✓	✓
	`/GluGluToContinToZZTo2e2mu_13TeV_MCFM701_pythia8/`[5,7]	0.00698 [169]	✓	✓
	`/GluGluToContinToZZTo2mu2tau_13TeV_MCFM701_pythia8/`[5,7]	0.00698 [169]	✓	✓
WZ	`/WZTo3LNu_TuneCP5_13TeV-amcatnloFXFX-pythia8/`[4]	4.43 [140]	X	✓
	`/WZTo3LNu_mllmin01_NNPDF31_TuneCP5_13TeV_powheg_pythia8/`[8]	4.43 [140] [9]	✓	X
	`/WZTo3LNu_13TeV-powheg-pythia8/`[6]	4.43 [140]	✓	X
	`/WZTo2L2Q_13TeV_amcatnloFXFX_madspin_pythia8/`[4]	5.6 [140]	X	✓
WW	`/WWTo2L2Nu_DoubleScattering_13TeV-pythia8/`[6]	0.223 **[PY]**	X	✓
	`/WpWpJJ_EWK-QCD_TuneCP5_13TeV-madgraph-pythia8/`[4]	0.0493×10^{-2} **[M,PY]**	X	✓
Wγ	`/WGToLNuG_01J_5f_TuneCUETP8M1_13TeV-amcatnloFXFX-pythia8/`[7]	1.92×10^{1} **[M,PY]**	X	✓
Zγ	`/ZGToLLG_01J_5f_TuneCP5_13TeV-amcatnloFXFX-pythia8/`[7]	55.5 **[M,PY]**	X	✓

[1] `RunIIFall17MiniAODv2-PU2017_12Apr2018_new_pmx_94X_mc2017_realistic_v14-v1/MINIAODSIM`

[2] `RunIIFall17MiniAODv2-PU2017_12Apr2018_94X_mc2017_realistic_v14_ext1-v1/MINIAODSIM`

[3] `RunIIFall17MiniAODv2-PU2017_12Apr2018_94X_mc2017_realistic_v14_ext2-v1/MINIAODSIM`

[4] `RunIIFall17MiniAODv2-PU2017_12Apr2018_94X_mc2017_realistic_v14-v1/MINIAODSIM`

[5] `RunIIFall17MiniAODv2-PU2017_12Apr2018_94X_mc2017_realistic_v14_ext1-v2/MINIAODSIM`

[6] `RunIIFall17MiniAODv2-PU2017_12Apr2018_94X_mc2017_realistic_v14-v2/MINIAODSIM`

[7] `RunIIFall17MiniAODv2-PU2017_12Apr2018_94X_mc2017_realistic_v14-v3/MINIAODSIM`

[8] `RunIIFall17MiniAODv2-PU2017_12Apr2018_94X_mc2017_realistic_v14-v4/MINIAODSIM`

[9] A cut of $m_{\ell\ell} > 4$ GeV was applied at the LHE level so that the same NLO cross section can be used as for the other WZ samples.

Table 8.11: List of of MC samples used to estimate and model top-quark related backgrounds for events gathered in 2017. The cross section used for each sample is given, where available cross sections from higher order calculation are used. Some cross section are directly extracted from the corresponding MC sample as the cross section is computed during matrix event generation, this indicated by labels for the usage of MADGRAPH5_AMC@NLO: **[M]**, POWHEG V2: **[POW]** and PYTHIA: **[PY]** (see Sec. 6.2.2). Additionally the usage in signal extraction and the training of ml methods is given.

Process	CMS internal sample name	Cross section [pb]	ml-training	signal ext.
$t\bar{t}$+jets	/TTTo2L2Nu_TuneCP5_13TeV-powheg-pythia8/[1]	88.4 [5, 170]	✓	✓
	/TTTo2L2Nu_TuneCP5_PSweights_13TeV-powheg-pythia8/[2]	88.4 [5, 170]	✓	✓
	/TTToSemiLeptonic_TuneCP5_13TeV-powheg-pythia8/[1]	365.25 [5, 170]	✓	✓
	/TTToSemiLeptonic_TuneCP5_PSweights_13TeV-powheg-pythia8/[2]	365.25 [5, 170]	✓	✓
	/TTToHadronic_TuneCP5_13TeV-powheg-pythia8/[2]	377.85 [5, 170]	✓	✓
	/TTToHadronic_TuneCP5_PSweights_13TeV-powheg-pythia8/[1]	377.85 [5, 170]	✓	✓
$t\bar{t}+\gamma+$ jets	/TTGJets_TuneCP5_13TeV-amcatnloFXFX-madspin-pythia8/[6,3]	4.215 **[M,PY]**	X	✓
$t\bar{t}W$	/TTWJetsToLNu_TuneCP5_13TeV-amcatnloFXFX-madspin-pythia8/[7]	0.196 [14, 171, 172]	X	✓
	/TTWJetsToLNu_TuneCP5_PSweights_13TeV-amcatnloFXFX-madspin-pythia8/[6]	0.196 [14, 171, 172]	X	✓
	/ttWJets_13TeV_madgraphMLM_pythia8/[6]	0.6008 [14]	✓	✓
$t\bar{t}Z$	/TTZToLLNuNu_M-10_TuneCP5_13TeV-amcatnlo-pythia8/[7]	2.81×10^{-1} [5, 14]	X	✓
	/TTZToLLNuNu_M-10_TuneCP5_PSweights_13TeV-amcatnlo-pythia8/[6]	2.81×10^{-1} [5, 14]	X	✓
	/TTZToLL_M-1to10_TuneCP5_13TeV-amcatnlo-pythia8/[7]	0.0822 [5, 14]	X	✓
	/ttZJets_13TeV_madgraphMLM-pythia8/[6,4]	2.81×10^{-1} [5, 14]	✓	X
$t\bar{t}WW$	/TTWW_TuneCP5_13TeV-madgraph-pythia8/[5]	0.006981 **[M,PY]**	X	✓
Single top quark	/ST_s-channel_4f_leptonDecays_TuneCP5_13TeV-amcatnlo-pythia8/[7]	3.364 [171, 172]	X	✓
	/ST_s-channel_4f_leptonDecays_TuneCP5_PSweights_13TeV-amcatnlo-pythia8/[6]	3.364 [171, 172]	X	✓
	/ST_t-channel_antitop_4f_inclusiveDecays_TuneCP5_13TeV-powhegV2-madspin-pythia8[7]	80.95 [171, 172]	X	✓
	/ST_t-channel_antitop_4f_InclusiveDecays_TuneCP5_PSweights_13TeV-powheg-pythia8[6]	80.95 [171, 172]	X	✓
	/ST_t-channel_top_4f_inclusiveDecays_TuneCP5_13TeV-powhegV2-madspin-pythia8/[1]	136.02 [171, 172]	X	✓
	/ST_t-channel_top_4f_InclusiveDecays_TuneCP5_PSweights_13TeV-powheg-pythia8/[6]	136.02 [171, 172]	X	✓
	/ST_tW_antitop_5f_inclusiveDecays_TuneCP5_13TeV-powheg-pythia8/[7]	35.85 [171, 172]	X	✓
	/ST_tW_antitop_5f_inclusiveDecays_TuneCP5_PSweights_13TeV-powheg-pythia8/[7]	35.85 [171, 172]	X	✓
	/ST_tW_top_5f_inclusiveDecays_TuneCP5_13TeV-powheg-pythia8/[7]	35.85 [171, 172]	X	✓
	/ST_tW_top_5f_inclusiveDecays_TuneCP5_PSweights_13TeV-powheg-pythia8/[1]	35.85 [171, 172]	X	✓
	/ST_tWll_5f_LO_TuneCP5_PSweights_13TeV-madgraph-pythia8/[8]	0.01096 **[M,PY]**	X	✓
Single top quark $+\gamma+$ jets	TGJets_leptonDecays_TuneCP5_PSweights_13TeV-amcatnlo-pythia8/[6]	1.018 **[M,PY]**	X	✓
Single top quark $+$Z	/tZq_ll_4f_ckm_NLO_TuneCP5_PSweights_13TeV-amcatnlo-pythia8[2]	0.07358 **[M,PY]**	X	✓
$tt\bar{t}\bar{t}$	/TTTT_TuneCP5_13TeV-amcatnlo-pythia8/[7]	8.21×10^{-3} **[M,PY]**	X	✓
	/TTTT_TuneCP5_PSweights_13TeV-amcatnlo-pythia8/[6]	8.21×10^{-3} **[M,PY]**	X	✓

[1] RunIIFall17MiniAODv2-PU2017_12Apr2018_new_pmx_94X_mc2017_realistic_v14-v1/MINIAODSIM

[2] RunIIFall17MiniAODv2-PU2017_12Apr2018_new_pmx_94X_mc2017_realistic_v14-v2/MINIAODSIM

[3] RunIIFall17MiniAODv2-PU2017_12Apr2018_94X_mc2017_realistic_v14_ext1-v2/MINIAODSIM

[4] RunIIFall17MiniAODv2-PU2017_12Apr2018_94X_mc2017_realistic_v14_ext1-v3/MINIAODSIM

[5] RunIIFall17MiniAODv2-PU2017_12Apr2018_new_pmx_94X_mc2017_realistic_v14_ext1-v1/MINIAODSIM

[6] RunIIFall17MiniAODv2-PU2017_12Apr2018_94X_mc2017_realistic_v14-v1/MINIAODSIM

[7] RunIIFall17MiniAODv2-PU2017_12Apr2018_94X_mc2017_realistic_v14-v2/MINIAODSIM

[8] RunIIFall17MiniAODv2-PU2017_12Apr2018_94X_mc2017_realistic_v14_ext1-v1/MINIAODSIM

Table 8.12: List of of MC samples used to estimate and model the DY and W+ jets backgrounds for events gathered in 2017. The cross section used for each sample is given, where available cross sections from higher order calculation are used. Some cross section are directly extracted from the corresponding MC sample as the cross section is computed during matrix event generation, this indicated by labels for the usage of MADGRAPH5_AMC@NLO: **[M]**, POWHEG V2: **[POW]** and PYTHIA: **[PY]** (see Sec. 6.2.2). Additionally the usage in signal extraction and the training of ml methods is given. Datasets marked with (†) are also utilized in the measurement of lepton charge misidentification.

Process	CMS internal sample name	Cross section [pb]	ml-training	signal ext.
$Z/\gamma \to \ell\ell$	/DYJetsToLxsrefL_M-10to50_TuneCP5_13TeV-madgraphMLM-pythia8/[1,2]	18610.0 [173]	✓	✓
	/DYJetsToLL_M-50_TuneCP5_13TeV-madgraphMLM-pythia8/[3,4] (†)	6077.22 [174]	✓	✓
	/DY1JetsToLL_M-50_TuneCP5_13TeV-madgraphMLM-pythia8/[5,6] (†)	998.61 **[M,PY]**	✓	✓
	/DY2JetsToLL_M-50_TuneCP5_13TeV-madgraphMLM-pythia8/[1,7] (†)	349.25 **[M,PY]**	✓	✓
	/DY3JetsToLL_M-50_TuneCP5_13TeV-madgraphMLM-pythia8/[1,7] (†)	127.52 **[M,PY]**	✓	✓
	/DY4JetsToLL_M-50_TuneCP5_13TeV-madgraphMLM-pythia8/[8] (†)	50.039 **[M,PY]**	✓	✓
	/DYJetsToLL_M-50_HT-70to100_TuneCP5_13TeV-madgraphMLM-pythia8[1] (†)	167.33 **[M,PY]**	✓	✓
	/DYJetsToLL_M-50_HT-100to200_TuneCP5_13TeV-madgraphMLM-pythia8[9,5] (†)	183.53 **[M,PY]**	✓	✓
	/DYJetsToLL_M-50_HT-200to400_TuneCP5_13TeV-madgraphMLM-pythia8/[8,5] (†)	55.411 **[M,PY]**	✓	✓
	/DYJetsToLL_M-50_HT-400to600_TuneCP5_13TeV-madgraphMLM-pythia8/[9,5] (†)	7.9592 **[M,PY]**	✓	✓
	/DYJetsToLL_M-50_HT-600to800_TuneCP5_13TeV-madgraphMLM-pythia8/[9] (†)	2.0041 **[M,PY]**	✓	✓
	/DYJetsToLL_M-50_HT-800to1200_TuneCP5_13TeV-madgraphMLM-pythia8/[9] (†)	0.92367 **[M,PY]**	✓	✓
	/DYJetsToLL_M-50_HT-1200to2500_TuneCP5_13TeV-madgraphMLM-pythia8/[1] (†)	0.22025 **[M,PY]**	✓	✓
	/DYJetsToLL_M-50_HT-2500toInf_TuneCP5_13TeV-madgraphMLM-pythia8/[9] (†)	0.004007 **[M,PY]**	✓	✓
	/DYJetsToLL_M-50_TuneCP5_13TeV-amcatnloFXFX-pythia8/[1,5]	6077.22 [174]	X	✓
	/DYJetsToLL_0J_TuneCP5_13TeV-amcatnloFXFX-pythia8/[1]	4843.6 **[M,PY]**	X	✓
	/DYJetsToLL_1J_TuneCP5_13TeV-amcatnloFXFX-pythia8/[1]	897.8 **[M,PY]**	X	✓
	/DYJetsToLL_2J_TuneCP5_13TeV-amcatnloFXFX-pythia8/[1]	335.8 **[M,PY]**	X	✓
W+jets	/WJetsToLNu_TuneCP5_13TeV-madgraphMLM-pythia8/[10,5]	61526.7 **[M,PY]**	✓	✓
	/W1JetsToLNu_TuneCP5_13TeV-madgraphMLM-pythia8/[10]	9442.49 **[M,PY]**	✓	✓
	/W2JetsToLNu_TuneCP5_13TeV-madgraphMLM-pythia8/[11]	3252.49 **[M,PY]**	✓	✓
	/W3JetsToLNu_TuneCP5_13TeV-madgraphMLM-pythia8/[1]	1153.42 **[M,PY]**	✓	✓
	/W4JetsToLNu_TuneCP5_13TeV-madgraphMLM-pythia8/[9]	634.05 **[M,PY]**	✓	✓
	/WJetsToLNu_HT-70To100_TuneCP5_13TeV-madgraphMLM-pythia8/[1]	1504.92 **[M,PY]**	✓	✓
	/WJetsToLNu_HT-100To200_TuneCP5_13TeV-madgraphMLM-pythia8/[8]	1625.08 **[M,PY]**	✓	✓
	/WJetsToLNu_HT-200To400_TuneCP5_13TeV-madgraphMLM-pythia8/[1]	477.96 **[M,PY]**	✓	✓
	/WJetsToLNu_HT-400To600_TuneCP5_13TeV-madgraphMLM-pythia8/[1]	67.441 **[M,PY]**	✓	✓
	/WJetsToLNu_HT-600To800_TuneCP5_13TeV-madgraphMLM-pythia8/[1]	15.096 **[M,PY]**	✓	✓
	/WJetsToLNu_HT-800To1200_TuneCP5_13TeV-madgraphMLM-pythia8/[1]	6.3626 **[M,PY]**	✓	✓
	/WJetsToLNu_HT-1200To2500_TuneCP5_13TeV-madgraphMLM-pythia8/[1]	1.2658 **[M,PY]**	✓	✓
	/WJetsToLNu_HT-2500ToInf_TuneCP5_13TeV-madgraphMLM-pythia8/[10]	0.009405 **[M,PY]**	✓	✓

[1] RunIIFall17MiniAODv2-PU2017_12Apr2018_94X_mc2017_realistic_v14-v1/MINIAODSIM

[2] RunIIFall17MiniAODv2-PU2017_12Apr2018_94X_mc2017_realistic_v14_ext1-v2/MINIAODSIM

[3] RunIIFall17MiniAODv2-PU2017RECOSIMstep_12Apr2018_94X_mc2017_realistic_v14-v1/MINIAODSIM

[4] RunIIFall17MiniAODv2-PU2017RECOSIMstep_12Apr2018_94X_mc2017_realistic_v14_ext1-v1/MINIAODSIM

[5] RunIIFall17MiniAODv2-PU2017_12Apr2018_94X_mc2017_realistic_v14_ext1-v1/MINIAODSIM

[6] RunIIFall17MiniAODv2-PU2017_12Apr2018_new_pmx_94X_mc2017_realistic_v14-v1/MINIAODSIM

[7] RunIIFall17MiniAODv2-PU2017_12Apr2018_new_pmx_94X_mc2017_realistic_v14_ext1-v2/MINIAODSIM

[8] RunIIFall17MiniAODv2-PU2017_12Apr2018_v2_94X_mc2017_realistic_v14-v2/MINIAODSIM

[9] RunIIFall17MiniAODv2-PU2017_12Apr2018_new_pmx_94X_mc2017_realistic_v14-v2/MINIAODSIM

[10] RunIIFall17MiniAODv2-PU2017_12Apr2018_94X_mc2017_realistic_v14-v3/MINIAODSIM

[11] RunIIFall17MiniAODv2-PU2017_12Apr2018_94X_mc2017_realistic_v14-v5/MINIAODSIM

Table 8.13: List of of MC samples used to estimate and model the triple boson backgrounds for events gathered in 2017. The cross section used for each sample is given, where available cross sections from higher order calculation are used. Some cross section are directly extracted from the corresponding MC sample as the cross section is computed during matrix event generation, this indicated by labels for the usage of MADGRAPH5_AMC@NLO: **[M]**, POWHEG V2: **[POW]** and PYTHIA: **[PY]** (see Sec. 6.2.2). Additionally the usage in signal extraction and the training of ml methods is given.

Process	CMS internal sample name	Cross section [pb]	ml-training	signal ext.
WWW	/WWW_4F_TuneCP5_13TeV-amcatnlo-pythia8/[1]	2.09×10^{-1} **[M,PY]**	X	✓
WWZ	/WWZ_4F_TuneCP5_13TeV-amcatnlo-pythia8/[1]	1.68×10^{-1} **[M,PY]**	X	✓
WZZ	/WZZ_TuneCP5_13TeV-amcatnlo-pythia8/[2]	5.70×10^{-2} **[M,PY]**	X	✓
ZZZ	/ZZZ_TuneCP5_13TeV-amcatnlo-pythia8/[2]	1.47×10^{-2} **[M,PY]**	X	✓
WZγ	/WZG_TuneCP5_13TeV-amcatnlo-pythia8/[2]	4.35×10^{-2} **[M,PY]**	X	✓

[1] RunIIFall17MiniAODv2-PU2017_12Apr2018_94X_mc2017_realistic_v14-v2/MINIAODSIM

[2] RunIIFall17MiniAODv2-PU2017_12Apr2018_94X_mc2017_realistic_v14-v1/MINIAODSIM

Table 8.14: List of of MC samples used to estimate and model the single Higgs boson backgrounds for events gathered in 2017. The cross section used for each sample is given, where available cross sections from higher order calculation are used. Some cross section are directly extracted from the corresponding MC sample as the cross section is computed during matrix event generation, this indicated by labels for the usage of MADGRAPH5_AMC@NLO: **[M]**, POWHEG V2: **[POW]** and PYTHIA: **[PY]** (see Sec. 6.2.2). Additionally the usage in signal extraction and the training of ml methods is given.

Process	CMS internal sample name	Cross section [pb]	ml-training	signal ext.
$\mathrm{W/Z+H}$	/VHToNonbb_M125_13TeV_amcatnloFXFX_madspin_pythia8/[1]	9.42×10^{-1} [14]	✓	✓
	/ZH_HToBB_ZToLL_M125_13TeV_powheg_pythia8/[2]	5.2×10^{-2} [14]	✓	✓
	/ZHToTauTau_M125_13TeV_powheg_pythia8/[2]	5.54×10^{-2} [14]	✓	✓
ggH	/GluGluHToTauTau_M125_13TeV_powheg_pythia8/[3,4]	3.05 [14]	✓	✓
	/GluGluHToZZTo4L_M125_13TeV_powheg2_JHUGenV7011_pythia8/[4,5,6]	1.30×10^{-2} [5, 14]	✓	✓
	/GluGluHToZZTo2L2Q_M125_13TeV_powheg2_JHUGenV7011_pythia8/[1]	0.17963 [5, 14]	✓	✓
	/GluGluHToWWToLNuQQ_M125_NNPDF31_TuneCP5_PSweights_13TeV_powheg_JHUGen710_pythia8/[1]	4.56 [5, 14]	✓	✓
	/GluGluHToWWTo2L2Nu_M125_13TeV_powheg2_JHUGen710_pythia8/[2]	1.10 [5, 14]	✓	✓
	/GluGluHToMuMu_M-125_TuneCP5_PSweights_13TeV_powheg_pythia8/[2,4]	1.06×10^{-2} [14]	✓	✓
	/GluGluHToBB_M125_13TeV_amcatnloFXFX_pythia8/[1]	2.83×10^{1} [14]	✓	✓
	/GluGluHToGG_M125_13TeV_amcatnloFXFX_pythia8/[1]	1.10×10^{-1} [14]	✓	✓
qqH	/VBFHToTauTau_M125_13TeV_powheg_pythia8/[7]	2.37×10^{-1} [14]	✓	✓
	/VBF_HToZZTo4L_M125_13TeV_powheg2_JHUGenV7011_pythia8/[4,8]	1.01×10^{-3} [5, 14]	✓	✓
	/VBFHToWWToLNuQQ_M125_NNPDF31_TuneCP5_PSweights_13TeV_powheg_JHUGen710_pythia8/[2]	3.55×10^{-1} [5, 14]	✓	✓
	/VBFHToWWTo2L2Nu_M125_13TeV_powheg2_JHUGenV714_pythia8/[2]	8.59×10^{-2} [5, 14]	✓	✓
	/VBFHToMuMu_M-125_TuneCP5_PSweights_13TeV_powheg_pythia8/[2]	8.23×10^{-4} [14]	✓	✓
	/VBFHToBB_M-125_13TeV_powheg_pythia8_weightfix/[2]	2.20 [14]	✓	✓
	/VBFHToGG_M125_13TeV_amcatnlo_pythia8/[2,4]	8.58×10^{-3} [14]	✓	✓
$\mathrm{t\bar{t}WH}$	/TTWH_TuneCP5_13TeV-madgraph-pythia8/[7]	1.58×10^{-3} [14]	X	✓
$\mathrm{t\bar{t}ZH}$	/TTZH_TuneCP5_13TeV-madgraph-pythia8/[7]	1.54×10^{-3} [14]	X	✓
tHq	/THQ_ctcvcp_4f_Hincl_13TeV_madgraph_pythia8/[2]	2.31×10^{-2} **[M,PY]**	✓	✓
tHW	/THW_ctcvcp_5f_Hincl_13TeV_madgraph_pythia8/[2]	5.09×10^{-3} **[M,PY]**	✓	✓
ttH	/ttHJetToNonbb_M125_TuneCP5_13TeV_amcatnloFXFX_madspin_pythia8/[7]	2.12×10^{-1} [14]	✓	✓

[1] RunIIFall17MiniAODv2-PU2017_12Apr2018_94X_mc2017_realistic_v14-v2/MINIAODSIM

[2] RunIIFall17MiniAODv2-PU2017_12Apr2018_94X_mc2017_realistic_v14-v1/MINIAODSIM

[3] RunIIFall17MiniAODv2-PU2017_12Apr2018_new_pmx_94X_mc2017_realistic_v14-v2/MINIAODSIM

[4] RunIIFall17MiniAODv2-PU2017_12Apr2018_94X_mc2017_realistic_v14_ext1-v1/MINIAODSIM

[5] RunIIFall17MiniAODv2-PU2017_12Apr2018_94X_mc2017_realistic_v14_ext3-v1/MINIAODSIM

[6] RunIIFall17MiniAODv2-PU2017_12Apr2018_94X_mc2017_realistic_v14_ext4-v1/MINIAODSIM

[7] RunIIFall17MiniAODv2-PU2017_12Apr2018_new_pmx_94X_mc2017_realistic_v14-v1/MINIAODSIM

[8] RunIIFall17MiniAODv2-PU2017_12Apr2018_94X_mc2017_realistic_v14_ext2-v2/MINIAODSIM

MC background samples 2018

Table 8.15: List of of MC samples used to estimate and model Di-Boson backgrounds for events gathered in 2018. The cross section used for each sample is given, where available cross sections from higher order calculation are used. Some cross section are directly extracted from the corresponding MC sample as the cross section is computed during matrix event generation, this indicated by labels for the usage of MADGRAPH5_AMC@NLO: **[M]**, POWHEG V2: **[POW]** and PYTHIA: **[PY]** (see Sec. 6.2.2). Additionaly the usage in signal extraction and the training of ml methods is given.

Process	CMS internal sample name	Cross section [pb]	ml-training	signal ext.
ZZ	/ZZTo4L_13TeV_powheg_pythia8/[1,2]	1.26 [140]	✓	✓
	/GluGluToContinToZZTo4tau_13TeV_MCFM701_pythia8/[3]	0.00349 [169]	✓	✓
	/GluGluToContinToZZTo4mu_13TeV_MCFM701_pythia8/[3,1]	0.00349 [169]	✓	✓
	/GluGluToContinToZZTo4e_13TeV_MCFM701_pythia8/[3,1]	0.00349 [169]	✓	✓
	/GluGluToContinToZZTo2e2tau_13TeV_MCFM701_pythia8/[4]	0.00698 [169]	✓	✓
	/GluGluToContinToZZTo2e2mu_13TeV_MCFM701_pythia8/[4]	0.00698 [169]	✓	✓
	/GluGluToContinToZZTo2mu2tau_13TeV_MCFM701_pythia8/[5]	0.00698 [169]	✓	✓
WZ	/WZTo3LNu_TuneCP5_13TeV-amcatnloFXFX-pythia8/[6,2]	4.43 [140]	X	✓
	/WZTo3LNu_mllmin01_NNPDF31_TuneCP5_13TeV_powheg_pythia8/[6]	4.43 [140][8]	✓	X
	/WZTo3LNu_TuneCP5_13TeV-powheg-pythia8/[1]	4.43 [140]	✓	X
	/WZTo2L2Q_13TeV_amcatnloFXFX_madspin_pythia8/[6]	5.6 [140]	X	✓
WW	/WWTo2L2Nu_13TeV-powheg/	12.2 [140]	X	✓
	/WWTo2L2Nu_DoubleScattering_13TeV-pythia8/[6]	0.223 **[PY]**	X	✓
	/WpWpJJ_EWK-QCD_TuneCP5_13TeV-madgraph-pythia8/[6]	0.0493×10^{-2} **[M,PY]**	X	✓
Wγ	/WGToLNuG_01J_5f_TuneCP5_13TeV-amcatnloFXFX-pythia8/[7]	1.92×10^{1} **[M,PY]**	X	✓
Zγ	/ZGToLLG_01J_5f_TuneCP5_13TeV-amcatnloFXFX-pythia8/[1]	55.59 **[M,PY]**	X	✓

[1] RunIIAutumn18MiniAOD-102X_upgrade2018_realistic_v15_ext1-v2/MINIAODSIM

[2] RunIIAutumn18MiniAOD-102X_upgrade2018_realistic_v15_ext2-v2/MINIAODSIM

[3] RunIIAutumn18MiniAOD-102X_upgrade2018_realistic_v15-v2/MINIAODSIM

[4] RunIIAutumn18MiniAOD-102X_upgrade2018_realistic_v15-v3/MINIAODSIM

[5] RunIIAutumn18MiniAOD-102X_upgrade2018_realistic_v15-v4/MINIAODSIM

[6] RunIIAutumn18MiniAOD-102X_upgrade2018_realistic_v15-v1/MINIAODSIM

[7] RunIIAutumn18MiniAOD-102X_upgrade2018_realistic_v15_ext1-v1/MINIAODSIM

[8] A cut of $m_{\ell\ell} > 4$ GeV was applied at the LHE level so that the same NLO cross section can be used as for the other WZ samples.

Table 8.16: List of of MC samples used to estimate and model top-quark related backgrounds for events gathered in 2016. The cross section used for each sample is given, where available cross sections from higher order calculation are used. Some cross section are directly extracted from the corresponding MC sample as the cross section is computed during matrix event generation, this indicated by labels for the usage of MADGRAPH5_AMC@NLO: **[M]**, POWHEG V2: **[POW]** and PYTHIA: **[PY]** (see Sec. 6.2.2). Additionally the usage in signal extraction and the training of ml methods is given.

Process	CMS internal sample name	Cross section [pb]	ml-training	signal ext.
$t\bar{t}$+jets	/TTTo2L2Nu_TuneCP5_13TeV-powheg-pythia8/[1]	88.4 [5, 170]	✓	✓
	/TTToSemiLeptonic_TuneCP5_13TeV-powheg-pythia8/[1]	365.25 [5, 170]	✓	✓
	/TTToHadronic_TuneCP5_13TeV-powheg-pythia8/[1]	377.85 [5, 170]	✓	✓
$t\bar{t}$ +γ+ jets	/TTGJets_TuneCP5_13TeV-amcatnloFXFX-madspin-pythia8/[1]	4.215 **[M,PY]**	X	✓
$t\bar{t}$W	/TTWJetsToLNu_TuneCP5_13TeV-amcatnloFXFX-madspin-pythia8/[2]	0.196 [14, 171, 172]	X	✓
	/ttWJets_TuneCP5_13TeV_madgraphMLM_pythia8/[2]	0.6008 [14]	✓	✓
$t\bar{t}$Z	/TTZToLL_M-1to10_TuneCP5_13TeV-madgraphMLM-pythia8/	8.22×10^{-2} [5, 14]	X	✓
	/TTZToLLNuNu_M-10_TuneCP5_13TeV-amcatnlo-pythia8/[2,1]	2.81×10^{-1} [5, 14]	X	✓
	/ttZJets_TuneCp5_13TeV_madgraphMLM_pythia8/[2]	2.81×10^{-1} [5, 14]	✓	X
$t\bar{t}$WW	/TTWW_TuneCP5_13TeV-madgraph-pythia8/[2]	0.006981 **[M,PY]**	X	✓
Single top quark	/ST_s-channel_4f_leptonDecays_TuneCP5_13TeV-madgraph-pythia8/[3]	3.364 [171, 172]	X	✓
	/ST_t-channel_top_4f_InclusiveDecays_TuneCP5_13TeV-powheg-madspin-pythia8/[1]	136.02 [171, 172]	X	✓
	/ST_t-channelKant_2015,Aliev_2011_4f_InclusiveDecays_TuneCP5_13TeV-powheg-madspin-pythia8/[1]	80.95 [171, 172]	X	✓
	/ST_tW_top_5f_inclusiveDecays_TuneCP5_13TeV-powheg-pythia8/[4]	35.85 [171, 172]	X	✓
	/ST_tW_antitop_5f_inclusiveDecays_TuneCP5_13TeV-powheg-pythia8/[4]	35.85 [171, 172]	X	✓
	/ST_tWll_5f_LO_TuneCP5_PSweights_13TeV-madgraph-pythia8/[4]	0.01096 **M,PY**	X	✓
Single top quark +γ+ jets	/TGJets_leptonDecays_TuneCP5_13TeV-madgraph-pythia8/[2]	1.018 **[M,PY]**	X	✓
Single top quark +Z	/tZq_ll_4f_ckm_NLO_TuneCP5_13TeV-madgraph-pythia8/[2]	0.07358 **[M,PY]**	X	✓
tttt	/TTTT_TuneCP5_13TeV-amcatnlo-pythia8/[2]	8.21×10^{-3} **[M,PY]**	X	✓

[1] RunIIAutumn18MiniAOD-102X_upgrade2018_realistic_v15-v1/MINIAODSIM

[2] RunIIAutumn18MiniAOD-102X_upgrade2018_realistic_v15_ext1-v2/MINIAOEDSIM

[3] RunIIAutumn18MiniAOD-102X_upgrade2018_realistic_v15_ext1-v4/MINIAODSIM

[4] RunIIAutumn18MiniAOD-102X_upgrade2018_realistic_v15_ext1-v1/MINIAODSIM

Table 8.17: List of of MC samples used to estimate and model the DY and W+ jets backgrounds for events gathered in 2018. The cross section used for each sample is given, where available cross sections from higher order calculation are used. Some cross section are directly extracted from the corresponding MC sample as the cross section is computed during matrix event generation, this indicated by labels for the usage of MADGRAPH5_AMC@NLO: **[M]**, POWHEG v2: **[POW]** and PYTHIA: **[PY]** (see Sec. 6.2.2). Additionally the usage in signal extraction and the training of ml methods is given. Datasets marked with (†) are also utilized in the measurement of lepton charge misidentification.

Process	CMS internal sample name	Cross section [pb]	ml-training	signal ext.
$Z/\gamma \to \ell\ell$	/DYJetsToLL_M-10to50_TuneCP5_13TeV-madgraphMLM-pythia8/[1]	18610.0 [173]	✓	✓
	/DYJetsToLL_M-50_TuneCP5_13TeV-madgraphMLM-pythia8/[2] (†)	6077.22 [174]	✓	✓
	/DY1JetsToLL_M-50_TuneCP5_13TeV-madgraphMLM-pythia8/[1] (†)	998.61 **[M,PY]**	✓	✓
	/DY2JetsToLL_M-50_TuneCP5_13TeV-madgraphMLM-pythia8/[1] (†)	349.25 **[M,PY]**	✓	✓
	/DY3JetsToLL_M-50_TuneCP5_13TeV-madgraphMLM-pythia8/[1] (†)	127.52 **[M,PY]**	✓	✓
	/DY4JetsToLL_M-50_TuneCP5_13TeV-madgraphMLM-pythia8/[2] (†)	50.039 **[M,PY]**	✓	✓
	/DYJetsToLL_M-50_HT-70to100_TuneCP5_PSweights_13TeV-madgraphMLM-pythia8[2] (†)	167.33 **[M,PY]**	✓	✓
	/DYJetsToLL_M-50_HT-100to200_TuneCP5_PSweights_13TeV-madgraphMLM-pythia8[1] (†)	183.53 **[M,PY]**	✓	✓
	/DYJetsToLL_M-50_HT-200to400_TuneCP5_PSweights_13TeV-madgraphMLM-pythia8/[1] (†)	55.411 **[M,PY]**	✓	✓
	/DYJetsToLL_M-50_HT-400to600_TuneCP5_PSweights_13TeV-madgraphMLM-pythia8/[3,4] (†)	7.9592 **[M,PY]**	✓	✓
	/DYJetsToLL_M-50_HT-600to800_TuneCP5_PSweights_13TeV-madgraphMLM-pythia8/[1] (†)	2.0041 **[M,PY]**	✓	✓
	/DYJetsToLL_M-50_HT-800to1200_TuneCP5_PSweights_13TeV-madgraphMLM-pythia8/[1] (†)	0.92367 **[M,PY]**	✓	✓
	/DYJetsToLL_M-50_HT-1200to2500_TuneCP5_PSweights_13TeV-madgraphMLM-pythia8/[1] (†)	0.22025 **[M,PY]**	✓	✓
	/DYJetsToLL_M-50_HT-2500toInf_TuneCP5_PSweights_13TeV-madgraphMLM-pythia8/[1] (†)	0.004007 **[M,PY]**	✓	✓
	/DYJetsToLL_M-50_TuneCP5_13TeV-amcatnloFXFX-pythia8/[2,5]	6077.22 [174]	X	✓
	/DYJetsToLL_0J_TuneCP5_13TeV-amcatnloFXFX-pythia8/[2]	4843.6 **[M,PY]**	X	✓
	/DYJetsToLL_1J_TuneCP5_13TeV-amcatnloFXFX-pythia8/[2]	897.8 **[M,PY]**	X	✓
	/DYJetsToLL_2J_TuneCP5_13TeV-amcatnloFXFX-pythia8/[2]	335.8 **[M,PY]**	X	✓
W+jets	/WJetsToLNu_TuneCP5_13TeV-madgraphMLM-pythia8/[1]	61526.7 **[M,PY]**	✓	✓
	/W1JetsToLNu_TuneCP5_13TeV-madgraphMLM-pythia8/[1]	9442.49 **[M,PY]**	✓	✓
	/W2JetsToLNu_TuneCP5_13TeV-madgraphMLM-pythia8/[1]	3252.49 **[M,PY]**	✓	✓
	/W3JetsToLNu_TuneCP5_13TeV-madgraphMLM-pythia8/[1]	1153.42 **[M,PY]**	✓	✓
	/W4JetsToLNu_TuneCP5_13TeV-madgraphMLM-pythia8/[1]	634.05 **[M,PY]**	✓	✓
	/WJetsToLNu_HT-70To100_TuneCP5_13TeV-madgraphMLM-pythia8/[2]	1504.92 **[M,PY]**	✓	✓
	/WJetsToLNu_HT-100To200_TuneCP5_13TeV-madgraphMLM-pythia8/[2]	1625.08 **[M,PY]**	✓	✓
	/WJetsToLNu_HT-200To400_TuneCP5_13TeV-madgraphMLM-pythia8/[2]	477.96 v	✓	✓
	/WJetsToLNu_HT-400To600_TuneCP5_13TeV-madgraphMLM-pythia8/[2]	67.441 **[M,PY]**	✓	✓
	/WJetsToLNu_HT-600To800_TuneCP5_13TeV-madgraphMLM-pythia8/[2]	15.096	✓	✓
	/WJetsToLNu_HT-800To1200_TuneCP5_13TeV-madgraphMLM-pythia8/[2]	6.3626 **[M,PY]**	✓	✓
	/WJetsToLNu_HT-1200To2500_TuneCP5_13TeV-madgraphMLM-pythia8/[2]	1.2658 **[M,PY]**	✓	✓
	/WJetsToLNu_HT-2500ToInf_TuneCP5_13TeV-madgraphMLM-pythia8/[2]	0.009405 **[M,PY]**	✓	✓

[1] RunIIAutumn18MiniAOD-102X_upgrade2018_realistic_v15-v2/MINIAODSIM

[2] RunIIAutumn18MiniAOD-102X_upgrade2018_realistic_v15-v1/MINIAODSIM

[3] RunIIAutumn18MiniAOD-102X_upgrade2018_realistic_v15-v7/MINIAODSIM

[4] RunIIAutumn18MiniAOD-102X_upgrade2018_realistic_v15_ext2-v3/MINIAODSIM

[5] RunIIAutumn18MiniAOD-102X_upgrade2018_realistic_v15_ext2-v1/MINIAODSIM

Table 8.18: List of of MC samples used to estimate and model the triple boson backgrounds for events gathered in 2018. The cross section used for each sample is given, where available cross sections from higher order calculation are used. Some cross section are directly extracted from the corresponding MC sample as the cross section is computed during matrix event generation, this indicated by labels for the usage of MADGRAPH5_AMC@NLO: **[M]**, POWHEG V2: **[POW]** and PYTHIA: **[PY]** (see Sec. 6.2.2). Additionally the usage in signal extraction and the training of ml methods is given.

Process	CMS internal sample name	Cross section [pb]	ml-training	signal ext.
WWW	`/WWW_4F_TuneCP5_13TeV-amcatnlo-pythia8/`[1]	2.09×10^{-1} **[M,PY]**	X	✓
WWZ	`/WWZ_TuneCP5_13TeV-amcatnlo-pythia8/`[1]	1.68×10^{-1} **[M,PY]**	X	✓
WZZ	`/WZZ_TuneCP5_13TeV-amcatnlo-pythia8/`[1]	5.70×10^{-2} **[M,PY]**	X	✓
ZZZ	`/ZZZ_TuneCP5_13TeV-amcatnlo-pythia8/`[1]	1.47×10^{-2} **[M,PY]**	X	✓

[1] `RunIIAutumn18MiniAOD-102X_upgrade2018_realistic_v15_ext1-v2/MINIAODSIM`

[2] `RunIIAutumn18MiniAOD-102X_upgrade2018_realistic_v15-v1/MINIAODSIM`

Table 8.19: List of of MC samples used to estimate and model the single Higgs boson backgrounds for events gathered in 2018. The cross section used for each sample is given, where available cross sections from higher order calculation are used. Some cross section are directly extracted from the corresponding MC sample as the cross section is computed during matrix event generation, this indicated by labels for the usage of MADGRAPH5_AMC@NLO: **[M]**, POWHEG v2: **[POW]** and PYTHIA: **[PY]** (see Sec. 6.2.2). Additionally the usage in signal extraction and the training of ml methods is given.

Process	CMS internal sample name	Cross section [pb]	ml-training	signal ext.
$\mathrm{W/Z+H}$	/VHToNonbb_M125_13TeV_amcatnloFXFX_madspin_pythia8/[1]	9.42×10^{-1} [14]	✓	✓
	/ZH_HToBB_ZToLL_M125_13TeV_powheg_pythia8/[1,2]	5.2×10^{-2} [14]	✓	✓
	/ZHToTauTau_M125_13TeV_powheg_pythia8/[1]	5.54×10^{-2} [14]	✓	✓
ggH	/GluGluHToTauTau_M125_13TeV_powheg_pythia8/[1]	3.05 [14]	✓	✓
	/GluGluHToZZTo4L_M125_13TeV_powheg2_JHUGenV7011_pythia8/[1]	1.30×10^{-2} [5, 14]	✓	✓
	/GluGluHToWWToLNuQQ_M125_13TeV_powheg2_JHUGenV714_pythia8/[3]	4.56 [5, 14]	✓	✓
	/GluGluHToWWTo2L2Nu_M125_13TeV_powheg2_JHUGen714_pythia8/[3]	1.10 [5, 14]	✓	✓
	/GluGluHToMuMu_M-125_TuneCP5_PSweights_13TeV_powheg_pythia8/[1,2]	1.06×10^{-2} [14]	✓	✓
	/GluGluHToBB_M125_13TeV_amcatnloFXFX_pythia8/[3]	2.83×10^{1} [14]	✓	✓
	/GluGluHToGG_M125_13TeV_amcatnloFXFX_pythia8/[3]	1.10×10^{-1} [14]	✓	✓
qqH	/VBFHToTauTau_M125_13TeV_powheg_pythia8/[2]	2.37×10^{-1} [14]	✓	✓
	/VBF_HToZZTo4L_M125_13TeV_powheg2_JHUGenV7011_pythia8/[1]	1.01×10^{-3} [5, 14]	✓	✓
	/VBFHToWWToLNuQQ_M125_13TeV_powheg_JHUGen_pythia8/[3]	3.55×10^{-1} [5, 14]	✓	✓
	/VBFHToWWTo2L2Nu_M125_13TeV_powheg2_JHUGenV714_pythia8/[3]	8.59×10^{-2} [5, 14]	✓	✓
	/VBFHToMuMu_M-125_TuneCP5_PSweights_13TeV_powheg_pythia8/[3]	8.23×10^{-4} [14]	✓	✓
	/VBFHToBB_M-125_13TeV_powheg_pythia8_weightfix/[3]	2.20 [14]	✓	✓
	/VBFHToGG_M125_13TeV_amcatnlo_pythia8/[3]	8.58×10^{-3} [14]	✓	✓
$\mathrm{t\bar{t}WH}$	/TTWH_TuneCP5_13TeV-madgraph-pythia8/[4]	1.58×10^{-3} [14]	X	✓
$\mathrm{t\bar{t}ZH}$	/TTZH_TuneCP5_13TeV-madgraph-pythia8/[4]	1.54×10^{-3} [14]	X	✓
tHq	/THQ_ctcvcp_4f_Hincl_13TeV_madgraph_pythia8/[3]	2.31×10^{-2} **[M,PY]**	✓	✓
tHW	/THW_ctcvcp_5f_Hincl_13TeV_madgraph_pythia8/[3]	5.09×10^{-3} **[M,PY]**	✓	✓
ttH	/ttHJetToNonbb_M125_TuneCp5_13TeV_amcatnloFXFX_madspin_pythia8/[3]	2.12×10^{-1} [14]	✓	✓

[1] RunIIAutumn18MiniAOD-102X_upgrade2018_realistic_v15-v2/MINIAODSIM

[2] RunIIAutumn18MiniAOD-102X_upgrade2018_realistic_v15_ext1-v1/MINIAODSIM

[3] RunIIAutumn18MiniAOD-102X_upgrade2018_realistic_v15-v1/MINIAODSIM

[4] RunIIAutumn18MiniAOD-102X_upgrade2018_realistic_v15_ext1-v2/MINIAODSIM

MC signal samples

Table 8.20: List of resonant ggHH samples for various resonant masses of particle χ. The samples for 2016 end with [1], [2] or [3], the samples for 2017 end with [4], [5] or [6] and the samples for 2018 end with [7] or [8]. The resonant mass samples are scaled to an inclusive ggHH cross section of 1 pb. The symbol V stands for both W and Z bosons.

Process	Spin	Sample name	Mass points (X)	Branching ratio[14]
ggHH $\to 4\tau$	0	/GluGluToRadionToHHTo4T_M-X[1,7]	250, 260, 270, 280, 300, 350, 400, 450, 500, 550, 600 , 650, 700, 750, 800, 900	0.003934
		/GluGluToRadionToHHTo4T_M-X[1]	340	
		/GluGluToRadionToHHTo4T_M-X[2,7]	1000	
		/GluGluToRadionToHHTo4Tau_M-X[3]	250, 260, 270, 280, 300, 350, 400, 450, 500, 550, 600, 650, 700, 750, 800, 850, 900, 1000	
		/GluGluToRadionToHHTo4T_M-X[1,4,7]	320	
		/GluGluToRadionToHHTo4T_M-X[7]	850	
	2	/GluGluToBulkGravitonToHHTo4T_M-X[2,7]	250, 260, 270, 280, 300, 320, 350, 400, 450, 500, 550, 600 , 650, 700, 750, 800, 850, 900, 1000	
		/GluGluToBulkGravitonToHHTo4Tau_M-X[3]	250, 260, 270, 280, 300, 350, 400, 450, 500, 550, 600, 650, 700, 750, 800, 900, 1000	
		/GluGluToBulkGravitonToHHTo4Tau_M-X[6]	320, 850	
ggHH $\to VV\tau\tau$	0	/GluGluToRadionToHHTo2V2Tau_M-X[2,4,7]	250, 260, 270, 280, 300, 320, 350, 400, 450, 500, 550, 650, 700, 750, 800, 850, 900, 1000	0.030092
		/GluGluToRadionToHHTo2V2Tau_M-X[2,6,7]	600	
	2	/GluGluToBulkGravitonToHHTo2V2Tau_M-X[2,4,7]	250, 260, 270, 280, 300, 320, 350, 400, 450, 500, 550 , 600, 650, 700, 750, 800, 850, 900, 1000	
ggHH $\to 4V$	0	/GluGluToRadionToHHTo4V_M-X[2,4,7]	250, 260, 270, 280, 300, 320, 350, 400, 450, 500, 600, 650, 700, 750, 800, 900	0.057547
		/GluGluToRadionToHHTo4V_M-X[2,4,8]	550, 850	
		/GluGluToRadionToHHTo4V_M-X[2,6]	1000	
	2	/GluGluToBulkGravitonToHHTo4V_M-X[2,4,7] GluGluToBulkGravitonToHHTo4V_M-X[2,4,8]	250, 260, 270, 280, 300, 320, 350, 400, 450, 500, 700 550, 600, 650, 750, 800, 850, 900, 1000	

[1] _narrow_TuneCUETP8M1_PSWeights_13TeV-madgraph-pythia8/RunIISummer16MiniAODv3-PUMoriond17_94X_mcRun2_asymptotic_v3-v2/MINIAODSIM

[2] _narrow_TuneCUETP8M1_PSWeights_13TeV-madgraph-pythia8/RunIISummer16MiniAODv3-PUMoriond17_94X_mcRun2_asymptotic_v3-v1/MINIAODSIM

[3] _narrow_13TeV-madgraph/RunIIFall17MiniAODv2-PU2017_12Apr2018_94X_mc2017_realistic_v14-v1/MINIAODSIM

[4] _narrow_TuneCP5_PSWeights_13TeV-madgraph-pythia8/RunIIFall17MiniAODv2-PU2017_12Apr2018_94X_mc2017_realistic_v14-v1/MINIAODSIM

[5] _narrow_13TeV-madgraph_correctedcfg/RunIIFall17MiniAODv2-PU2017_12Apr2018_94X_mc2017_realistic_v14-v2/MINIAODSIM

[6] _narrow_TuneCP5_PSWeights_13TeV-madgraph-pythia8/RunIIFall17MiniAODv2-PU2017_12Apr2018_94X_mc2017_realistic_v14-v2/MINIAODSIM

[7] _narrow_TuneCP5_PSWeights_13TeV-madgraph-pythia8/RunIIAutumn18MiniAOD-102X_upgrade2018_realistic_v15-v2/MINIAODSIM

[8] _narrow_TuneCP5_PSWeights_13TeV-madgraph-pythia8/RunIIAutumn18MiniAOD-102X_upgrade2018_realistic_v15-v1/MINIAODSIM

Table 8.21: List of LO non-resonant ggHH samples for various EFT BSM points as described in Sec. 6.2.4. The samples are scaled to an inclusive ggHH cross section of 1 pb. The symbol V stands for both W and Z bosons. A few samples were privately produced in addition to the central CMS samples to increase the training statistics. These samples are aquivalent to the centrally produced ones and use the same code for generation. The LO non-resonant ggHH samples are used soley for the training of BDTs and not in signal extraction.

Process	Sample name	EFT BSM points (JHEP04BMX)	Year	Branching ratio[14]
$ggHH \to 4\tau$	/GluGluToHHTo4Tau_node_X[1]	SM, box, 2, 3, 4, 5, 6, 7, 8, 9, 10, 11, 12	2016	0.003934
	/GluGluToHHTo4Tau_node_X[3]	SM, 2, 3, 7, 9, 12	2017	
	/GluGluToHHTo4Tau_node_X[4]	1, 4, 5, 6, 8, 10, 11		
	(privately produced)	SM, 1, 4, 7, 12		
	/GluGluToHHTo4T_node_X[5]	SM, 1, 2, 3, 4, 5, 6, 7, 8, 9, 10, 11, 12	2018	
$ggHH \to VV\tau\tau$	/GluGluToHHTo2V2Tau_node_X[2]	SM, 1, 2, 3, 4, 5, 6, 7, 8, 9, 10, 11, 12	2016	0.030092
	/GluGluToHHTo2V2Tau_node_X[3]	SM, 2, 3, 4, 5, 6, 7, 8, 9, 10, 11, 12	2017	
	/GluGluToHHTo2V2tau_node_X[4]	1		
	(privately produced)	SM, 1, 4, 7, 12		
	/GluGluToHHTo2V2Tau_node_X[5]	SM, 1, 2, 3, 4, 5, 6, 7, 8, 9, 10, 11, 12	2018	
$ggHH \to 4V$	/GluGluToHHTo4V_node_X[2]	SM, 1, 2, 3, 4, 5, 6, 7, 8, 9, 10, 11, 12	2016	0.057547
	/GluGluToHHTo4V_node_X[3]	SM, 2, 3, 4, 5, 6, 7, 8, 9, 10, 11, 12	2017	
	/GluGluToHHTo4V_node_X[4]	1		
	(privately produced)	SM, 1, 4, 7, 12		
	/GluGluToHHTo4V_node_X[5]	SM, 1, 2, 3, 4, 5, 6, 7, 8, 9, 10, 11, 12	2018	

[1] _13TeV-madgraph/RunIISummer16MiniAODv3-PUMoriond17_94X_mcRun2_asymptotic_v3-v2/MINIAODSIM

[2] _TuneCUETP8M1_PSWeights_13TeV-madgraph-pythia8/RunIISummer16MiniAODv3-PUMoriond17_94X_mcRun2_asymptotic_v3-v1/MINIAODSIM

[3] _13TeV-madgraph_correctedcfg/RunIIFall17MiniAODv2-PU2017_12Apr2018_94X_mc2017_realistic_v14-v1/MINIAODSIM

[4] _TuneCP5_PSWeights_13TeV-madgraph-pythia8_correctedcfg/RunIIFall17MiniAODv2-PU2017_12Apr2018_94X_mc2017_realistic_v14-v1/MINIAODSIM

[5] _TuneCP5_PSWeights_13TeV-madgraph-pythia8/RunIIAutumn18MiniAOD-102X_upgrade2018_realistic_v15-v2/MINIAODSIM

Table 8.22: List of non-resonant NLO ggHH samples for four values of κ_λ as used in the signal extraction. The sample names ending with [1], [2] or [3] belong to 2016, 2017 and 2018 data taking year, respectively. The samples are normalized to an inclusive HH production cross section of 1 pb and reweighted for the extraction of limits in various EFT BM scenarios (see Sec. 6.2.4) or normalized to NNLO cross section as described in Sec. 2.3 and used as input to the physic models described in Sec. 7.2.1. The normalization already takes into account the branching ratio of the corresponding HH decay mode [14]. The symbol V stands for both W and Z bosons.

Process	Sample name	κ_λ	Cross section [pb]
$\mathrm{ggHH} \to 4\tau$	/GluGluToHHTo4Tau_node_cHHH0[1,2,3]	0	2.7429×10^{-4}
	/GluGluToHHTo4Tau_node_cHHH1[1,2,3]	1	1.2213×10^{-4}
	/GluGluToHHTo4Tau_node_cHHH2p45[1,2,3]	2.45	5.163×10^{-5}
	/GluGluToHHTo4Tau_node_cHHH5[1,2,3]	5	3.5865×10^{-4}
$\mathrm{ggHH} \to VV\tau\tau$	/GluGluToHHTo2V2Tau_node_cHHH0[1,2,3]	0	2.09816×10^{-3}
	/GluGluToHHTo2V2Tau_node_cHHH1[1,2,3]	1	9.3427×10^{-4}
	/GluGluToHHTo2V2Tau_node_cHHH2p45[1,2,3]	2.45	3.9491×10^{-4}
	/GluGluToHHTo2V2Tau_node_cHHH5[1,2,3]	5	2.74351×10^{-3}
$\mathrm{ggHH} \to 4V$	/GluGluToHHTo4V_node_cHHH0[1,2,3]	0	4.0125×10^{-3}
	/GluGluToHHTo4V_node_cHHH1[1,2,3]	1	1.78668×10^{-3}
	/GluGluToHHTo4V_node_cHHH2p45[1,2,3]	2.45	7.5522×10^{-4}
	/GluGluToHHTo4V_node_cHHH5[1,2,3]	5	5.24666×10^{-3}

[1] _TuneCUETP8M1_PSWeights_13TeV-powheg-pythia8/RunIISummer16MiniAODv3-PUMoriond17_94X_mcRun2_asymptotic_v3-v1/MINIAODSIM

[2] _TuneCP5_PSWeights_13TeV-powheg-pythia8/RunIIFall17MiniAODv2-PU2017_12Apr2018_94X_mc2017_realistic_v14-v1/MINIAODSIM

[3] _TuneCP5_PSWeights_13TeV-powheg-pythia8/RunIIAutumn18MiniAOD-102X_upgrade2018_realistic_v15-v1/MINIAODSIM

Table 8.23: List of non-resonant qqHH samples for seven combinations ofc_V, c_{2V} and κ_λ coupling scenarios. The sample names ending with [1], [2] or [3] belong to 2016, 2017 and 2018 data taking period, respectively. The samples are normalized to N3LO cross section and already take into account the branching ratio of the corresponding HH decay mode. For this the LO cross section obtained from the MC simulation (See 6.2.2) is scalled by the appropriate κ-factor ($\sigma_{\mathrm{N3LO}}/\sigma_{\mathrm{LO}}$) from [148]. Both saples with and without the `dipoleRecoil` generator feature are used as indicated in the table. The samples in 2017 with enabled `dipoleRecoil` are used for an additional modelling systematic as described in Sec. 7.1.

Process	Sample name	c_V	c_{2V}	κ_λ	`dipoleRecoil` enabled	Cross section [pb]	
						2016	2017/2018
$\mathrm{qqHH} \to 4\tau$	`/VBFHHTo4T_CV_1_C2V_1_C3_1_dipoleRecoilOff`[1,2,3]	1	1	1	X	6.79×10^{-6}	
	`/VBFHHTo4T_CV_1_C2V_1_C3_1_dipoleRecoilOn`[2,3]				✓		
	`/VBFHHTo4T_CV_1_C2V_1_C3_2_dipoleRecoilOff`[1,2,3]	1	1	2	X	5.628×10^{-6}	5.597×10^{-6}
	`/VBFHHTo4T_CV_1_C2V_2_C3_1_dipoleRecoilOff`[1,2,3]	1	2	1	X	5.6616×10^{-5}	5.593×10^{-5}
	`/VBFHHTo4T_CV_1_C2V_2_C3_1_dipoleRecoilOn`[2,3]				✓		
	`/VBFHHTo4T_CV_1_C2V_1_C3_0_dipoleRecoilOff`[1,2,3]	1	1	0	X	1.8062×10^{-5}	1.813×10^{-5}
	`/VBFHHTo4T_CV_0_5_C2V_1_C3_1_dipoleRecoilOff`[1,2,3]	0.5	1	1	X	4.2791×10^{-5}	4.2578×10^{-5}
	`/VBFHHTo4T_CV_1_5_C2V_1_C3_1_dipoleRecoilOff`[1,2,3]	1.5	1	1	X	2.60945×10^{-4}	2.59704×10^{-4}
	`/VBFHHTo4T_CV_1_C2V_0_C3_1_dipoleRecoilOff`[1,2,3]	1	0	1	X	1.07126×10^{-4}	1.06527×10^{-4}
$\mathrm{qqHH} \to VV\tau\tau$	`/VBFHHTo2V2Tau_CV_1_C2V_1_C3_1_dipoleRecoilOff`[1,2,3]	1	1	1	X	5.1938×10^{-5}	
	`/VBFHHTo2V2Tau_CV_1_C2V_1_C3_1_dipoleRecoilOn`[2,3]				✓		
	`/VBFHHTo2V2Tau_CV_1_C2V_1_C3_2_dipoleRecoilOff`[1,2,3]	1	1	2	X	4.305×10^{-5}	4.2815×10^{-5}
	`/VBFHHTo2V2Tau_CV_1_C2V_2_C3_1_dipoleRecoilOff`[1,2,3]	1	2	1	X	4.33091×10^{-4}	4.27841×10^{-4}
	`/VBFHHTo2V2Tau_CV_1_C2V_2_C3_1_dipoleRecoilOn`[2,3]				✓		
	`/VBFHHTo2V2Tau_CV_1_C2V_1_C3_0_dipoleRecoilOff`[1,2,3]	1	1	0	X	1.38167×10^{-4}	1.38689×10^{-4}
	`/VBFHHTo2V2Tau_CV_0_5_C2V_1_C3_1_dipoleRecoilOff`[1,2,3]	0.5	1	1	X	3.27333×10^{-4}	3.25704×10^{-4}
	`/VBFHHTo2V2Tau_CV_1_5_C2V_1_C3_1_dipoleRecoilOff`[1,2,3]	1.5	1	1	X	1.99611×10^{-3}	1.98662×10^{-3}
	`/VBFHHTo2V2Tau_CV_1_C2V_0_C3_1_dipoleRecoilOff`[1,2,3]	1	0	1	X	8.19465×10^{-4}	8.14887×10^{-4}
$\mathrm{qqHH} \to 4V$	`/VBFHHTo4V_CV_1_C2V_1_C3_1_dipoleRecoilOff`[1,2,3]	1	1	1	X	9.9326×10^{-5}	
	`/VBFHHTo4V_CV_1_C2V_1_C3_1_dipoleRecoilOn`[2,3]				✓		
	`/VBFHHTo4V_CV_1_C2V_1_C3_2_dipoleRecoilOff`[1,2,3]	1	1	2	X	8.2329×10^{-5}	8.1879×10^{-5}
	`/VBFHHTo4V_CV_1_C2V_2_C3_1_dipoleRecoilOff`[1,2,3]	1	2	1	X	8.28237×10^{-4}	8.18197×10^{-4}
	`/VBFHHTo4V_CV_1_C2V_2_C3_1_dipoleRecoilOn`[2,3]				✓		
	`/VBFHHTo4V_CV_1_C2V_1_C3_0_dipoleRecoilOff`[1,2,3]	1	1	0	X	2.64229×10^{-4}	2.65227×10^{-4}
	`/VBFHHTo4V_CV_0_5_C2V_1_C3_1_dipoleRecoilOff`[1,2,3]	0.5	1	1	X	6.25988×10^{-4}	6.22873×10^{-4}
	`/VBFHHTo4V_CV_1_5_C2V_1_C3_1_dipoleRecoilOff`[1,2,3]	1.5	1	1	X	3.81734×10^{-3}	3.79918×10^{-3}
	`/VBFHHTo4V_CV_1_C2V_0_C3_1_dipoleRecoilOff`[1,2,3]	1	0	1	X	1.56714×10^{-3}	1.55838×10^{-3}

[1] `-TuneCUETP8M1_PSweights_13TeV-madgraph-pythia8/RunIISummer16MiniAODv3-PUMoriond17_94X_mcRun2_asymptotic_v3-v1/MINIAODSIM`

[2] `-TuneCP5_PSweights_13TeV-madgraph-pythia8/RunIIFall17MiniAODv2-PU2017_12Apr2018_94X_mc2017_realistic_v14-v2/MINIAODSIM`

[3] `-TuneCP5_PSweights_13TeV-madgraph-pythia8/RunIIAutumn18MiniAOD-102X_upgrade2018_realistic_v15-v2/MINIAODSIM`

Appendix D Signal region plots of the BDT input variables in the $3\ell + 1\tau_h$ channel

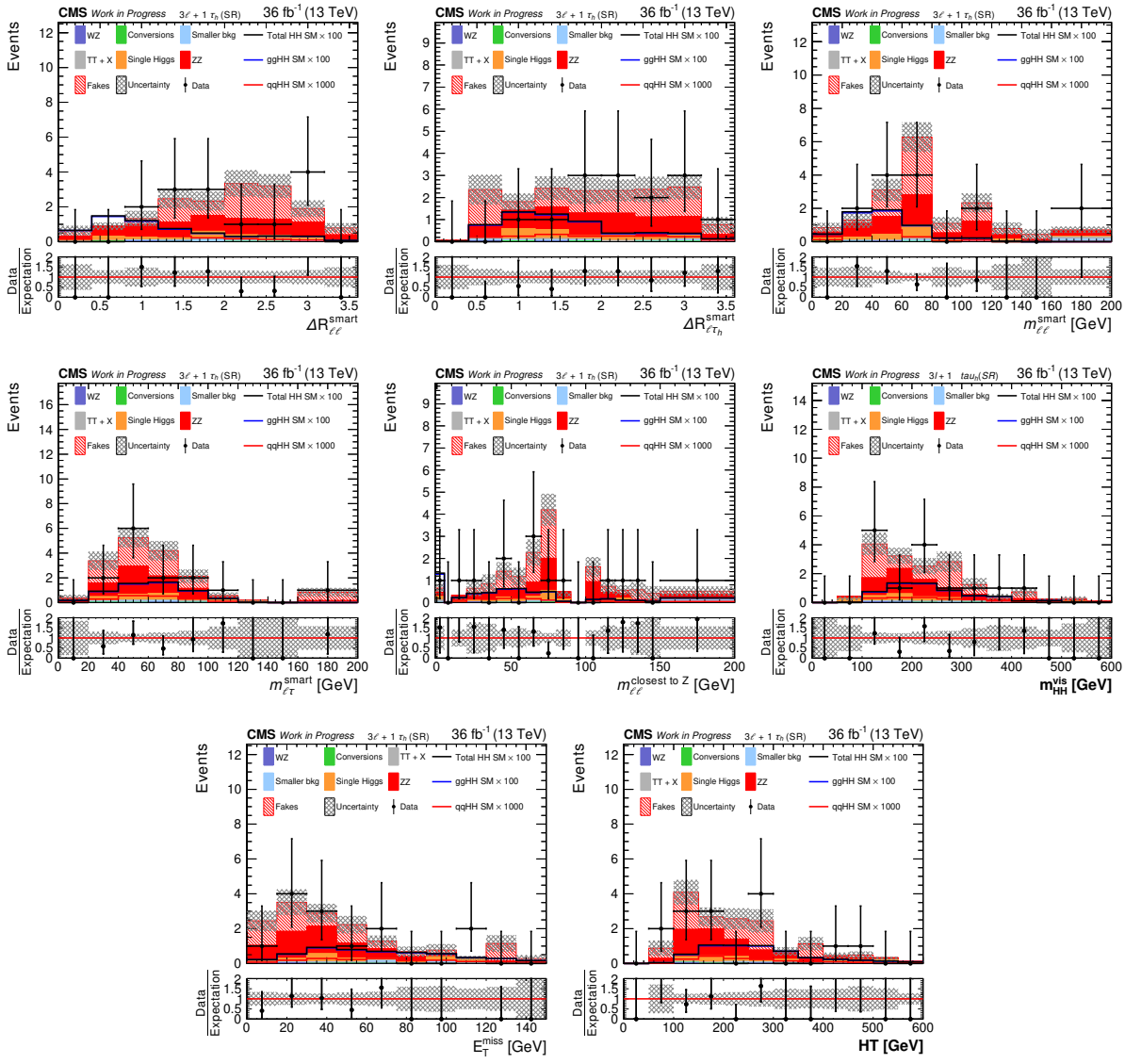

Figure 8.1: Distribution of the $3\ell + 1\tau_h$ BDT input variables the signal regions. The distributions are shown for the 2016 dataset. The shown uncertainty bands corresponds to statistical uncertainty contributions only.

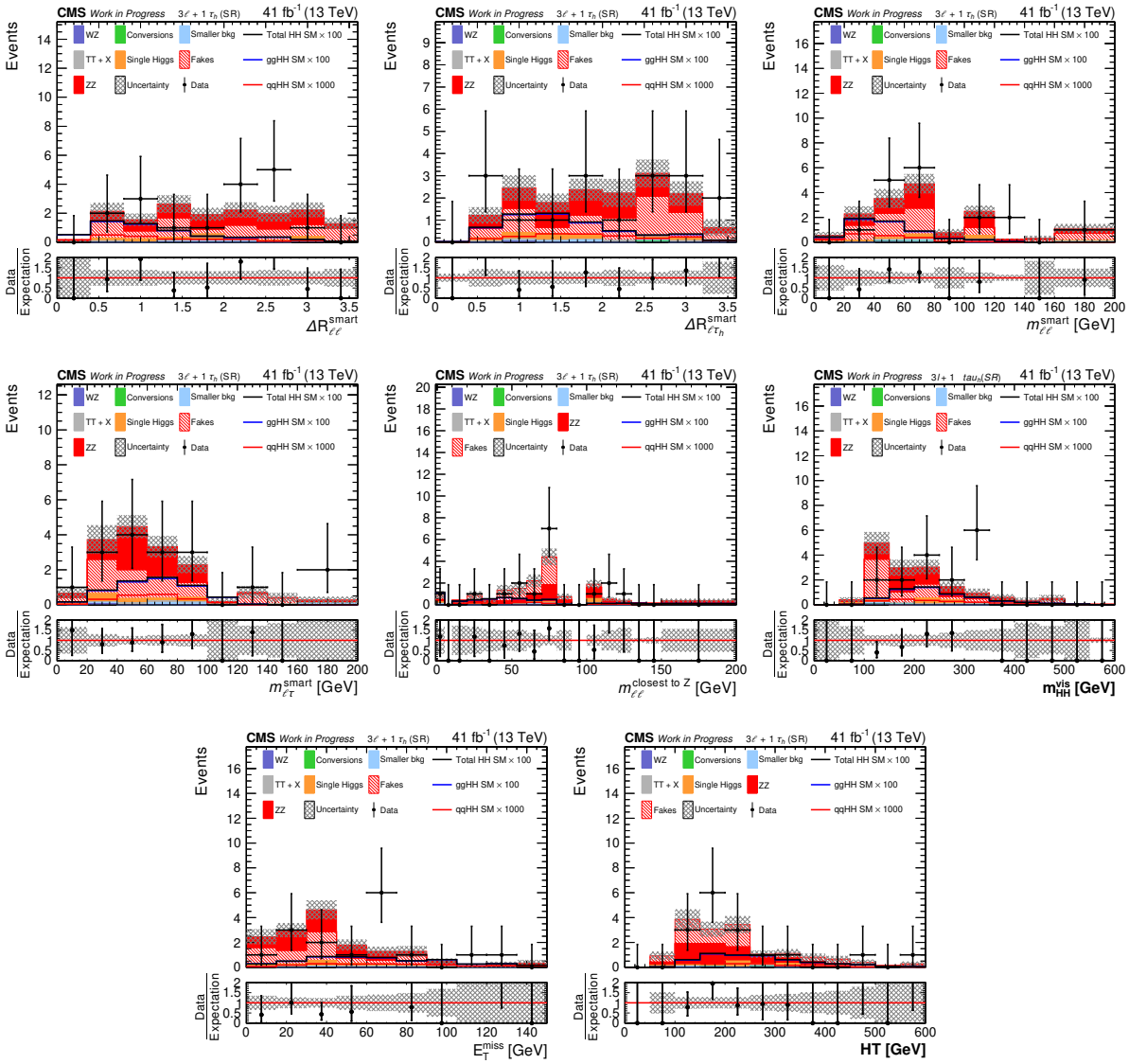

Figure 8.2: Distribution of the $3\ell + 1\tau_h$ BDT input variables the signal regions. The distributions are shown for the 2017 dataset. The shown uncertainty bands corresponds to statistical uncertainty contributions only.

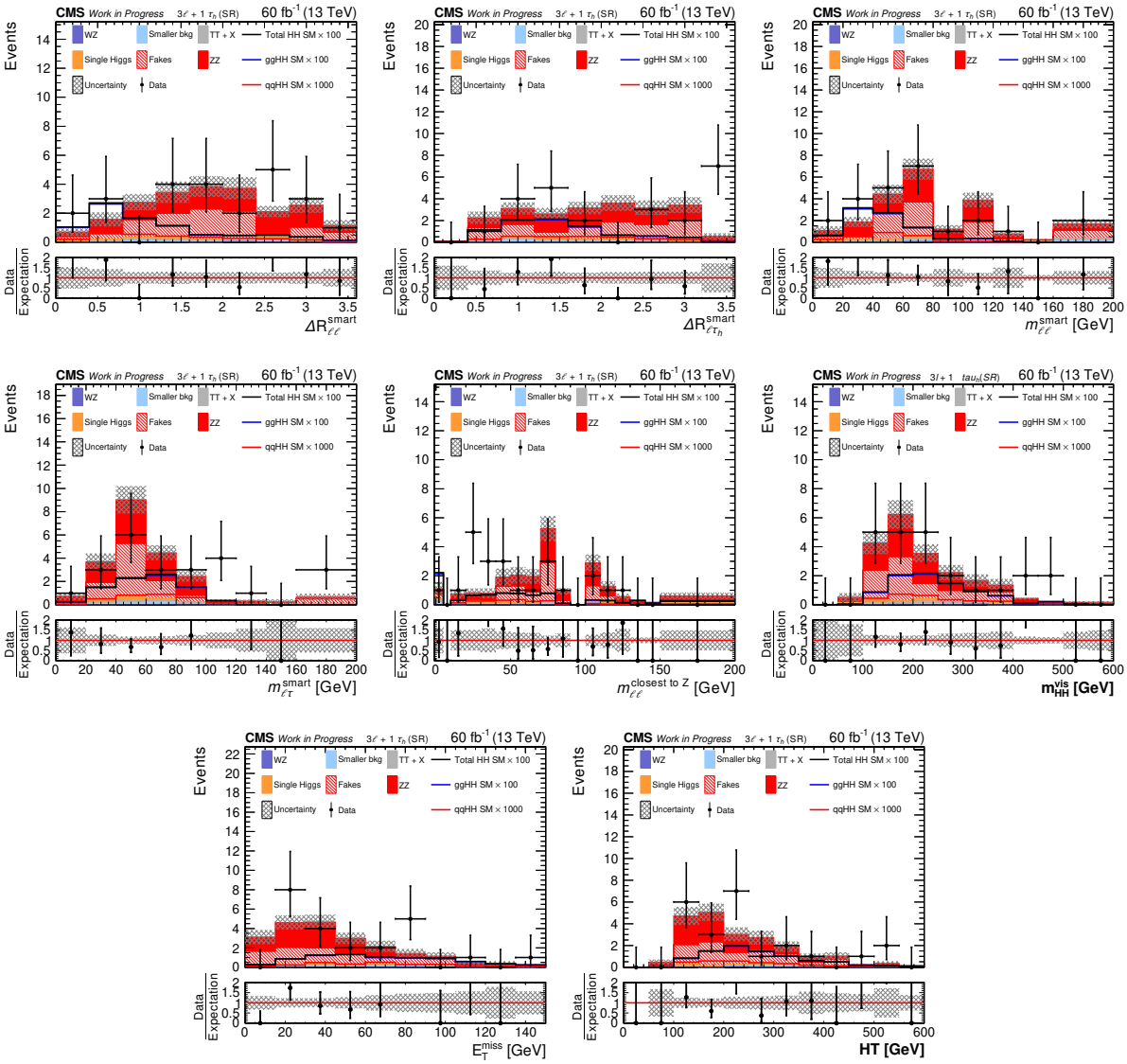

Figure 8.3: Distribution of the $3\ell + 1\tau_h$ BDT input variables the signal regions. The distributions are shown for the 2018 dataset. The shown uncertainty bands corresponds to statistical uncertainty contributions only.

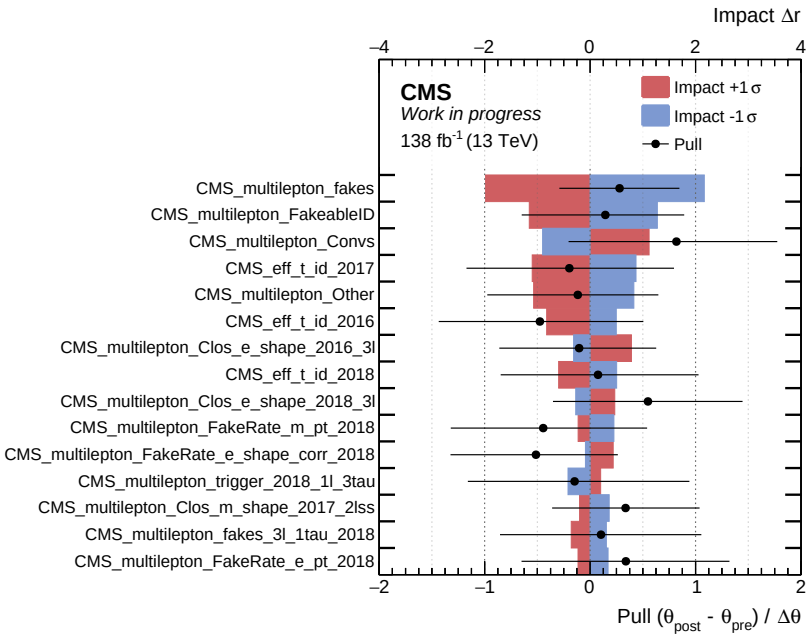

Figure 8.4: Pulls and impacts for nuisance parameters in the combined HH $\rightarrow$ Multilepton signal extraction fit with the JHEP04BM7 tuned nonRes BDT output in all seven Multilepton channels and the kinematic distributions in the 3ℓCR and 4ℓCR for all three years using SM like non-resonant HH signal. (Page 1/16)

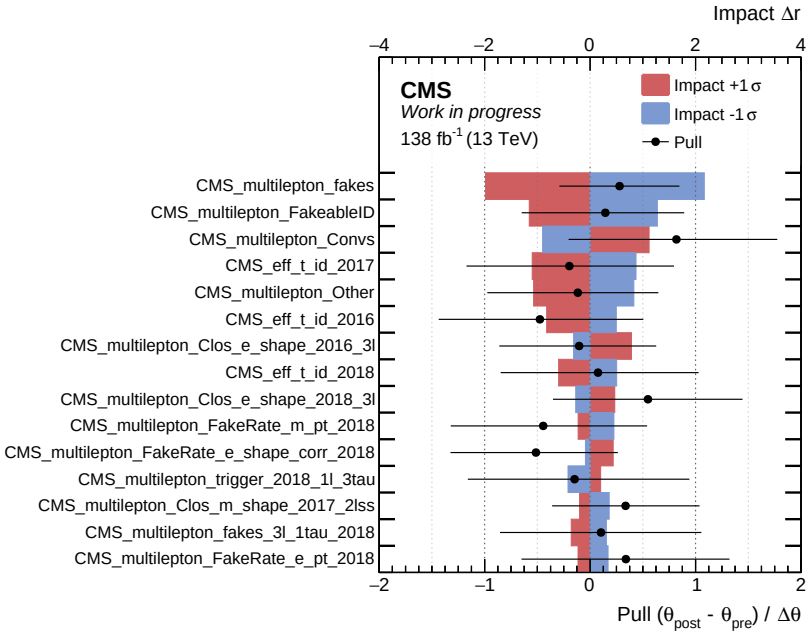

Figure 8.5: Pulls and impacts for nuisance parameters in the combined HH $\rightarrow$ Multilepton signal extraction fit with the JHEP04BM7 tuned nonRes BDT output in all seven Multilepton channels and the kinematic distributions in the 3ℓCR and 4ℓCR for all three years using SM like non-resonant HH signal. (Page 2/16)

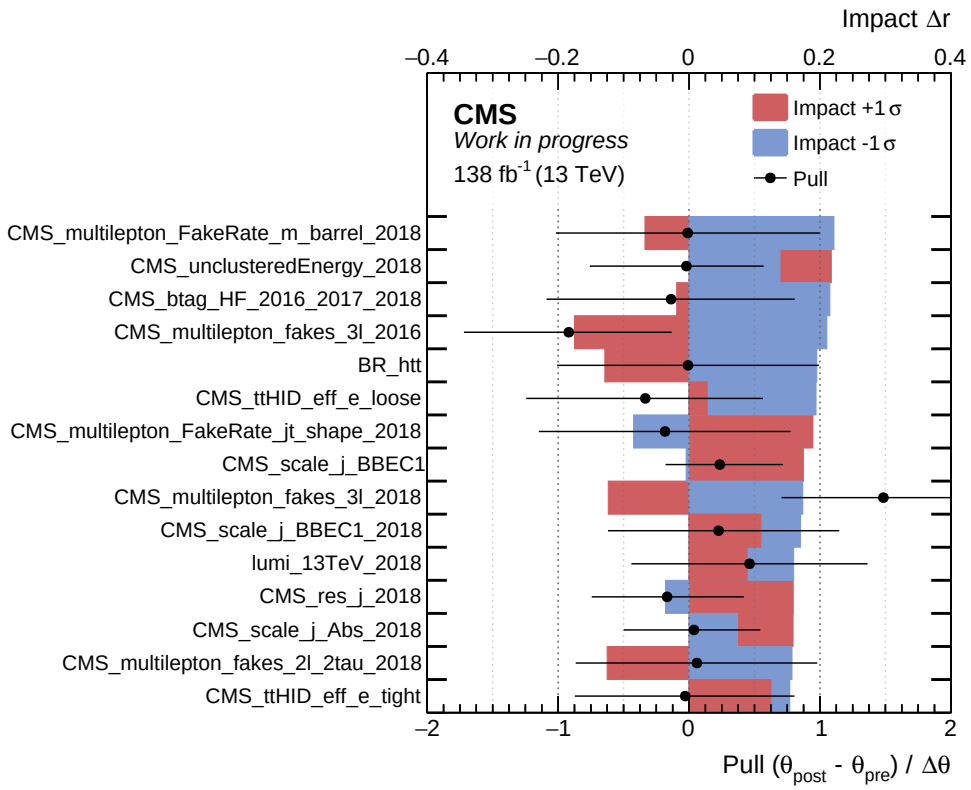

Figure 8.6: Pulls and impacts for nuisance parameters in the combined HH → Multilepton signal extraction fit with the JHEP04BM7 tuned nonRes BDT output in all seven Multilepton channels and the kinematic distributions in the 3ℓCR and 4ℓCR for all three years using SM like non-resonant HH signal. (Page 3/16)

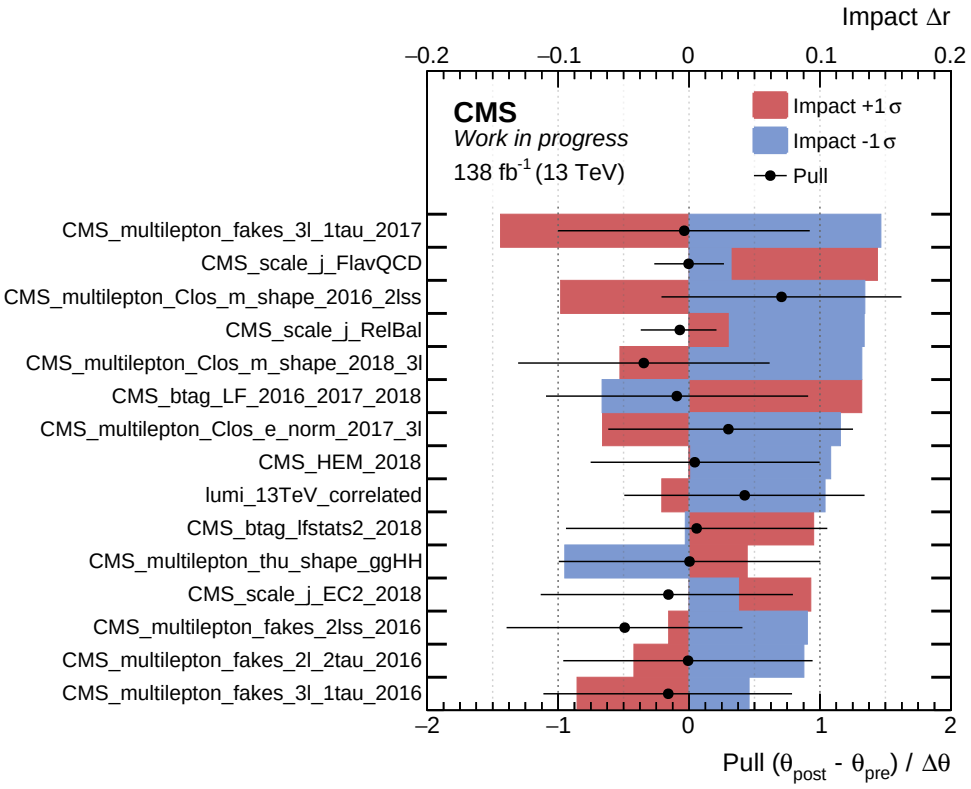

Figure 8.7: Pulls and impacts for nuisance parameters in the combined HH → Multilepton signal extraction fit with the JHEP04BM7 tuned nonRes BDT output in all seven Multilepton channels and the kinematic distributions in the 3ℓCR and 4ℓCR for all three years using SM like non-resonant HH signal. (Page 4/16)

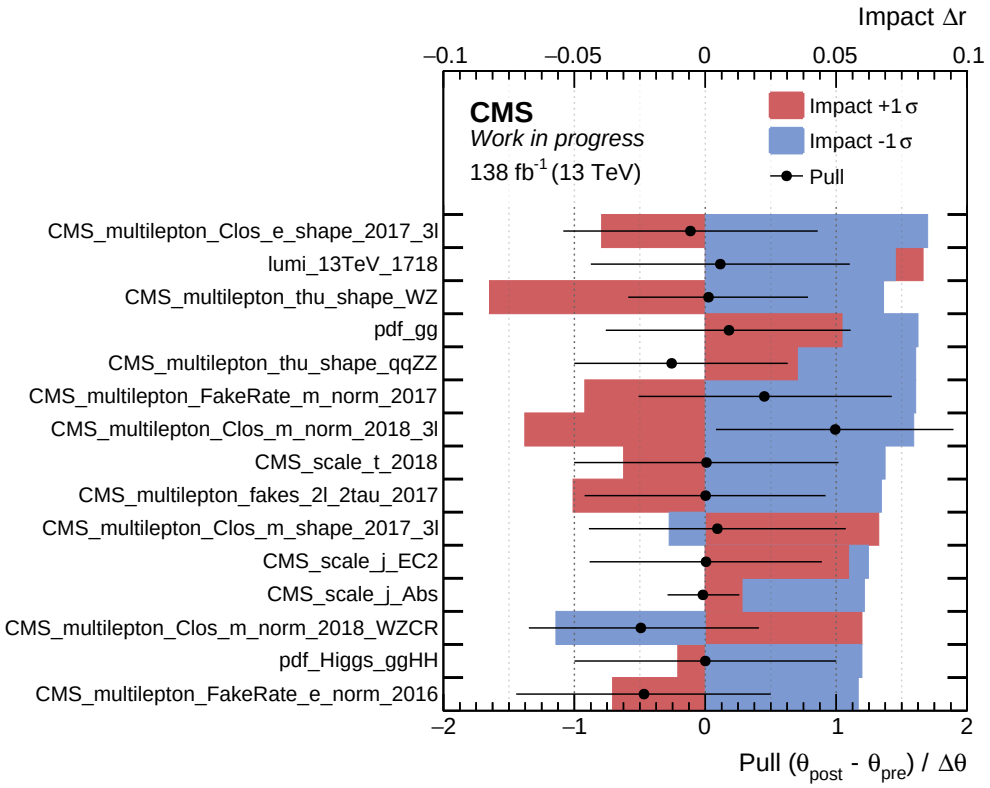

Figure 8.8: Pulls and impacts for nuisance parameters in the combined HH $\rightarrow$ Multilepton signal extraction fit with the JHEP04BM7 tuned nonRes BDT output in all seven Multilepton channels and the kinematic distributions in the 3ℓCR and 4ℓCR for all three years using SM like non-resonant HH signal. (Page 5/16)

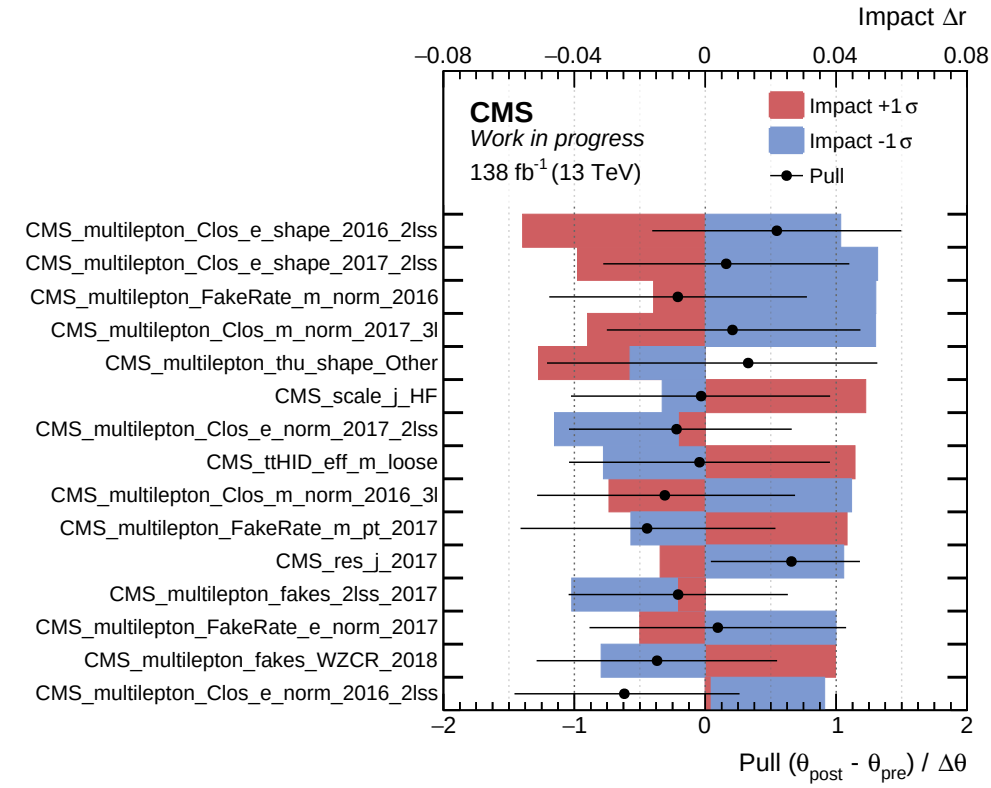

Figure 8.9: Pulls and impacts for nuisance parameters in the combined HH $\rightarrow$ Multilepton signal extraction fit with the JHEP04BM7 tuned nonRes BDT output in all seven Multilepton channels and the kinematic distributions in the 3ℓCR and 4ℓCR for all three years using SM like non-resonant HH signal. (Page 6/16)

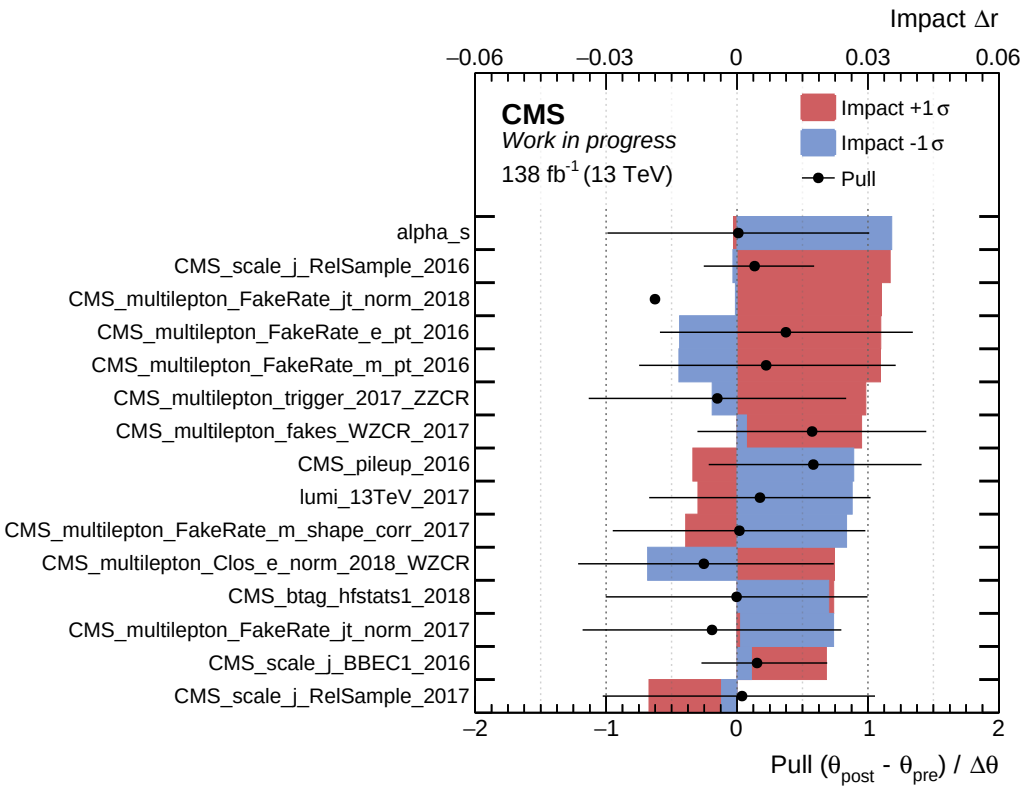

Figure 8.10: Pulls and impacts for nuisance parameters in the combined HH $\rightarrow$ Multilepton signal extraction fit with the JHEP04BM7 tuned nonRes BDT output in all seven Multilepton channels and the kinematic distributions in the 3ℓCR and 4ℓCR for all three years using SM like non-resonant HH signal. (Page 7/16)

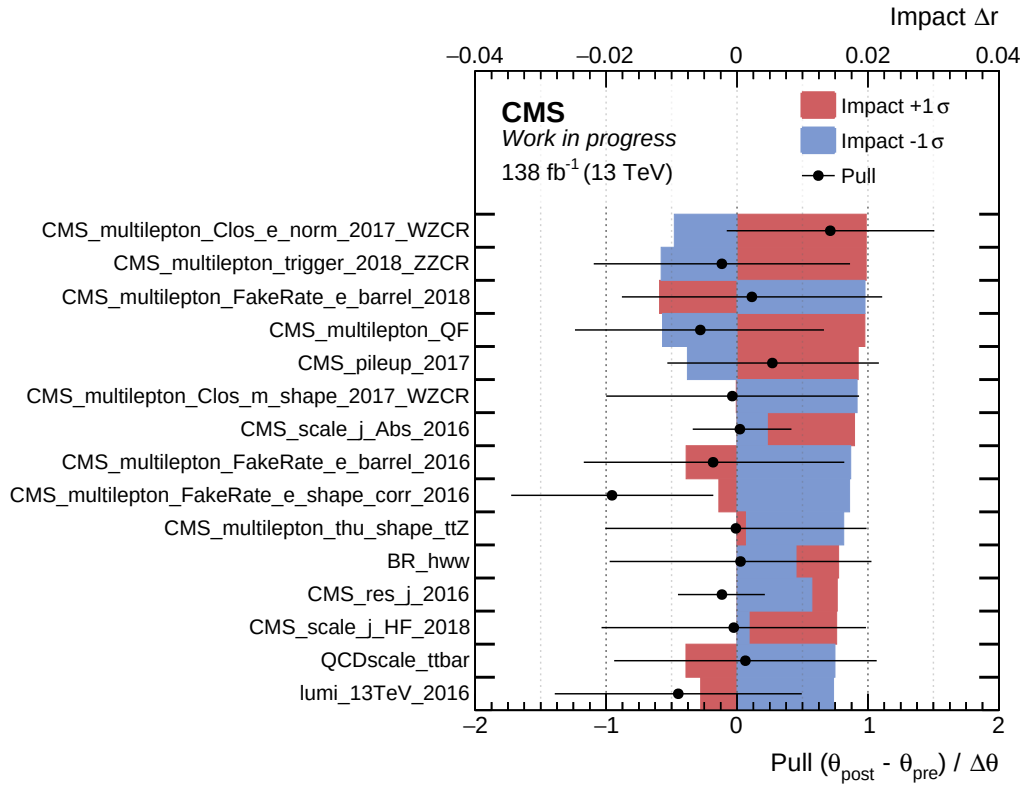

Figure 8.11: Pulls and impacts for nuisance parameters in the combined HH $\rightarrow$ Multilepton signal extraction fit with the JHEP04BM7 tuned nonRes BDT output in all seven Multilepton channels and the kinematic distributions in the 3ℓCR and 4ℓCR for all three years using SM like non-resonant HH signal. (Page 8/16)

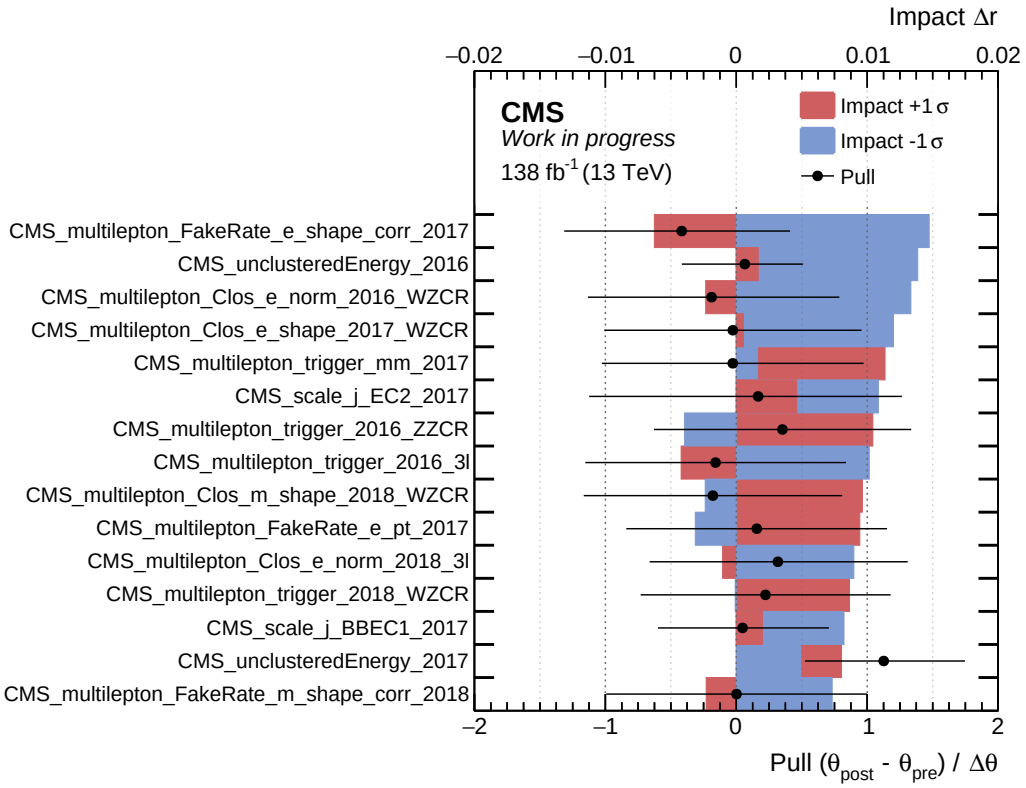

Figure 8.12: Pulls and impacts for nuisance parameters in the combined HH $\rightarrow$ Multilepton signal extraction fit with the JHEP04BM7 tuned nonRes BDT output in all seven Multilepton channels and the kinematic distributions in the 3ℓCR and 4ℓCR for all three years using SM like non-resonant HH signal. (Page 9/16)

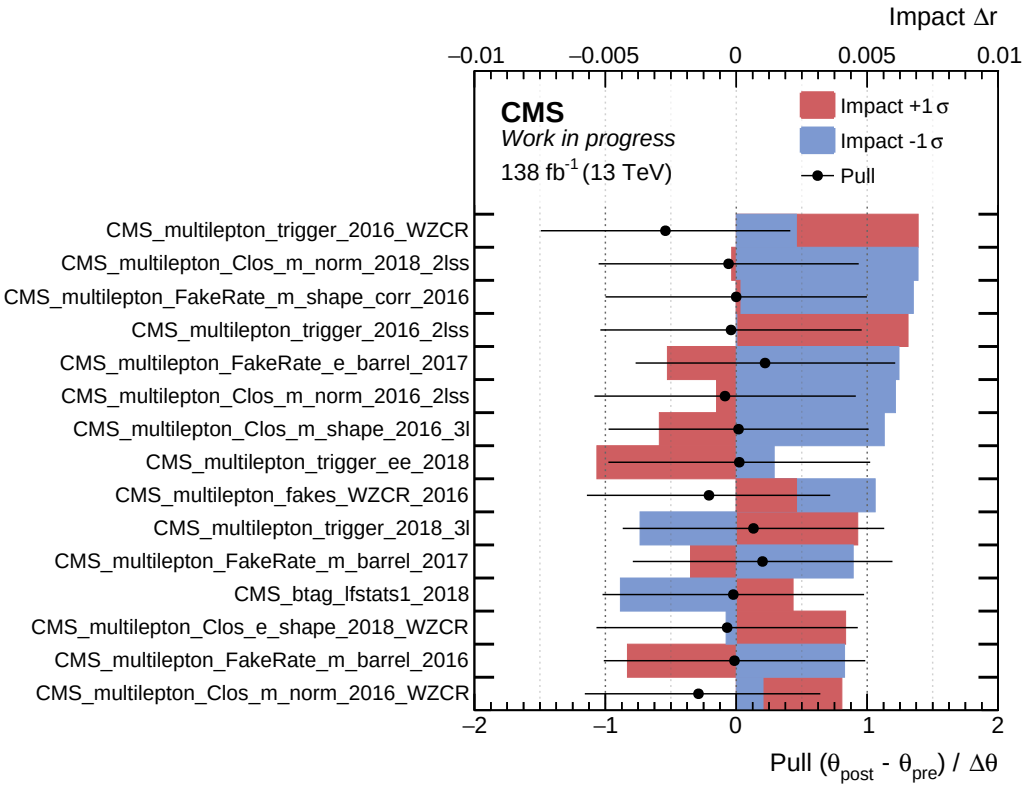

Figure 8.13: Pulls and impacts for nuisance parameters in the combined HH $\rightarrow$ Multilepton signal extraction fit with the JHEP04BM7 tuned nonRes BDT output in all seven Multilepton channels and the kinematic distributions in the 3ℓCR and 4ℓCR for all three years using SM like non-resonant HH signal. (Page 10/16)

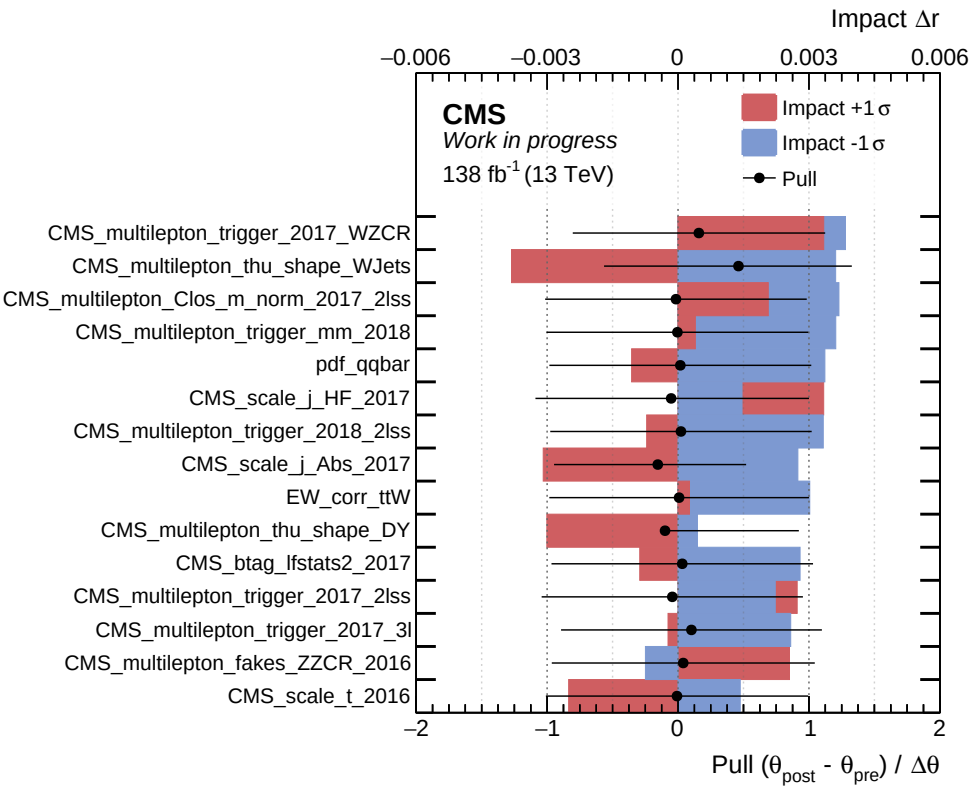

Figure 8.14: Pulls and impacts for nuisance parameters in the combined HH $\rightarrow$ Multilepton signal extraction fit with the JHEP04BM7 tuned nonRes BDT output in all seven Multilepton channels and the kinematic distributions in the 3ℓCR and 4ℓCR for all three years using SM like non-resonant HH signal. (Page 11/16)

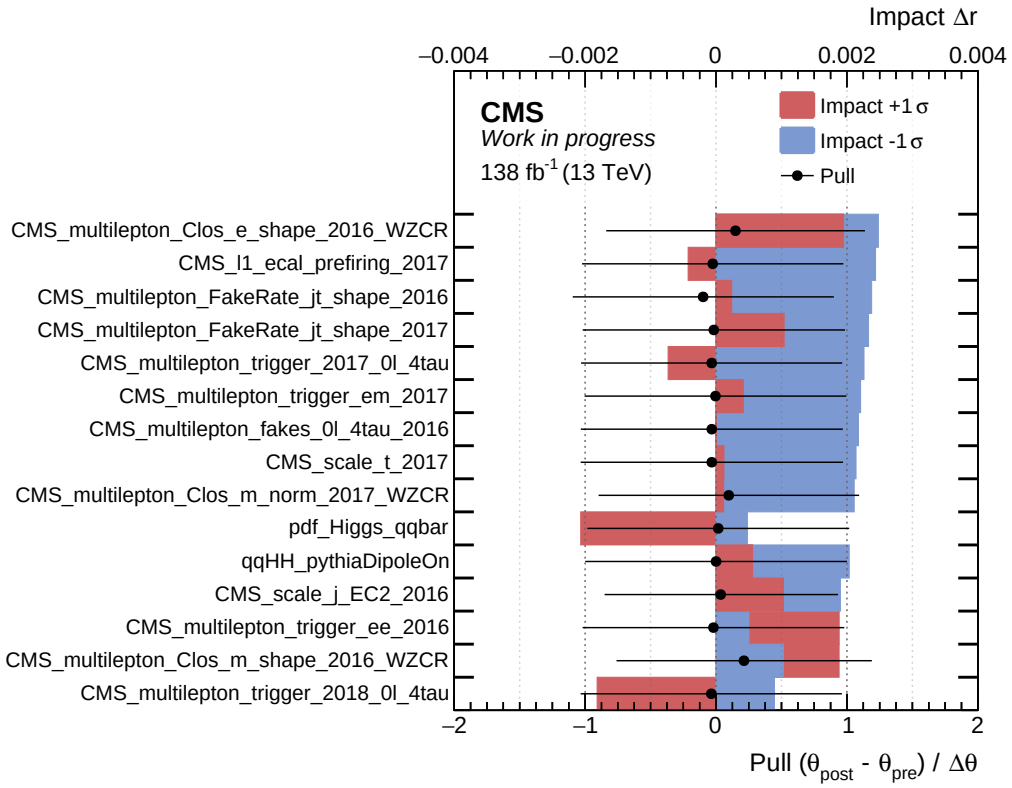

Figure 8.15: Pulls and impacts for nuisance parameters in the combined HH $\rightarrow$ Multilepton signal extraction fit with the JHEP04BM7 tuned nonRes BDT output in all seven Multilepton channels and the kinematic distributions in the 3ℓCR and 4ℓCR for all three years using SM like non-resonant HH signal. (Page 12/16)

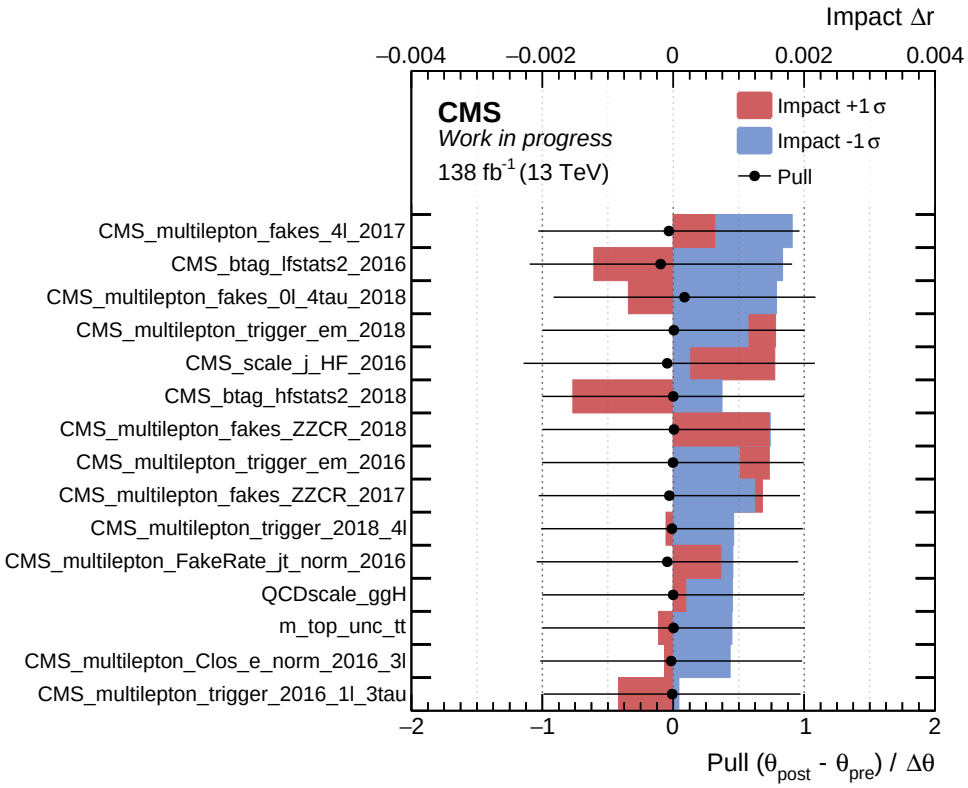

Figure 8.16: Pulls and impacts for nuisance parameters in the combined HH $\rightarrow$ Multilepton signal extraction fit with the JHEP04BM7 tuned nonRes BDT output in all seven Multilepton channels and the kinematic distributions in the 3ℓCR and 4ℓCR for all three years using SM like non-resonant HH signal. (Page 13/16)

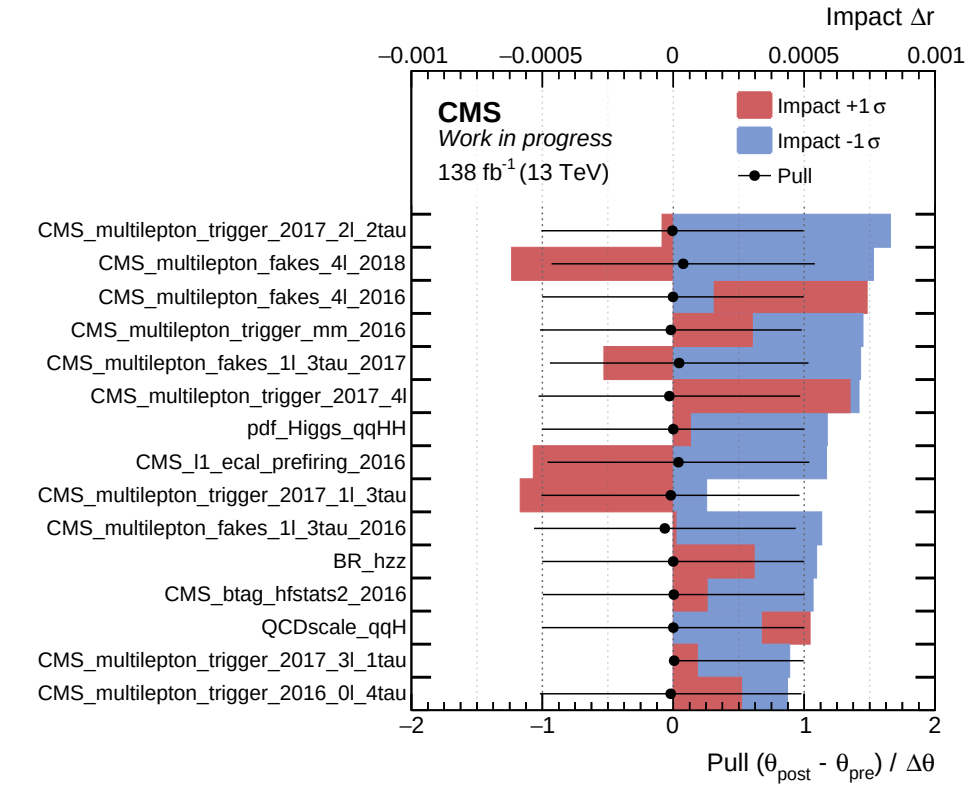

Figure 8.17: Pulls and impacts for nuisance parameters in the combined HH $\rightarrow$ Multilepton signal extraction fit with the JHEP04BM7 tuned nonRes BDT output in all seven Multilepton channels and the kinematic distributions in the 3ℓCR and 4ℓCR for all three years using SM like non-resonant HH signal. (Page 14/16)

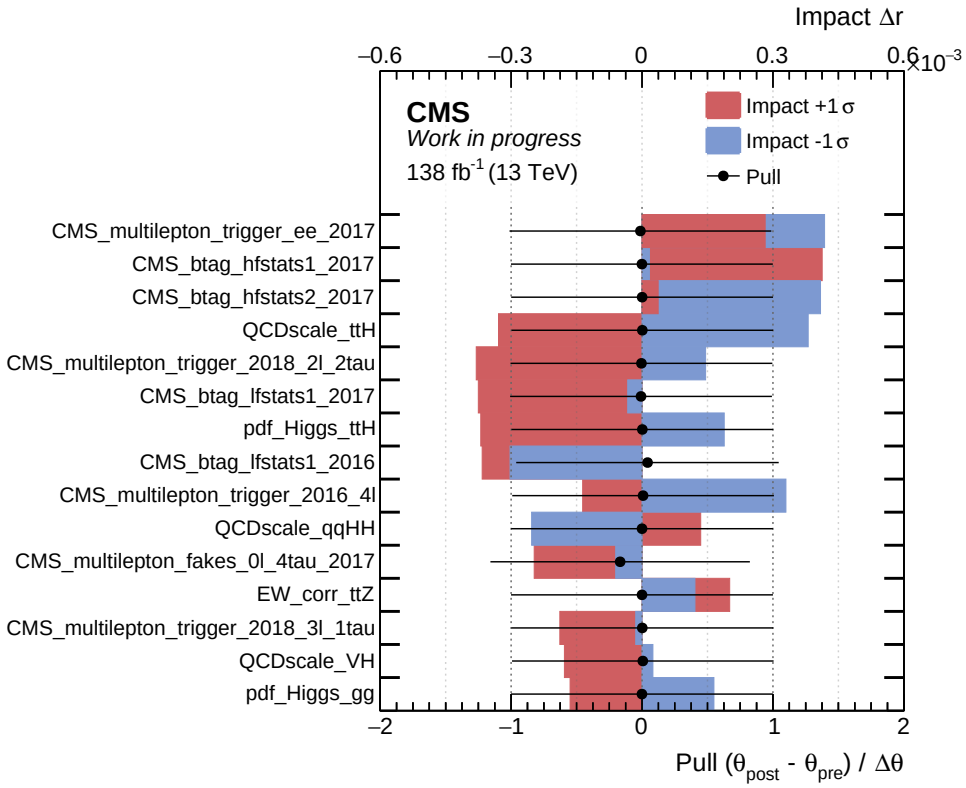

Figure 8.18: Pulls and impacts for nuisance parameters in the combined HH $\rightarrow$ Multilepton signal extraction fit with the JHEP04BM7 tuned nonResBDT output in all seven Multilepton channels and the kinematic distributions in the 3ℓCR and 4ℓCR for all three years using SM like non-resonant HH signal. (Page 15/16)

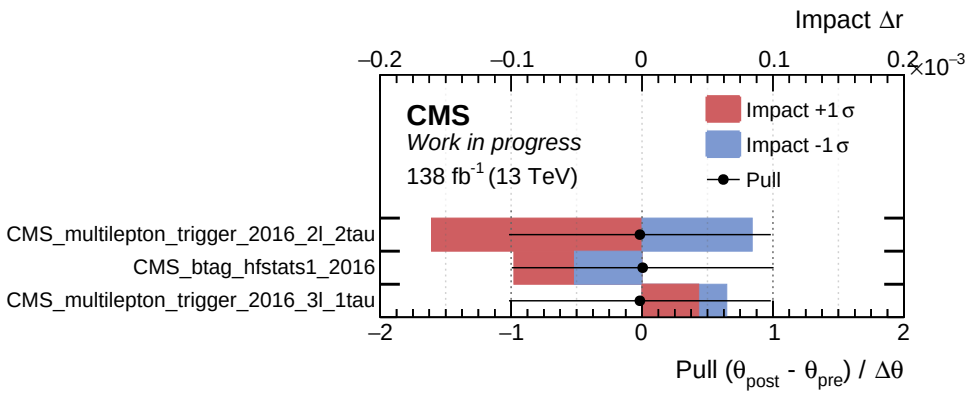

Figure 8.19: Pulls and impacts for nuisance parameters in the combined HH $\rightarrow$ Multilepton signal extraction fit with the JHEP04BM7 tuned nonRes BDT output in all seven Multilepton channels and the kinematic distributions in the 3ℓCR and 4ℓCR for all three years using SM like non-resonant HH signal. (Page 16/16)

Postfit $0\ell 4\tau_h$

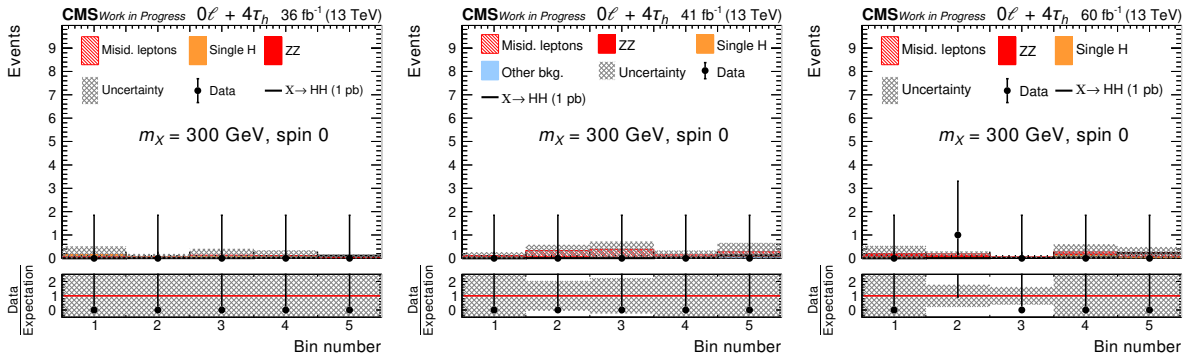

Figure 8.20: Postfit plots (2016-2018) for the $0\ell + 4\tau_h$ channel with resonant ggHH signal for the spin-0 case and $m_\chi = 300\,\text{GeV}$ (scaled to 1 *pb*).

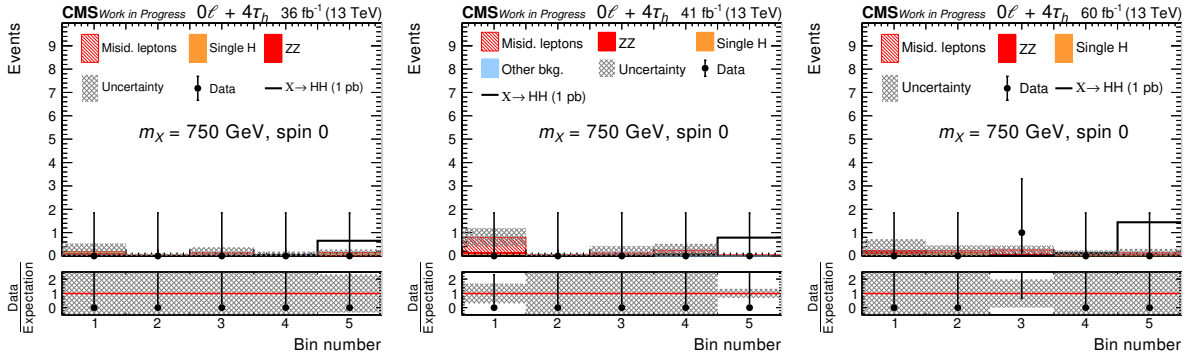

Figure 8.21: Postfit plots (2016-2018) for the $0\ell + 4\tau_h$ channel with resonant ggHH signal for the spin-0 case and $m_\chi = 750\,\text{GeV}$ (scaled to 1 *pb*).

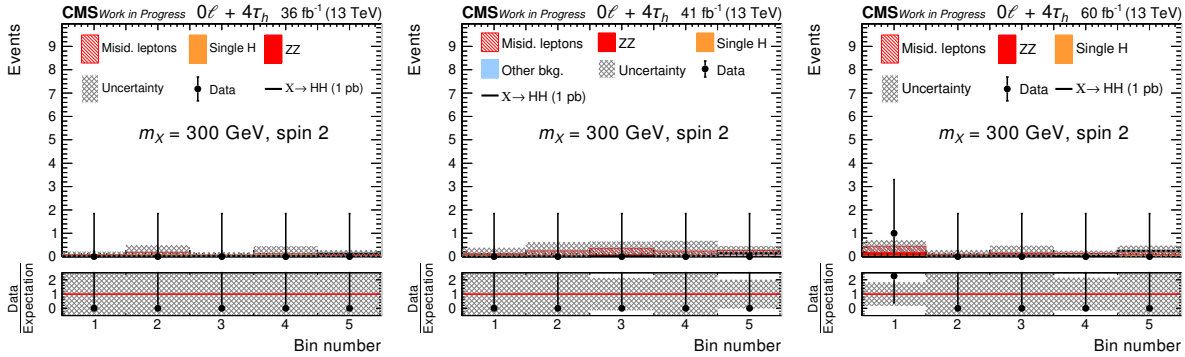

Figure 8.22: Postfit plots (2016-2018) for the $0\ell + 4\tau_h$ channel with resonant ggHH signal for the spin-2 case and $m_\chi = 300\,\text{GeV}$ (scaled to 1 *pb*).

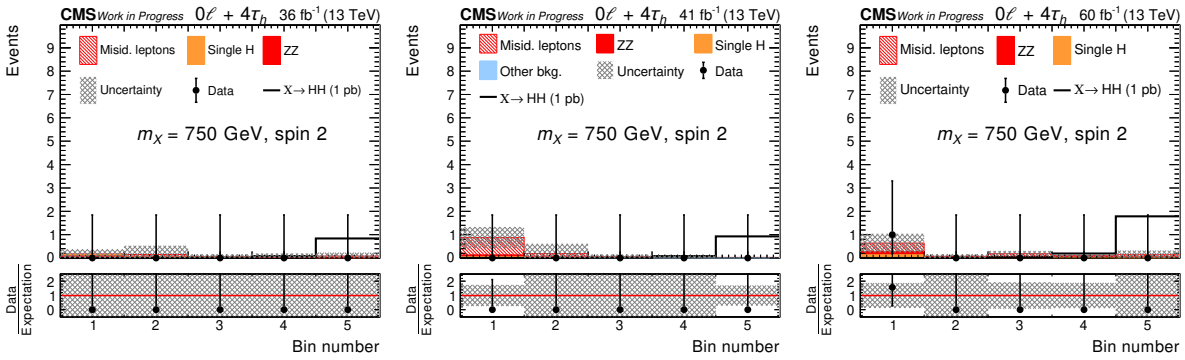

Figure 8.23: Postfit plots (2016-2018) for the $0\ell + 4\tau_h$ channel with resonant ggHH signal for the spin-2 case and $m_\chi = 750\,\text{GeV}$ (scaled to 1 pb).

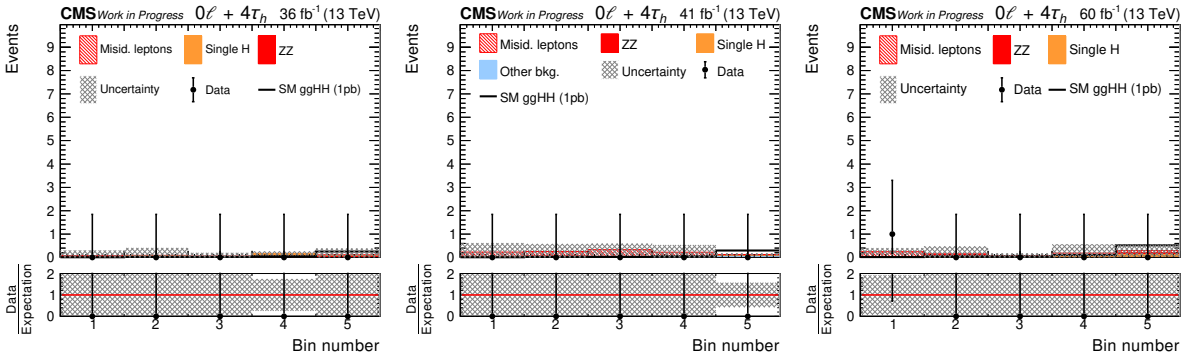

Figure 8.24: Postfit plots (2016-2018) for the $0\ell + 4\tau_h$ channel with SM non-resonant ggHH signal on the SM optimized nonRes BDT output (scaled to 1 pb).

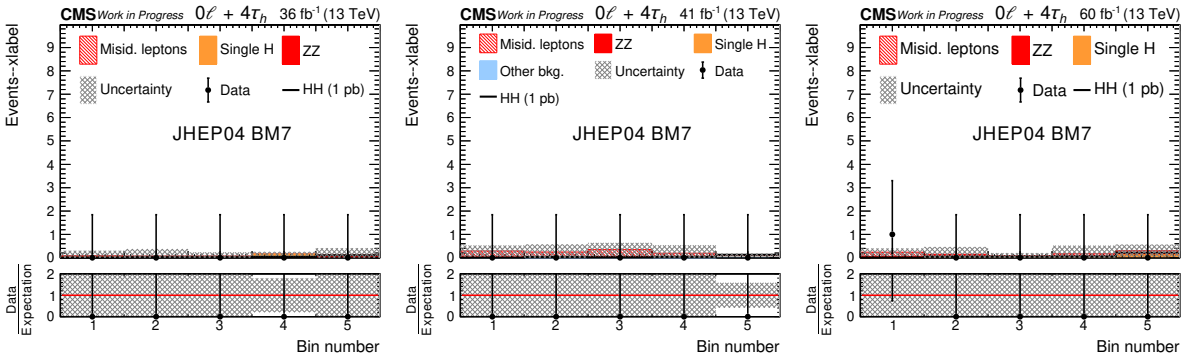

Figure 8.25: Postfit plots (2016-2018) for the $0\ell + 4\tau_h$ channel with non-resonant ggHH signal for the JHEP04BM7 scenario (scaled to 1 pb).

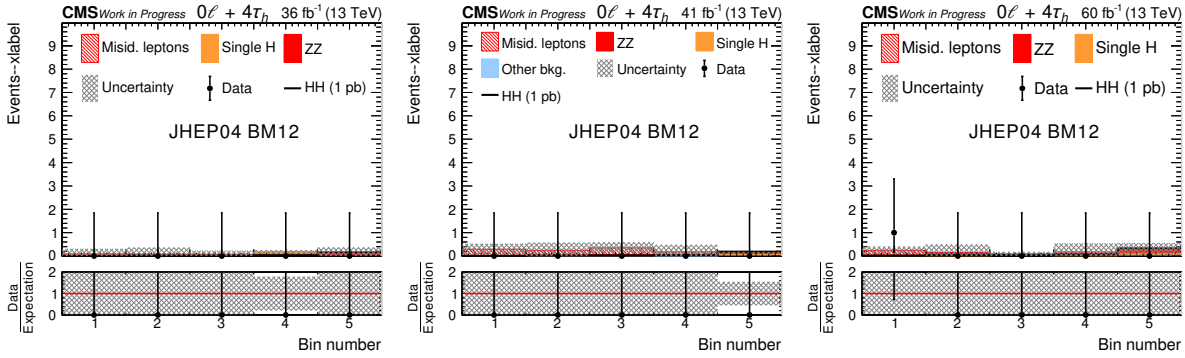

Figure 8.26: Postfit plots (2016-2018) for the $0\ell + 4\tau_h$ channel with non-resonant ggHH signal for the JHEP04BM12 scenario (scaled to 1 *pb*).

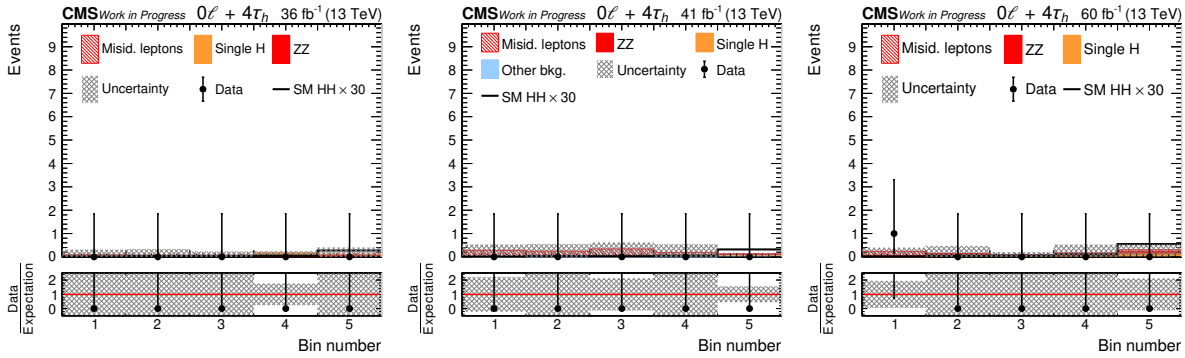

Figure 8.27: Postfit plots (2016-2018) for the $0\ell + 4\tau_h$ channel with SM like non-resonant HH signal on the JHEP04BM7 optimized nonRes BDT output (scaled to $30 \times \sigma_{HH}^{SM}$).

Postfit $1\ell 3\tau_h$

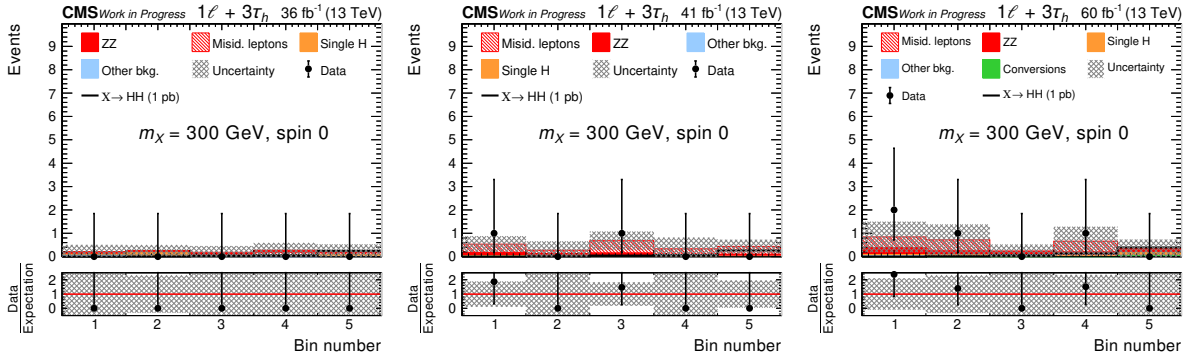

Figure 8.28: Postfit plots (2016-2018) for the $1\ell + 3\tau_h$ channel with resonant ggHH signal for the spin-0 case and $m_\chi = 300\,\text{GeV}$ (scaled to 1 *pb*).

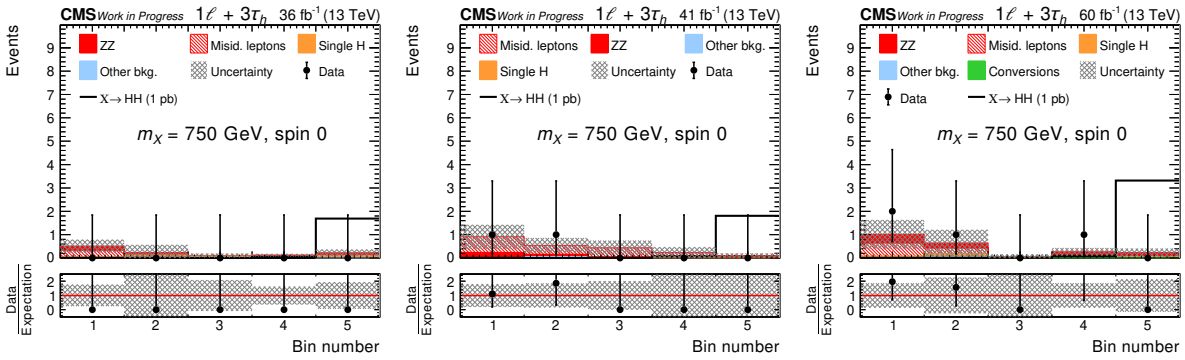

Figure 8.29: Postfit plots (2016-2018) for the $1\ell + 3\tau_h$ channel with resonant ggHH signal for the spin-0 case and $m_\chi = 750\,\text{GeV}$ (scaled to $1\,pb$).

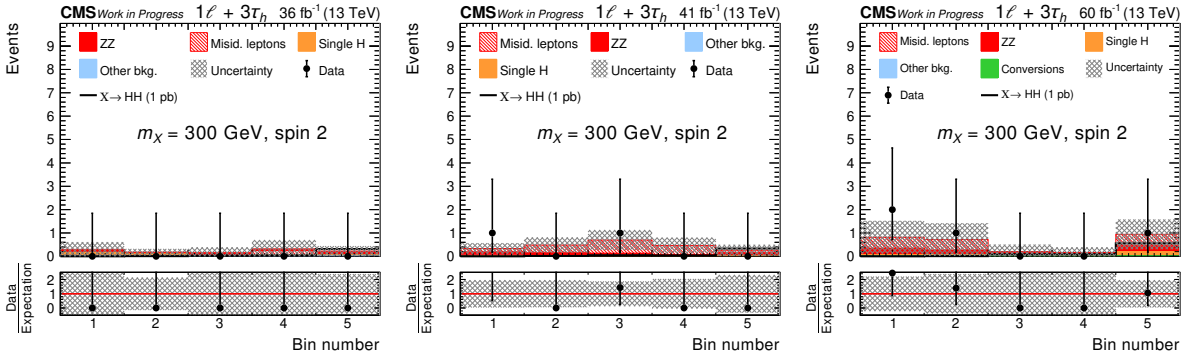

Figure 8.30: Postfit plots (2016-2018) for the $1\ell + 3\tau_h$ channel with resonant ggHH signal for the spin-2 case and $m_\chi = 300\,\text{GeV}$ (scaled to $1\,pb$).

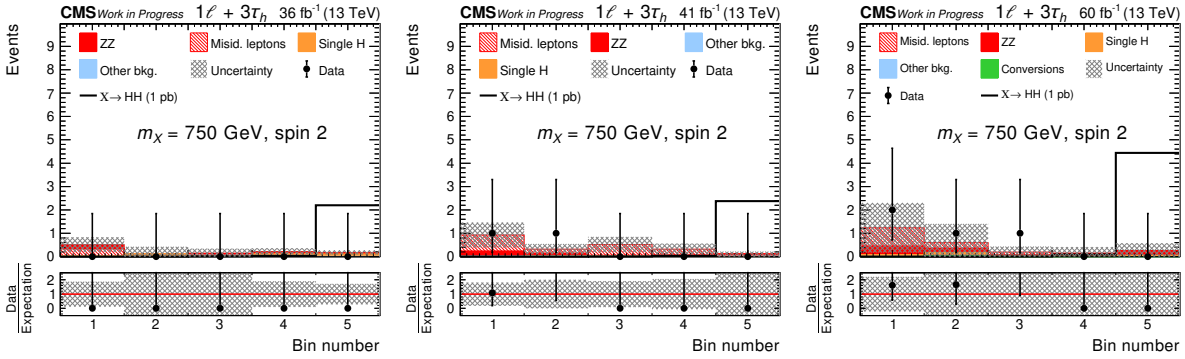

Figure 8.31: Postfit plots (2016-2018) for the $1\ell + 3\tau_h$ channel with resonant ggHH signal for the spin-2 case and $m_\chi = 750\,\text{GeV}$ (scaled to $1\,pb$).

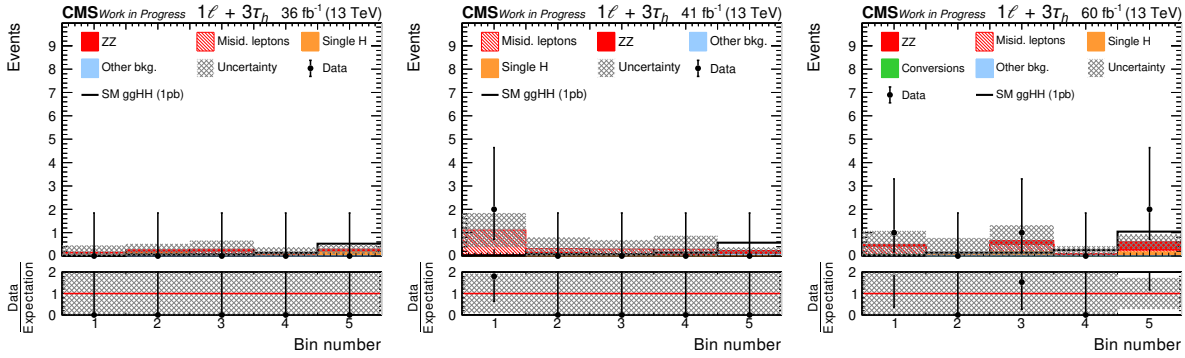

Figure 8.32: Postfit plots (2016-2018) for the $1\ell + 3\tau_h$ channel with SM non-resonant ggHH signal on the SM optimized nonRes BDT output (scaled to 1 *pb*).

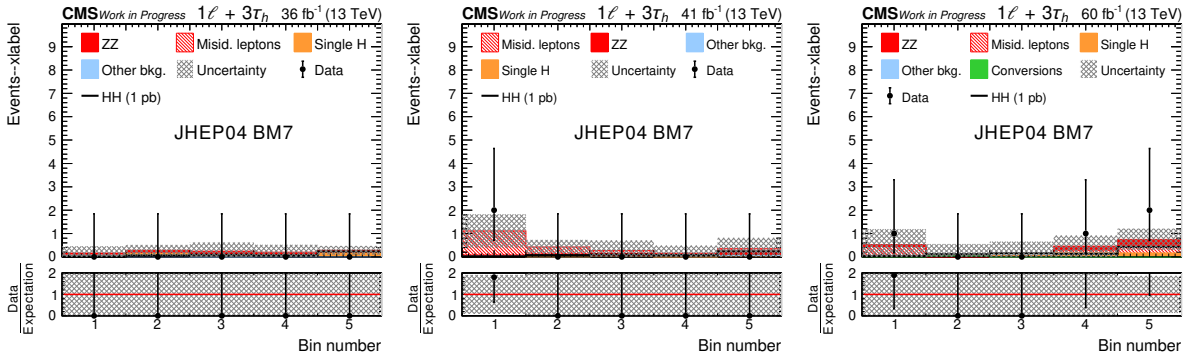

Figure 8.33: Postfit plots (2016-2018) for the $1\ell + 3\tau_h$ channel with non-resonant ggHH signal for the JHEP04BM7 scenario (scaled to 1 *pb*).

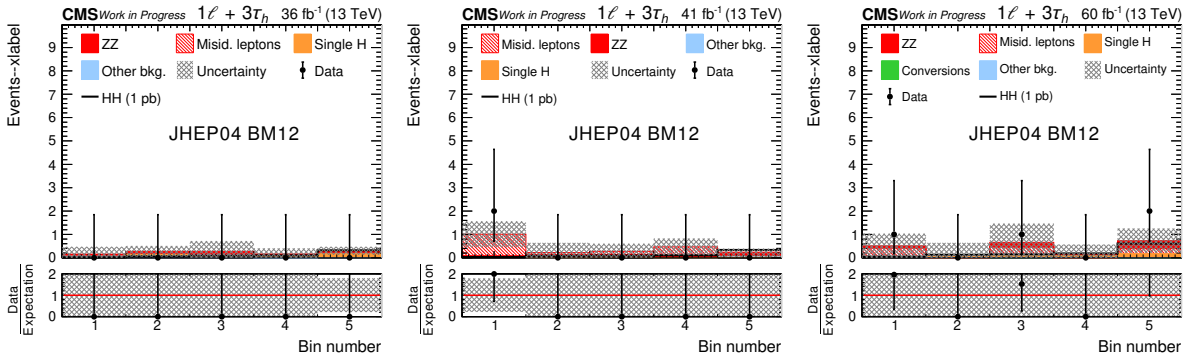

Figure 8.34: Postfit plots (2016-2018) for the $1\ell + 3\tau_h$ channel with non-resonant ggHH signal for the JHEP04BM12 scenario (scaled to 1 *pb*).

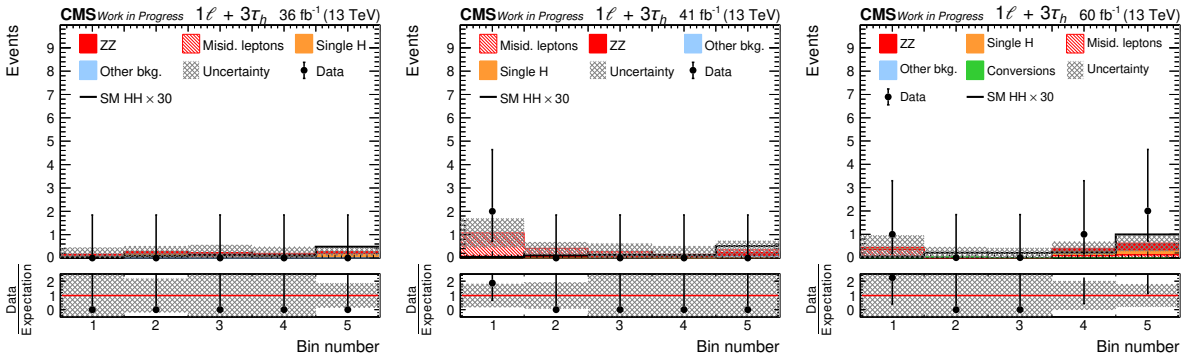

Figure 8.35: Postfit plots (2016-2018) for the $1\ell + 3\tau_h$ channel with SM like non-resonant HH signal on the JHEP04BM7 optimized nonRes BDT output (scaled to $30 \times \sigma_{HH}^{SM}$).

Postfit $2\ell 2\tau_h$

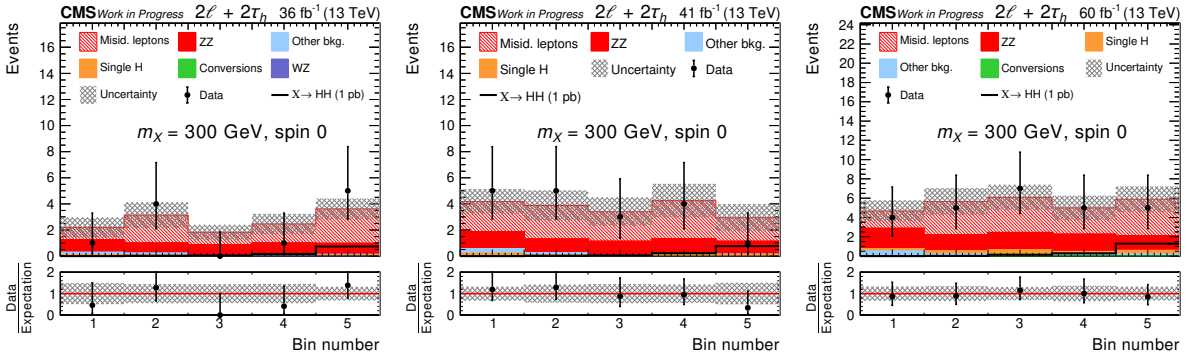

Figure 8.36: Postfit plots (2016-2018) for the $2\ell + 2\tau_h$ channel with resonant ggHH signal for the spin-0 case and $m_\chi = 300\,\text{GeV}$ (scaled to $1\,pb$).

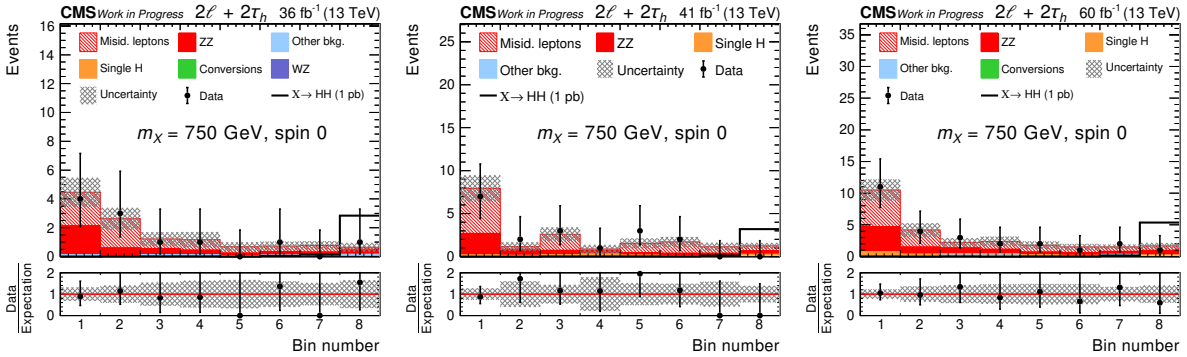

Figure 8.37: Postfit plots (2016-2018) for the $2\ell + 2\tau_h$ channel with resonant ggHH signal for the spin-0 case and $m_\chi = 750\,\text{GeV}$ (scaled to $1\,pb$).

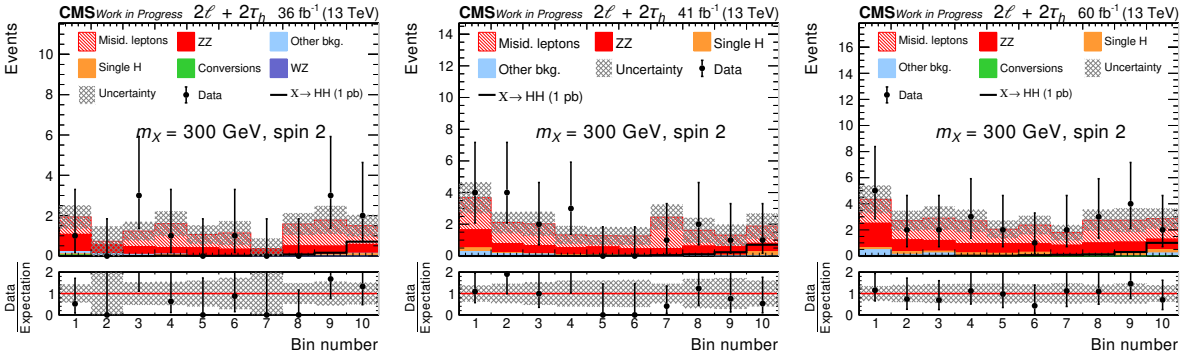

Figure 8.38: Postfit plots (2016-2018) for the $2\ell + 2\tau_h$ channel with resonant ggHH signal for the spin-2 case and $m_\chi = 300\,\text{GeV}$ (scaled to 1 pb).

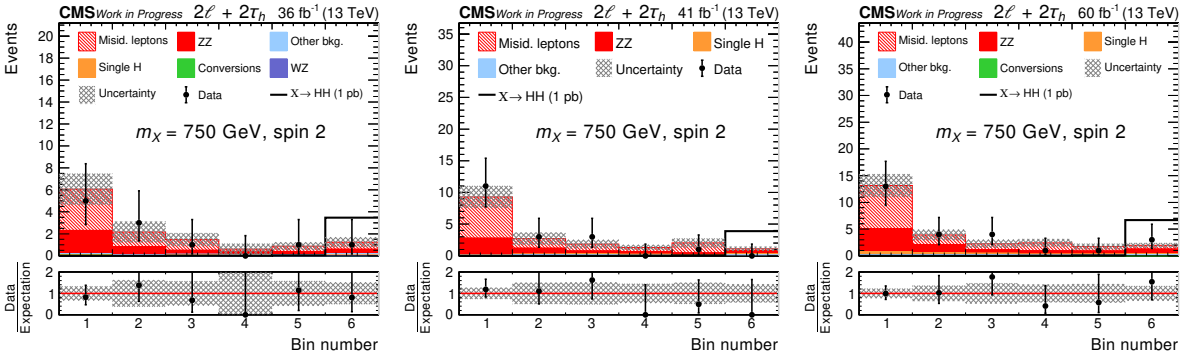

Figure 8.39: Prefit plots (2016-2018) for the $2\ell + 2\tau_h$ channel with resonant ggHH signal for the spin-2 case and $m_\chi = 750\,\text{GeV}$ (scaled to 1 pb).

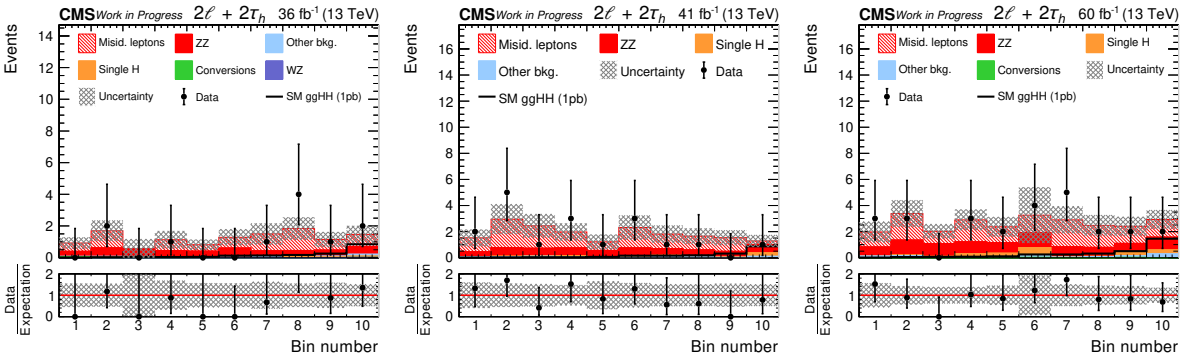

Figure 8.40: Postfit plots (2016-2018) for the $2\ell + 2\tau_h$ channel with SM non-resonant ggHH signal on the SM optimized nonRes BDT output (scaled to 1 pb).

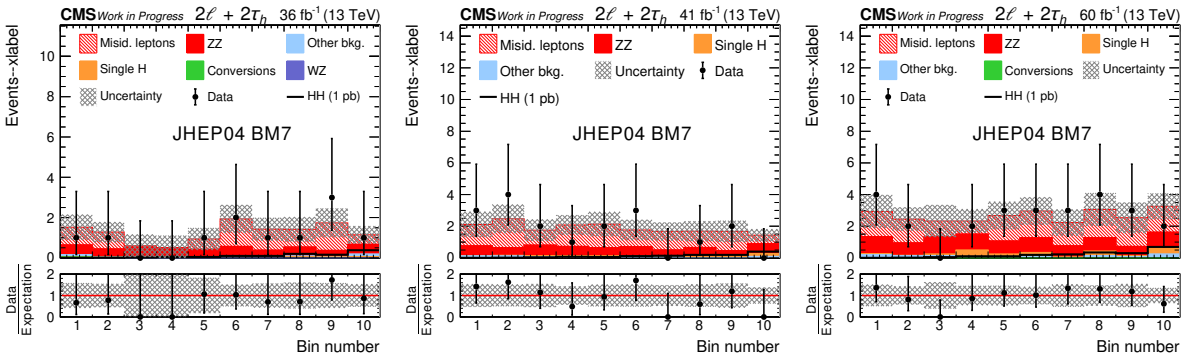

Figure 8.41: Postfit plots (2016-2018) for the $2\ell + 2\tau_h$ channel with non-resonant ggHH signal for the JHEP04BM7 scenario (scaled to 1 *pb*).

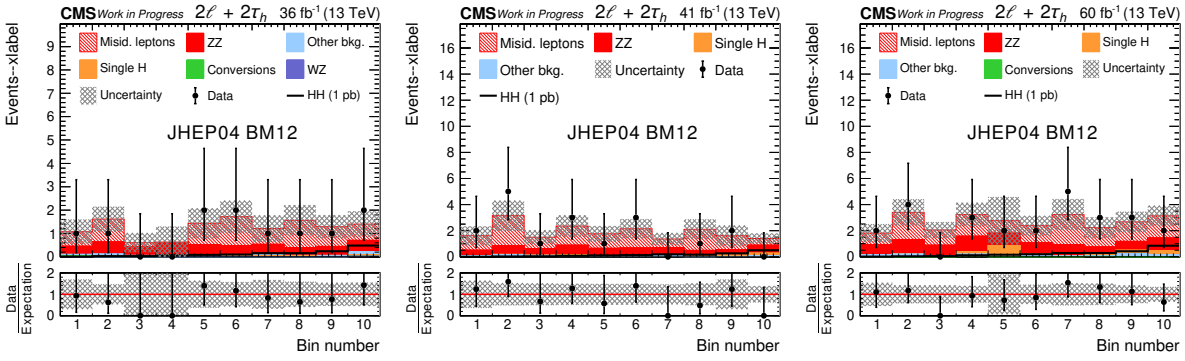

Figure 8.42: Postfit plots (2016-2018) for the $2\ell + 2\tau_h$ channel with non-resonant ggHH signal for the JHEP04BM12 scenario (scaled to 1 *pb*).

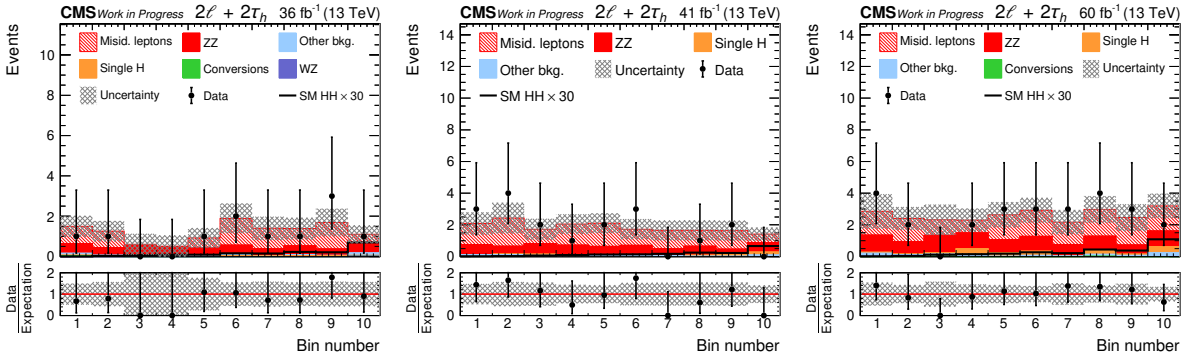

Figure 8.43: Postfit plots (2016-2018) for the $2\ell + 2\tau_h$ channel with SM like non-resonant HH signal on the JHEP04BM7 optimized nonRes BDT output (scaled to $30 \times \sigma_{HH}^{SM}$).

Postfit $3\ell 1\tau_h$

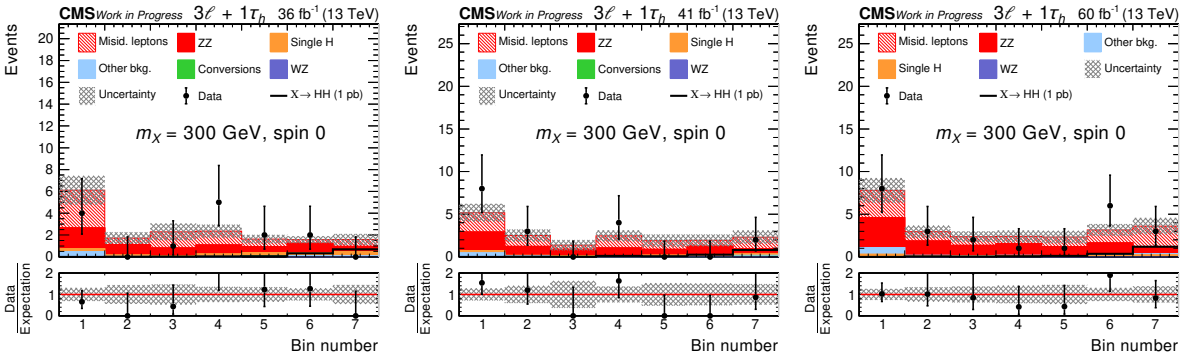

Figure 8.44: Postfit plots (2016-2018) for the $3\ell + 1\tau_h$ channel with resonant ggHH signal for the spin-0 case and $m_\chi = 300\,\text{GeV}$ (scaled to 1 pb).

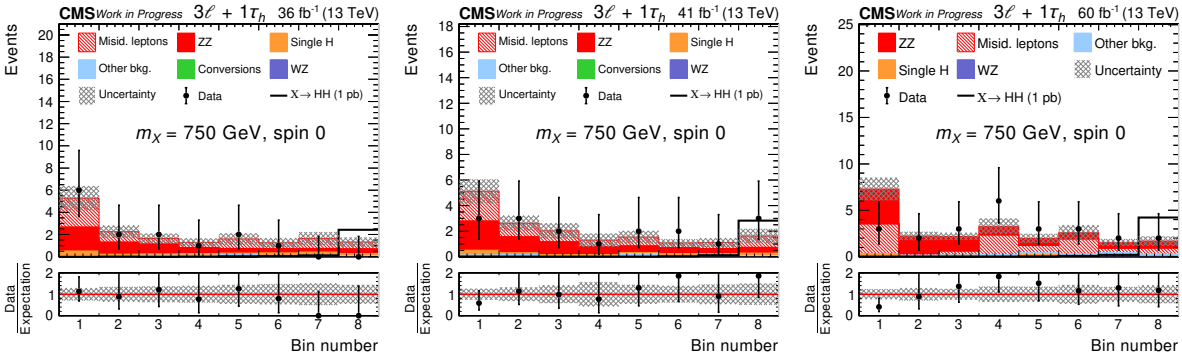

Figure 8.45: Postfit plots (2016-2018) for the $3\ell + 1\tau_h$ channel with resonant ggHH signal for the spin-0 case and $m_\chi = 750\,\text{GeV}$ (scaled to 1 pb).

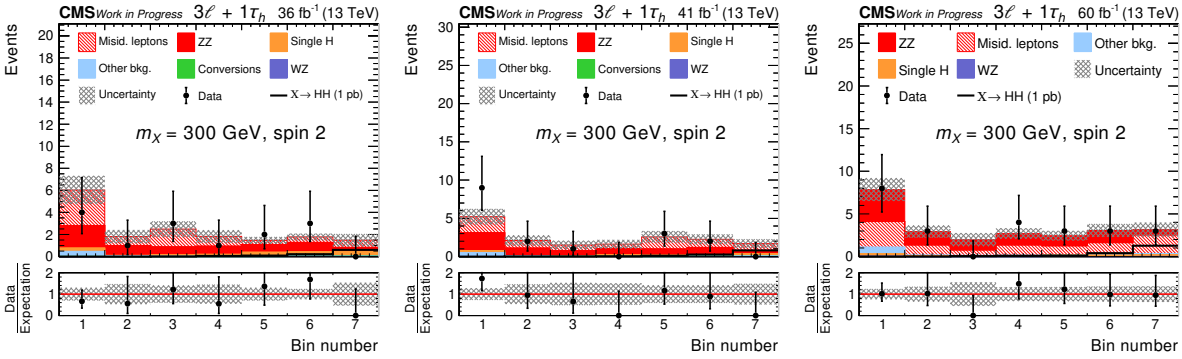

Figure 8.46: Postfit plots (2016-2018) for the $3\ell + 1\tau_h$ channel with resonant ggHH signal for the spin-2 case and $m_\chi = 300\,\text{GeV}$ (scaled to 1 pb).

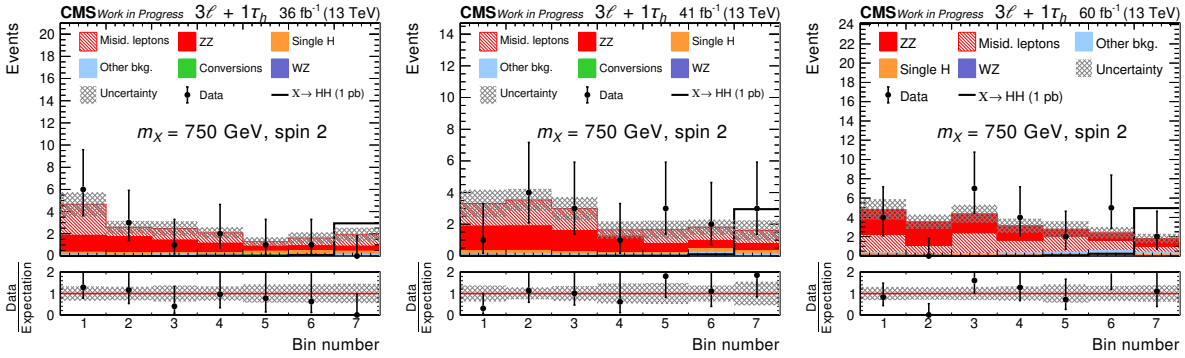

Figure 8.47: Postfit plots (2016-2018) for the $3\ell + 1\tau_h$ channel with resonant ggHH signal for the spin-2 case and $m_\chi = 750\,\text{GeV}$ (scaled to 1 pb).

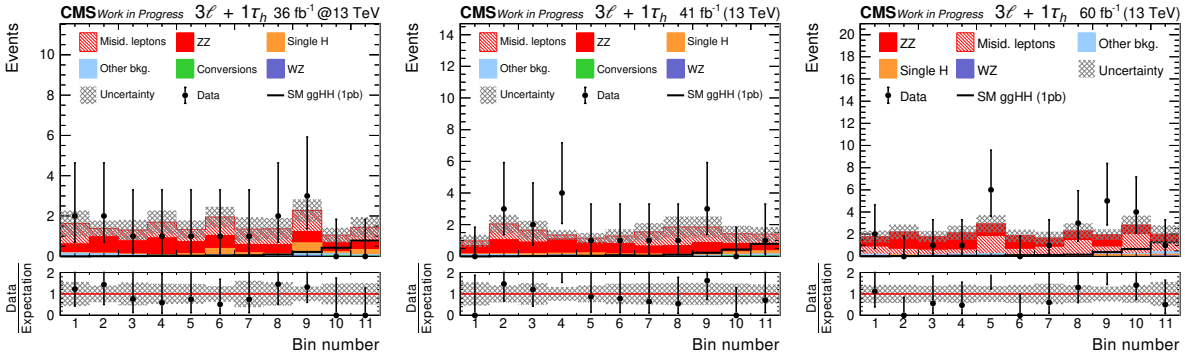

Figure 8.48: Postfit plots (2016-2018) for the $3\ell + 1\tau_h$ channel with SM non-resonant ggHH signal on the SM optimized nonRes BDT output (scaled to 1 pb).

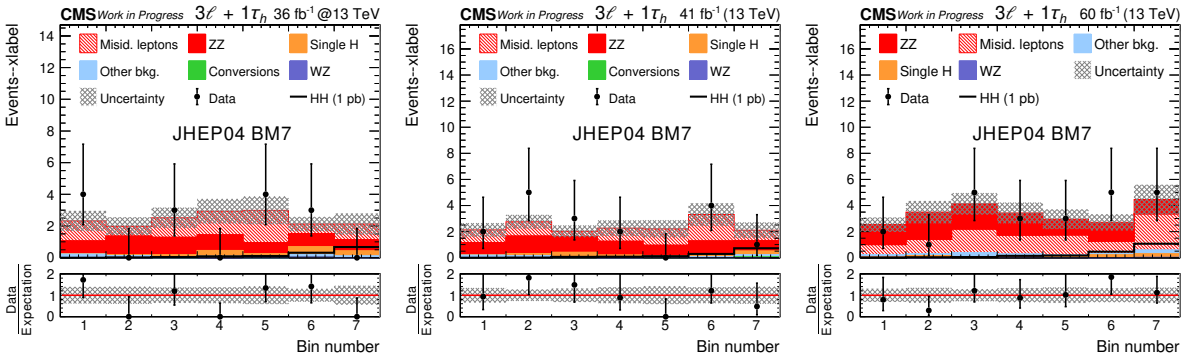

Figure 8.49: Postfit plots (2016-2018) for the $3\ell + 1\tau_h$ channel with non-resonant ggHH signal for the JHEP04BM7 scenario (scaled to 1 pb).

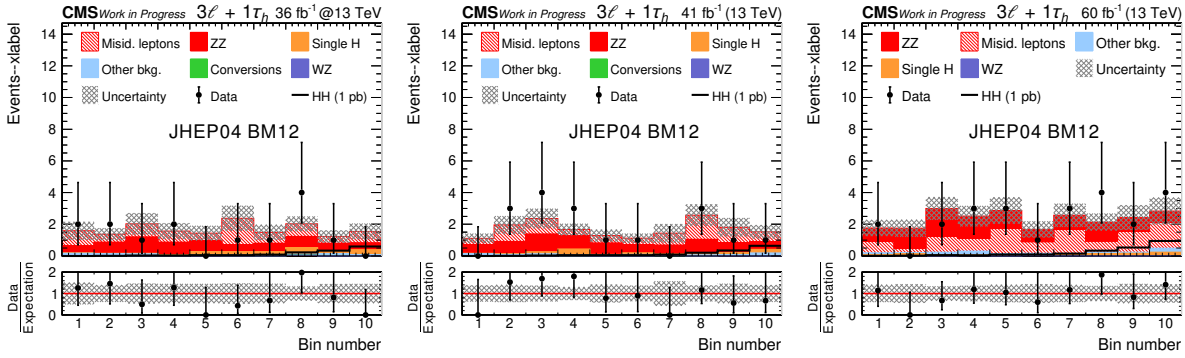

Figure 8.50: Postfit plots (2016-2018) for the $3\ell + 1\tau_h$ channel with non-resonant ggHH signal for the JHEP04BM12 scenario (scaled to 1 *pb*).

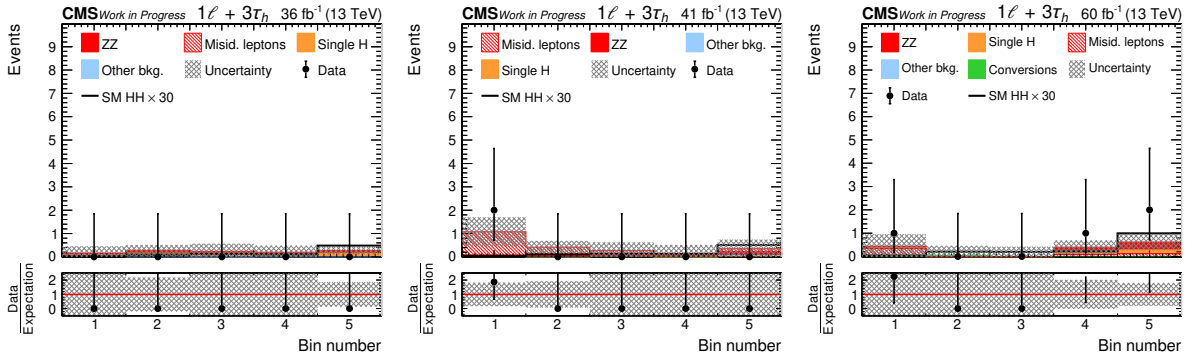

Figure 8.51: Postfit plots (2016-2018) for the $3\ell + 1\tau_h$ channel with SM like non-resonant HH signal on the JHEP04BM7 optimized nonRes BDT output (scaled to $30 \times \sigma_{HH}^{SM}$).

Postfit 2ℓ(ss) + 0/1 τ_h

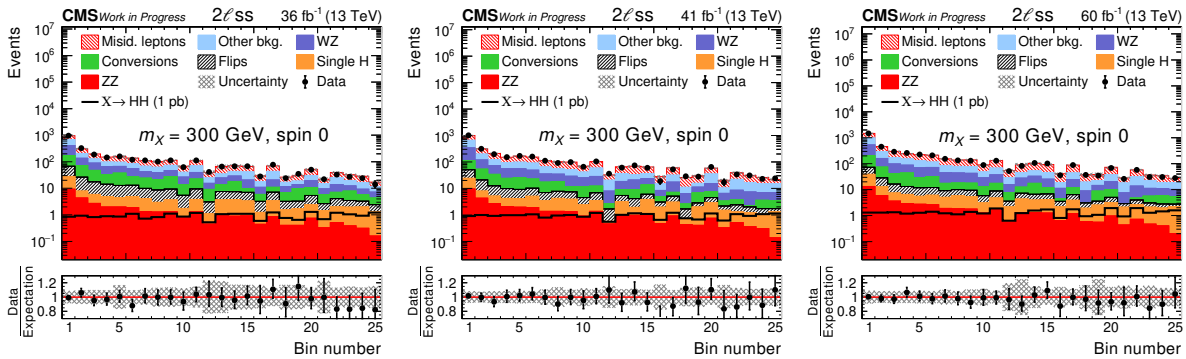

Figure 8.52: Postfit plots (2016-2018) for the 2ℓ(ss) + 0/1 τ_h channel with resonant ggHH signal for the spin-0 case and $m_\chi = 300\,\text{GeV}$ (scaled to 1 *pb*).

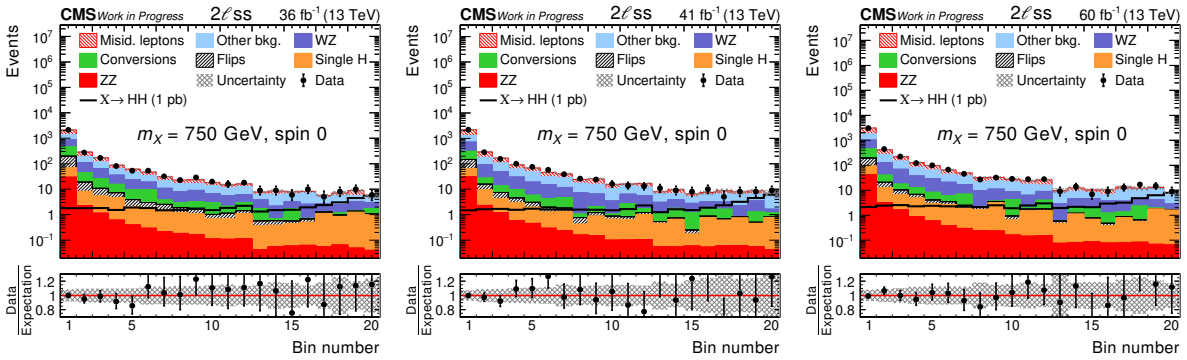

Figure 8.53: Postfit plots (2016-2018) for the $2\ell(\text{ss}) + 0/1\ \tau_\text{h}$ channel with resonant ggHH signal for the spin-0 case and $m_\chi = 750\,\text{GeV}$ (scaled to 1 pb).

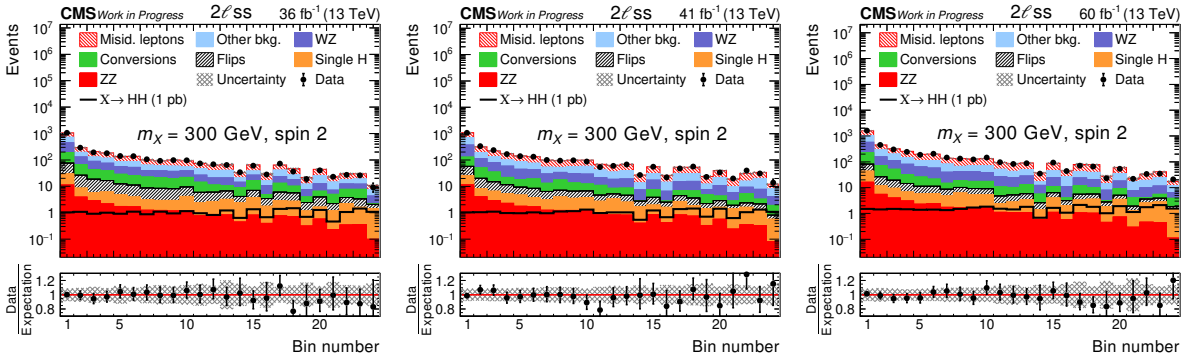

Figure 8.54: Postfit plots (2016-2018) for the $2\ell(\text{ss}) + 0/1\ \tau_\text{h}$ channel with resonant ggHH signal for the spin-2 case and $m_\chi = 300\,\text{GeV}$ (scaled to 1 pb).

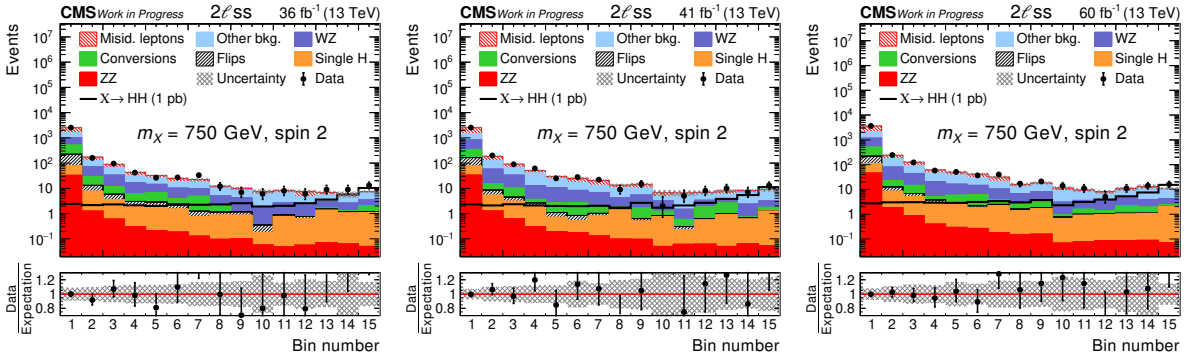

Figure 8.55: Postfit plots (2016-2018) for the $2\ell(\text{ss}) + 0/1\ \tau_\text{h}$ channel with resonant ggHH signal for the spin-2 case and $m_\chi = 750\,\text{GeV}$ (scaled to 1 pb).

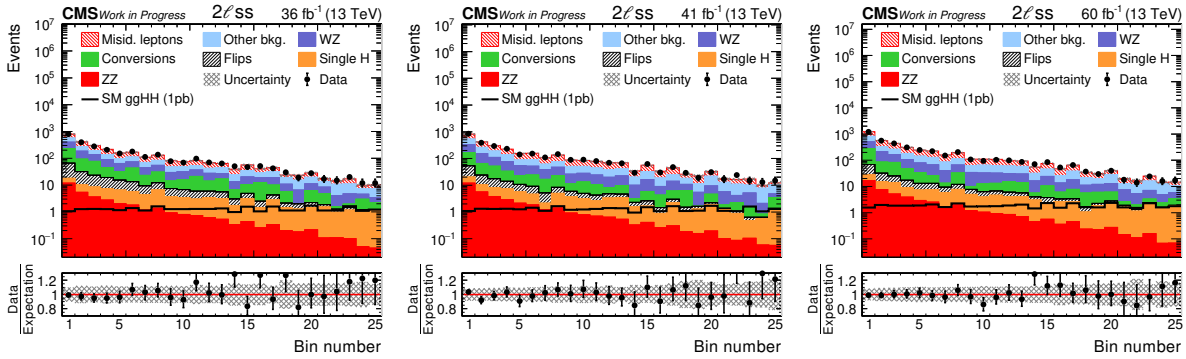

Figure 8.56: Postfit plots (2016-2018) for the 2ℓ(ss) + 0/1 τ_h channel with SM non-resonant ggHH signal on the SM optimized nonRes BDT output (scaled to 1 *pb*).

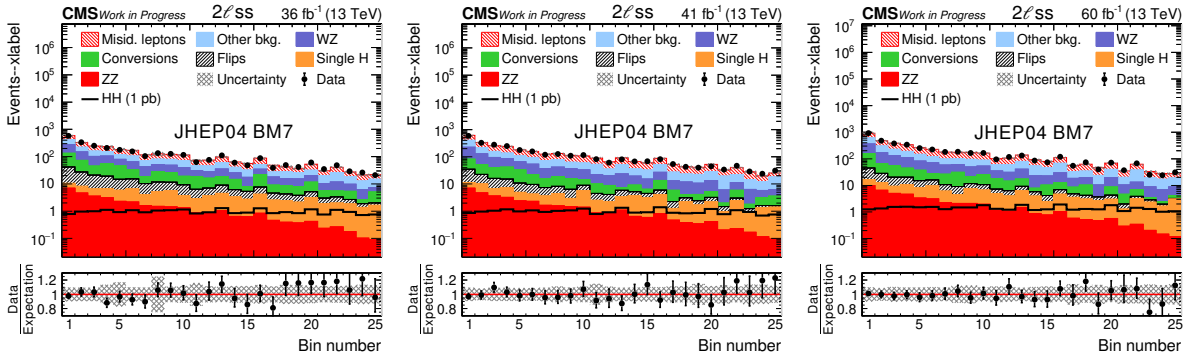

Figure 8.57: Postfit plots (2016-2018) for the 2ℓ(ss) + 0/1 τ_h channel with non-resonant ggHH signal for the JHEP04BM7 scenario (scaled to 1 *pb*).

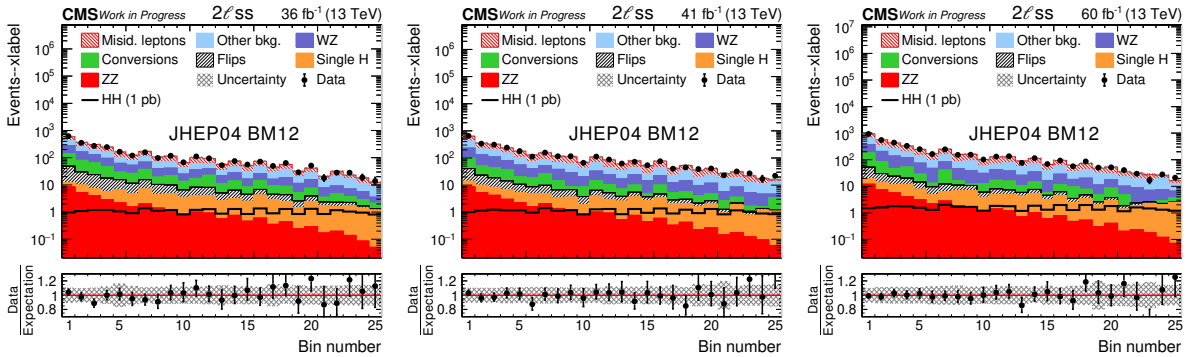

Figure 8.58: Postfit plots (2016-2018) for the 2ℓ(ss) + 0/1 τ_h channel with non-resonant ggHH signal for the JHEP04BM12 scenario (scaled to 1 *pb*).

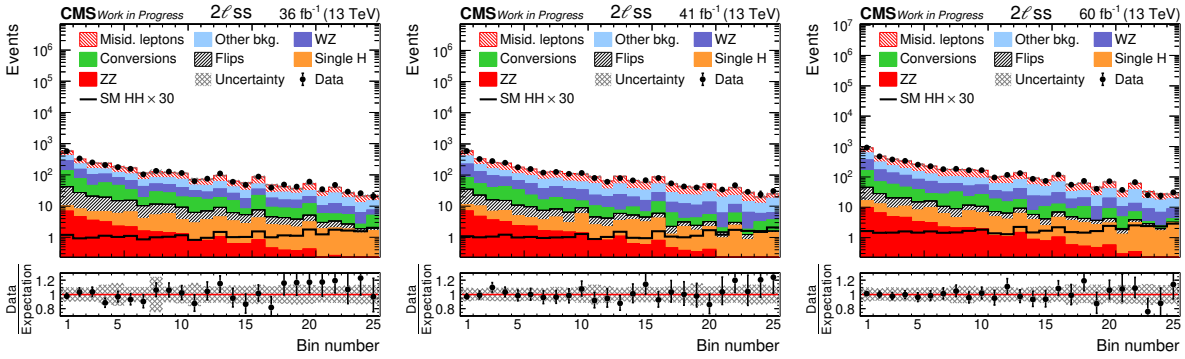

Figure 8.59: Postfit plots (2016-2018) for the 2ℓ(ss) + 0/1 τ_h channel with SM like non-resonant HH signal on the JHEP04BM7 optimized nonRes BDT output (scaled to $30 \times \sigma_{HH}^{SM}$).

Postfit $3\ell + 0\tau_h$

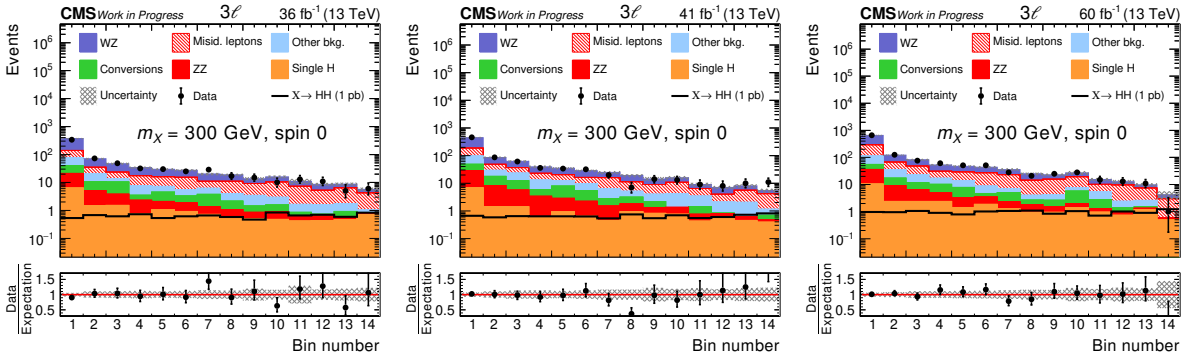

Figure 8.60: Postfit plots (2016-2018) for the $3\ell + 0\tau_h$ channel with resonant ggHH signal for the spin-0 case and $m_\chi = 300\,\text{GeV}$ (scaled to $1\,pb$).

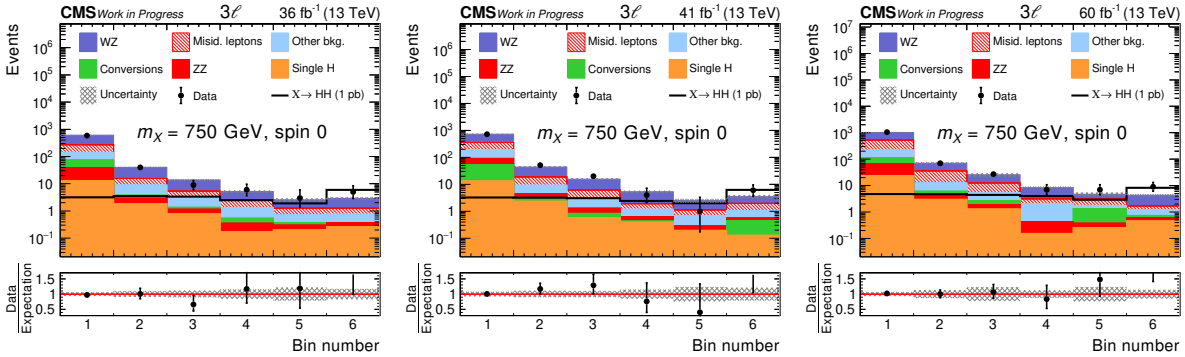

Figure 8.61: Postfit plots (2016-2018) for the $3\ell + 0\tau_h$ channel with resonant ggHH signal for the spin-0 case and $m_\chi = 750\,\text{GeV}$ (scaled to $1\,pb$).

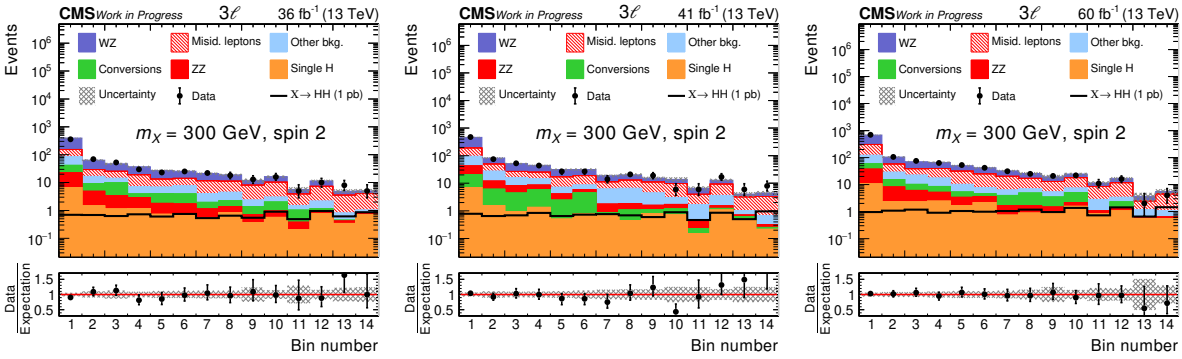

Figure 8.62: Postfit plots (2016-2018) for the $3\ell + 0\tau_h$ channel with resonant ggHH signal for the spin-2 case and $m_\chi = 300\,\text{GeV}$ (scaled to 1 *pb*).

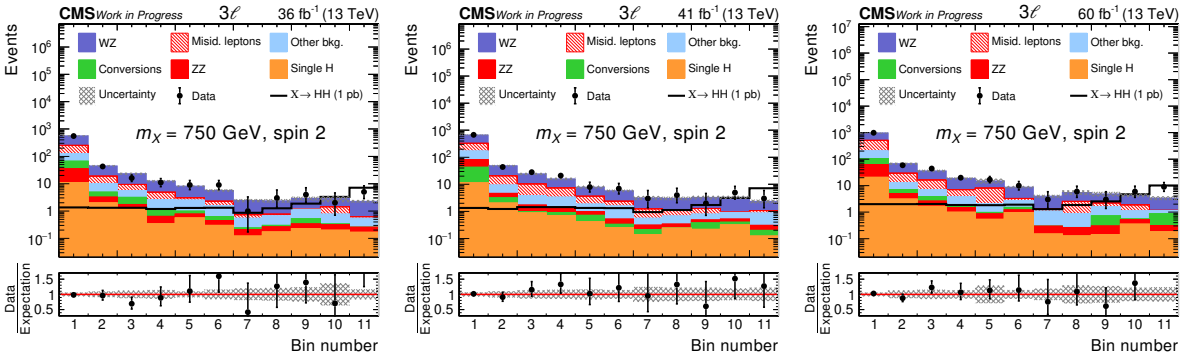

Figure 8.63: Postfit plots (2016-2018) for the $3\ell + 0\tau_h$ channel with resonant ggHH signal for the spin-2 case and $m_\chi = 750\,\text{GeV}$ (scaled to 1 *pb*).

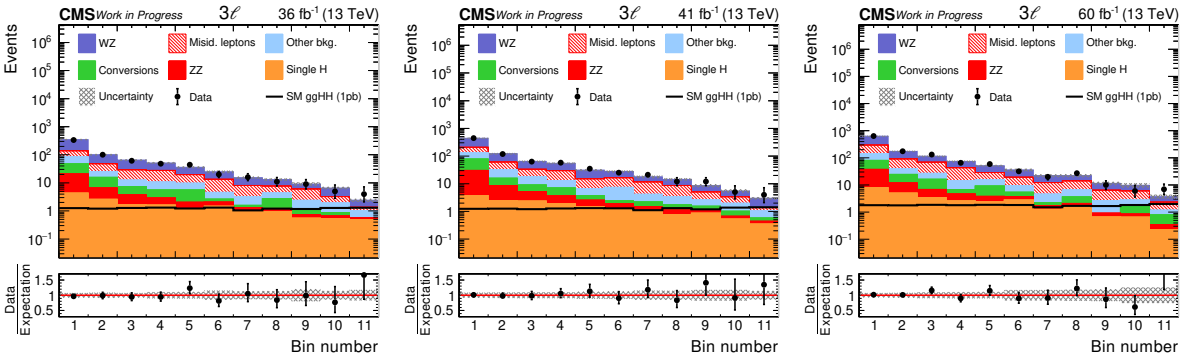

Figure 8.64: Postfit plots (2016-2018) for the $3\ell + 0\tau_h$ channel with SM non-resonant ggHH signal on the SM optimized nonRes BDT output (scaled to 1 *pb*).

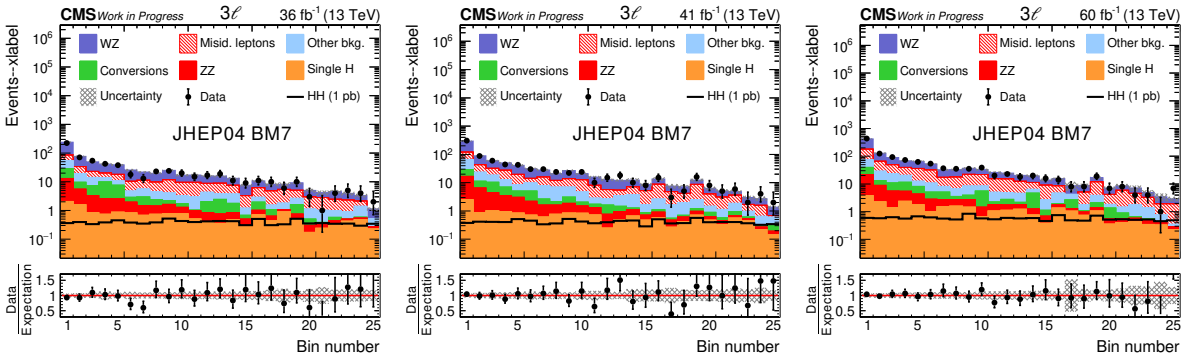

Figure 8.65: Postfit plots (2016-2018) for the $3\ell + 0\tau_h$ channel with non-resonant ggHH signal for the JHEP04BM7 scenario (scaled to 1 *pb*).

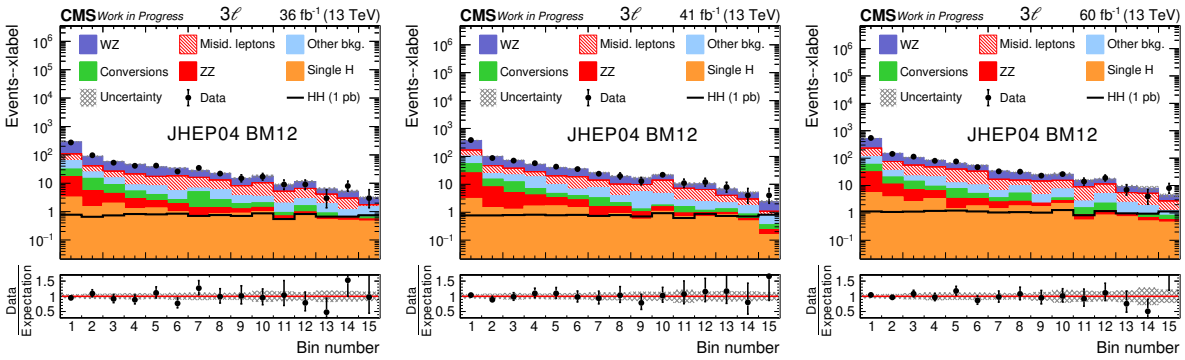

Figure 8.66: Postfit plots (2016-2018) for the $3\ell + 0\tau_h$ channel with non-resonant ggHH signal for the JHEP04BM12 scenario (scaled to 1 *pb*).

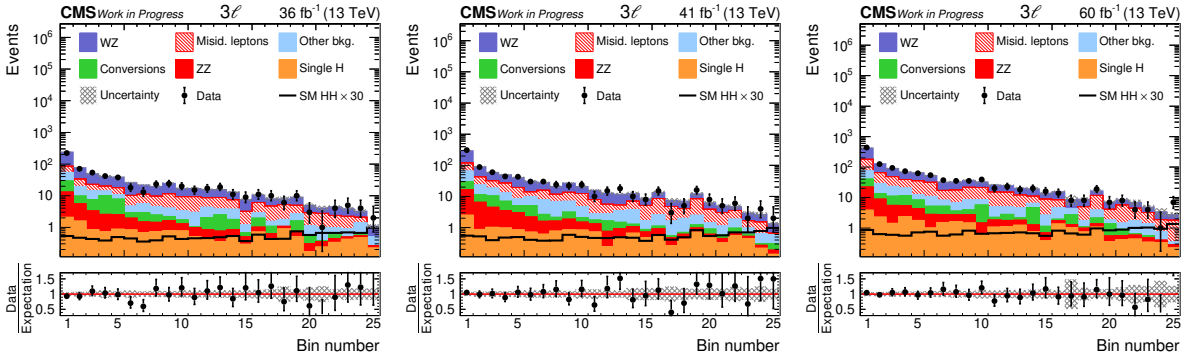

Figure 8.67: Postfit plots (2016-2018) for the $3\ell + 0\tau_h$ channel with SM like non-resonant HH signal on the JHEP04BM7 optimized nonRes BDT output (scaled to $30 \times \sigma_{HH}^{SM}$).

Postfit 4ℓ

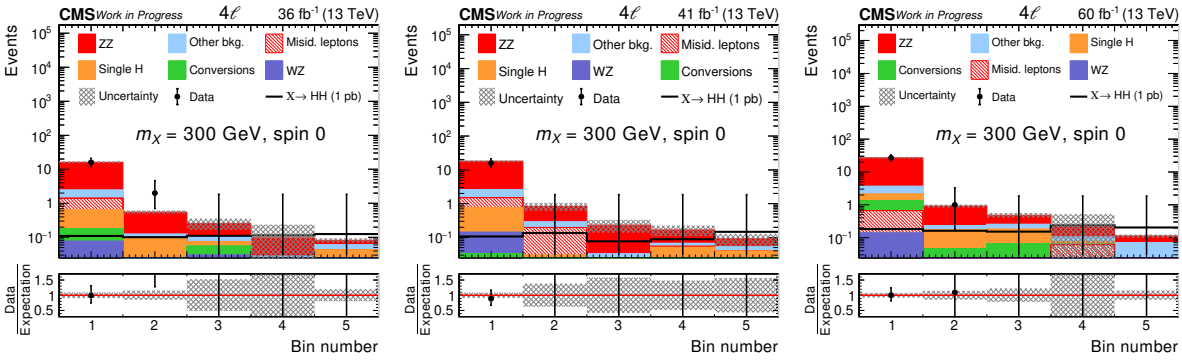

Figure 8.68: Postfit plots (2016-2018) for the 4ℓ channel with resonant ggHH signal for the spin-0 case and $m_\chi = 300\,\text{GeV}$ (scaled to 1 *pb*).

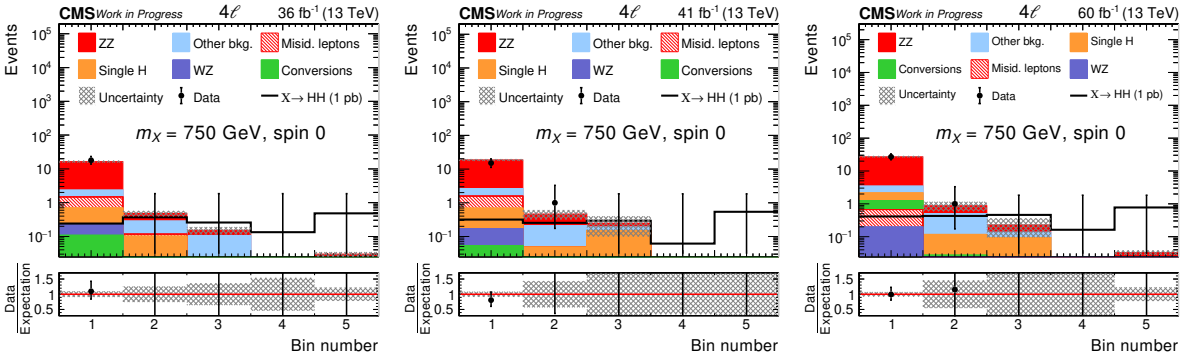

Figure 8.69: Postfit plots (2016-2018) for the 4ℓ channel with resonant ggHH signal for the spin-0 case and $m_\chi = 750\,\text{GeV}$ (scaled to 1 *pb*).

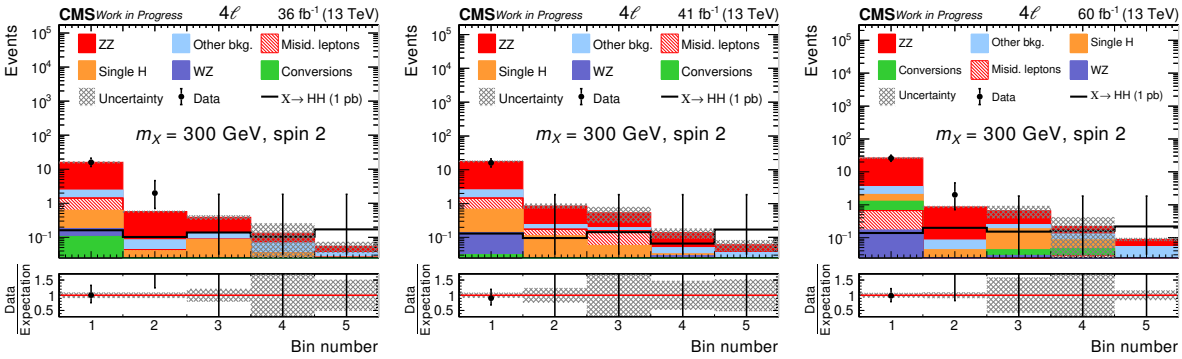

Figure 8.70: Postfit plots (2016-2018) for the 4ℓ channel with resonant ggHH signal for the spin-2 case and $m_\chi = 300\,\text{GeV}$ (scaled to 1 *pb*).

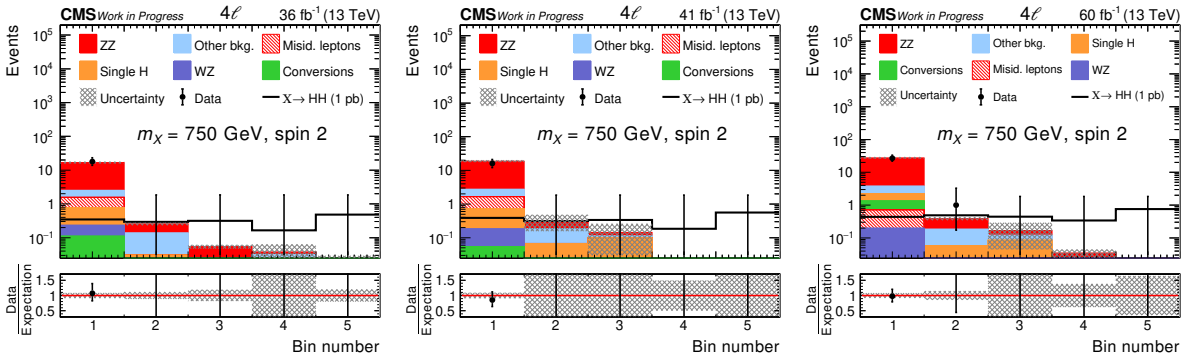

Figure 8.71: Postfit plots (2016-2018) for the 4ℓ channel with resonant ggHH signal for the spin-2 case and $m_\chi = 750\,\text{GeV}$ (scaled to 1 pb).

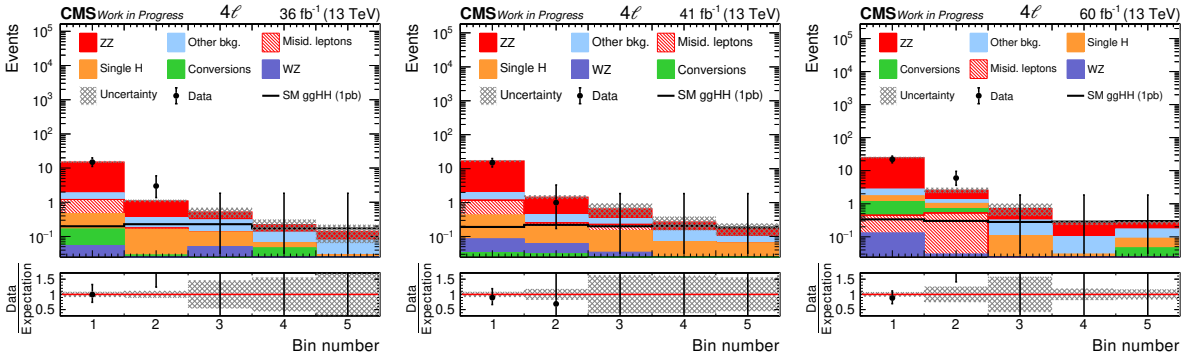

Figure 8.72: Postfit plots (2016-2018) for the 4ℓ channel with SM non-resonant ggHH signal on the SM optimized nonRes BDT output (scaled to 1 pb).

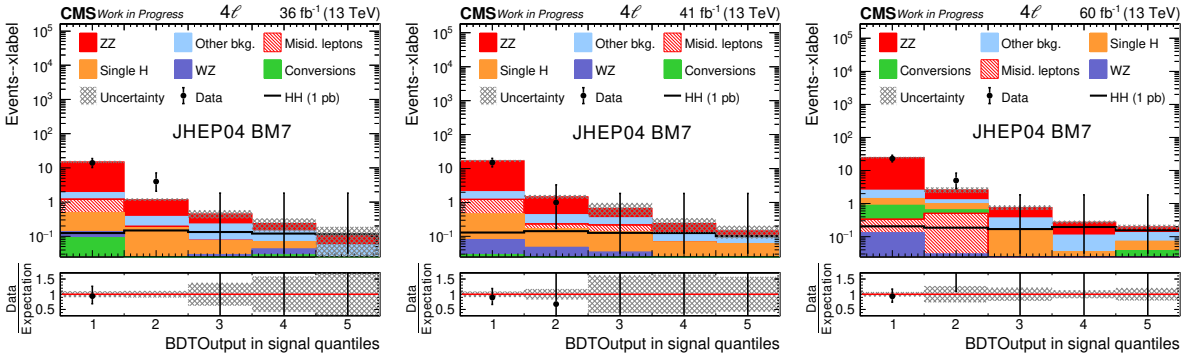

Figure 8.73: Postfit plots (2016-2018) for the 4ℓ channel with non-resonant ggHH signal for the JHEP04BM7 scenario (scaled to 1 pb).

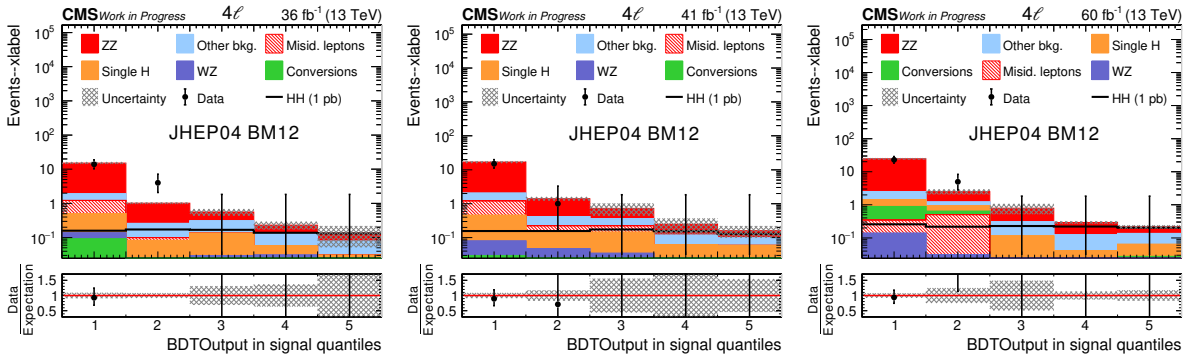

Figure 8.74: Postfit plots (2016-2018) for the 4ℓ channel with non-resonant ggHH signal for the JHEP04BM12 scenario (scaled to 1 *pb*).

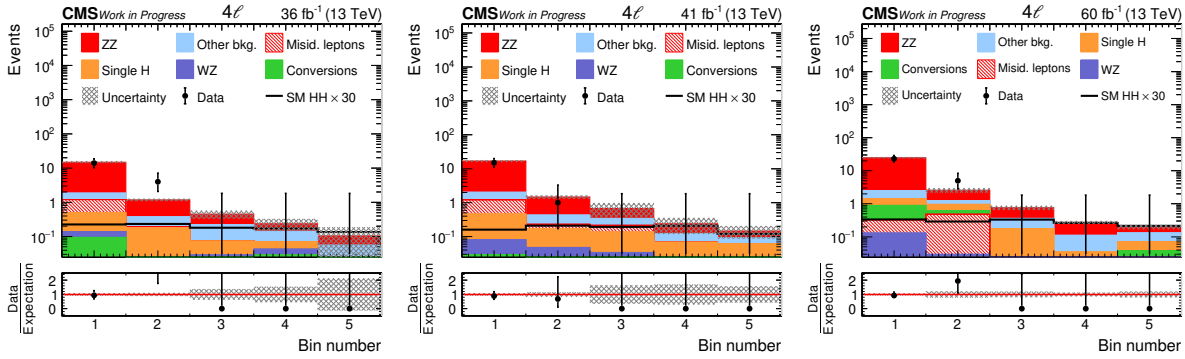

Figure 8.75: Postfit plots (2016-2018) for the 4ℓ channel with SM like non-resonant HH signal on the JHEP04BM7 optimized nonRes BDT output (scaled to $30 \times \sigma_{\mathrm{HH}}^{\mathrm{SM}}$).

Postfit 3ℓ CR and 4ℓ CR

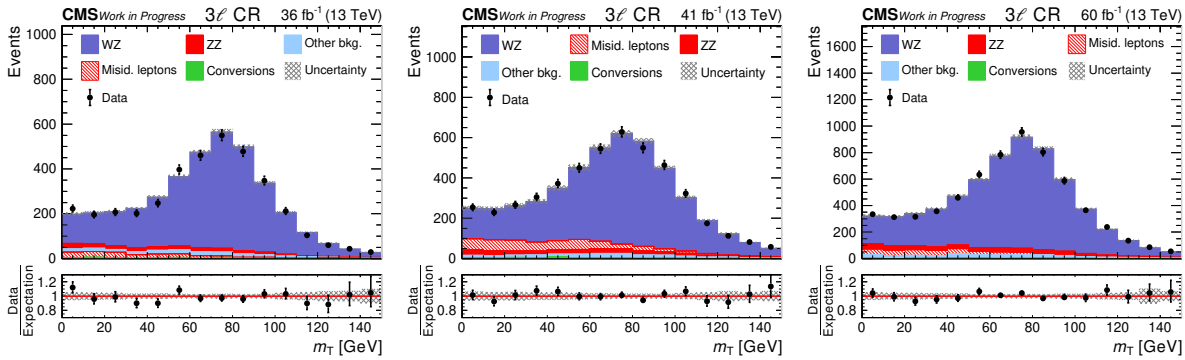

Figure 8.76: Postfit plots (2016-2018) for the 3ℓ CR.

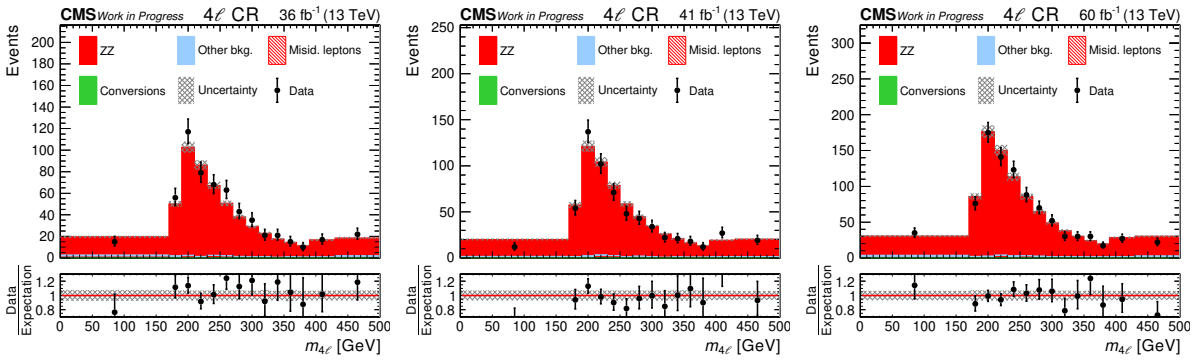

Figure 8.77: Postfit plots (2016-2018) for the 4ℓCR.